VRIJE UNIVERSITEIT

Structure and dynamics of active actin-myosin networks

An *in vitro* perspective

ACADEMISCH PROEFSCHRIFT

ter verkrijging van de graad Doctor
aan de Vrije Universiteit Amsterdam,
op gezag van de rector magnificus
prof.dr. L.M. Bouter,
in het openbaar te verdedigen
ten overstaan van de promotiecommissie
van de faculteit der Exacte Wetenschappen
op vrijdag 21 oktober 2011 om 9.45 uur
in de aula van de universiteit,
De Boelelaan 1105

door
Marina Soares e Silva

geboren te Porto, Portugal

Promotoren:

Prof. dr. Gijsje H. Koenderink
Prof. dr. Frederick C. MacKintosh

Contents

Chapter 1

Introduction

Cells are wonderfully complex microcosms and also the building blocks that allow living organisms to reproduce and survive. Ultimately, the cellular machinery supports the evolution of species of different organisms. Cells divide and grow by actively changing shape, thus allowing organisms to thrive. These shape changes are supported by the cytoskeleton, a mechanical scaffold of filamentous proteins in the cytoplasm. The actin cortex is the principal cytoskeletal component which provides cells with the drive for active shape changes. It consists of actin filaments and myosin II motor filaments which form a network with contractile properties. Myosin motors generate forces that propagate through the network structure and locally remodel it so as to fulfill functions as diverse as cell division or cellular rearrangement in tissues. This thesis aims at understanding how contractility on a molecular scale leads to cell-scale active behavior. To this end, a bottom-up quantitative approach is used based on the assembly of a minimal model of the actin cortex. This approach allows for a systematic study of the physical phenomena that contribute, in concert with biochemical regulatory networks, to cell contractility and opens the way for modeling of such out-of-equilibrium materials. Additionally, minimal model systems of the membrane-actin cortex interaction provide insights in the effect of confinement on the structure of the cortex. In this chapter I introduce the cell as the basic unit of life and describe how it is able to carry out contractility-driven functions. I focus on the actin cortex, the cell component which drives changes in cellular shape leading both to intracellular pattern formation and to rearrangements at the tissue/body level. Finally, I briefly review biophysical experimental studies and theories on the structure and dynamics of the actin cortex and provide an outline of the thesis.

1.1 The cell: life in a nutshell

Life on Earth relies on an essential building block called the cell. This basic functional unit represents the beginning of the life cycle for most organisms, with the rare exception of entities such as viruses. The latter are difficult to place on a defined position on the axis of living versus non-living matter. The cell represents the smallest minimal operational component for life to be maintained. Some organisms, such as bacteria or unicellular eukaryotes, are in fact restricted to a single cell as a form of body during their entire life. However, as the amount of genetic information increases so does the possibility to explore more complex developmental programs and to translate them into highly structured bodies. As this happens communication and cooperation between cells becomes relevant. The epitome of such cellular cooperation is the complexity found in higher eukaryotes such as animals and plants. These multicellular organisms embody a number of different types of tissues where cells execute different functions and operate as part of specialized organs.

This intricate complexity has long been a powerful source of curiosity to the scientific community. Amidst complex body forms we have learned to recognize, categorize and reproduce the patterns that living beings, ourselves included, display. Organs, tissues and cells are the motifs that organize along various sorts of axes of symmetry to give rise to fully formed and functional bodies. Perhaps the most beautiful snapshots of such patterns and symmetries have been captured in the 19th century by the hand of German naturalist and comparative zoology professor Ernst Haeckel (Fig. 1.1). With much detail but at the same time allowing room for his own artistic creativity he produced numerous aquarelles, later turned to lithographs, of animals, plants and microbes emphasizing their underlying body plan symmetries [1]. His nature-inspired illustrations remain an intuitive summary of the extreme diversity and staggering degrees of complexity that emerge in living organisms. In this manner, he captured the patterns emerging from the continuous and dynamic interaction of genetics and the environment. These are the interactions that lead to the organization of single cells and of cells into complex organisms.

Common to all these organisms are their basic cellular mechanisms and type of cellular structures. Irrespective of the obvious differences in complexity and specificity of functions, all cells are essentially compartments carrying genetic information. While in prokaryotes like bacteria this information is not separated into any sub-compartments inside the cell body, eukaryotes contain a nucleus, bounded by an internal membrane that separates the genetic information from the rest of the cell medium, the cytoplasm (Fig. 1.2). Both prokaryotic and eukaryotic cells have a boundary with the external environment called the plasma membrane. This boundary confines cellular components but it allows exchanges with the surroundings or

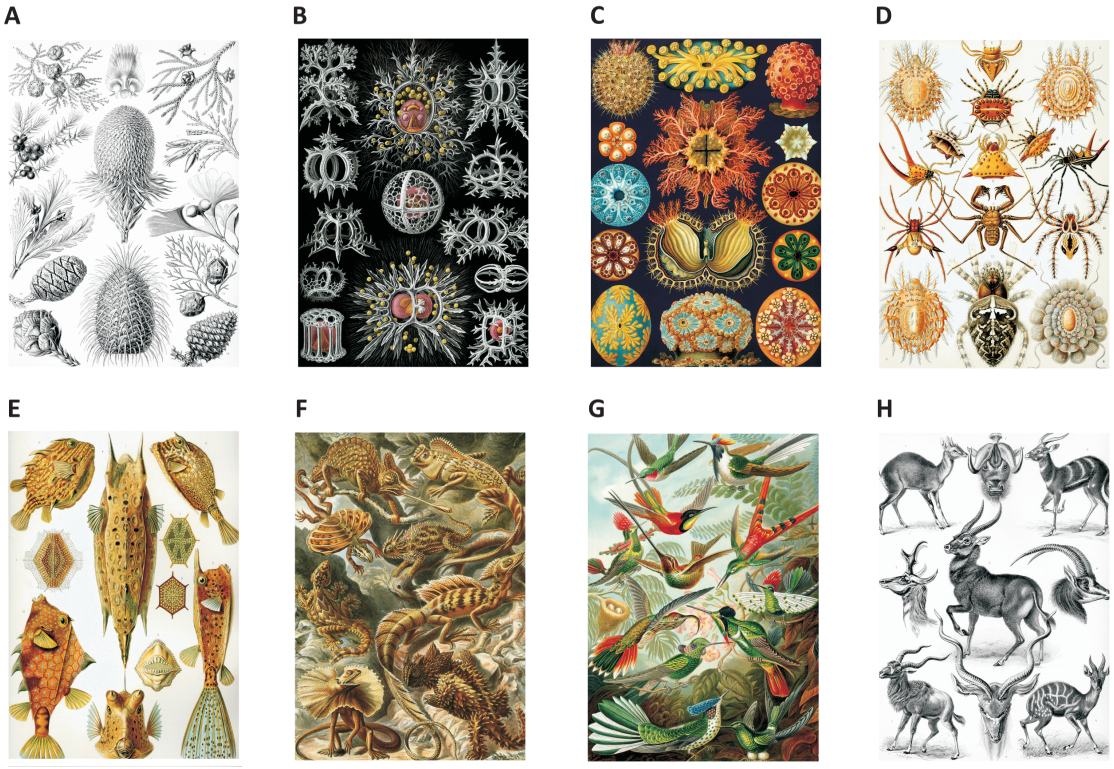

Figure 1.1: Art forms in Nature or how patterns catch the beholder's eye. Facsimiles of Ernst Haeckel's lithographs of various eukaryote groups of kingdoms Plantae (A.), Protozoa (B.) and Animalia (C-H) (in Kunstformen der Natur, 1904 REF). **A.** Conifer pines (Coniferae). **B.** Amoeboid radiolarians (sub-phylum Radiolaria). **C.** Sea squirts (class Ascidiacea) **D.** Arachnids (class Arachnida). **E.** Cowfishes (Ostraciidae). **F.** Lizards (sub-order Lacertilia). **G.** Hummingbirds (family Trochilidae) **H.** Antelopes (Antilopina).

with neighboring cells in a tissue. Furthermore, cells perform functions that are at the basis of the growth and reproduction of living organisms, which include cell division, cell locomotion, and tissue morphogenesis.

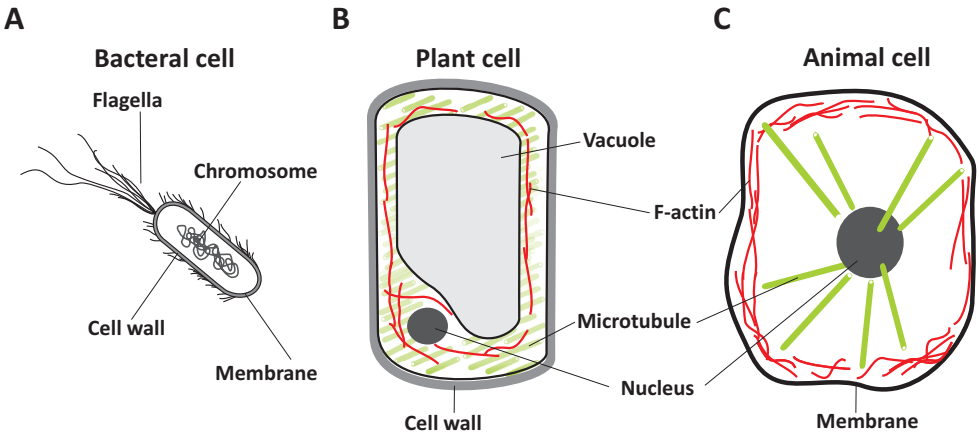

Figure 1.2: Schematic drawing of different cells. **A.** Prokaryotic cell of an *Escherichia coli* bacterium. **B.** Plant cell. **C.** Animal cell.

1.2 The cell as an active and dynamic material

The descriptive works of many naturalists, including Haeckel's [1] have generated an immense wealth of information and helped us understand the anatomy of living organisms. These works have also paved the way for the birth of genetics, as well as for Darwin's studies on evolution. However, with the discovery of Brownian motion [2] and Einstein's work describing its implication for the statistical physics of matter [3] coupled with the dawn of molecular biology describing the structure and function of cellular components, cells began to be perceived as more than simple static *small bag of things*.

Many biophysical techniques and microscopic technologies were developed to explore the structure and dynamics of the living cell, which as any other soft material is constantly subject to thermal fluctuations, but simultaneously operates outside the laws of thermodynamical equilibrium [4]. In cells, fluctuations emerge as a result not only of random thermal motion, but also as a consequence of active processes. These include material exchanges across the cellular membrane that require chemical energy to counteract unfavorable diffusion gradients. Other examples of active cellular processes are those where the cell must drastically change shape like division, loco-

motion and morphogenetic movements leading to tissue organization. This thesis focuses on identifying the origin of the latter contractile processes. These are undertaken by the cytoskeleton, a scaffold of proteins that confers mechanical integrity to cells while also enabling their changes in shape.

1.2.1 The cytoskeleton and the actin cortex

The cytoskeleton is composed of a set of semiflexible biopolymers with different mechanical properties and functions (Fig. 1.3A top). These biopolymers can be characterized by their resistance to bend under the influence of thermal fluctuations. Their bending rigidity determines the length scale over which their backbones remain straight when thermally fluctuating, known as the persistence length (Fig. 1.3A bottom). Microtubules are filaments that are rather stiff on the length scale of the cell, with a persistence length of millimeters [5] (Fig. 1.3B). Among other functions microtubules are responsible for the mechanical integrity of most living eukaryotic cells (except in plants in which a cellulose wall confers mechanical support) [6]. The actin cortex in its turn is composed of filaments that form a network that can actively contract and thus enables the cell to change its shape. This network comes into action when newly duplicated cells separate during division or at the leading edge of a *crawling* cell. Actin filaments (F-actin) are orders of magnitude more flexible than microtubules and have a $17\,\mu\mathrm{m}$ persistence length [5] (Fig. 1.3C). Finally, intermediate filaments are tissue specific biopolymers with an alpha-helical central rod conserved domain, with no known enzymatic activity and whose subunits belong to a heterogeneous group of proteins. A rather well conserved intermediate filament is lamin, which organizes into a meshwork that lines the inner side of the nuclear membrane (Fig. 1.3D) [7]. Intermediate filaments are the cytoskeletal filaments most sensitive to thermal motion, with a persistence length as small as $0.5 - 1\,\mu\mathrm{m}$ [8].

Actin-based structures display a diversity of architectures that reflect their different functions. These structures are composed of actin filaments, polar semiflexible biopolymers that assemble actively from globular actin monomers in an ATP-dependent manner (the structure and F-actin assembly dynamics are described in detail in *chapter 2*). The actin cortex is a randomly organized network of F-actin that exists as a thin layer underneath the cell membrane and provides mechanical stability (Fig. 1.3A). Additionally, actin-filled membrane protrusions form in cells that must move or probe their surroundings [9]. For example, the lamellipodium that emerges at the front of a migrating cell is a quasi-2D sheet of polymerizing filaments of actin that push the membrane in the direction of motion [10, 11]. Thin membrane protrusions filled with actin known as filopodia act as mechanochemical probes for the cell surroundings [12].

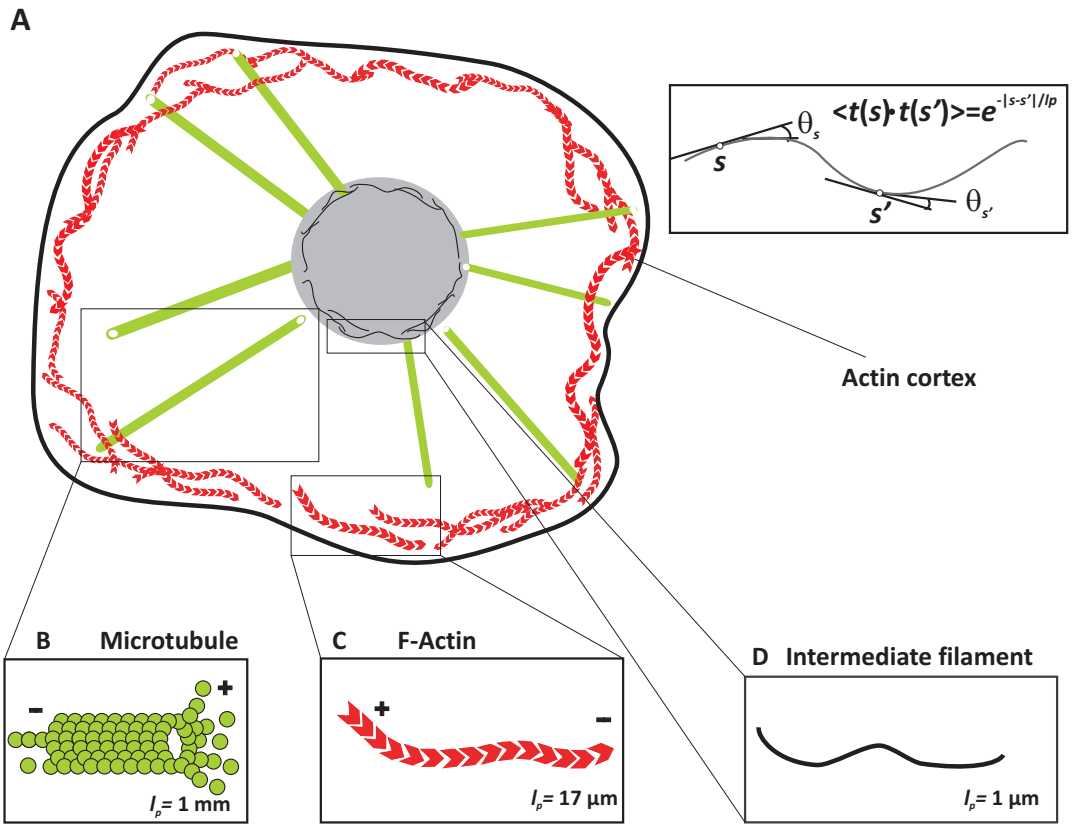

Figure 1.3: **A.** *Top* Schematic drawing of the cell cytoskeleton and its main components. *On the right* Schematic drawing of the persistence length of polymers in response to thermal fluctuations. The persistence length l_p quantifies the decay length of the correlation between tangent vectors $\vec{t}$ to points *s* and *s'* along the polymer contour length *l*. *Bottom* Zoom in on each of the main filamentous components: **B.** Microtubules, polar polymers of tubulin monomers with a plus or growing end and a slower growing minus end. These are stiff polymers of the length scale of the cell with a millimeter persistence length l_p. **C.** Intermediate filaments forming the nuclear lamina. **D.** Filamentous actin (F-actin) polymerized into a polar filament from globular actin monomers (F-actin forms a double helice of globular monomers, here simplified to one strand for representation purposes). On the scale of the cell F-actin is rather flexible with a persistence length on the order of micrometers.

The organization of actin in these structures is extensively regulated by a myriad of actin binding proteins which include filament crosslinkers, filament-nucleating enzymes and motor proteins like myosins [13]. Actin crosslinkers like fascin or filamin organize the network structure into either bundled or isotropic networks [14]. Nucleators of actin like the ARP 2/3 complex lead to the formation of branched networks *in vitro* [15] and have been reported to organize the actin in the lamellipodium of migrating fish keratocytes into branches [11]. While gelsolin and cofilin restrict filament polymerization, profilin favors it [13]. Finally, myosins represent a multifunctional group of actin binding motors with different functions that are divided into 15 classes [16].

Myosin motor functions are organism- and tissue-specific and include the transport of cargo material by myosin V [17] and the mechanical connection of actin bundles in the ear stereocilia of vertebrates by myosin I [17]. The first myosin to be described was myosin II, a dimer with a N-terminal head domain and C-terminal tail domain [16] (the structure of myosin molecules is described in detail in *chapter 2*). The myosin II head domain binds directly to F-actin and it exerts a power stroke as it moves towards the plus-end of actin and consumes ATP. The tail domains of myosin II attach to each other to form bipolar structures with heads pointing outwards called myosin thick filaments. The latter, extensively described in skeletal muscle cells, are an assembly of hundreds of motors able to slide antiparallel actin filaments of the sarcomere (Fig. 1.4A) towards each other as they walk to the actin plus end. This results in an effective contraction of the sarcomere [18]. In non-muscle cells, myosin II minifilaments are composed of only up to tens of motors molecules and they are responsible for a myriad of processes that result in an active change of cell shape [19].

1.2.2 Myosin-II dependent contractile processes in the actin cytoskeleton

The tension generated by myosin II motor filaments is the driving force of contractile processes both at the cell and at the tissue level (Fig. 1.4B). During cell division actin organizes into a ring-like structure at the center of the dividing cell. Myosin minifilaments colocalize with this actin structure [20] and produce a force able to constrict the cell and divide it into two daughter cells each carrying their genetic information in the chromosomes (Fig. 1.5A). Another example of myosin contractility takes place in the cortex during cell locomotion. While at the leading edge of the migrating cell actin polymerization propels the cell forward as the filaments grow against the membrane, at the back myosin filaments contract the network so as to detach the rear end of the cell from the substrate and propel it in the same direction of movement (Fig.

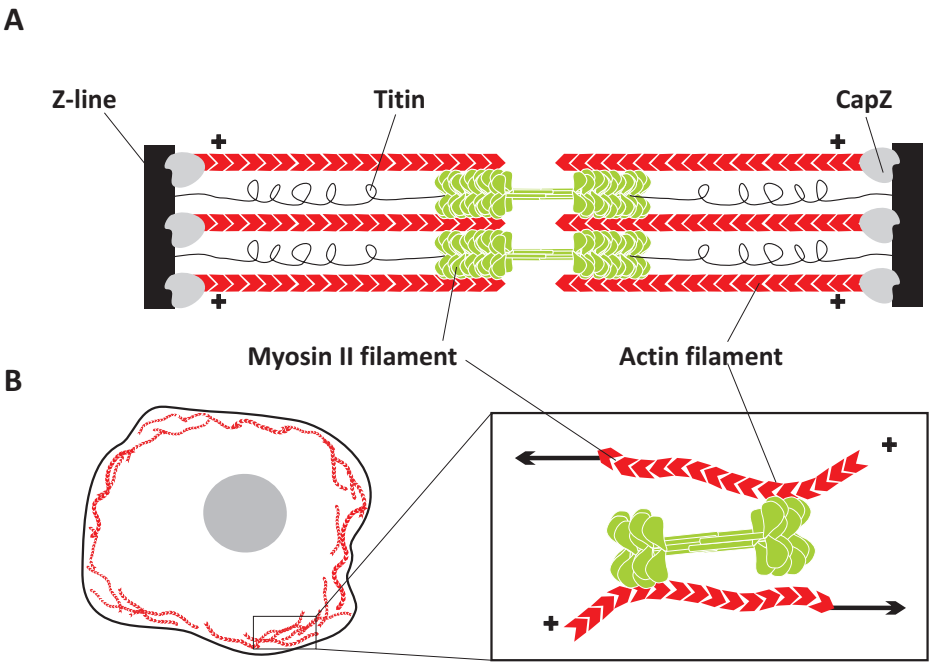

Figure 1.4: Schematics of contractility generated by myosin II assemblies. **A.** Schematic of a sarcomere, the muscle fiber contractile unit. In physiological conditions, myosin molecules assemble tail to tail into bipolar structures with heads pointing outwards (myosin filaments) and thus become effectively processive. At each instant they have a number of their heads attached to actin filaments and as they walk to their barbed or plus end (plus sign) they contract the symmetrical parts of the sarcomere towards each other. **B.** In isotropic networks like the actin cortex, myosin filaments slide actin filaments past each other in the network and generate contractile tension when the actin filaments are crosslinked to each other.

1.5B).

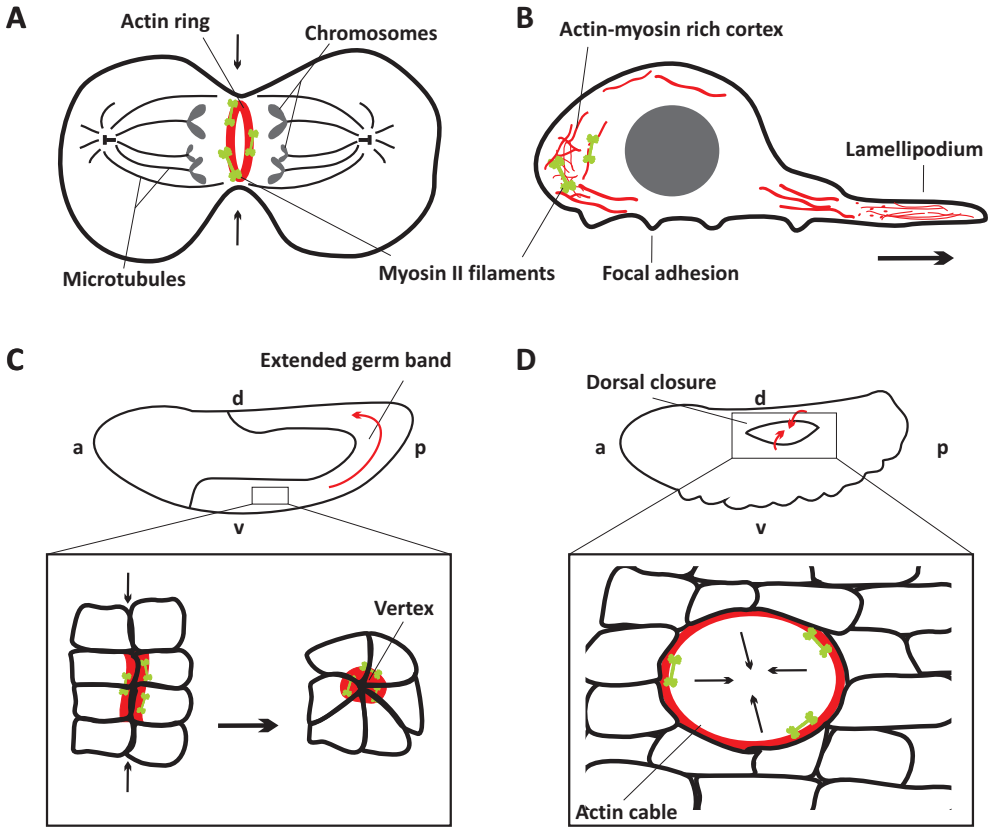

Figure 1.5: Schematic drawings of different contractile phenomena driven by actin-myosin. **A.** Myosin II motors generate force that leads to contractile ring constriction and ultimately results in cell separation during cytokinesis. **B.** Cell locomotion is driven at the lamellipodium by polymerizing forces of F-actin assembling, and the back of the cell the cortex is contracted by myosin filaments so as to *carry* the rear of the cell in the same direction of motion. **C.** During germ band extension actin-myosin cables form along the antero-posterior interfaces between neighboring cells. Later these collapse due to actin contractility into a vertex which leads to the formation of rosettes of cells that are responsible for the net extension of the germ band and elongation of the embryo body. **D.** Morphogenetic events during embryo development are driven by the constriction of a supracellular actin cable that is pulled upon by myosin II.

Actin-myosin has also been reported to regulate various contractile processes in developing tissues [21]. Among these morphogenesis-related phenomena is the movement of the germ layers in early embryos. During elongation of the body axis (a few hours after eggs are layed) in Drosophila melanogaster (fruit fly) early embryos, a tissue called the germ band (Fig. 1.5C, top) narrows along the dorso-ventral axis

of the embryo (vertical axis in the schematic, bottom left in Fig. 1.5 C) while it elongates along the antero-posterior axis (horizontal axis in the schematic, bottom left in Fig. 1.5C) [22]. This is a myosin motor-driven process where actin and myosin form cables along the antero-posterior axis of neighboring cells that also contract along it [23, 24]. This leads to the rearrangement of interfaces of neighboring cells, culminating in formation of a vertex and organization of cells into rosettes (bottom right, Fig. 1.5C) [25]. The latter are the functional units that drive the extension of the embryo germ band along the antero-posterior axis to generate body elongation [25]. After the embryo has undergone body elongation, cells of the amnioserosa on the dorsal surface of the embryo decrease the gap between the cephalic region and the dorsal part of the body [26]. This is a process coordinated by the formation of a supracellular actin-myosin ring-like structure that contracts to close the gap on the amnioserosa (Fig. 1.5D) [26].

1.3 Cellular microrheology reflects the out-of-equilibrium behavior of the cytoskeleton

During the past two decades, several studies sought to study *in vivo* the origin of the mechanical properties of the cell [27, 28, 29, 30, 31]. To this end many microrheological approaches have been developed so as to probe different cellular compartments such as the actin cortex or the microtubule- and intermediate filament-rich center of the cytoplasm. These methods are based on the time-resolved tracking of the spatial coordinates of particles applied to the surface of [27, 28, 32], inserted in [30, 33, 34] or endogenous to the cell [31, 35, 36]. The variations in particle positions reflect the fluctuations of the probed structure, which in turn are tightly connected to its mechanical properties.

The cell is a viscoelastic material whose mechanical properties are in great part defined by the susceptibility of its cytoskeletal filaments to fluctuate. Like any other semiflexible polymer, cytoskeletal biopolymers are prone to thermally fluctuate. However, recent work on the microrheology of different types of cells has shown that such cells exhibit a clear departure from thermal (equilibrium) behavior [30, 37, 38]. This deviation is attributed to active phenomena in the cytoplasm such as the transport of cellular material by microtubule binding motors [33, 35] or the contractile fluctuations induced by myosin motors in the actin cortex [34, 38, 39]. However, it is not straightforward to disentangle the contribution of thermal and non-random out-of-equilibrium fluctuations to the mechanical properties of the cell *in vivo*. For that purpose bottom-up biophysics has focused on the investigation of minimal models of cellular components that mimic *in vivo* behavior [40].

1.4 Minimal model systems to decipher the origins of cytoskeletal non-thermal dynamics

Cellular complexity is simultaneously the source of many interesting physical puzzles as well as an obstacle to understanding them. To overcome the barrier of complexity and yet to form a complete understanding of cells, minimal model systems mimicking specific cellular components have been devised. These pave the way for an integrated thorough study of cells. Many biophysicists have focused on the structure and dynamics of the actin cytoskeleton using such bottom-up approaches [15, 41, 42, 43, 44, 45, 46]. The minimal model principle provides tools to study the single molecule interactions of cytoskeletal filaments and associated binding motors [47], but also tools to understand how collections of motor molecules interacting with actin filaments can lead to meso-scale active network behavior. Studies of bulk actin networks have been largely used as minimal model systems. Originally, such systems have been used mostly as a a basis to understand the underlying mechanical properties of actin networks [44, 41, 43, 46, 45], and more recently several studies moved on to the out-of-equilibrium behavior of actin networks containing active myosin motors (*chapter 4*, [48, 49, 50, 51].

1.4.1 *In vitro* reconstituted actin networks

The mechanical properties of actin networks confer to cells the ability to swiftly adapt their shape to perform different functions. Many researchers have focused efforts on understanding what underlying factors tune actin structure and mechanics. Such work includes a vast number of experiments on how crosslinkers of actin lead to network strain stiffening at high strains [52, 53] or how they tune structure [54]. Other studies investigated the influence of actin density on structure [41, 55, 56, 57] and dynamics [44] of the network. These studies were based on assays using bulk actin networks, whose composition and structure was modulated by the controlled addition of crosslinkers. Complementary to this, research on active actin-myosin gels has focused on understanding how the myosin II motor remodels the network structure and mechanical properties by generating internal stresses [49, 58, 59, 60] and identifying the underlying dynamics of these out-of-equilibrium materials [48, 49, 50, 51] (Fig. 1.6A). Nonetheless, a clear connection between the emergence of patterns and its relation with active local contractile fluctuations remains to be elucidated.

In contrast with bulk approaches which focus on presupposed continuum, isotropic and boundary-insensitive actin gels, confinement studies investigate the influence of container size and boundaries on the network structure and dynamics by polymerizing actin networks inside vesicles [61] or liposomes [62] (Fig. 1.6B). These works

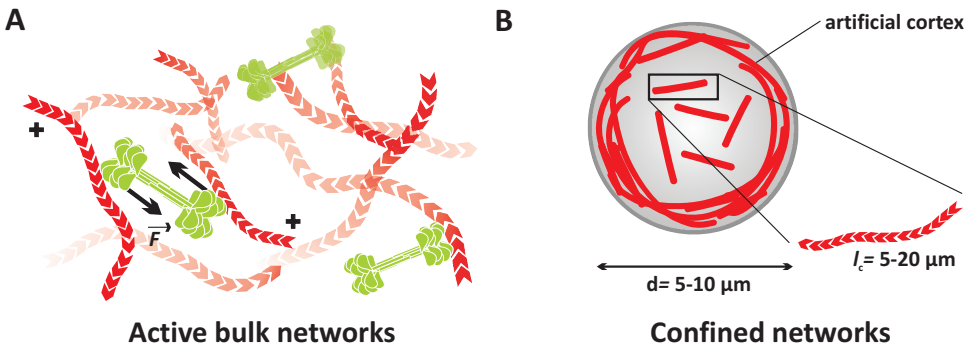

Figure 1.6: Minimal models to study structure and dynamics of actin networks. **A.** Schematic drawing of an active bulk composite actin network. Actin filaments are crosslinked and pulled upon (in crosslinked networks) by myosin filaments which modulate the network structure and mechanics. **B.** The effect of the cell membrane on actin organization has been studied in soft confinement (using artificial liposomes or vesicles).

have reported the spontaneous formation of a thin cortical actin shell on the inside of these spherical soft containers [61]. This arrangement results from alignment of the filament with the boundary to minimize their bending energy whenever their contour length is comparable to the container diameter [63]. In soft confinement, however, a systematic variation of container size is not easy. In addition to systematically studying the effect of container size, it would be interesting to also test the effect of geometries other than spherical so as to assess the influence of the confining cellular shape on cytoskeletal biopolymers.

1.4.2 Active gel models

Active materials have captivated the interest of physicists as they at once provide a means to elucidate the mechanics and dynamics of living materials and exhibit thus far underexplored out-of-equilibrium physical phenomena. The structure of active gels has been intensively investigated with *in vitro* minimal systems [63, 59, 60, 64, 65, 66], and several hydrodynamic theories have been able to describe pattern formation of 2D actively assembled topologies assuming that the gel is a homogenous continuum [64, 67, 68, 69]. These coarse-grained mesoscale models of active polar gels successfully predict patterns of self-organization in systems of small motor aggregates that sort polar rigid-like filaments. Microtubules and their kinesin motors are a system well understood under these assumptions of medium continuity and filament polarity essential for pattern formation [64, 69].

Actin and myosin are a different system, since actin filaments are rather flexi-

ble polymers (persistence length $\sim 15\,\mu\mathrm{m}$ [5]) compared to microtubules (persistence length $\sim 1\,\mathrm{mm}$ [5]) and since myosin motors assemble in large bipolar clusters containing up to hundreds of molecules. Microscopic theories, inspired by theories developed for microtubule-kinesin systems, suggested that the collective myosin motor dynamics lead to a network stiffening at high frequencies while facilitating softening at zero frequencies [70]. Other theoretical work of active actin-myosin networks focused on the actual microscopic implications of motor-generated stresses on active networks dynamics [71, 72, 73]. These theories too assume that the actin gel is a continuum and describe force centers as dipoles randomly distributed within the isotropic network. They are able to capture the experimentally observed actin network stiffening that emerges from the out-of-equilibrium motor-induced contractile fluctuations [50, 51]. A clear cut connection between pattern formation and dynamics and how force distribution and fluctuations influence network remodeling is still lacking. This thesis addresses this interesting puzzle.

1.5 Scope of this thesis

In this thesis, I present experimental research on the structure and dynamics of actin networks under the influence of myosin motors or spatial confinement. I use an *in vitro* approach where I study minimal model systems composed of purified actin and myosin. To test the influence of myosin on actin organization and dynamics, I use confocal microscopy and particle tracking microrheology on bulk networks. To test the influence of confinement on actin organization, I polymerize actin in cell-sized hardwall microchambers.

In *chapter 2*, I introduce the methods used to reconstitute actin-myosin networks *in vitro*. The processes of protein purification and fluorescent labeling are described in detail. Moreover, the experimental techniques used to characterize the mechanical properties of actin filaments and networks are introduced, and I describe the characterization of the structure and self-assembly of myosin into bipolar filaments.

In *chapter 3*, I study out-of-equilibrium self-organization in actin networks driven by myosin motor activity, using fluorescence confocal microscopy. I demonstrate that myosin causes actin network coarsening in a multi-stage condensation process. The motors initially self-organize into myosin clusters, which then condense adjacent actin into dense shells. Interestingly, these foci-like patterns closely resemble *in vivo* structures observed in various organisms and cell stages, which are involved in myosin-dependent developmental processes and cell division and migration. We propose a new physical mechanism that explains how coarsening and permanent coalescence can emerge in weakly crosslinked actin networks based on the fact that actin filaments have an asymmetric force-extension behavior.

In *chapter 4*, I investigate the consequences of motor activity for dynamics in actin networks. A microrheological approach is used to study non-equilibrium fluctuations caused by myosin contractile activity. I embedded micro-sized probe spheres in actin-myosin networks and measured their displacements with bright field microscopy. I find markedly non-thermal particle trajectories, with periods of nondirected (random) motion interspersed with episodes of active, directed motion. We develop an automated segmentation analysis of particle trajectories to quantify the spatiotemporal frequency of this directed motion. We demonstrate that the frequency of directed motion is highest in early stages of sample aging, when the sample is still coarsening due to motor-driven coalescence, as reported in chapter 3. From ensemble averaged analysis, we retrieve signatures of out-of-equilibrium dynamics activity, such as a diffusive-like mean squared displacement and an enhanced non-Gaussianity of the displacement distribution functions. We have evidence of infrequent correlated motions of multiple particles, which occur only in early stages of sample aging. This work indicates that physical models of nonequilibrium dynamics in active gels should take into account the time-dependent, heterogeneous network structure.

Finally, in *chapter 5*, I investigate how steric confinement, which mimics cell boundaries, influences the spatial organization of dense solutions of actin filaments. I polymerized fluorescently labeled actin networks inside hardwall microchambers with inert surfaces, manufactured with photolithographic techniques. I demonstrate that the actin filaments spontaneously organize into bundle-like structures above a threshold concentration. These bundles align with the longest axis of anisometric chambers and with the diagonal in isometric (square or circular) chambers. We propose that bundling occurs due to the concerted effect of quasi-2D confinement of the longest filaments in the polydisperse length distribution, and depletion interactions induced by the shortest filaments. This mechanism differs from the isotropic-to-nematic transition previously observed in bulk networks, which occurs at much higher actin concentrations. We propose that the steady-state orientation of the bundles results from a competing liquid-crystalline ordering in the chamber center and alignment along the boundaries. This ordering effect of confinement might influence organization of the *in vivo* actin cytoskeleton, especially in confining spaces such as the plant cell cortex or thin membrane protrusions, in conjunction with biochemical regulation and actin-membrane adhesion.

References

[1] Ann Weissman. Ernst haeckel: Art forms in nature. 2006.

[2] R. Brown. A brief account of microscopical observations made in the months of june, july and august, 1827, on the particles contained in the pollen of plants; and on the general existence of active molecules in organic and inorganic bodies. *Phil. Mag.*, 4:161–173, 1828.

[3] A. Einstein. ber die von der molekulartheoretischen theorie der wrme geforderten bewegung von in ruhenden flssigkeiten suspendierten teilchen. *Ann. d. Phys*, 332(17):549–560, 1905.

[4] C. Brangwynne, G. Koenderink, F. MacKintosh, and D. Weitz. Intracellular transport by active diffusion. *Trends in Cell Biology*, 19(9):423–427, 2009.

[5] F. Gittes, B. Mickey, J. Nettleton, and J Howard. Flexural rigidity of microtubules and actin filaments measured from thermal fluctuations in shape. *J. Cell Biol.*, 120(4):923 –934, 1993.

[6] B. Alberts, A. Johnson, J. Lewis, M. Raff, K. Roberts, and P. Walter. *Molecular Biology of the Cell.* Garland Science, New York, 5th edition, 2008.

[7] H. Herrmann and U. Aebi. Intermediate filaments: molecular structure, assembly mechanism, and integration into functionally distinct intracellular scaffolds. *Annu. Rev. Biochem.*, 73(1):749–789, 2011.

[8] L. Kreplak and D. Fudge. Biomechanical properties of intermediate filaments: from tissues to single filaments and back. *BioEssays*, 29(1):26–35, 2007.

[9] R. Furukawa, M. Fechheimer, and K. Jeon. The structure, function, and assembly of actin filament bundles. In *A Survey of Cell Biology*, volume 175, pages 29–90. Academic Press, 1997.

[10] J. Small, M. Herzog, and K. Anderson. Actin filament organization in the fish keratocyte lamellipodium. *J. Cell Biol.*, 129(5):1275 –1286, 1995.

REFERENCES

[11] A. Verkhovsky, O. Chaga, S. Schaub, T. Svitkina, J. Meister, and G. Borisy. Orientational order of the lamellipodial actin network as demonstrated in living motile cells. *Molecular Biology of the Cell*, 14(11):4667–4675, 2003.

[12] P. Mattila and P. Lappalainen. Filopodia: molecular architecture and cellular functions. *Nat. Rev. Mol. Cell Biol.*, 9(6):446–454, 2008.

[13] C. Dos Remedios, D. Chhabra, M. Kekic, I. Dedova, M. Tsubakihara, D. Berry, and N. Nosworthy. Actin binding proteins: regulation of cytoskeletal microfilaments. *Physiol. Rev.*, 83(2):433 –473, 2003.

[14] O. Lieleg, M. Claessens, and A. Bausch. Structure and dynamics of cross-linked actin networks. *Soft Matter*, 6(2):218–225, 2010.

[15] R. Mullins, J. Heuser, and T. Pollard. The interaction of arp2/3 complex with actin: nucleation, high affinity pointed end capping, and formation of branching networks of filaments. *Proc. Natl. Acad. Sci. USA*, 95(11):6181 –6186, 1998.

[16] JR Sellers. Myosins: a diverse superfamily. *Biochim. Biophys. Acta.*, 1496(1):3–22, 2000.

[17] R. Tuxworth and M. Titus. Unconventional myosins: anchors in the membrane traffic relay. *Traffic*, 1(1):11–18, 2000.

[18] H. Huxley. Electron microscope studies on the structure of natural and synthetic protein filaments from striated muscle. *J. Mol. Biol.*, 7:281–308, 1963.

[19] E Korn and J. Hammer. Myosins of nonmuscle cells. *Annu. Rev. Biophys. Biophys. Chem.*, 17:23–45, 1988.

[20] D.N. Robinson and J.A. Spudich. Mechanics and regulation of cytokinesis. *Curr. Opin. Cell Biol.*, 16:182–188, 2004.

[21] A. Martin. Pulsation and stabilization: contractile forces that underlie morphogenesis. *Dev. Biol.*, 341:114–125, 2010.

[22] K. Irvine and E. Wieschaus. Cell intercalation during *Drosophila* germband extension and its regulation by pair-rule segmentation genes. *Development*, 120(4):827 –841, 1994.

[23] R. Fernandez-Gonzalez, S. Simoes, J. Röper, S. Eaton, and J. Zallen. Myosin II dynamics are regulated by tension in intercalating cells. *Dev. Cell*, 17(5):736–743, 2009.

[24] M. Rauzi, P. Verant, T. Lecuit, and P. Lenne. Nature and anisotropy of cortical forces orienting drosophila tissue morphogenesis. *Nat. Cell Biol.*, 10(12):1401–1410, 2008.

[25] J. Blankenship, S. Backovic, J. Sanny, O. Weitz, and J. Zallen. Multicellular rosette formation links PlanarCellPolarity to tissue morphogenesis. *Dev. Cell*, 11(4):459–470, 2006.

[26] S. Noselli. *Drosophila*, actin and videotape - new insights in wound healing. *Nat. Cell Biol.*, 4(11):E251–E253, 2002.

[27] N. Wang, J. Butler, and D. Ingber. Mechanotransduction across the cell surface and through the cytoskeleton. *Science*, 260(5111):1124 –1127, 1993.

[28] B Fabry, G. Maksym, J. Butler, M. Glogauer, D. Navajas, and J. Fredberg. Scaling the microrheology of living cells. *Phys. Rev. Lett.*, 87(14):148102, 2001.

[29] S. Hu, J. Chen, B. Fabry, Y. Numaguchi, A. Gouldstone, D. Ingber, J. Fredberg, J. Butler, and N. Wang. Intracellular stress tomography reveals stress focusing and structural anisotropy in cytoskeleton of living cells. *Am. J. Physiol. Cell Physiol.*, 285:C1082–C1090, 2003.

[30] A. Caspi, R. Granek, and M. Elbaum. Enhanced diffusion in active intracellular transport. *Phys. Rev. Lett.*, 85(26):5655–5658, 2000.

[31] A. Lau, B. Hoffmann, A. Davies, JC. Crocker, and T. Lubensky. Microrheology, stress fluctuations, and active behavior of living cells. *Phys. Rev. Lett.*, 91(19):198101–4, 2003.

[32] B. Fabry, G. Maksym, J. Butler, M. Glogauer, D. Navajas, N. Taback, E. Millet, and J. Fredberg. Time scale and other invariants of integrative mechanical behavior in living cells. *Phys. Rev. E*, 68(4):041914, 2003.

[33] D. Arcizet, B. Meier, E. Sackmann, J. Raedler, and D. Heinrich. Temporal analysis of active and passive transport in living cells. *Phys. Rev. Lett.*, 101(24):248103–4, 2008.

[34] C. Hale, S. Sun, and D. Wirtz. Resolving the role of actoymyosin contractility in cell microrheology. *PLoS One*, 4(9):e7054, 2009.

[35] D. Robert, T. Nguyen, F. Gallet, and C. Wilhelm. *In vivo* determination of fluctuating forces during endosome trafficking using a combination of active and passive microrheology. *PLoS One*, 5(4):e10046, 2009.

[36] A. Snezhko, K. Barlan, I. Aranson, and V. Gelfand. Statistics of active transport in *Xenopus* melanophores cells. *Biophys. J.*, 99(10):3216–3223, 2010.

[37] C. Brangwynne, F. MacKintosh, and D. Weitz. Force fluctuations and polymerization dynamics of intracellular microtubules. *Proc. Natl. Acad. Sci. USA*, 104(41):16128 –16133, 2007.

[38] F. Gallet, D. Arcizet, P. Bohec, and A. Richert. Power spectrum of out-of-equilibrium forces in living cells: amplitude and frequency dependence. *Soft Matter*, 5(15):2947–2953, 2009.

[39] M. Balland, A. Richert, and F. Gallet. The dissipative contribution of myosin II in the cytoskeleton dynamics of myoblasts. *Eur. Biophys. J.*, 34(3):255–261–261, 2005.

[40] D. Fletcher and R. Mullins. Cell mechanics and the cytoskeleton. *Nature*, 463(7280):485–492, 2010.

[41] J. Kaes, H. Strey, J. Tang, D. Finger, R. Ezzell, E. Sackmann, and P. Janmey. F-actin, a model polymer for semiflexible chains in dilute, semidilute, and liquid crystalline solutions. *Biophys. J.*, 70(2):609–625, 1996.

[42] P. Janmey, S. Lind, H. Yin, and T. Stossel. Effects of semi-dilute actin solutions on the mobility of fibrin protofibrils during clot formation. *Biochim. Biophys. Acta*, 841(2):151–158, 1985.

[43] M. Gardel, M. Valentine, J. Crocker, A. Bausch, and D. Weitz. Microrheology of entangled F-Actin solutions. *Phys. Rev. Lett.*, 91(15):158302–5, 2003.

[44] I. Wong, M. Gardel, D. Reichman, E. Weeks, M. Valentine, A. Bausch, and D. Weitz. Anomalous diffusion probes microstructure dynamics of entangled f-actin networks. *Phys. Rev. Lett.*, 92(17):178101–4, 2004.

[45] J. Tang and Paul A. Janmey. The polyelectrolyte nature of f-actin and the mechanism of actin bundle formation. *J. Biol. Chem.*, 271(15):8556 –8563, 1996.

[46] P. Janmey, S. Hvidt, J. Käs, D. Lerche, A. Maggs, E. Sackmann, M. Schliwa, and T. Stossel. The mechanical properties of actin gels. elastic modulus and filament motions. *J. Biol. Chem.*, 269(51):32503–32513, 1994.

[47] J. Finer, R. Simmons, and J. Spudich. Single myosin molecule mechanics: piconewton forces and nanometre steps. *Nature*, 368(10):113–119, 1994.

[48] C. Brangwynne, G. Koenderink, F. Mackintosh, and D. Weitz. Nonequilibrium microtubule fluctuations in a model cytoskeleton. *Phys. Rev. Lett.*, 100(11):118104, 2008.

[49] GH Koenderink, Z Dogic, F Nakamura, PM Bendix, FC MacKintosh, JH Hartwig, TP Stossel, and DA Weitz. An active biopolymer network controlled by molecular motors. *Proc. Natl. Acad. Sci. U.S.A.*, 106(36):15192–7, 2009.

[50] D. Mizuno, C. Tardin, C. Schmidt, and F. MacKintosh. Nonequilibrium mechanics of active cytoskeletal networks. *Science*, 315(5810):370–373, 2007.

[51] T. Toyota, D. Head, C. Schmidt, and D. Mizuno. Non-Gaussian athermal fluctuations in active gels. *Soft Matter*, 7(7):3234–3239, 2011.

[52] M. Norstrom and M. Gardel. Shear thickening of f-actin networks crosslinked with non-muscle myosin IIB. *Soft Matter*, 7(7):3228–3233, 2011.

[53] M. Gardel, J. Shin, F. MacKintosh, L. Mahadevan, P. Matsudaira, and D. Weitz. Elastic behavior of cross-linked and bundled actin networks. *Science*, 304(5675):1301 –1305, 2004.

[54] O. Lieleg, K. Schmoller, M. Claessens, and A. Bausch. Cytoskeletal polymer networks: viscoelastic properties are determined by the microscopic interaction potential of cross-links. *Biophys. J.*, 96(11):4725–4732, 2009.

[55] R. Furukawa, R. Kundra, and M. Fechheimer. Formation of liquid crystals from actin filaments. *Biochemistry*, 32(46):12346–12352, 1993.

[56] B. Gentry, D. Smith, and J. Käs. Buckling-induced zebra stripe patterns in nematic f-actin. *Phys. Rev. E*, 79:031916–27, 2009.

[57] J. Viamontes, P. Oakes, and J. Tang. Isotropic to nematic liquid crystalline phase transition of F-Actin varies from continuous to first order. *Phys. Rev. Lett.*, 97(11):118103–4, 2006.

[58] F. Backouche, L. Haviv, D. Groswasser, and A. Bernheim-Groswasser. Active gels: dynamics of patterning and self-organization. *Phys Biol.*, 3(4):264–273, 2006.

[59] David M. Smith, Falko Ziebert, David Humphrey, Cynthia Duggan, Matthias Steinbeck, Walter Zimmermann, and Josef A. Kas. Molecular motor-induced instabilities and crosslinkers determine biopolymer organization. *Biophys. J.*, 93:4445 – 4452, 2007.

[60] S. Köhler, V. Schaller, and A. Bausch. Structure formation in active networks. *Nat. Mater.*, 10(6):462–468, 2011.

[61] L. Limozin, M. Bärmann, and E. Sackmann. On the organization of self-assembled actin networks in giant vesicles. *Eur. Phys. J. E*, 10(4):319–330, 2003.

[62] M. Claessens, R. Tharmann, K. Kroy, and A. Bausch. Microstructure and viscoelasticity of confined semiflexible polymer networks. *Nat. Phys.*, 2(3):186–189, 2006.

[63] M. Lagomarsino, C. Tanase, J. Vos, A. Emons, B. Mulder, and M. Dogterom. Microtubule organization in Three-Dimensional confined geometries: Evaluating the role of elasticity through a combined in vitro and modeling approach. *Biophys. J.*, 92(3):1046–1057, 2007.

[64] F. Nédélec, T. Surrey, A. Maggs, and S. Leibler. Self-organization of microtubules and motors. *Nature*, 389(6648):305–308, 1997.

[65] T. Surrey, F. Nédélec, S. Leibler, and E. Karsenti. Physical properties determining self-organization of motors and microtubules. *Science*, 292(5519):1167–71, 2001.

[66] C. Hentrich and T. Surrey. Microtubule organization by the antagonistic mitotic motors kinesin-5 and kinesin-14. *J. Cell Biol.*, 189(3):465–480, 2010.

[67] K. Kruse, J. Joanny, F. Julicher, J. Prost, and K. Sekimoto. Asters, vortices, and rotating spirals in active gels of polar filaments. *Phys. Rev. Lett.*, 92(7):078101, 2004.

[68] JF Joanny, F Julicher, K Kruse, and J Prost. Hydrodynamic theory for multicomponent active polar gels. *New. J. Physics*, 9:422, 2007.

[69] N. Nédélec, T. Surrey, and A. Maggs. Dynamic concentration of motors in microtubule arrays. *Phys. Rev. Lett.*, 86(14):3192–3195, 2001.

[70] T. Liverpool, M. Marchetti, J. Joanny, and J. Prost. Mechanical response of active gels. *Europhy. Lett.*, 85(1), 2009.

[71] F. MacKintosh and A. Levine. Nonequilibrium mechanics and dynamics of motor-activated gels. *Phys. Rev. Lett.*, 100(1):018104, 2008.

[72] D. Head and D. Mizuno. Nonlocal fluctuation correlations in active gels. *Phys. Rev. E*, 81(4):041910–11, 2010.

[73] A. Levine and F. MacKintosh. The mechanics and fluctuation spectrum of active gels. *J. Phys. Chem. B*, 113(12):3820–3830, 2009.

Chapter 2

In vitro reconstitution of actin-myosin networks

Contractile forces generated in the actin-myosin cytoskeleton contribute to cellular phenomena such as cell migration and cell division. In this thesis, we use an in vitro bottom-up approach to elucidate how actin and myosin interact to give rise to network-scale contractile behavior. We circumvent the complexity associated with the native contractile machinery by assembling a minimal model system of purified skeletal muscle actin and myosin II. In this chapter we describe the purification and reconstitution of actin and myosin filaments, and characterize the viscoelastic and structural properties of actin networks and the assembly and structure of synthetic myosin thick filaments.

2.1 Introduction

Living cells are complex systems composed of many different functional modules. One approach to study how these modules function and how their integration produces global cellular behavior is to reconstitute in vitro model systems in which cell complexity is stripped down to its bare minimum. Such minimal models have been successfully used to study mechanical and dynamical properties of the cytoskeleton, the protein scaffold that gives cells shape and mechanical stability, but also functional and mechanical plasticity [1],[2]. In this thesis we follow this approach with the goal to clarify 1) how molecular interactions between myosin motors and actin filaments lead to emergent contractile behavior at the network scale and 2) how simple physical constraints like confinement influence actin self-organization. Passive actin networks and the effect of different types of crosslinking proteins on their rheological and structural properties have been studied in depth using in vitro reconstitution and microscopy and rheological methods [3]. Studies of active networks containing myosin motors are more scarce. Myosin II is a molecular motor protein with two motor domains (or heads) and a long tail which mediates oligomerization to form bipolar filaments. In vitro experiments have used myosin in three different forms: the one-headed subfragment S1, the two-headed subfragment heavy meromyosin (HMM), and synthetic filaments assembled from whole (uncleaved) myosin II.

The subfragments S1 and HMM can be prepared from myosin by digestion with enzymes that cleave at specific positions in the protein [4] . Since the sub-fragments lack the tail domain that is responsible for myosin oligomerization, they are soluble independent of the buffer conditions. This makes it easier to handle these proteins in vitro. However, since invididual motor heads have a rather low duty ratio of only 2% at mM ATP concentrations, the subfragments cannot walk processively along actin filaments [5]. S1 fragments were shown to affect the rheology of actin networks at high frequency [6]. HMM was shown to have minimal effects on the rheology and network structure at high ATP, but as the HMM consumes the available ATP and generates ADP, it becomes processive and the motors can collectively slide actin filaments [7]. At zero ATP (rigor conditions), HMM acts as a transient crosslinker [8]. Interestingly, HMM fragments can collectively contract or even extend actin filament bundles pushed close to a surface by methylcellulose [9]. Bipolar myosin filaments are more processive than myosin subfragments. Classical studies of *superprecipitation* showed macroscopic contraction of actin networks driven by skeletal muscle or smooth muscle myosin II [10, 11, 12]. More recent experiments demonstrated that macroscopic contraction by myosin filaments requires network crosslinking [11, 12]. However, actin bundles are contracted even in the absence of crosslinks [13]. In uncrosslinked networks, myosin filaments can cause network fluidization by sliding

actin filaments past one another [14]. In bundled networks, myosin filaments can create patterns of bundles or asters [15, 16].

A clear relation between microscopic motor activity and network-level changes in structure is still lacking. In this thesis we reconstitute a minimal system of actin filaments and skeletal muscle myosin II motors that exhibits contractile activity, and study structural and dynamic properties on the network scale. To study how cell boundaries may influence the organization of the actin cytoskeleton, we created a minimal model comprised of actin-filled microwells. Such in vitro assays enable a tight control over the molecular composition and complexity of the system. Additionally, photolithographic microfabrication techniques provided us a means to systematically vary the geometry and size of confining environments.

In this chapter we describe the reconstitution and characterization of actin and myosin filaments. *Section* 2.2 describes the purification and reconstitution of actin, and the characterization of the filament length distribution and network microstructure and rheology. *Section* 2.3 describes the preparation of myosin and the characterization of myosin thick filament assembly and morphology.

2.2 Preparation and characterization of F-actin

Actin filaments are right-handed double-helices composed of globular monomers (G-actin) [17]. Actin filaments constitute up to 20% of the protein of striated muscle cells [17, 18] and are also the principal protein component of non-muscle cells [19]. In this thesis we use G-actin from rabbit psoas muscle (upper leg), a commonly used G-actin source [20]. In solution at low ionic strength, actin is monomeric. However, at neutral or slightly acidic pH, high ionic strength (KCl concentration 50 mM) and elevated temperature, G-actin spontaneously self-assembles into filaments (F-actin) [17]. This assembly is an active polymerization process as it requires ATP hydrolysis. ATP-bound G-actin monomers have a high affinity for the barbed or growing end of actin filaments. This end is also commonly denoted as the plus end (Fig. 2.1A, right-hand side, dark red). As monomers are added to the filament, ATP slowly hydrolyzes so that the pointed (or minus) end is enriched in ADP-G-actin, which eventually dissociates from the filament (Fig. 2.1A left-hand side, white monomers with red outline). Although ADP-G-Actin does have a non-negligible association rate to the pointed end of actin filaments, its dissociation is predominant. This results in constant growth at the barbed end and constant shortening at the pointed end, a phenomenon known as treadmilling. In steady-state conditions, actin filaments have a constant length. The length distribution of actin filaments is exponential [21] and can be shifted to smaller lengths by adding the actin-binding protein gelsolin (see details in *section 2.2.2*).

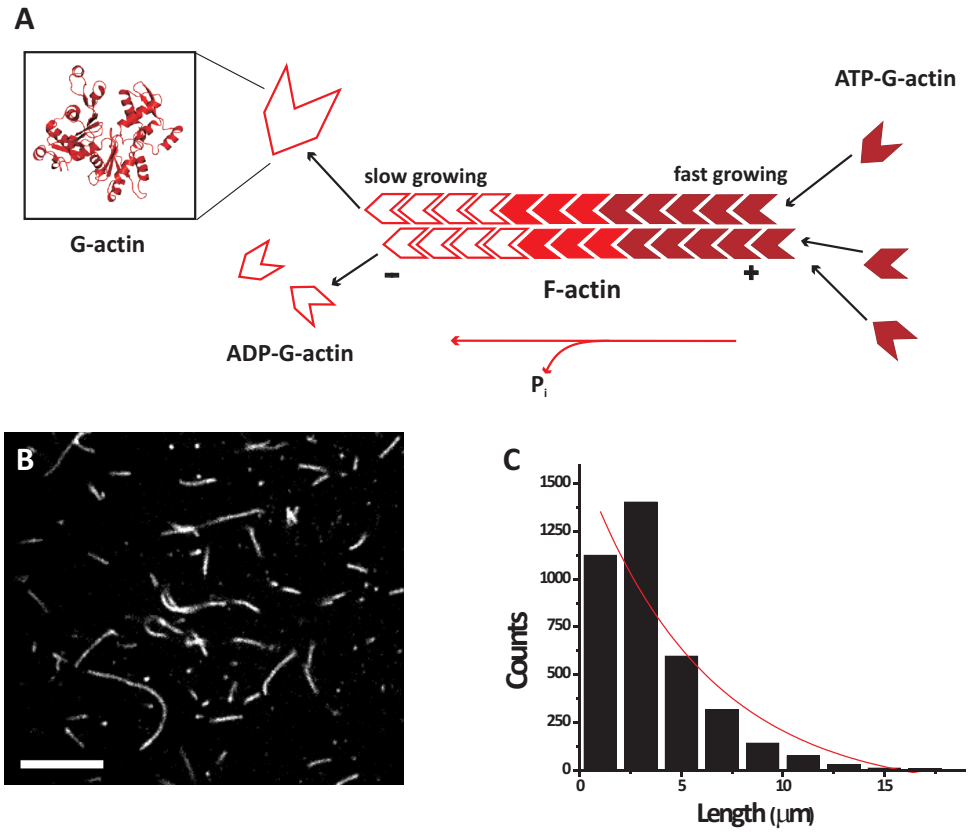

Figure 2.1: Fig 2.1 *In vitro* assembly of actin networks. **A.** Schematic drawing of F-actin self-assembly. ATP-bound actin monomers (dark red, right-hand side) assemble at the barbed or plus end (+), while ADP-bound actin (white monomers, left-hand side) detach from the pointed or minus (-) end. ATP-bound actin monomers (red) undergo ATP hydrolysis, releasing inorganic phosphate (Pi) (thin red arrows). *Inset* Ribbon diagram of a G-actin monomer in the ADP state (RCSB Protein Database structure nr. 1J6Z, http://www.rcsb.org/pdb/home/home.do). **B.** Confocal micrograph of fluorescently labeled filaments embedded inside a three-dimensional unlabeled actin network. The filaments are gently curved, reflecting their semiflexibility, characterized by a thermal persistence length of $\sim 15\,\mu$m. Scale bar $10\,\mu$m. **C.** Length distribution for 3711 filaments. The first bin is an underestimation of the actual frequency of short filaments due to image resolution limitations. The red line represents an exponential fit to the data. The average length is $6\,\mu$m.

2.2.1 Actin purification

Monomeric (G-) actin was purified from rabbit psoas skeletal muscle without column purification [20]. The purification proceeds in two phases, first the preparation of acetone powder and then actin extraction. In the first phase, minced muscle tissue is treated with a concentrated KCl solution ($0.3\,\mathrm{M}$) to remove myosin II, which can be extracted in parallel (see *section 2.3*). The minced muscle undergoes a series of steps of rinsing first with $NaHCO_3$ ($50\,\mathrm{mM}$) to increase the pH to 8-8.5 and then with distilled water. Several steps of dehydration with acetone at $4°C$ are performed, using in total $5\,\mathrm{L}$ of acetone per $500\,\mathrm{g}$ of muscle tissue. The final dry fibrous material is dried overnight in a fume hood and the powder is stored at $-80°C$. Typically, $\sim 30\,\mathrm{g}$ acetone powder is obtained from $\sim 500\,\mathrm{g}$ meat. In the second phase, actin is extracted by stirring the acetone powder in a low ionic strength chilled G-buffer ($2\,\mathrm{mM}$ Tris-HCl, $0.2\,\mathrm{mM}$ Na_2ATP, $0.2\,\mathrm{mM}$ $CaCl_2$, $0.2\,\mathrm{mM}$ dithiothreitol (DTT), $0.5\,\mathrm{mM}$ NaN_3, pH 8.0) for 30 minutes, using $20\,\mathrm{mL}$ buffer per gram of acetone powder. Afterwards, the solution is filtered to remove solid material and centrifuged to clear the actin-rich supernatant. G-actin is polymerized and incubated in a concentrated KCl solution ($0.6\,\mathrm{M}$) to remove tropomyosin, a protein which regulates actin-myosin interactions in muscle [22]. Actin is next depolymerised at low temperature in G-buffer by an overnight dialysis against G-buffer. The final actin concentration is determined by measuring light absorption at $290\,\mathrm{nm}$ using an extinction coefficient of $1.1\,\mathrm{cm}^2/\mathrm{mg}$ [20]. Typically about $50\,\mathrm{mg}$ actin is recovered from $10\,\mathrm{g}$ of acetone powder. G-actin is snap-frozen in liquid nitrogen and stored at $-80°C$ in G-buffer ($2\,\mathrm{mM}$ Tris-HCl, $0.2\,\mathrm{mM}$ Na_2ATP, $0.2\,\mathrm{mM}$ $CaCl_2$, $0.2\,\mathrm{mM}$ dithiothreitol (DTT), $0.5\,\mathrm{mM}$ NaN_3, pH 8.0). All the data reported in this thesis were obtained with one batch of G-actin. According to SDS-PAGE (Sodium Dodecyl Sulphate-Polyacrylamide Gel Electrophoresis) results, this batch was practically free of contaminants (Fig. 2.2, actin band outlined in red). G-actin labeled with biotin was purchased from Cytoskeleton (Tebu Bio), and G-actin labeled with the fluorescent dye Alexa488 or Alexa568 was purchased from Invitrogen.

2.2.2 Actin polymerization and length distribution

G-actin was assembled into filaments by mixing G-actin with ice chilled buffer to final concentrations of $50\,\mathrm{mM}$ KCl, $2\,\mathrm{mM}$ $MgCl_2$, $0.1\,\mathrm{mM}$ MgATP, $1\,\mathrm{mM}$ dithiothreitol (DTT) and $25\,\mathrm{mM}$ Imidazole (pH 7.4). G-actin was always added last, and assembly was initiated by incubating the mixture at room temperature. To determine the length distribution of the actin filaments, we embedded a low density of fluorescently labeled actin filaments (pre-polymerized at a concentration of $1\,\mathrm{mg/mL}$) in unlabeled networks of $1\,\mathrm{mg/mL}$ actin (Fig. 2.1B). The lengths were measured for 3711 filaments

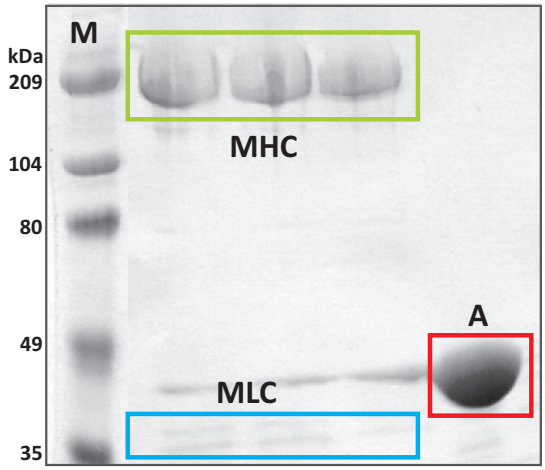

Figure 2.2: Purified skeletal myosin II and actin are largely free of contaminants. The SDS-PAGE gel stained with Coomassie Blue reveals for myosin the myosin heavy chains (MHC, green box), myosin light chains (MLC, blue box), and some residual actin. For actin, there is an actin band (A, red box), and small bands corresponding to low molecular weight contaminants (black arrow). $30\,\mu g$ of protein per lane were loaded. M is the marker lane.

from confocal micrographs using the NeuronJ plugin of ImageJ (http://rsbweb.nih.gov/ij/). The length distribution was approximately exponential, consistent with prior reports [21, 23]. The average length was $6\,\mu m$ (Fig. 2.1C). To alter the average length, gelsolin was included in the mixture. Gelsolin caps the barbed end of actin filaments, thereby preventing addition of ATP-bound G-actin and consequent filament growth [24]. The average length of F-actin in the presence of gelsolin is inversely proportional to the gelsolin to actin molar ratio, R_GA. Given that actin filaments have 370 monomers per $1\,m$ length, the average length L= (1/370 R_GA) (assuming that gelsolin is fully active) [21].

2.2.3 Microstructure of actin networks

In this thesis we study organization and dynamics of actin networks in a concentration regime where the filaments are sterically entangled. Entanglements set in above a threshold concentration commonly denoted as the overlap concentration. For rigid rods, this threshold can be estimated as the point where the volumes swept by freely rotating filaments start to contact. Thus, the threshold number density is approximately equal to $1/L^{-3}$ [25, 26]. For actin filaments with an average length of $6\,\mu m$, the overlap density is expected to be around $5 \times 10^{-3}\,\text{chains}/\mu m^3$, which corresponds to a volume fraction of 4×10^{-6} and weight concentration of $0.01\,mg/mL$.

An overlap concentration in this range was experimentally confirmed by confocal microscopy imaging [27]. The dynamics of filaments in an entangled network are described by the so-called tube model (Fig. 2.3A). Each filament is confined to a virtual tube formed by the surrounding filaments. This tube has a diameter D_e and a length L_e. The entanglement (or deflection) length L_e is the characteristic distance between points of contact of the test filament with the tube wall [28]. The filaments are free to slide longitudinally in the tube, but transverse motion is severely hampered by contacts with other chains. Entangled systems still have a large enough free volume to favor an isotropic distribution of rod orientations, which maximizes the orientational entropy. However, when the filament density is increased further, the free volume is reduced and the filaments tend to align, which leads to a transition from the isotropic to a nematic state (I-N) [29]. For filaments with an average length of $6\,\mu\mathrm{m}$, this liquid crystalline transition occurs around $5\,\mathrm{mg/mL}$. This phenomenon is explored in chapter 5. The entanglement points in entangled F-actin networks can be crosslinked by incorporating biotin-labeled actin monomers into the actin filaments, which can be crosslinked by the protein streptavidin. We polymerized actin with varying proportions of biotinylated actin monomers and used a constant 1:25 streptavidin:actin molar ratio. Crosslinks prevent filament reptation and stress relaxation, and provide elastic resistance against pulling forces exerted by myosin motors. This favors build-up of contractile stress [30, 31].

To characterize the microstructure of the networks, we performed confocal microscopy on fluorescently labeled $1\,\mathrm{mg/mL}$ actin samples. Networks were assembled at pH 7.4 in $25\,\mathrm{mM}$ imidazole-HCl, $50\,\mathrm{mM}$ KCl, $0.1\,\mathrm{mM}$ MgATP, $2\,\mathrm{mM}$ $MgCl_2$, $1.25\,\mathrm{mM}$ creatine phosphate (CP), $26\,\mathrm{units/mL}$ creatine kinase (CK), and $1\,\mathrm{mM}$ DTT. Filaments were fluorescently labeled by co-assembling G-actin with $5\,\mathrm{mole\%}$ Alexa488-labeled G-actin. To prevent photobleaching, we added $2\,\mathrm{mM}$ Trolox [32]. Confocal microscopy revealed that networks were overall homogenous and isotropic for all crosslinking conditions (Fig. 2.4). We could not distinguish single filaments in the confocal images. The mesh size of the networks is around $300\,\mathrm{nm}$ [33], which is smaller than the diffraction limit. An additional factor that decreases the spatial resolution is the thermal undulations of the actin filaments.

2.2.4 Viscoelastic properties of actin networks

Entangled actin networks are viscoelastic due to steric constraints on stress relaxation. The entanglement points, with a spacing L_e, limit transverse motion of the filaments within a tube of diameter D_e. L_e and D_e are related by a scaling relation,

$$L_e \propto D_e^{2/3} L_p^{1/3},$$

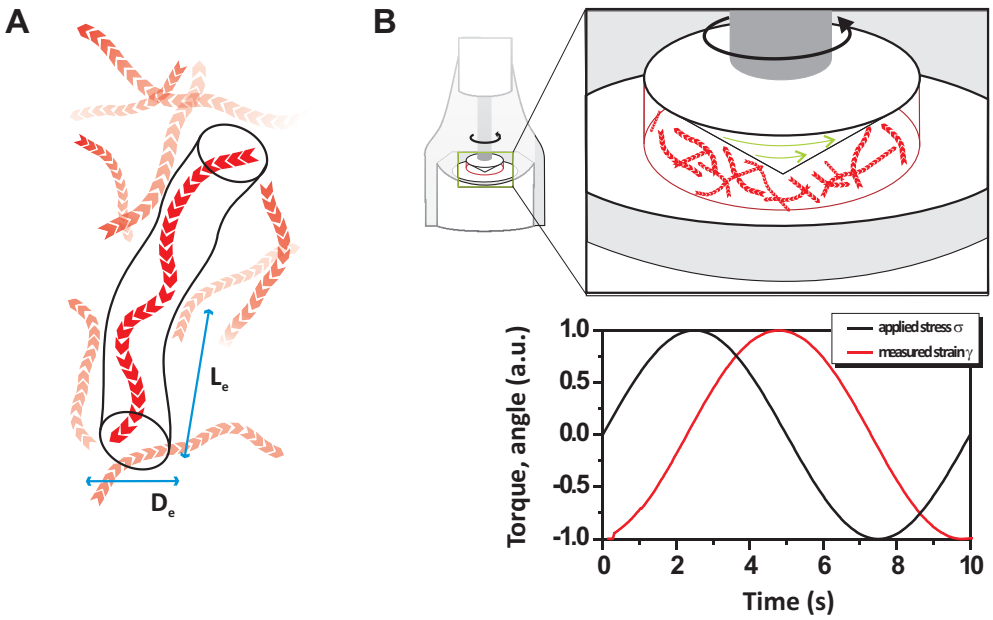

Figure 2.3: Viscoelastic properties of actin networks probed by macroscopic rheometry. **A.** The linear viscoelasticity of entangled networks of semiflexible filaments such as F-actin can be described by the tube model. Schematic drawing of a single polymer chain confined to a virtual tube with diameter D_e, which is defined by entanglement points with surrounding filaments which are spaced apart by a distance L_e. **B.** *Top panel* Actin networks were formed *in situ* in a rheometer (left-hand side) between a steel bottom plate and a cone (inset, right-hand side). Green arrows represent the shear strain applied by rotating the cone. *Bottom panel* Typical oscillatory-strain measurement (data courtesy of Izabela Piechocka). By oscillating the top plate, a sinusoidal strain γ (black line) is applied, and the resulting sinusoidal stress σ (red line) is measured. Data are normalized by the maximum stress and strain in the cycle. **C.** Polymerization curve of passive actin network (no myosin) at 1 mg/mL at $25°C$, showing the elastic and viscous shear modulus probed with a small oscillatory shear with a strain amplitude of 0.5%. The curves are averages over 4 independent experiments using CP20-1 and PP20 geometries. **D.** Plot of the frequency dependent storage and loss modulus of $1\,\mathrm{mg/mL}$ actin networks without crosslinking (black triangles, N=6) and with weak crosslinking (red squares, N=2, 1:1000 biotin-actin:actin ratio).

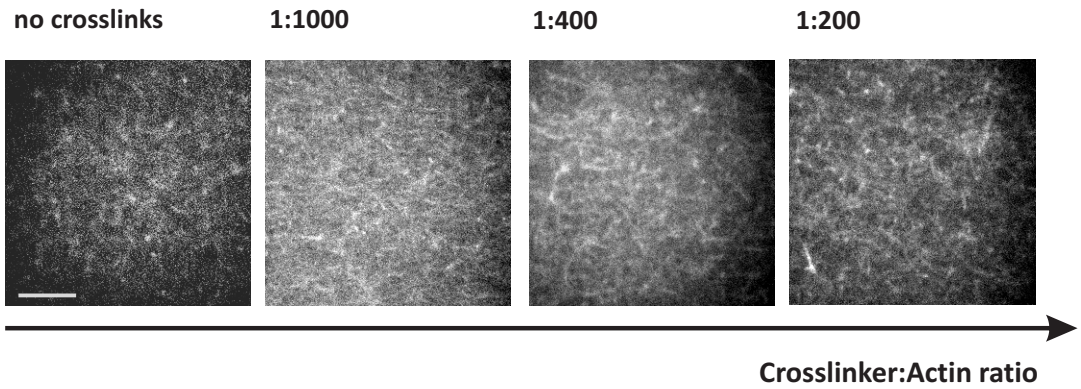

Figure 2.4: Fluorescence micrographs of passive actin networks (no myosin) with different crosslink (biotin-actin) densities. Crosslinking does not change the overall network structure up to a biotin-actin concentration of 0.12 $10\,\mu$M (at an actin concentration of $23.8\,\mu$M). Above this concentration, the network structure looks somewhat coarser, but no distinct aligned or ordered patterns are visible. Scale bar, $10\,\mu$m.

which involves the filament persistence length, L_p [34]. Depending on the time scale on which the system is probed, the network response is either elastic or viscous. An imposed stress can only relax once the filaments have reptated out of their tube. This time scale τ_D (reptation time) is strongly length-dependent, according to [26]:

$$\tau_D = L^2/\pi^2,$$

For typical actin filament lengths, τ_D takes values of minutes to hours [33]. Actin networks are elastic when probed on time scales shorter than τ_D, and are viscous on longer time scales. We measured the viscoelastic properties of actin solutions using a stress-controlled rotational rheometer (Anton Paar MCR501, Graz, Austria). The networks were formed *in situ* (Fig. 2.4B) between a steel bottom plate and a steel cone (CP20-1) or plate (PP20) with diameter of $20\,\mathrm{mm}$. The plate temperature was set to $25°C$ using a Peltier system. The bottom plate is immobile, and the top plate can be rotated to apply an oscillatory stress. The instrument uses feedback to control the strain. We probed the viscoelastic properties of actin networks by applying a small oscillatory strain $\gamma(t)$ of amplitude γ_0 and frequency ω:

$$\gamma(t) = \gamma_0 \sin t\omega.$$

The shear modulus $G^*(\omega)$ follows from the stress response σ,

$$\sigma(t) = \sigma_0 \sin t\omega + \delta = \gamma(t)G^*(\omega),$$

where δ represents the phase difference between the applied strain and the measured stress [35]. The shear modulus is a complex quantity with an in-phase, elastic component G' and an out-of-phase, viscous component, G'':

$$G^*(\omega) = G^{'}(\omega) + iG^{''}(\omega).$$

Network formation was monitored by applying an oscillatory shear stress at a frequency of $0.5\,\mathrm{Hz}$ using a strain amplitude of 0.5%, which is small enough not to perturb the network. Actin solutions were initially liquid but upon warming to $25°C$ immediately became elastic as a result of actin polymerization. Within 30 minutes, the elastic and viscous moduli reached constant values. The fully formed networks were more elastic than viscous, and had an elastic modulus of 0.4-0.6 Pa at $0.5\,\mathrm{Hz}$ (N=4) (Fig. 2.5A), consistent with prior reports (30, 36) [30, 31, 32, 33, 34, 35, 36]. The standard deviation was rather large because the measured torque was close to the $10\,\mathrm{nN/m}$ sensitivity limit of the instrument. To characterize the frequency dependence of the shear moduli of the fully formed network, we applied a sinusoidal strain with a small strain amplitude of 5% to remain in the linear elastic regime, and a frequency that was decreased from 3.6 to $0.2\,\mathrm{rad/s}$. The shear moduli were only weakly dependent on the frequency of oscillation (black triangles, Fig. 2.5B). There was no evidence of terminal relaxation at low frequencies, as G' always remained larger than G'' within the range of frequencies probed. The loss tangent

$$\tan\delta = G^{''}/G',$$

was 0.3, indicating that the actin networks are only weakly elastic. This is consistent with values previously reported for actin networks of $1\,\mathrm{mg/mL}$ [36]. Crosslinking with 1:1000 biotin and 1:25 streptavidin caused a small increase of the elastic and viscous moduli, and made the elastic modulus frequency-independent (red squares, Fig. 2.5B).

2.3 Preparation and characterization of skeletal muscle myosin II

Myosin II is the molecular motor responsible for cell contractility, which is crucial for processes such as cell division and locomotion. To exert contractile forces, myosin II assembles into bipolar filaments which can pull actin filaments towards one another.

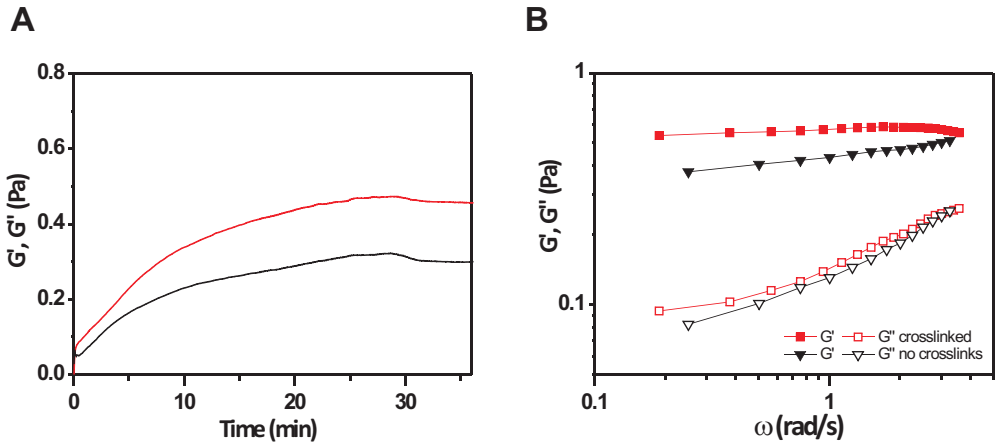

Figure 2.5: Viscoelastic properties of actin networks probed by macroscopic rheometry - II.**A.** Polymerization curve of passive actin network (no myosin) at 1 mg/mL at $25°C$, showing the elastic and viscous shear modulus probed with a small oscillatory shear with a strain amplitude of 0.5%. The curves are averages over 4 independent experiments using CP20-1 and PP20 geometries. **B.** Plot of the frequency dependent storage and loss modulus of $1\,\mathrm{mg/mL}$ actin networks without crosslinking (black triangles, N=6) and with weak crosslinking (red squares, N=2, 1:1000 biotin-actin:actin ratio).

To systematically study how forces generated by myosin motor filaments influence the structure and dynamics of actin networks, we used myosin II purified from rabbit skeletal muscle.

Myosin II is a double headed molecular motor consisting of 6 subunits. Each molecule is composed of 2 heavy (HC) chains and 4 light chains (LC) (Fig. 2.6A) [37]. The two HC can be divided into head and tail domains, which are connected at the neck region. The tail domains form a rod-like coiled-coil structure with a length of $\sim 150\,\mathrm{nm}$. The globular head or motor domain contains binding sites for ATP and F-actin. This allows the head to exert a power stroke and walk towards the plus end of an actin filament (Fig. 2.6B). Each HC is associated with one regulatory (Fig. 2.6A, orange), and one essential (Fig. 2.6A, blue) LC. The phosphorylation state of the regulatory LC (rLC) controls the activity of the motor domain in smooth muscle and non-muscle cells (37). In skeletal muscle cells, myosin II is constitutively active and is therefore not controlled directly by the rLC. Both light chains mechanically stiffen the neck region, which functions as a lever arm during the power stroke [37].

Purified skeletal muscle myosin II in solutions of high salt (KCl) concentration is *monomeric* (each molecule is a heterohexamer, for practical purposes we refer to subunits of myosin filaments as monomers), but when the salt concentration is decreased towards physiological conditions (below $0.2\,\mathrm{M}$ KCl the myosin tail domains associate to form myosin thick filaments [38, 39, 40] (Fig. 2.4C). The proposed model of assembly involves the formation of a myosin dimer, which nucleates small bipolar structures [41, 42, 43]. It is unlikely that these bipolar structures, commonly named minifilaments [44], associate together to form thick filaments [38]. Instead it is likely that filaments grow by addition of dimers, which has been reported to be a rather fast event [45]. These synthetic filaments are structurally similar to native skeletal muscle thick filaments. Both display a bipolar tapered or spindle-like structure with a central bare zone [38].

In vitro filament assembly is influenced by several factors besides ionic strength. Filaments formed at low pH are longer than those formed in alkaline buffers [38]. C-protein, a myosin crosslinker that connects thick filaments to the M-line of sarcomeres in skeletal muscle also influences filamentogenesis [39]. Filament length distributions obtained in the presence of C-protein are narrower and the average length is shorter than for pure myosin II. The assembly procedure also affects the length distribution. Fast dilution from high to low KCl concentration leads to rather short filaments ($1\,\mu\mathrm{m}$) [38, 39] that form in a time scale of minutes [38] and whose size reaches a steady state on the time scale of hours [46]. Synthetic myosin filaments formed slowly by dialysis, over periods of several hours, have a constant length once the desired ionic strength is reached and are longer by a factor of 6 than those prepared by fast assembly [39]. Synthetic myosin filaments resemble native thick filaments the

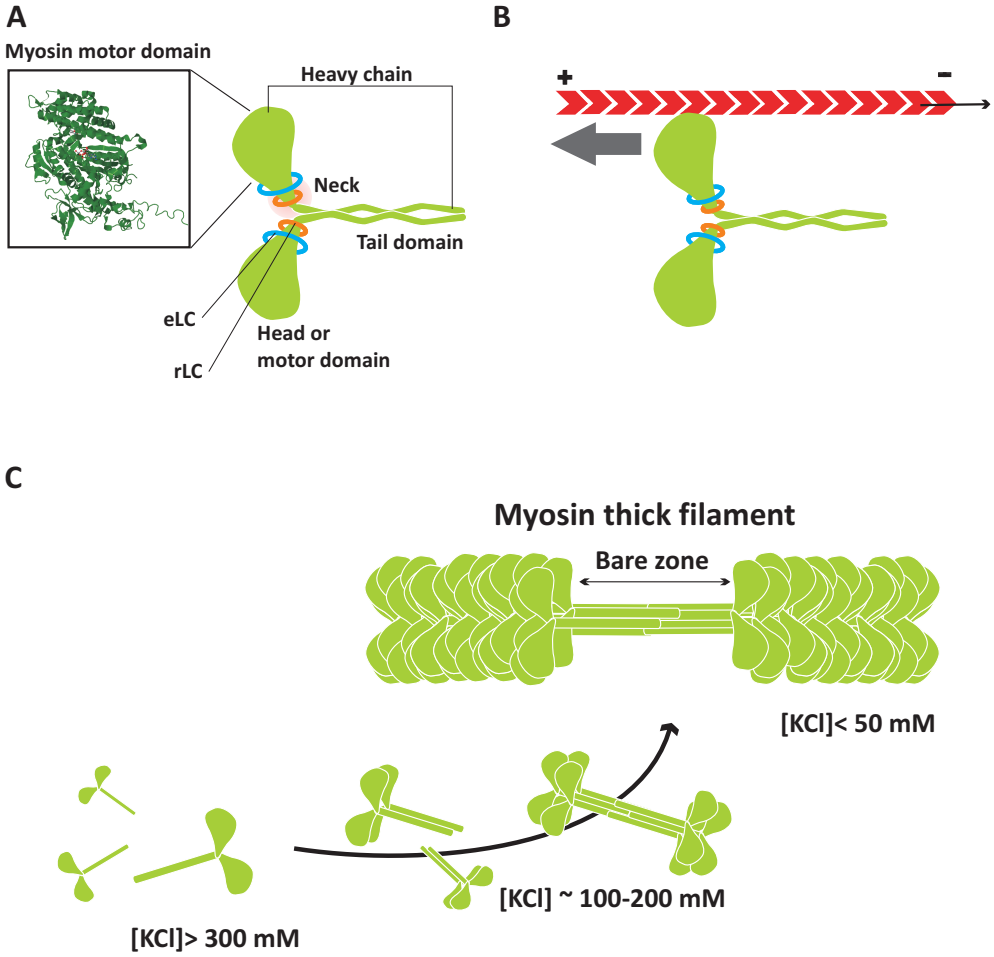

Figure 2.6: Self-assembly of myosin filaments. **A.** Myosin II is a hexameric protein composed of two heavy chains (green) and four light chains (two regulatory light chains, in orange, and two essential light chains, in blue). The heavy chains coil around each other to form the tail domain. The head domain contains two motor domains which bind ATP and F-actin. *Inset* Ribbon diagram of myosin II complexed with the inhibitor tribromodichloropseudilin (RCSB Protein Database structure nr. 2XO8 http://www.rcsb.org/pdb/home/home.do). **B.** Diagram of salt-dependent in vitro assembly of myosin into bipolar filaments (light chains are not displayed). Myosin remains monomeric above 300 mM KCl, but assembles tail-to-tail into filaments of increasing size as the KCl concentration is lowered. Filaments formed at low (50 mM) KCl are known as synthetic thick filaments and are composed of hundreds of myosin molecules ($\sim$ 100 under our conditions). The myosin tails form a central bare zone, and the myosin heads point outwards. At KCl concentrations of $\sim$ 100-200 mM, myosin forms smaller filaments composed of tens of molecules, named minifilaments.

closest when assembly is achieved by fast dilution at pH 6.5-7 to a KCl concentration between 100-$200\,\mathrm{mM}$. These buffer conditions are similar to in vivo conditions [38]. In our assays we assembled filaments at $50\,\mathrm{mM}$ KCl and pH 7.4, which yields filaments with lengths on the order of a micrometer (conditions of assembly described in detail in *section 2.3.3*).

2.3.1 Myosin purification

Myosin II was purified from rabbit psoas skeletal muscle. Myosin II is obtained as a by-product of the first step of the actin purification procedure described in *section 2.2.1*. Myosin is extracted with a chilled high molarity potassium chloride buffer ($0.3\,\mathrm{M}$ KCl, $150\,\mathrm{mM}$ KH_2PO_4, $20\,\mathrm{mM}$ EDTA, $5\,\mathrm{mM}$ $MgCl_2$, $1\,\mathrm{mM}$ ATP, pH 6.5) for 15-20 minutes from the minced muscle (47). The extraction reaction is halted by adding cold distilled water and letting the protein precipitate at $4°C$ for a minimum of 3 hours. After removal of the supernatant, the white precipitate is pelleted and resuspended in a high salt buffer ($1\,\mathrm{M}$ KCl, $600\,\mathrm{mM}$ KH_2PO_4, $10\,\mathrm{mM}$ EDTA, $1\,\mathrm{mM}$ DTT, pH 6.5). The myosin is further purified by several dialysis steps against buffers with decreasing molarities of potassium chloride (but always above $0.3\,\mathrm{M}$, to avoid filament assembly), interspersed with one additional precipitation in water [47]. The final product is stored at $-20°C$ in a high salt buffer with glycerol ($0.6\,\mathrm{M}$ KCl, $25\,\mathrm{mM}$ KH_2PO_4, $10\,\mathrm{mM}$ EDTA, $1\,\mathrm{mM}$ DTT, pH 6.5, 50% w/w glycerol). Activity was preserved for at least 48 months. In contrast, we found that storage of snap-frozen myosin without glycerol at $-80°C$ caused degradation of motor activity, as evident from motility assays with heavy meromyosin [48]. Fresh myosin solutions were prepared by dialysis against AB300 buffer (300 mM KCl, 4 mM $MgCl_2$, 1 mM DTT, $25\,\mathrm{mM}$ Imidazole, pH 7.4). The protein concentration was determined by absorption measurements at $280\,\mathrm{nm}$ using an extinction coefficient of $0.53\,\mathrm{cm}^2/\mathrm{mg}$ [47].

Fluorescent labeling of myosin with DyLight NHS Ester 488 or 594 (Perbio) was performed according to a protocol adapted from [49]. This labeling preserves the reversible assembly of myosin into synthetic filaments and its actin-activated MgATPase activity. All procedures were performed at $4°C$. Myosin was first assembled into synthetic filaments by a 2 hour dialysis against a low-salt buffer ($10\,\mathrm{mM}$ Hepes, $50\,\mathrm{mM}$ KCl, $0.2\,\mathrm{mM}$ EGTA, $2\,\mathrm{mM}$ MgATP, $2\,\mathrm{mM}$ $MgCl_2$, pH 7.0). To the clear top layer of the dialyzed myosin, a 20-fold molar excess of the fluorescent dye (from a $10\,\mathrm{mM}$ stock in dimethylsulfoxide) was slowly added. After incubation on ice and in the dark for 1 hour, the labeling reaction was stopped by addition of $20\,\mathrm{mM}$ D-Lysine. Unreacted dye was removed by dialyzing the myosin solution for at least 3 hours against a buffer containing $10\,\mathrm{mM}$ Hepes, $50\,\mathrm{mM}$ KCl and $0.2\,\mathrm{mM}$ EGTA, pH 7.0. After addition of $10\,\mathrm{mM}$ $MgCl_2$, the fluorescent myosin filaments were pelleted by centrifugation for

10 min at $8000\,\mathrm{g}$. The myosin pellet was resuspended in a minimal volume of high-salt buffer favoring filament disassembly ($0.6\,\mathrm{M}$ KCl, $50\,\mathrm{mM}$ KH_2PO_4 and $1\,\mathrm{mM}$ DTT, pH 7.5) and the solution was dialyzed against the same buffer overnight. Aggregates were removed by centrifugation ($10\,\mathrm{min}$ at $8000\,\mathrm{g}$). The labeling stoichiometry varied between 1.7 and 2.7 dye molecules per myosin molecule, as deduced from the ratio between the absorbance at $280\,\mathrm{nm}$ and at the wavelength where the dye has its maximal absorbance. The labeled myosin was stored at $-20°C$ in monomeric form in a high salt buffer with glycerol ($0.6\,\mathrm{M}$ KCl, $50\,\mathrm{mM}$ KH_2PO_4 and $1\,\mathrm{mM}$DTT, pH 7.5, 50% glycerol).

2.3.2 Characterization of myosin filament assembly by analytical ultracentrifugation

We used analytical ultracentrifugation (AUC) to measure the molecular weight of myosin II in monomer and filament form. Molecules in a solution submitted to a centrifugal force will migrate in their container a distance *dr* over a time *dt*, at a velocity *u*. The sedimentation velocity is inversely proportional to the centrifugal field, $\Omega^2 r$, where Ω is the angular velocity of the centrifuge rotor and r is the radial position of the particle in the centrifugal field. The ratio between the velocity of the particle and the centrifugal field is known as the sedimentation coefficient s and given by the Svedberg equation

$$s = \frac{dr/dt}{\Omega^2 r}, [50]$$

where s is commonly expressed in Svedbergs (S), where $1\,\mathrm{S}$ is $1 \times 10^{-13}\,\mathrm{seconds}$. Particle sedimentation can be monitored by measuring the concentration profile along the radial direction of the centrifuge cell. Analytical ultracentrifuges are equipped with an optical detection system which scans the absorbance profile of centrifuge cells with an optically transparent window as a function of time (Fig. 2.7A, schematics), yielding sedimentation profiles as in figure 2.6A (monomeric myosin at $300\,\mathrm{mM}$ KCl) and Fig. 2.7B (filaments at $150\,\mathrm{mM}$ KCl). Each yellow and blue line represents one complete scan along the radius of the cell. To determine the sedimentation coefficient, data sets are modeled by the Lamm equation

$$\frac{\delta\chi(r,t)}{\delta t} = \frac{1}{r}\frac{\delta}{\delta r}\left[rD\frac{\delta\chi(r,t)}{\delta r} - s\Omega^2 r^2 \chi(r,t)\right], [50]$$

which is a transport equation describing the concentration distribution $\delta\chi$ of sedimenting particles with diffusion coefficient D as a function of time t and radial position r.

The sedimentation constant provides information about the shape and size of the centrifuged particles. For rod-like particles such as myosin filaments, the aspect

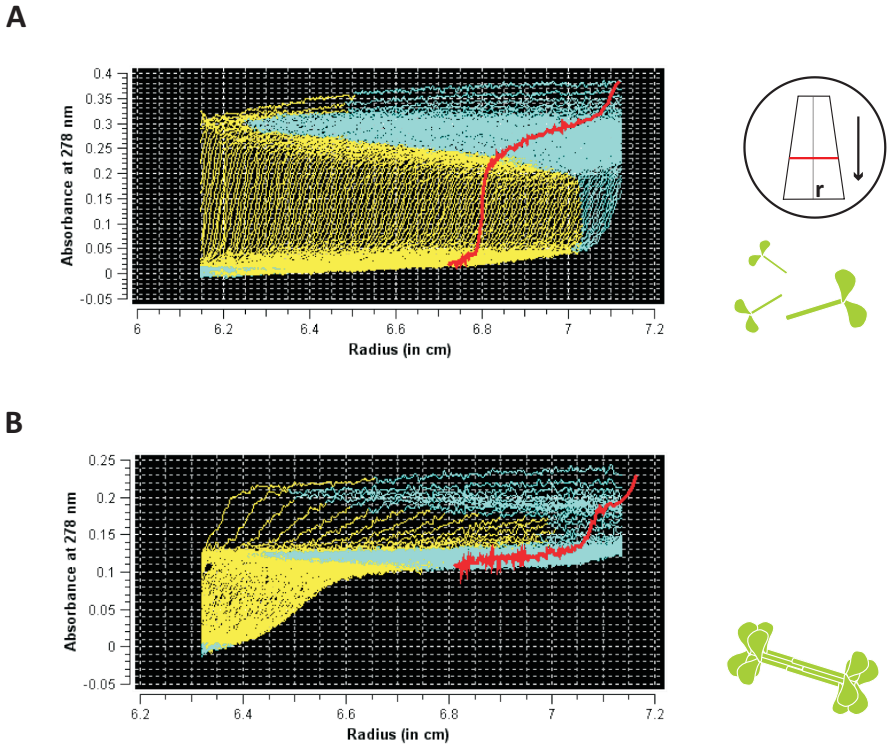

Figure 2.7: Characterization of myosin assembly state by analytical ultracentrifugation. The myosin concentration was $2\,\mu\mathrm{M}$ and sedimentations profiles were obtained at $20°C$. **A.** Sedimentation profiles of myosin monomers (in a $300\,\mathrm{mM}$ KCl solution) plotted with UltraScan software. Each yellow or blue profile represents one complete absorbance scan along the centrifuge cell. *Schematics* Top view of centrifuge cell; the red boundary represents the sedimentation front of the sedimenting particles. The black arrow represents the direction of the centrifugal force and r is the radial position. **B.** Sedimentation profiles of myosin minifilaments (assembled in a $150\,\mathrm{mM}$ KCl solution). Red lines represents fits to find the baseline concentration and the plateau concentration necessary to estimate the sedimentation coefficient following the Van Holde-Weischet method.

ratio (length/diameter ratio) can in principle be determined by measuring the sedimentation coefficient extrapolated to infinite dilution [51]. However, this was not attempted in this thesis.

At the Van 't Hoff Laboratory (Debye Institute, University of Utrecht), we measured sedimentation coefficients on a Beckmann Coulter Optima XLA with absorbance optics using a wavelength of $280\,\mathrm{nm}$ and a An-60Ti rotor thermostatted at $20°C$. Centrifugal forces applied were between $32256 \times g$ and $290304 \times g$, where $9.81\,\mathrm{m/s^2}$. The measurements were restricted to myosin concentrations above $0.9\,\mathrm{mL}$, because otherwise the absorbance signal was too low. In future, this may perhaps be improved by labeling myosin with a fluorescent dye giving an absorbance in the visible. Data were analyzed with UltraScan, an AUC software package which estimates sedimentation constants for populations of particles of different sizes using the Van Holde-Weischet method (http://www.ultrascan.uthscsa.edu). We obtained a sedimentation coefficient for myosin in a solution of $300\,\mathrm{mM}$ KCl of $5.7\,\mathrm{S}$, in close agreement with prior values of 5.1-$5.2\,\mathrm{S}$ in buffers of the same pH and ionic strength (38). Moreover, there was only one sedimenting species, indicating that the myosin stock solution is homogeneous and contains only myosin monomers. For a myosin solution incubated for 3 minutes in the presence of $150\,\mathrm{mM}$ KCl, two distinct particle populations were detected, namely a monomeric fraction (62.2%) with a sedimentation coefficient of $3.9\,\mathrm{S}$ and a fraction of minifilaments (28.9%) with a sedimentation coefficient of $155\,\mathrm{S}$. The sedimentation coefficient of the minifilaments is comparable to values reported at KCl concentrations of 100 and $200\,\mathrm{mM}$ KCl [38].

2.3.3 Characterization of myosin filament morphology by Atomic Force Microscopy

To determine the morphology and size of the synthetic myosin thick filaments assembled in vitro, we performed atomic force microscopy (AFM). We assembled filaments by fast dilution of myosin in a $300\,\mathrm{mM}$ KCl buffer into a buffer of $25\,\mathrm{mM}$ imidazole-HCl (pH 7.4), $0.1\,\mathrm{mM}$ MgATP, $2\,\mathrm{mM}$ $MgCl_2$, $1\,\mathrm{mM}$ DTT, $1.25\,\mathrm{mM}$ creatine phosphate (CP), $26\,\mathrm{units/mL}$ creatine kinase (CK), and varying KCl concentration (50, 70, 100 or $150\,\mathrm{mM}$). After 1 minute assembly, filaments were deposited on freshly cleaved Muscovite Mica V4 (Electron Microscopy Sciences,Washington) spincoated with an adhesive layer of nitrocellulose (Collodion, Sigma Aldrich, Germany). Buffer was shaken off; washing to remove salts was not necessary thanks to the hydrophobic nature of the nitrocellulose surface. Filaments were dried in air. Imaging was performed on a Veeco Dimension 3100 AFM (Veeco, New York, USA) in tapping mode on dry samples with MPP-12100-10 tips, which have a $8\,\mathrm{nm}$ nominal radius and a spring constant of $5\,\mathrm{N/m}$ (Veeco, New York, USA). Three-dimensional images were created

from height images with Gwyddion1 software (http://gwyddion.net/).The myosin filaments appeared as spindle-shaped rods with tapered ends (Fig. 2.8A-D). This morphology is consistent with other reports [38, 52]. The filaments were spindle shaped for all KCl concentrations. Previously, filaments formed in a $25\,\mathrm{mM}$ Tris-HCl buffer of pH 7.5 containing $100\,\mathrm{mM}$ KCl were reported to exhibit lateral projections and to resemble twigs [38]. We did not observe such structures, which could be related to the difference in buffer (imidazole versus Tris) or the presence of $2\,\mathrm{mM}$ Mg^{2+} in our buffer. Mg^{2+} has been reported to promote the assembly process [53].Filament lengths were measured on 27-83 filaments per condition using WSxM software [54] and Gwydion (http://gwyddion.net/).

First, a profile was drawn along the filament backbone, following its curvature. The end points of the filament were defined as the points on the profile which have a height equal to the background height. At each KCl concentration, the filaments were rather polydisperse in length (Fig. 2.8E). However, the average length showed a decrease with increasing KCl concentration, consistent with previous reports [38, 39]. The filaments had an average length of $0.85\,\mu\mathrm{m}$ when formed at $50\,\mathrm{mM}$ KCl, and $0.63\,\mu\mathrm{m}$ when formed at $150\,\mathrm{mM}$ KCl. The filament diameter was estimated from the height in AFM topography images, for 20 filaments per condition. We observed heights on the order of 2-$5\,\mu\mathrm{m}$ (Fig. 2.8F). This is smaller than the 5-$10\,\mu\mathrm{m}$ heights reported elsewhere [52], potentially due to a collapse of the filaments when they are dried on the surface. To test this possibility, the myosin filaments will need to be imaged in liquid, which preserves the native state of the filaments, and perhaps will need to be fixed with glutaraldehyde, to avoid collapse. The height profiles do not show clear evidence of a bare zone in the center of the filaments. This is consistent with earlier electron microscopy observations of filaments formed at pH 7.5, where also no clear bare zone was observed [38].

2.4 Acknowledgments

We thank Saskia Duineveld, Marjolein Vinkenoog-Kuit, Izabela Piechocka and members of the Bio-organization group at AMOLF for crucial help with protein purification and labeling, Erwin Peterman and Gijs Wuite for their kind hospitality at the VU, where we did the first actin and myosin purifications, and Jeanette Nguyen for providing the length distribution of actin filaments. Marijn Korsten performed systematic studies of synthetic myosin filament assembly by AFM and AUC. We thank Dominique Thies-Weesie and Albert Philipse (Van't Hoff Laboratory for Physical and Colloid Chemistry, Debye Institute, University of Utrecht) for helpful discussions on AUC and for performing sedimentation measurements and data analysis.

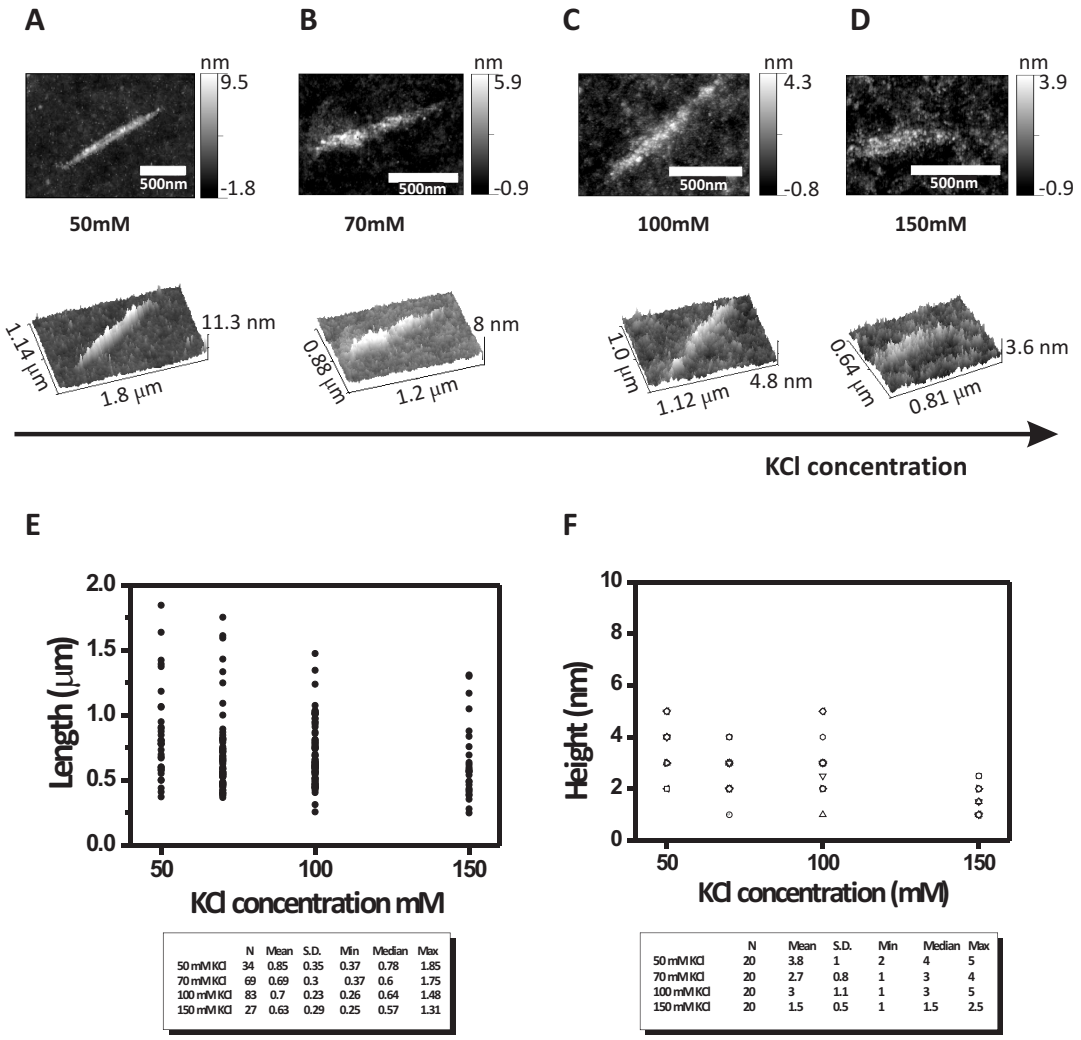

	N	Mean	S.D.	Min	Median	Max
50 mM KCl	34	0.85	0.35	0.37	0.78	1.85
70 mM KCl	69	0.69	0.3	0.37	0.6	1.75
100 mM KCl	83	0.7	0.23	0.26	0.64	1.48
150 mM KCl	27	0.63	0.29	0.25	0.57	1.31

	N	Mean	S.D.	Min	Median	Max
50 mM KCl	20	3.8	1	2	4	5
70 mM KCl	20	2.7	0.8	1	3	4
100 mM KCl	20	3	1.1	1	3	5
150 mM KCl	20	1.5	0.5	1	1.5	2.5

Figure 2.8: Characterization of myosin filament morphology and size by atomic force microscopy. **A-D.** Micrographs of synthetic myosin filaments assembled in vitro at different KCl concentrations ranging from 50 to $150\,\mathrm{mM}$ KCl. *Top panels* Height images with gray scale representing the height in nanometers. Scale bars $500\,\mathrm{nm}$. *Bottom panels* Corresponding 3D-rendering. **E.** Filament length distribution for different KCl concentrations. *Table* Corresponding length statistics. **F.** Filament height distributions for different KCl concentrations with N=20 per condition. *Table* Corresponding height statistics.

References

[1] D. Fletcher and R. Mullins. Cell mechanics and the cytoskeleton. *Nature*, 463(7280):485–492, 2010.

[2] E. Karsenti, F Nédélec, and T Surrey. Modelling microtubule patterns. *Nat. Cell. Biol.*, 8(11):1204–11, 2006.

[3] O. Lieleg, M. Claessens, and A. Bausch. Structure and dynamics of cross-linked actin networks. *Soft Matter*, 6(2):218–225, 2010.

[4] Stephen J. Kron, Y. Toyoshima, T. Uyeda, and J. Spudich. [33] assays for actin sliding movement over myosin-coated surfaces. In *Molecular Motors and the Cytoskeleton*, volume 196, pages 399–416. Academic Press, 1991.

[5] JT Finer, RM Simmons, and JA Spudich. Single myosin molecule mechanics: piconewton forces and nanometre steps. *Nature*, 368(10):113–119, 1994.

[6] L. Le Goff, F. Amblard, and E. Furst. Motor-driven dynamics in actin-myosin networks. *Phys. Rev. Lett.*, 88(1):018101, 2002.

[7] J Uhde, M Keller, E Sackmann, A Parmeggiani, and E Frey. Internal motility in stiffening actin-myosin networks. *Phys. Rev. Lett.*, 93(26):268101, 2004.

[8] O. Lieleg, M. Claessens, Y. Luan, and A. Bausch. Transient binding and dissipation in cross-linked actin networks. *Phys. Rev. Lett.*, 101(10):108101–4, 2008.

[9] Y. Tanaka-Takiguchi, T. Kakei, A. Tanimura, A. Takagi, M. Honda, H. Hotani, and K. Takiguchi. The elongation and contraction of actin bundles are induced by double-headed myosins in a motor concentration-dependent manner. *J. Mol. Biol.*, 341(2):467–476, 2004.

[10] L. Janson and D. Taylor. *In vitro* models of tail contraction and cytoplasmic streaming in amoeboid cells. *J. Cell Biol.*, 123(2345-56), 1993.

[11] EW Janson, J Kolega, and DL Taylor. Modulation of contraction by gelation/solation in a reconstituted motile model. *J. Cell Biol.*, 114(5):1005–15, 1991.

[12] P. Bendix, G. Koenderink, D. Cuvelier, Z. Dogic, B. Koeleman, W. Brieher, C. Field, L Mahadevan, and D. Weitz. A quantitative analysis of contractility in active cytoskeletal protein networks. *Biophys. J.*, 94(8):3126–36, 2008.

[13] T. Thoresen, M. Lenz, and M. Gardel. Reconstitution of contractile actomyosin bundles. *Biophys. J.*, 100(11):2698–2705, 2011.

[14] D. Humphrey, C. Duggan, D. Saha, D. Smith, and J. Käs. Active fluidization of polymer networks through molecular motors. *Nature*, 416(6879):413–416, 2002.

[15] F. Backouche, L. Haviv, D. Groswasser, and A. Bernheim-Groswasser. Active gels: dynamics of patterning and self-organization. *Phys Biol.*, 3(4):264–273, 2006.

[16] S. Köhler, V. Schaller, and A. Bausch. Structure formation in active networks. *Nat. Mater.*, 10(6):462–468, 2011.

[17] C. Dos Remedios, D. Chhabra, M. Kekic, I. Dedova, M. Tsubakihara, D. Berry, and N. Nosworthy. Actin binding proteins: regulation of cytoskeletal microfilaments. *Physiol. Rev.*, 83(2):433 –473, 2003.

[18] J. Vandekerckhove, G. Bugaisky, and M. Buckingham. Simultaneous expression of skeletal muscle and heart actin proteins in various striated muscle tissues and cells. a quantitative determination of the two actin isoforms. *J. Biol. Chem.*, 261(4):1838 –1843, 1986.

[19] T. Pollard and J. Cooper. Actin, a central player in cell shape and movement. *Science*, 326(5957):1208 –1212, 2009.

[20] J. Pardee and J. Spudich. Purification of muscle actin. *Methods Enzymol.*, 85:164–181, 1982.

[21] S. Burlacu, P. Janmey, and J. Borejdo. Distribution of actin filament lengths measured by fluorescence microscopy. *Am. J. Physiol. Cell Physiol.*, 262(3):C569–577, 1992.

[22] J. Spudich and S. Watt. The regulation of rabbit skeletal muscle contraction. *J. Biol. Chem.*, 246(15):4866 –4871, 1971.

[23] P. Janmey and T. Stossel. Kinetics of actin monomer exchange at the slow growing ends of actin filaments and their relation to the elongation of filaments shortened by gelsolin. *J. Muscle Res. Cell Motil.*, 7(5):446–454, 1986.

[24] H. Yin and T. Stossel. Control of cytoplasmic actin gel-sol transformation by gelsolin, a calcium-dependent regulatory protein. *Nature*, 281(5732):583–586, 1979.

[25] P. de Gennes and J. Prost. *The Physics of Liquid Crystals*. Clarendon, Oxford, 1993.

[26] M. Doi and S. Edwards. *The theory of polymer dynamics*. Number 73 in International Series of Monographs on Physics. Oxford University Press, Oxford, 1988.

[27] J. Käs, H. Strey, J. Tang, D. Finger, R. Ezzell, E. Sackmann, and P. Janmey. F-actin, a model polymer for semiflexible chains in dilute, semidilute, and liquid crystalline solutions. *Biophys. J.*, 70(2):609–625, 1996.

[28] Theo Odijk. Translational friction coefficient of hydrodynamically screened rodlike macromolecules. *Macromolecules*, 19(7):2073–2074, 1986.

[29] L. Onsager. The effects of shape on the interaction of colloidal particles. *Ann. N. Y. Acad. Sci.*, 51(4):627–659, 1949.

[30] G. Koenderink, Z. Dogic, F. Nakamura, P. Bendix, F. MacKintosh, J. Hartwig, T. Stossel, and D. Weitz. An active biopolymer network controlled by molecular motors. *Proc. Natl. Acad. Sci. U.S.A.*, 106(36):15192–7, 2009.

[31] D. Mizuno, C. Tardin, C. Schmidt, and F. MacKintosh. Nonequilibrium mechanics of active cytoskeletal networks. *Science*, 315(5810):370–373, 2007.

[32] W. Koopmans, A. Brehm, C. Logie, T. Schmidt, and J. van Noort. Single-Pair FRET microscopy reveals mononucleosome dynamics. *J. Fluoresc.*, 17(6):785–795–795, 2007.

[33] C. Schmidt, M. Bärmann, Gerhard Isenberg, and E. Sackmann. Chain dynamics, mesh size, and diffusive transport in networks of polymerized actin: a quasielastic light scattering and microfluorescence study. *Macromolecules*, 22(9):3638–3649, 1989.

[34] D. Morse. Viscoelasticity of tightly entangled solutions of semiflexible polymers. *Phys. Rev. E*, 58(2):1237–1240, 1998.

[35] C. Macosko. *Rheology:principles, measurements, and applications*. Wiley-VCH, Hoboken, NJ, USA., 1994.

[36] M. Gardel, M. Valentine, J. Crocker, A. Bausch, and D. Weitz. Microrheology of entangled F-Actin solutions. *Phys. Rev. Lett.*, 91(15):158302–5, 2003.

[37] B. Alberts, A. Johnson, J. Lewis, M. Raff, K. Roberts, and P. Walter. *Molecular Biology of the Cell*. Garland Science, New York, 5th edition, 2008.

[38] B. Kaminer and A. Bell. Myosin filamentogenesis: Effects of pH and ionic concentration. *J. Mol. Biol.*, 20(2):391–394, 1966.

[39] J. Koretz. Effects of c-protein on synthetic myosin filament structure. *Biophys. J.*, 27(3):433–446, 1979.

[40] J. Davis. Assembly processes in vertebrate skeletal thick filament formation. *Annu. Rev. Biophys. Biophys. Chem.*, 17:217–39, 1988.

[41] J. Davis, J. Buck, and E. Greene. The myosin dimer: an intermediate in the self-assembly of the thick filament of vertebrate skeletal muscle. *FEBS Letters*, 140(2):293–297, 1982.

[42] J. Koretz. Hybridization and reconstitution of thick-filament structure. *Methods Enzymol.*, 85 Pt B:20–55, 1982.

[43] T. Pollard. Structure and polymerization of *Acanthamoeba* myosin-ii filaments. *J. Cell Biol.*, 95(3):816 –825, 1982.

[44] E. Reisler, C. Smith, and G. Seegan. Myosin minifilaments. *J. Mol. Biol.*, 143(1):129–145, 1980.

[45] Isao Katsura and Haruhiko Noda. Further studies on the formation of reconstituted myosin filaments. *J. Biochem.*, 73(2):245–256, 1973.

[46] A D Saad, J D Pardee, and D A Fischman. Dynamic exchange of myosin molecules between thick filaments. *Proc. Natl. Acad. Sci. USA*, 83(24):9483–9487, 1986.

[47] S. Margossian and S. Lowey. Preparation of myosin and its subfragments from rabbit skeletal muscle. *Methods Enzymol.*, 85:55–71, 1982.

[48] S. Kron and J. Spudich. Fluorescent actin filaments move on myosin fixed to a glass surface. *Proc. Natl. Acad. Sci. USA*, 83(17):6272 –6276, 1986.

[49] R. DeBiasio, L. Wang, G. Fisher, and D. Taylor. The dynamic distribution of fluorescent analogues of actin and myosin in protrusions at the leading edge of migrating swiss 3T3 fibroblasts. *J. Cell Biol.*, 107(6):2631–45, 1988.

[50] J. Lebowitz, M. Lewis, and P. Schuck. Modern analytical ultracentrifugation in protein science: a tutorial review. *Protein Science*, 11(9):2067–2079, 2002.

[51] Z. Dogic, A. Philipse, S. Fraden, and J. Dhont. Concentration-dependent sedimentation of colloidal rods. *J. Chem. Phys.*, 113(18):8368–8380, 2000.

[52] A. Brown, A. Hategan, D. Safer, Y. Goldman, and D. Discher. Cross-correlated TIRF/AFM reveals asymmetric distribution of force-generating heads along self-assembled, "synthetic" myosin filaments. *Biophys. J.*, 96(5):1952–60, 2009.

[53] I. Pinset-Harstrom and J. Truffy. Effect of adenosine triphosphate, inorganic phosphate and divalent cations on the size and structure of synthetic myosin filaments. an electron microscope study. *J. Mol. Biol.*, 134(1):173–188, 1979.

[54] I. Horcas, R. Fernandez, J. Gomez-Rodriguez, J. Colchero, J. Gomez-Herrero, and A. Baro. WSXM: a software for scanning probe microscopy and a tool for nanotechnology. *Rev. Sci. Instrum.*, 78(1):013705–8, 2007.

Chapter 3

Active multistage coarsening of actin networks driven by myosin motors

In cells, many vital processes involve myosin-driven motility that actively remodels the actin cytoskeleton and changes cell shape. In this chapter we study how the collective action of myosin motors organizes actin filaments into contractile structures in a simplified model system devoid of biochemical regulation. We show that this self-organization occurs through an active multistage coarsening process. First, motors form dense foci by moving along the actin network structure followed by coalescence. Then the foci accumulate actin filaments in a shell around them. These actomyosin condensates eventually cluster due to motor-driven coalescence. We propose that the physical origin of this multistage aggregation is the highly asymmetric load response of actin filaments: they can support large tensions but buckle easily under piconewton compressive loads. Since the motor-generated forces well exceed this threshold, buckling is induced on the connected actin network which resists motor-driven filament sliding. We show how this buckling can give rise to the accumulation of actin shells around myosin foci and subsequent coalescence of foci into superaggregates. This new physical mechanism provides an explanation for the formation and contractile dynamics of disordered condensed actomyosin states observed in vivo.

Based on manuscript Marina Soares e Silva, Martin Depken, Björn Stuhrmann, Marijn Korsten, Fred C. MacKintosh and Gijsje H. Koenderink. *Active multistage coarsening of actin networks driven by myosin motors.* 2011 PNAS 108 (23) Doi: 10.1073/pnas.1016616108. Martin devised and described the model in this chapter.

All videos referred to in the text can be viewed at: http://www.pnas.org/content/early/2011/05/12/1016616108/suppl/DCSupplemental (Video captions in *Appendix 6.3.*)

3.1 Introduction

Cells undergo dramatic changes in shape and internal organization during vital processes such as migration and division. These changes involve remodeling of the cytoskeleton partly driven by collective physical interactions between molecular motors and cytoskeletal filaments. The motors use adenosine triphosphate (ATP) as fuel and hydrolyze it to actively generate forces and move along filaments [1]. Multiheaded motors or complexes of motors may crosslink neighboring filaments and generate relative motion between them. Kinesin and dynein motors interact with microtubules to form the mitotic spindle, which is responsible for chromosome segregation [2]. Myosin motors interact with filamentous actin (F-actin) to form complex arrays such as the contractile ring driving cell division [3, 4] and contractile networks that drive cell migration [4] and polarizing cortical flows [5, 6].

To identify the biophysical processes underlying cytoskeletal organization, many *in vitro* model systems of purified motors and filaments that lack biochemical regulation have been recently developed. It is known that kinesins can organize microtubules into polarity sorted asters, as well as vortex or bundle states [7, 8, 9, 10]. These structures resemble physiological arrays such as the mitotic spindle [11]. In contrast to microtubules, purified F-actin does not form well-defined structures when motors are added. Actin-myosin II solutions remain disordered at high levels of ATP [12, 13, 14] and generate dense condensates which appear internally unstructured if the ATP level is lowered or when the actin filaments are crosslinked [15, 16, 17, 18]. Interestingly, similar dense condensates appear in cells during myosin-driven shape changes of the actin cytoskeleton. Formation of the contractile ring in dividing fibroblasts [19] and C. elegans embryos [20] both involve large scale flows and coalescence of dense actomyosin condensates. Similarly, the lamellipodium of migrating cells displays dense myosin aggregates [21, 22]. Wounded cells display similar phenomena, with accumulation of myosin foci at the wound border and fusion of these foci into a tight ring capable of constriction [23]. Collective shape changes in epithelial cell layers also seem to be driven by the transient formation of myosin spots which subsequently fuse [24, 25, 26, 27].

The physical mechanism of self-organization in the actin-myosin cytoskeleton remains unknown. There are several theoretical models describing pattern formation in motor-filament systems [7, 28]. These models predict the emergence of ordered aster, vortex, and bundle architectures due to polarity sorting which relies on unidirectional motion of motors along the filaments they connect. Such patterns are also predicted from symmetry considerations, resulting in general hydrodynamic theories of active polar gels [29, 30, 31]. These patterns are consistent with experimental observations in microtubule-kinesin mixtures ([7, 8]), but are different from the

disordered condensed states seen in actin-myosin mixtures. Microscopic theories model the filaments as rigid and the motors as small, highly processive clusters. Microtubules are indeed rigid and nearly rodlike [32], and their associated motors tend to be highly processive [1], explaining the success of the proposed models in elucidating experimental observations. Unlike kinesins, most myosins are not processive and must act together in large macromolecular assemblies of several tens to hundreds of molecules [33]. In addition to the difference in motor processivity, F-actin is 1000-fold less rigid than microtubules and is known to buckle under compressive loads of fractions of a piconewton [32, 32]. In densely crosslinked networks, these microscopic features suggest that the collective organization of myosin and actin into force-generating cellular machines is not driven by polarity sorting but by a different organizing mechanism.

Here we use a model system of purified actin and myosin to uncover the physical mechanism by which myosin motors organize F-actin into contractile structures. We demonstrate that myosin actively drives a multistage coarsening process that brings actin filaments into disorganized condensates that resemble structures seen *in vivo*. We suggest a new microscopic mechanism that can explain this multistage process in terms of buckling of the actin network under the random internal forces generated by motors in such an isotropic structure. This mechanism is fundamentally different from polarity sorting mechanisms operating in microtubule/kinesin systems [7, 8]. Furthermore, this mechanism depends crucially on the open meshwork structure of actin networks, which is not well captured by continuum mechanical modeling that is frequently applied in active gel theories at larger scales [34, 35, 36].

3.2 Material and Methods

3.2.1 Actomyosin network reconstitution

Myosin synthetic filaments were formed at room temperature by dilution of myosin II in $25\,\mathrm{mM}$ imidazole buffer (pH 7.4) with $300\,\mathrm{mM}$ KCl to $70\,\mathrm{mM}$ KCl. To this end, myosin stock solution in $25\,\mathrm{mM}$ imidazole, $4\,\mathrm{mM}$ $MgCl_2$, pH 7.4 containing $300\,\mathrm{mM}$ KCl was mixed on ice with all buffer components, resulting in a final KCl concentration of $70\,\mathrm{mM}$ KCl. Myosin filaments were formed for 5 minutes at room temperature. Actin-myosin networks were prepared in assembly buffer with final concentrations of $25\,\mathrm{mM}$ imidazole-HCl, $0.1\,\mathrm{mM}$ MgATP, $50\,\mathrm{mM}$ KCl, $0.1\,\mathrm{mM}$ MgATP, $2\,\mathrm{mM}$ $MgCl_2$, $1\,\mathrm{mM}$ DTT, and pH 7.4. To prevent photobleaching, we added $2\,\mathrm{mM}$ Trolox [37], and to prevent ATP depletion, we included a regeneration mixture containing $1.25\,\mathrm{mM}$ creatine phosphate (Roche Diagnostics, Almere, the Netherlands) and $26\,\mathrm{units/mL}$ creatine kinase (Roche Diagnostics, Almere, the Netherlands) [14, 16]. The actin network was

fluorescently labeled by mixing Alexa488-labeled G-actin and unlabeled actin in a 1:20 molar ratio. We inserted a controlled number of crosslink points into the actin filaments by co-polymerizing biotinylated G-actin with unlabeled G-actin in a molar ratio of 1:1000. The number of available crosslink points per actin filament is about 2, based on an average filament length of $6\,\mu\mathrm{m}$ and assuming that crosslink points occur in equally probable random placement along the filaments. Excess streptavidin (streptavidin:actin molar ratio of 1:25) was included to form crosslinks between the biotinylated actin filaments. The molar ratio between myosin and actin was varied between 1:300 and 1:50. For all samples myosin was mixed with all buffers first, allowing the formation of synthetic filaments at room temperature. Finally, G-actin was added and the sample was quickly transferred to a flow cell composed of a glass slide and coverslip separated by a $25\,\mu\mathrm{m}$ FEP spacer (Fluorinated Ethylene Propylene Copolymer, Goodfellow) and closed with silicone grease (Baysilone, GE Bayer). The flow cell surface was passivated beforehand with $0.1\,\mathrm{mg/mL}$ κ-casein diluted in assembly to avoid non-specific interactions with the networks. The final structure of the patterns was unaffected when myosin monomers were added last to the polymerizing actin. However, this mixing sequence slowed the process of active coalescence down. Actin polymerization did not seem to affect the self-organization process: a fully formed actin network was present before any spatial inhomogeneities in actin or myosin density appeared. Rheology experiments suggested that network formation was complete within about 30 minutes (see Fig. 2.5A in *chapter 2*). As a further test that actin polymerization has no influence on self-organization, we mixed myosin filaments with preformed actin filaments, and indeed found the same final contracted states (Fig. 3.2). Details on protein purification and labeling and AFM imaging of myosin filaments are given in *chapter 2*.

3.2.2 Fluorescence microscopy

Samples were imaged within 5 minutes after mixing with a spinning disk confocal microscope (CSU22, Yokogawa Electric Corp.) on a DMIRB Leica inverted microscope. The sample was excited with $561\,\mathrm{nm}$ laser light (Melles Griot) or $488\,\mathrm{nm}$ laser light (Coherent Inc.). Images were recorded with a cooled EM-CCD camera (C9100, Hamamatsu Photonics) using an exposure time of 50-100 ms. Image stacks were obtained by scanning through the z-direction in steps of $100\,\mathrm{nm}$ with a piezo-driven 100x (1.3 NA) oil immersion objective (PL Fluotar Leica).

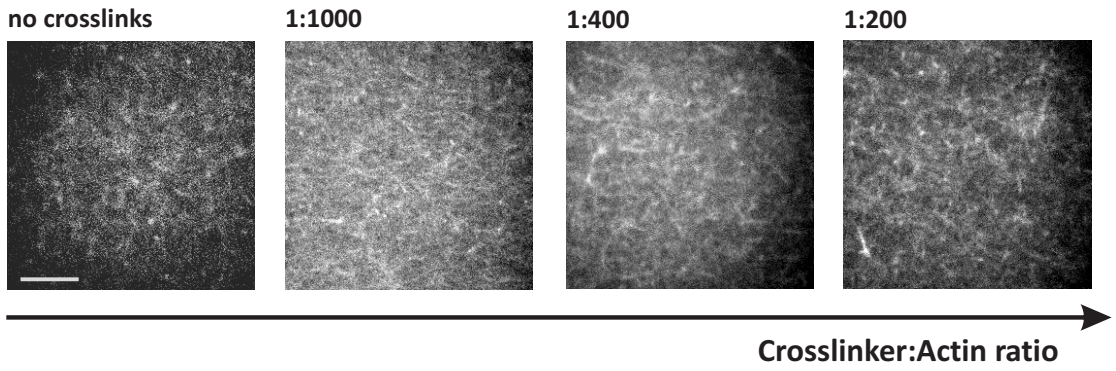

Figure 3.1: Passive actin network formation. **A.** Fluorescence micrographs of passive actin networks (no myosin) with different crosslinker (biotin-actin) densities. Crosslinking does not change the overall network structure up to a concentration of $0.12\,\mathrm{M}$ (at an actin concentration of $23.8\,\mathrm{M}$). Above this threshold, the network structure looks somewhat coarser, but no distinct aligned or ordered patterns are visible. Actin was polymerized in the presence of $50\,\mathrm{mM}$ KCl, $2\,\mathrm{M}$ $MgCl_2$ and $100\,\mu\mathrm{m}$ MgATP. Scale bar $10\,\mu\mathrm{m}$.

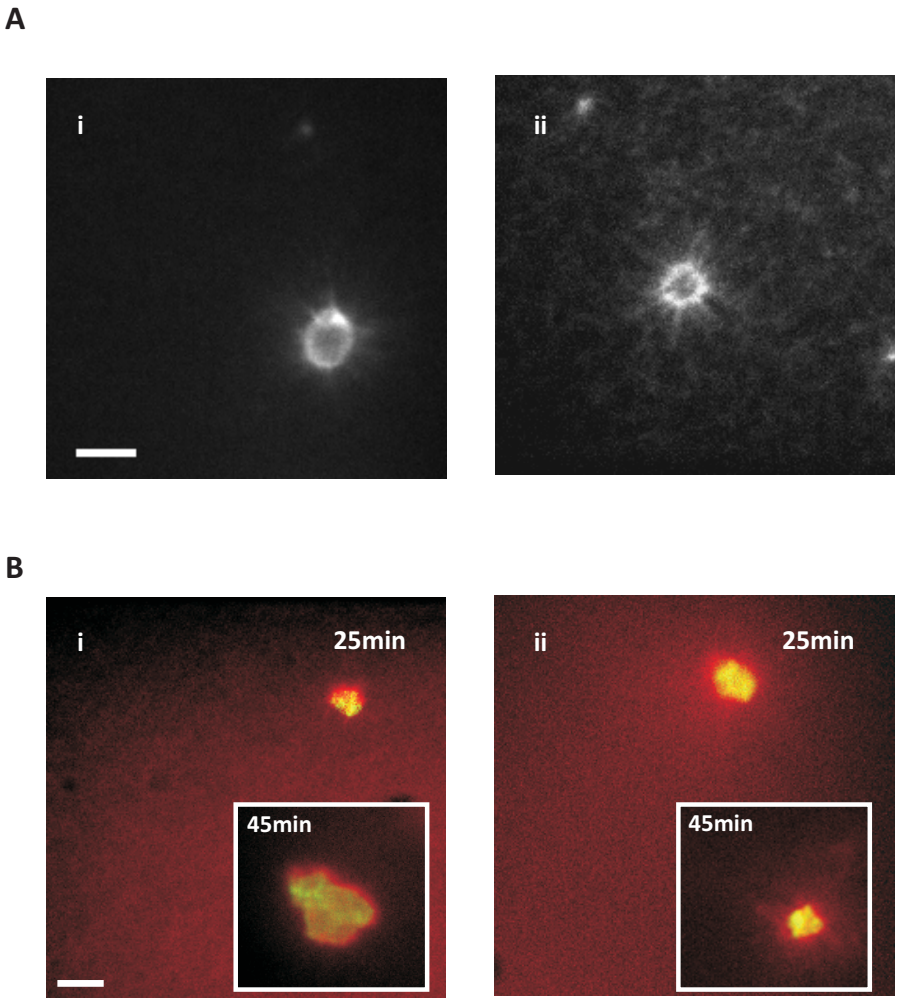

Figure 3.2: Active pattern formation in actomyosin networks is not affected by actin dynamics. **A.** Stabilizing actin filaments does not alter the multistage coarsening process. ***i*** Fluorescent micrograph of a network of labeled actin and unlabeled myosin filaments (myosin:actin ratio is 1:200) 35 min after polymerization in the presence of phalloidin (phalloidin:actin molar ratio is 1:1). Image shows example of a ring-like actin structure with a size of about $5\,\mu$m. The crosslinker:actin ratio is 1:1000. Scale bar is $5\,\mu$m. ***ii*** Fluorescent micrograph of control network without phalloidin. **B.** Mixing preformed actin filaments with myosin filaments does not alter the multistage coarsening process. ***i*** Fluorescent micrograph of a network of labeled actin filaments and myosin filaments (myosin:actin ratio is 1:200) 25 min after mixing. Image shows example of an actin/myosin condensate with a size of approximately $4\,\mu$m. Scale bar, $5\,\mu$m. *Inset* Example of a condensate 45 min after mixing. The crosslinker:actin ratio is 1:1000. ***ii***Fluorescent micrograph of control network 25 min after mixing of preformed myosin filaments with monomeric actin. *Inset* Example of a condensate 45 min after mixing.

3.2.3 Image analysis

To determine the size of actin condensates, we binarized 8-bit images in Image J (http://rsbweb.nih.gov/ij/) and measured the major radius of each feature using the "Measure" command. Data are shown as averages S.D. Kymographs were made with the Kymograph plugin for Image J by J. Rietdorf (FMI Basel, Switzerland) and A. Seitz (EMBL, Heidelberg, Germany).

3.3 Results

To examine how actin filament reorganization emerges from the collective activity of molecular motors, we reconstituted a minimal model system from purified proteins. F-actin was polymerized from monomers at a $1\,\mathrm{mg/mL}$ concentration to form homogeneous networks with no preferred filament orientation or polarity. To generate active internal stresses, we added skeletal muscle myosin II. Myosin II has two identical head domains with binding sites for actin filaments and ATP, and a coiled-coil tail domain [1]. Individual myosin motors are nonprocessive: they release immediately after taking one step towards the plus end of an actin filament. However, multiple myosins can assemble tail-to-tail into bipolar filaments with motor heads at each end (in green, Fig. 3.3D) [38]. Such assemblies have an increased collective duty cycle, allowing them to transiently crosslink actin filaments (in red, Fig. 3.3D).

Moreover, their bipolar geometry enables myosin heads to pull actin filaments of opposite orientations towards each other, as shown by the arrows. We used myosin filaments with an average length of $0.69\,\mu\mathrm{m}$ (Fig. 3.3E) or 100 myosin motors [39]. This size is larger than the size of myosin minifilaments in nonmuscle cells, which have 10-30 motors [21, 22]. A test with minifilaments of 16 skeletal muscle myosins showed little effect on actin filament reorganization (Fig. 3.4A-C). However, we expect that minifilaments of nonmuscle myosin, in particular myosin IIB, will be more processive since this myosin has a higher duty ratio than its muscle counterpart (*Appendix 6.1*, Table A1).

Active self-organization was initiated by polymerizing actin in the presence of preformed myosin filaments and $100\,\mu\mathrm{M}$ ATP. Motor activity was kept constant by an enzymatic ATP regeneration system [16]. To enable observation of the network structure by microscopy, we fluorescently labeled actin and myosin. Within two minutes after mixing, actin was polymerized into a homogeneous network (red in Fig. 3.3A i). The myosin filaments were initially homogeneously dispersed in the network (green dots indicated by arrow). However, after about 5 minutes, the myosin was redistributed into bright foci (green in Fig. 3.3A ii). The F-actin network was still homogeneous (Fig. 3.3A iii). After about 30 minutes, the myosin foci were surrounded

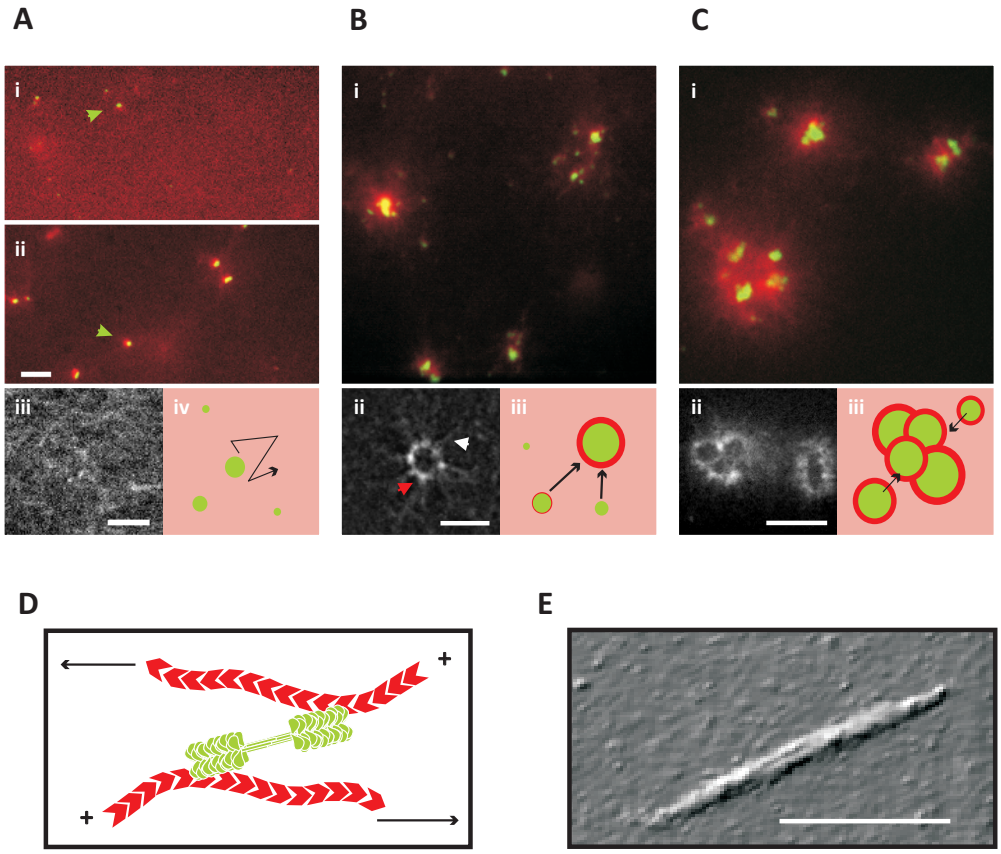

Figure 3.3: Actin-myosin networks self-organize through a three-stage coalescence process. **A.** ***i*** Fluorescence micrograph of an active network, taken 2 minutes after initiating actin polymerization in the presence of myosin bipolar filaments (1:200 myosin:actin). The actin network is homogenous and isotropic (red) and randomly crosslinked by active motors (green). ***ii*** After 6 minutes, the motors accumulate in larger structures (scale bar $10\,\mu\mathrm{m}$). ***iii*** The actin network is still homogeneous in this stage. Scale bar $5\,\mu\mathrm{m}$. ***iv*** In Stage 1 the actin network is homogeneous (pink) and contains small myosin foci (green) which move along the actin network (black arrow). **B.** ***i*** After 30 minutes, the actin network is organized in thin shells (red) around myosin foci (green). ***ii*** High-resolution image of an actomyosin condensate shows that actin filaments form a ring-like set of patches (red arrow) with actin filaments radiating out (white arrow). Scale bar $5\,\mu\mathrm{m}$. ***iii*** In Stage 2, myosin foci are surrounded by thin actin shells and small foci move towards larger immobile foci (arrows). **C.** ***i*** After 45 minutes, actomyosin condensates are packed in large superstructures. ***ii*** High-resolution image of a superstructure, showing merged actin ring-like structures. Scale bar $10\,\mu\mathrm{m}$. ***iii*** In Stage 3, superaggregates form by contractile coarsening (black arrows). **D.** Network activity results from bipolar myosin filaments (green) sliding actin filaments (red) of opposite orientation towards one another (arrows). **E.** AFM image of a myosin filament. Scale bar $0.5\,\mu\mathrm{m}$.

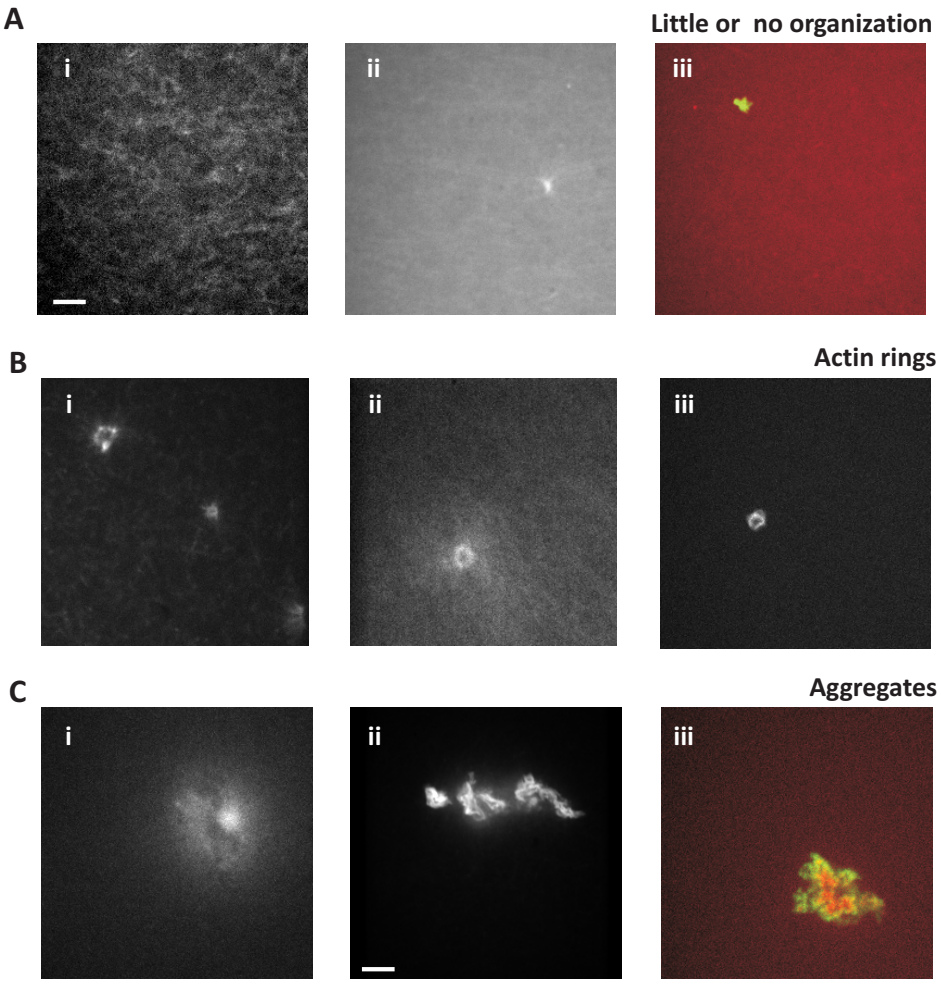

Figure 3.4: Myosin processivity affects *in vitro* actin active organization. **A-C.** Minifilaments of skeletal myosin II assembled at $150\,\mathrm{mM}$ KCl are seldom able to reorganize actin networks. **A.** Fluorescent micrographs of active networks ***i,ii*** with labeled actin and doubly labeled ***iii*** with actin in red and myosin in green. In the presence of myosin II minifilaments, networks often remain overall homogenous without evidence of active foci formation. **B.** Fluorescent micrographs of active networks with labeled actin. Rings rarely emerge in actin networks in the presence of minifilaments. **C.** Fluorescent micrographs of active networks i,ii with labeled actin and doubly labeled iii with actin in red and myosin in green. Often, disordered aggregates appear in the network. Scale bar, $5\,\mu\mathrm{m}$. All fields of view are the same size except figure C ii, where the scale bar is $10\,\mu\mathrm{m}$.

by actin rings (red in Fig 3.3B i). These rings are reminiscent of actin rings observed in the presence of skeletal myosin minifilaments and the actin bundler fascin [40]. However, high-resolution images of the rings with only actin fluorescently labeled (to avoid spectral crosstalk with myosin) revealed that they were not composed of a continuous band of actin filaments, but rather of a collection of compact actin aggregates with a size below $1\,\mu\mathrm{m}$ (Fig. 3.3B ii, red arrow). The rings were surrounded by a diffuse halo of actin filaments which radiated outward (Fig. 3.3B ii, white arrow). Three-dimensional image stacks further revealed that, rather than forming flat rings, actin deposited in a shell all around the myosin foci (Video S1 and Fig. 3.5A). These actin-myosin condensates were initially isolated structures within the actin network, but after 30-45 minutes we observed larger structures that appeared to be aggregates of actomyosin condensates (Fig. 3.3C i). High-resolution images showed that each aggregate consisted of a few hollow actin rings stuck together (Fig. 3.3C ii). Three-dimensional image stacks showed that these actin rings were again not flat, but that actin formed shells around the myosin foci (Video S2). Each aggregate contained several myosin foci with actin intercalated between them (Fig. 3.5B), suggesting that they result from coalescence of multiple actomyosin condensates.

These observations suggest that myosin motors drive coalescence of actin into disordered aggregates through a multistage process. To elucidate the transition pathway between these stages, we studied the dynamics of the myosin motors and the actin network in each stage by time-lapse imaging.

In the first stage, the myosin filaments were homogeneously distributed in the network. We tracked the filaments over time and found that they were strikingly mobile (Fig. 3.6A and Video S3). Many filaments moved by a sequence of straight runs, punctuated by abrupt changes in direction. The long run lengths indicate the motors were not simply diffusing in solution, but moved on the F-actin network. Occasionally, two neighboring myosin filaments came together and fused into a small myosin focus (Fig. 3.6B and Video S4). Upon meeting, small foci sometimes coalesced further into larger myosin foci (Fig. 3.6C and Video S5). Once the myosin foci reached a size similar to the average pore size ($300\,\mathrm{nm}$), they no longer moved since their motion was presumably hindered by the actin mesh. Nonetheless, they could still grow by coalescence with smaller mobile aggregates.

Initially, myosin foci formation did not drastically reshape the actin network (sketched in Fig. 3.3A iv). However, once myosin foci became immobile, they were able to capture actin from the surrounding network (Videos S6 and S7). Such events account for the deposition of dense actin patches on the surface of the myosin foci (sketched in Fig. 3.3B iii). The condensation of actin into shells around myosin foci was typically complete within 30 minutes. Yet, the networks continued to display striking manifestations of contractile activity. Often, two neighboring actomyosin

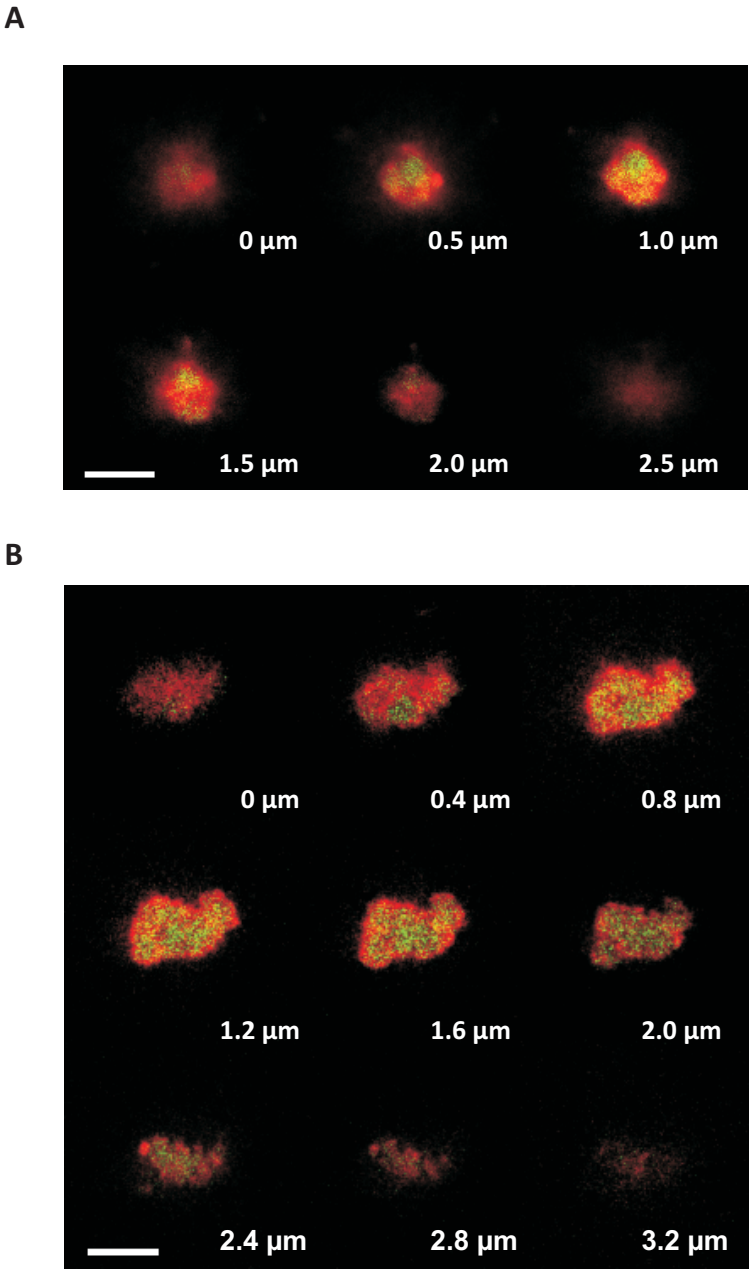

Figure 3.5: Stack of confocal microscopy x-y slices of fluorescently labeled actin-myosin condensates (myosin in green and actin in red). Scale bars, $5\,\mu\mathrm{m}$. **A.** Sequence of xy-slices of an actomyosin condensate at 1:200 motor:actin ratio. Myosin is in the center, and an actin shell surrounds it. **B.** Sequence of xy-slices of a superaggregate composed of several actomyosin condensates at 1:50 motor:actin ratio. Each myosin focus within the condensate is surrounded by a shell of actin.

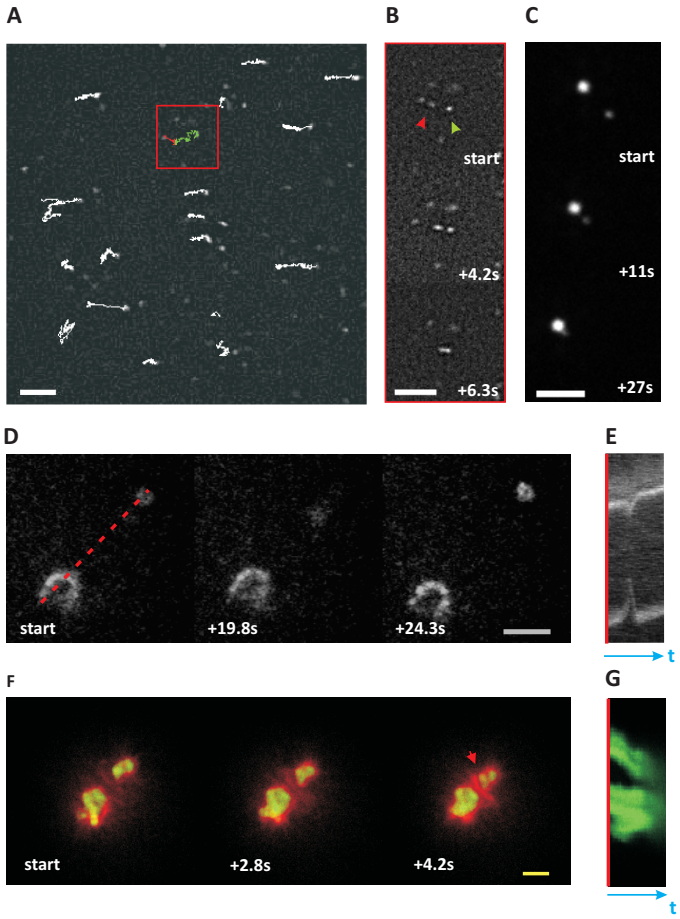

Figure 3.6: Dynamics of actin/myosin coalescence. **A.** Trajectories of myosin filaments moving on an actin network (1:200 myosin:actin; 3 minutes after sample preparation). Red and green traces represent two filaments that coalesce after an active walk. Scale bar $5\,\mu$m. **B.** Time-lapse image sequence of coalescing myosin filaments corresponding to the green and red traces (see arrows). Scale bar $5\,\mu$m. **C.** Time-lapse image sequence of two fusing myosin foci. Scale bar $5\,\mu$m. **D.** Time-lapse image sequence of two actomyosin condensates (red arrows, actin labeled) undergoing a contractile fluctuation (1:200 motors). Scale bar, $10\,\mu$m. **E.** Kymograph constructed along red dashed line in D. **F.** Time-lapse image sequence of two actomyosin aggregates that coalesce and accumulate actin between them (red arrow, 1:50 myosin:actin). Scale bar, $10\,\mu$m. **G.** Kymograph constructed along red dashed line in F.

condensates were suddenly pulled towards one another and then recoiled. An example of such a contractile fluctuation event is displayed in Fig. 3.6D (see Video S8 and Fig. 3.7A, top panel). Usually we observed only one recoil, but sometimes recoils occurred twice (Video S9 and Fig. 3.7A bottom panel) or even three times (Video S10 and Fig. 3.7B).

Kymographs show that the actin condensates approach and recoil at velocities of $\sim 0.3\,\mu\mathrm{m/s}$ (Fig. 3.6E). The myosin foci apparently build up tension over a processivity time window of several tens of seconds, until they unbind from the F-actin leading to an abrupt release of the built-up elastic stress. These observations are consistent with prior indirect observations of contractile network fluctuations based on motions of embedded probe particles [16, 41]. Especially at larger motor densities, contraction often resulted in permanent coalescence, likely reflecting the dissipation of elastic stresses before the motors disengage. An example of such a coalescence event is displayed in figure 3.6F, where two myosin foci (green) approach each other (Fig. 3.6G) and compact the actin (red) between them (Video S11). Surprisingly, myosin foci were able to attract each other over distances of up to $25\,\mu\mathrm{m}$, about 5 times the average length of the actin filaments. This observation suggests that the actin network between myosin foci is sufficiently connected by myosin crosslinks to mediate long-range force transmission. Since the network is disordered on this scale (tens to hundreds of mesh sizes), it is unlikely that filament polarity is the main origin of the directed motion. In a few cases, we observed cable-like actin structures between actomyosin foci which shortened over time (see Video S12). Contractile coalescence continued until the resulting clusters were too far apart to interact (sketched in Fig. 3.3C iii). This final state was typically reached within 100 minutes.

The extent of aggregation strongly depended on motor density. Higher motor densities increased the probability of irreversible coalescence. At a myosin:actin ratio of 1:200, only half of the contractile events (N=55) resulted in permanent coalescence, whereas at a myosin:actin ratio of 1:50 most events (N=29) resulted in permanent coalescence (Fig. 3.7C). Accordingly, the final steady state at low motor density showed small isolated foci (1:300 and 1:200 in Fig. 3.8A), whereas high motor densities resulted in large superaggregates (1:50 in Fig. 3.8A). To quantify this enhanced tendency for coalescence at high motor densities, we measured the overall size of actin aggregates in steady state. The average size increased from $1.8\,\mu\mathrm{m}$ at low (1:300) myosin:actin ratio to $5.3\,\mu\mathrm{m}$ at high (1:50) myosin:actin ratio (Fig. 3.8B and *Appendix 6.1.* Table 2). As shown in the insets, this larger size was caused by an increased number of myosin foci at the aggregate core, while the thickness of the actin shell remained constant.

The increasing tendency for coarsening with rising motor density is probably the combined outcome of a larger contractile driving force and larger connectivity

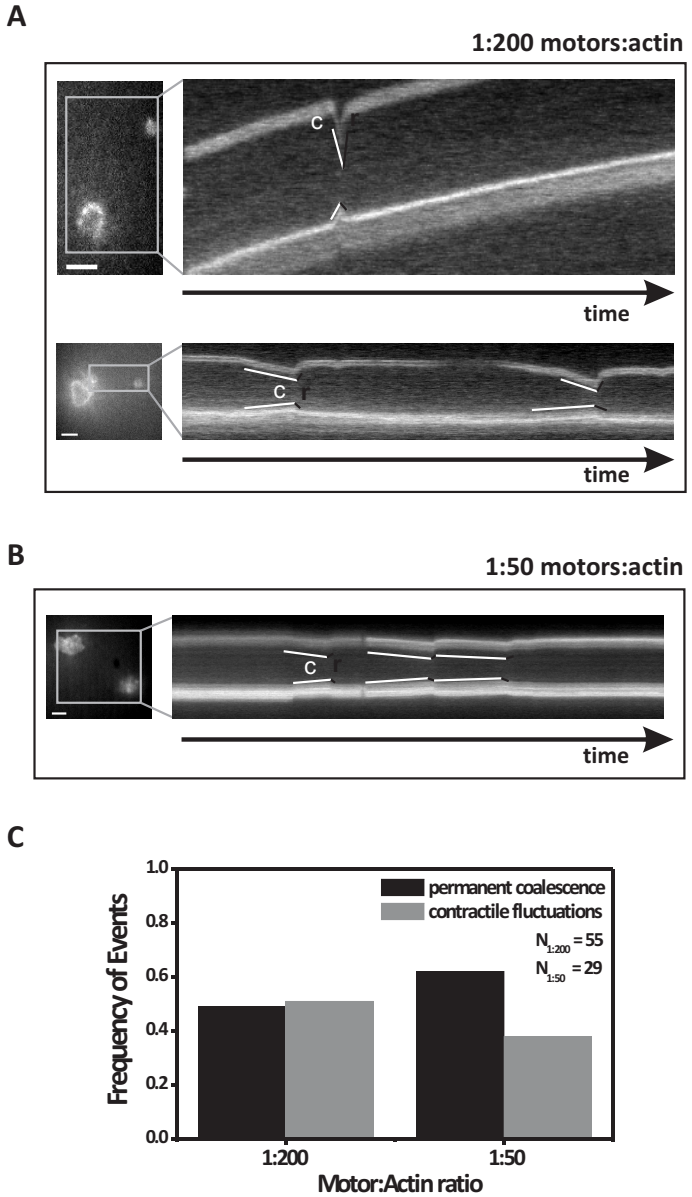

Figure 3.7: Myosin concentration influences the dynamics of actin network contractility. **A-B.** Snapshots of actomyosin condensates (labeled actin only) with corresponding kymographs of contractile fluctuation events. White lines indicate contracting period (c) and black lines indicate relaxation/recoil (r). Scale bars, $5\,\mu$m. **A.** Top: Two ring-like actin structures move towards each other and relax. Total kymograph duration $612\,$s. Bottom: Two small actin structures move towards each other and relax two consecutive times. Total kymograph duration 133 s. The crosslinker:actin ratio is 1:1000 and the myosin:actin ratio is 1:200. **B.** Two large actin structures slowly move towards each other and then relax three consecutive times. Total kymograph duration $154\,$s. The crosslinker:actin ratio is 1:1000 and the myosin:actin ratio is 1:50. **C.** Statistics of permanent coalescence versus contractile fluctuation events of actomyosin condensates in actin-myosin networks as a function of myosin:actin molar ratio.

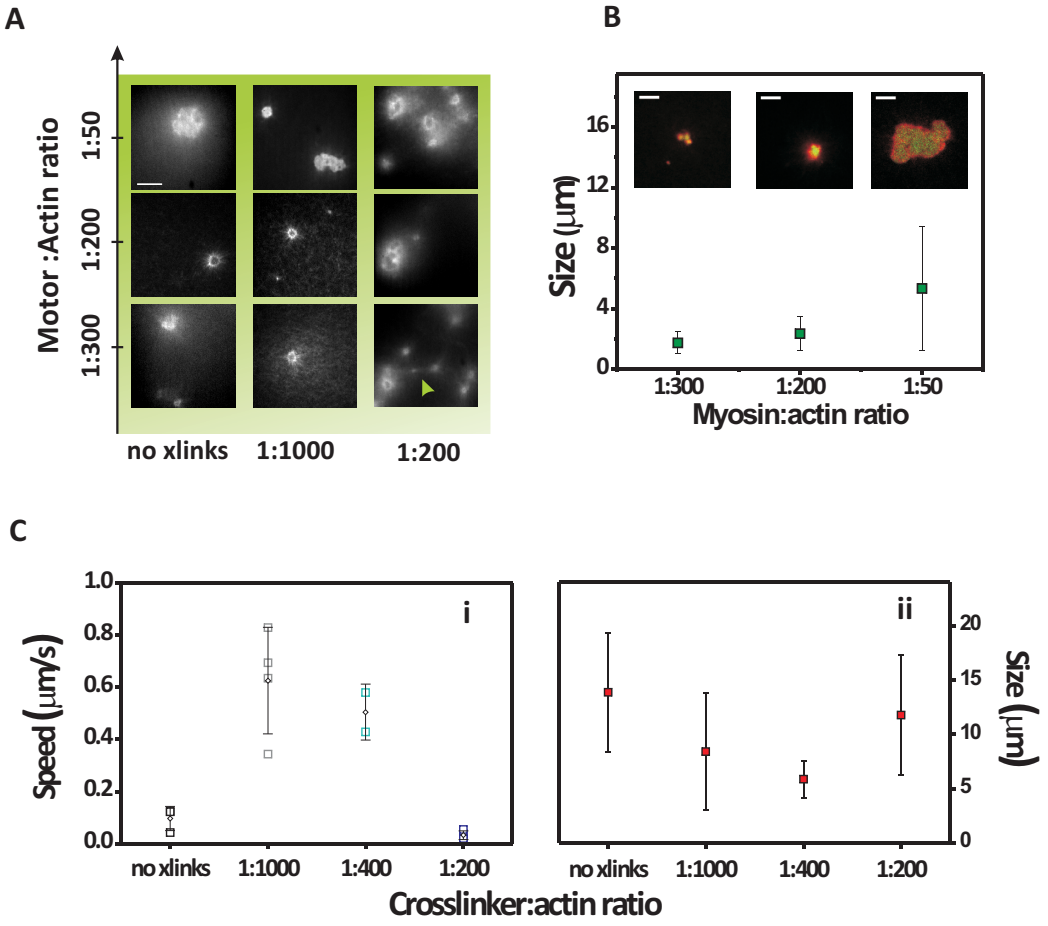

Figure 3.8: Active coarsening is promoted by increased motor and crosslink density. **A.** Steady-state actin patterns observed in active networks containing varying concentrations of myosin motors and biotin-streptavidin crosslinks. Scale bar, $10\,\mu\mathrm{m}$. **B.** The average size of actomyosin condensates increases with increasing motor density (1:400 biotin:actin). Inset: Confocal images show that this size increase results from an increased degree of coalescence. Scale bars $5\,\mu\mathrm{m}$. **C.** ***i*** The average speed of foci movement depends non-monotonically on crosslink density (actin:myosin ratio 1:50). Open squares represent individual data points; open diamonds represent the average speed for each crosslinker density. ***ii*** The crosslinker density-dependence of the size of actomyosin condensates mirrors that of the contraction speed. All error bars represent standard deviations of the mean.

due to motor crosslinking. We assessed the effect of network connectivity on contractility by adding passive crosslinkers. F-actin was doped with varying amounts of biotin-actin and crosslinked with streptavidin at a fixed streptavidin:actin ratio (1:25). Biotin-streptavidin crosslinks are near-permanent, generating elastic behavior on time scales that are long compared to the lifetime of myosin-actin attachments. We used low crosslink densities to ensure a homogeneous actin network structure (Fig. 3.1A) and prevent macroscopic contraction (15, 17). In the presence of crosslinkers, actin again formed patches around myosin foci, and the resulting actomyosin condensates coalesced. However, coalescence occurred at much lower motor density (myosin:actin ratio 1:200) than in the absence of crosslinkers (1:50) (Fig. 3.8A). This confirms our hypothesis that increased network connectivity promotes contractile coarsening. Interestingly, adding crosslinks also influenced the coalescence dynamics. In the absence of crosslinks, merging foci had velocities of $\sim 0.10\,\mu\mathrm{m/s}$ (Fig. 3.8C i and *Appendix 6.1*, Table 2). Crosslinking substantially increased the velocity, to a maximum of $\sim 0.6\,\mu\mathrm{m/s}$ at a biotin:actin ratio of 1:1000. However, at high crosslinker densities (1:200) the velocity fell back to $0.03\,\mu\mathrm{m/s}$. The size of the actomyosin condensates showed a reverse dependence on crosslinking, with smallest sizes where the coalescence speed was highest (Fig. 3.8C ii and *Appendix 6.1*, Table 2). We expect that increasing network connectivity leads to a trade-off between a higher velocity as a greater fraction of filaments is connected to others, and a decreased velocity as the passive stress opposing the active contraction increases. In the most crosslinked networks, the foci were connected by bundle-like actin structures (green arrow in last panel of Fig. 3.8A). While these structures probably facilitate contraction, they are likely connected to the background actin network, thus impeding coalescence.

3.4 Discussion

Based upon fluorescence microscopy of active actin/myosin networks, we conclude that myosin drives the formation of disordered actomyosin condensates through a multistage coarsening process. Actin filaments are compacted into dense clouds around large myosin foci and these actomyosin condensates then contract into larger superaggregates. The resulting structures are intrinsically three-dimensional (3D), in strong contrast to the more two-dimensional (2D) aggregates reported previously, such as rings formed in fascin-bundled actomyosin systems [40] and vortices formed in actomyosin networks on surfaces [42]. Although planar ring structures might relate to the vortex-like states predicted by active gel theories [29, 31, 43], such features are intrinsically 2D patterns and are topologically not possible in 3D [44]. Thus, the non-planar, shell-like, structures we observe must form by another mechanism.

In most active gel theories, the driving force for self-organization comes from small, processive motors or motor clusters. By contrast, we find that large motor assemblies drive the active remodeling in this actin/myosin system. Myosin motor filaments spontaneously form foci, beginning from a uniform distribution in an isotropic actin network. Motors and small motor foci perform random walks on the network: they bind to actin filaments, move along and switch between them, coalescing as they meet (Stage 1, Fig. 3.9A). The apparent, large-scale diffusion constant D of this process should be $D \approx vl \approx 1\,\mathrm{m/s^2}$. Here v is the typical speed of myosin aggregates ($1\,\mu\mathrm{m/s}$) and l is the typical run length between direction changes($\approx 1\,\mu\mathrm{m}$, Fig. 3.6E), which we assume to be somewhat larger than the mesh size. Since we expect the internal dynamics of the myosin load cycle to be rate limiting, D should be insensitive to aggregate size. As the foci grow to a size comparable to the mesh size of the network, however, their motion will be impeded by elastic interactions with the network. The accumulation of motor filaments into foci occurs without significant concurrent F-actin transport. This differs from self-organization in mixtures of microtubules and kinesin oligomers, where the motors accumulate into foci as they focus microtubules into radial arrays [8, 9].

Figure 3.9 Once the myosin foci reach a certain size, they initiate Stage 2 of the assembly process by drawing actin in. Due to the random directions of actin filaments in an isotropic network, the net force exerted by a myosin focus (Fig. 3.9B, IMF or immobilized myosin focus) should grow as $N^{1/2}$, where N is the number of actin filaments it interacts with. Eventually, the net force should be sufficient to overcome elastic constraints and perform dissipative work remodelling the local network structure. Collectively, the myosin heads projecting from each focus can exert either an expansive or a compressive force on the surrounding network of actin filaments. We propose that stochastic alternations between expansion and compression will have the net effect of pulling in actin towards a myosin focus (Fig. 3.9B). The physical argument is that actin filaments have a highly asymmetric response to axial loading: they strongly resist stretching but not compression. Under compression, an actin segment of length L readily buckles at a critical force $f_c \sim \pi^2 K_B T l_p / L^2$, where the persistence length $l_p \sim 17\,\mu\mathrm{m}$ [32]. For a segment of micrometer length or longer, this force is less than $1\,\mathrm{pN}$ [45]. The internal forces generated by a single myosin filament already well exceed this buckling threshold [16, 34]. Thus, a net expansive force over a patch of actin connected to a myosin focus will be strongly opposed by the high stretch modulus of the actin filaments within the patch. By contrast, a net compressive force will buckle the actin filaments, drawing actin in. This mechanical asymmetry is necessary and sufficient for actin to accumulate, as detailed in the *Appendix 6.2*. Bridging of buckled structures by (transient) myosin crosslinking to other actin filaments will further enhance this accumulation (Fig. 3.9B, IMF surrounded by crumpled actin, A).

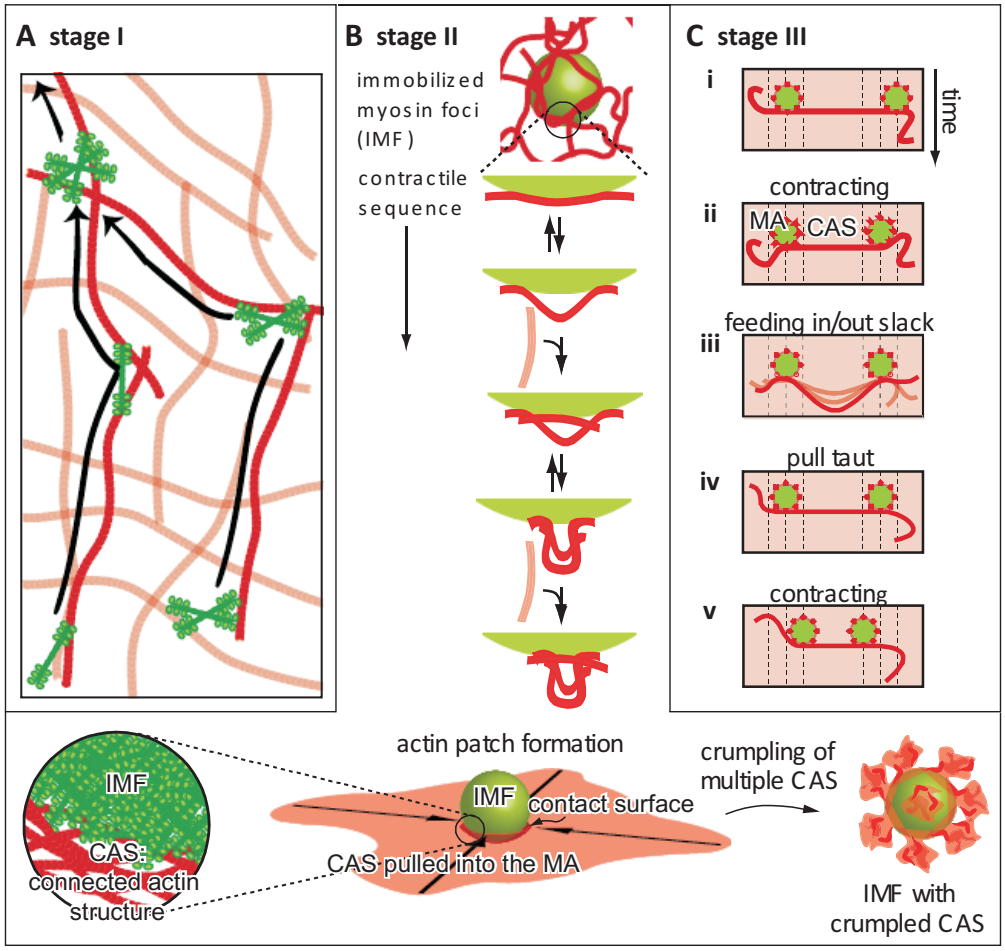

Figure 3.9: Proposed multistage mechanism of myosin-driven self-organization of actin networks. **A.** Stage 1: Myosin filaments or aggregates thereof, move actively on the actin network and coalesce upon meeting. **B.** Stage 2: An immobilized myosin focus (IMF) accumulates a cloud of actin patches in a stochastic sequence of expansive steps (resulting in marginal extension) and contractile steps (resulting in buckling, made permanent by subsequent bridging). The myosin foci have a large interaction surface with the surrounding actin via the protruding myosin heads. Compressive forces exerted by the focus cause the actin to buckle at the surface and form a crumpled actin structure (A). **C.** Stage 3: Two actomyosin aggregates (MA, in green) interact isotropically with the background actin network (shaded red) and will move together by interacting via a connected cluster of actin filaments (represented by a red line). This contraction involves net extension of the connecting actin structure, which brings the foci together, followed by net contraction, which pushes in slack due to buckling. Slack needs to be pulled out before the foci can move closer together.

In the final stage of the coalescence process (Stage 3), actomyosin condensates coalesce into large superaggregates. We propose that if two myosin foci happen to exert forces on the same connected cluster of actin filaments, they will eventually coalesce, again due to the asymmetric load response of actin filaments. If the net forces of the two foci happen to stretch the connecting actin structure, its resistance to extension will force the foci together (panel ii in Fig Fig. 3.9C). If the net forces of the two foci instead happen to compress the connecting actin structure, it will buckle and push in slack between the two foci rather than bearing the load and pushing them apart (panel iii in Fig Fig. 3.9C). Before the random forces can pull the aggregates together again (panel v in Fig. 3.9C), any material buckled during prior compressive loads must be pulled out (panel iv in Fig. 3.9C). Only when the connecting structure is taut can it exert significant forces on the foci. Then the myosin foci will tend to be driven toward each other. Instead of the coherent, unidirectional motion normally associated with motor transport, this model predicts that foci will move in an incoherent, intermittent fashion (see *Appendix 6.2* and Video S13). The time-dependent motion of coalescing foci is consistent with this prediction (Fig. 6.1, in *Appendix 6.2*).

The physical mechanism for actomyosin self-organization outlined above differs substantially from prior models of self-organization in active gels. The nonlinear buckling events that are crucial in our mechanism cannot be captured by linear hydrodynamic theories[29, 30, 31, 43]and hitherto have not been part of microscopic theories [29, 46] or simulations [7, 28, 43]. Both hydrodynamic and microscopic theories were inspired by experiments in microtubule/kinesin systems [7, 8, 10]. These systems differ from actin/myosin systems in at least two aspects. First, microtubules have a persistence length of several millimeters [32] and are therefore less easily buckled by motor-driven forces. We expect that bundling F-actin should bring the system closer to microtubule systems. Indeed some experimental work points to this: in actomyosin systems bundled by fascin, the final steady states are networks of asters reminiscent of microtubules organized by kinesins [40]. In vivo, actin asters with dense clusters of myosin at their center were observed in fibroblasts stimulated to contract with cytochalasin D [47]. Such asters had a uniform polarity with actin plus-ends pointing inwards, as expected in case of polarity sorting by plus-end directed motors. Second, force centers in active microtubule gels were small, processive motor clusters interacting mostly with microtubule pairs, whereas the force centers in active actin gels are large myosin aggregates interacting with many actin filaments. At a large scale, these force centers can be modeled as force dipoles in a continuum (visco)elastic background. However, on the micrometer scale on which actin reorganizes in our experiments, it is unlikely that continuum elasticity represents a realistic description, especially in view of the asymmetric, nonlinear response of the individual filaments. Thus, a more microscopic model is needed (*Appendix 6.2*).

Our work suggests that mechanisms of self-organization in motor-filament systems are not strictly universal, but depend on the biophysical characteristics of both filaments and motors. This non-universality is biologically relevant: the physiological function of microtubule arrays differs from that of actin arrays. Microtubules form well-focused mitotic spindle poles, to accomplish high-fidelity separation of the duplicated chromosomes [2]. In contrast, actomyosin aggregates appear in cells from diverse tissues and organisms as transient structures that coalesce into larger arrays that exert contractile forces. Examples include the formation of contractile rings driving cytokinesis [3, 4] and wound healing [23], and the formation of contractile networks driving deformation of epithelial cell layers in developing embryos [24, 25] and polarizing cortical flows [5, 6]. Our findings suggest that the formation and subsequent colescence of myosin foci *in vivo* [26] can emerge spontaneously from physical interactions between actin filaments and motors. However, Rho-mediated signaling events certainly contribute to the localized assembly and activation of myosin alongside with purely biophysical effects by changing myosin's phosphorylation state [48]. Localized Rho zones for instance lead to localized assembly of active myosin foci in the cleavage furrow [20, 49] and in wound borders [23]. Interestingly, the size of the actomyosin condensates *in vitro* is comparable to the size of condensates observed *in vivo* (*Appendix 6.1*, Table 3). It will be interesting to test the activity of purified non-muscle myosins in our assay. Muscle and non-muscle myosins differ in duty ratio, sliding velocity, and filament size (*Appendix 6.1*, Table 1). Non-muscle myosin IIB is substantially more processive than muscle myosin II, which should suppress the dissolution of actomyosin condensates and enhance the late stages of coalescence. Nonmuscle myosins also have a substantially smaller sliding velocity than muscle myosin II, which should reduce the coalescence rate.

Even though our reconstituted assay mimics self-organized structures and dynamics of actomyosin in cells, there is an important difference. Our *in vitro* structures are irreversible once assembled, whereas cellular structures dissolve and reform on time scales of minutes. The low $(0.1\,\mathrm{mM})$ ATP level in the *in vitro* assay compared to the typical mM ATP level in nonmuscle cells may contribute to the enhanced stability of the structures. This low level was a prerequisite for active coarsening by skeletal muscle myosin II. At mM ATP concentrations, we did not observe active contractility (Fig.3.10) in line with prior studies [12, 13]. We attribute this ATP dependence to the low duty ratio of skeletal muscle myosin II. With excess ATP, the duty ratio is only 4%, but lowering the ATP concentration to $100\,\mathrm{M}$ increases the duty ratio about fourfold [12, 13, 50].

In addition to the different ATP level, multiple factors that cause dynamic remodeling in cells are absent in our assay. Disassembly will likely require actin depolymerization and monomer recycling. The actin filaments in our experiments were

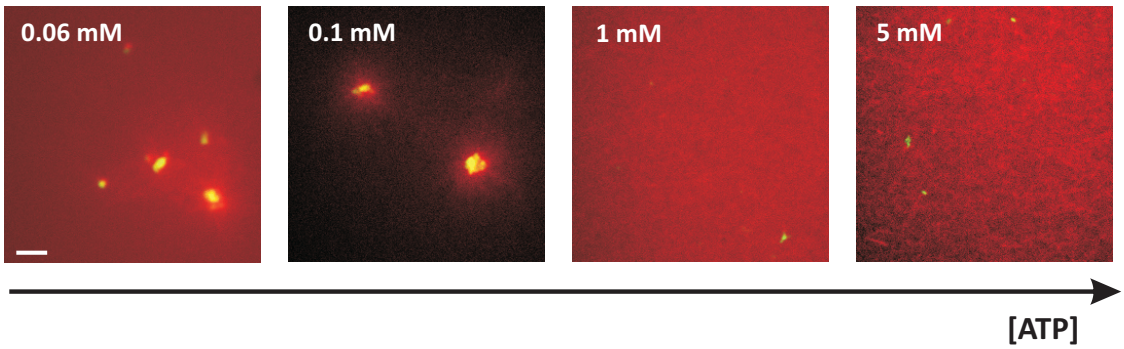

Figure 3.10: ATP concentration modulates pattern formation in active actin-myosin networks. Fluorescence micrographs of actomyosin networks (actin in red and myosin in green) taken at different ATP concentrations. At levels of 60-100 μM ATP, myosin is sufficiently processive to cause the formation of actomyosin condensates. In contrast, the actin network remains homogeneous and the myosin filaments remain homogeneously dispersed in the network at mM ATP concentrations, indicating that myosin is not sufficiently processive to cause network reorganization. Scale bar, 5 μm. Samples from panels A-D. contain 1:200 myosin:actin and the crosslinker:actin ratio is 1:1000.

not stabilized and were, thus, in a state of constant treadmilling. Nonetheless, this treadmilling process is very slow [51] and stabilization of actin with phalloidin indeed did not change the self-organization process (Fig.3.2A). However, cells contain protein factors which accelerate depolymerization or sever F-actin. It will be interesting to incorporate some of these regulators in our assay [52]. Another contribution to fast pattern renewal in cells may be the transient nature of physiological actin-crosslinking proteins. Notably, a recent *in vitro* study of actin networks bundled with fascin showed that myosin could spontaneously disassemble contractile structures [40]. There may be an interplay between myosin force production and force-induced dissociation of crosslink proteins which controls the lifetime of cellular contractile structures [53, 54]. Finally, assembly of cellular actomyosin condensates into ordered structures such as contractile rings depends not only on myosin contractility but also on forces produced by actin disassembly [23, 55].

3.5 Conclusion

We have shown that myosin motors organize actin filaments into contracted states through a multistage aggregation process. We propose a new physical mechanism that can account for this process based on motor-induced buckling in connected actin structures. The fact that the reconstituted system is able to mimic cellular self-organized states and their contractile dynamics suggests that physical interactions contribute to the regulation of cell and tissue morphogenesis.

3.6 Outlook

Stripping cellular systems of their complexity creates multiple possibilities of exploring how their different components contribute to a specific cell process. In this thesis I have explored how motor protein density modulates both structure and dynamics of active actin networks (*chapters 3 and 4*). In *chapter 3*, I also addressed the question how crosslinking of actin filaments affects network reorganization by motors. I used artificial biotin-streptavidin crosslinks, which are rigid and nearly irreversible. I showed that increasing the density of crosslinks per actin filament promotes contractile coarsening of actin-myosin networks up to a characteristic crosslinker:actin molar ratio of 1:400 (see Fig. 3.8). Up to this crosslinker concentration, the networks are in a regime of rather weak and isotropic crosslinking. Above this ratio, the network undergoes macroscopic contraction, a phenomenon previously observed in similar *in vitro* systems [15, 17]. Figure 3.11 shows confocal images of actin-myosin networks in the regime of high crosslink density. Above 1:400 crosslinks:actin, the actin

network reorganizes at a global scale, reflecting the enhanced network connectivity. This massive reorganization can take as little time as 5 minutes in networks with high motor (1:50 myosin:actin) and crosslink (1:20-1:200 biotin:actin) densities. In highly connected actin gels, the network irreversibly coarsens to very dense clusters of irregular shell-like structures (ring-like in the displayed confocal z-slices). Studies of active networks of actin filaments bundled by the physiological actin-binding protein fascin revealed myosin-driven formation of asters, 2D-rings and swirls of actin [40, 56]. Contrary to biotin-streptavidin, fascin forms unipolar actin bundles [57], and it is conceivable that the resulting bundle polarity is a determinant of the apparently reversible assembly of such structures.

The above described *in vitro* model system hints at how cells may regulate their actin cytoskeletal structures relying on different types of crosslinkers. Crosslinkers with distinct functions have been reported to locate to specific structures *in vivo*: some actin crosslinkers like α-actinin isotropically crosslink actin in transient structures like the contractile ring [58], while fascin localizes to more stable bundle-like structures in filopodia, bristles and stereocilia [57]. To understand which factors promote active large scale contraction of actin networks, it would be useful to test *in vitro* the effect of different physiological crosslinkers that are potentially involved in transient actin structure formation. I predict that such assembly will sensitively depend on a proper balance of motor activity and crosslinker density, where the motors themselves also affect network connectivity.

There are also additional factors that may influence network connectivity and thereby contractility, namely actin-binding proteins that regulate the length of F-actin. The longer the filaments, the more likely they are to sterically hinder or entangle with each other [59], thus increasing network connectivity. Several actin-binding proteins directly control F-actin length. Gelsolin, an actin capping protein limits the length of actin filaments by capping their plus ends [60]. In preliminary *in vitro* assays, I tested the effect of reducing filament length on pattern formation in active actin-myosin networks. Adding gelsolin in a molar ratio of 1:740 to G-actin causes reduces reduction in average filament length from 6 to $2\,\mu\mathrm{m}$. This length reduction had a dramatic effect on pattern formation (Fig. 3.12). Instead of undergoing a multistep coarsening process, the networks displayed a rather homogenous structure throughout the $\sim$ 1.5 hours of the assay. Small threadlike aggregates of myosin (shown in green) are distributed randomly throughout the actin network (shown in red). In addition to this, there were no obvious contractile fluctuations in the network (data not shown). Cells could make use of actin length regulators such as gelsolin as a strategy to dynamically regulate the formation of transient contractile structures. It would be interesting to systematically test the effect of the length of F-actin on organization of active networks to assess which is the minimum connectivity required for force

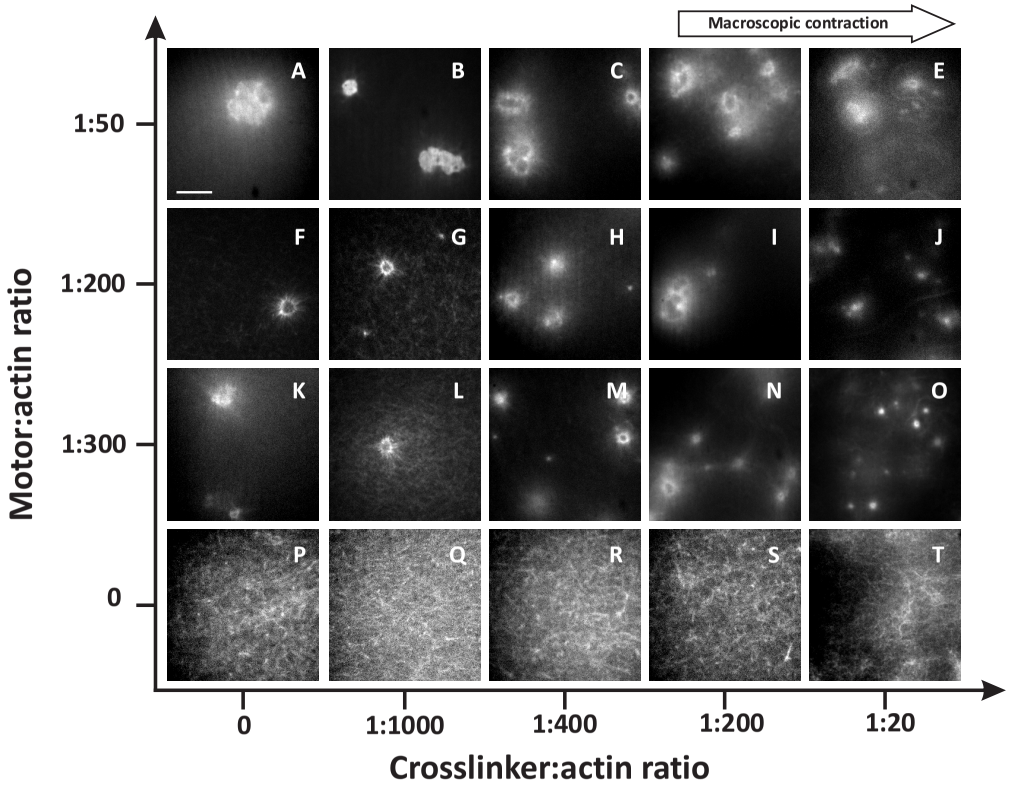

Figure 3.11: The active formation of actin patterns is modulated by the densities of motors and crosslinkers relative to the actin concentration. Confocal micrographs of the phase space for actin networks (with a fixed concentration of 1 mg/mL) with increasing amounts of crosslinkers (biotin-actin : actin molar ratio) and myosin motors (myosin : actin molar ratio). Scale bar is $10\,\mu$m.

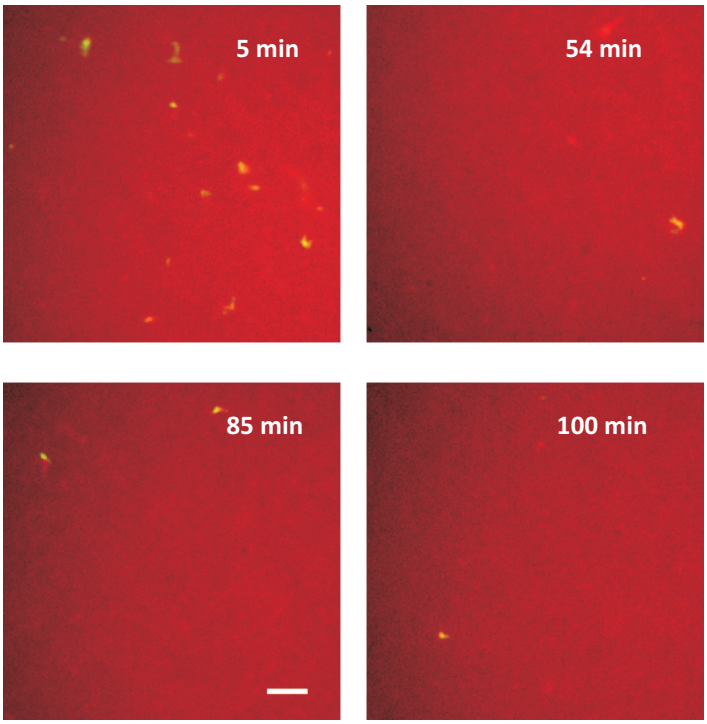

Figure 3.12: Decreasing the length of actin filaments reduces the extent of active network coarsening. Confocal micrographs of the time evolution of actin (red) and myosin (green) networks assembled in the presence of 1:740 gelsolin:actin (giving an average actin filament length of $\sim 2\,\mu\mathrm{m}$). The actin concentration is 1 mg/mL, the myosin:actin ratio is 1:200 and the crosslinker:actin ratio is 1:1000. Scale bar is $5\,\mu\mathrm{m}$.

propagation and therefore contractility of the network.

3.7 Acknowledgments

We thank S. Duineveld, M. Kuit-Vinkenoog, and I. Piechocka with help in protein purification and M. Gardel and M. Lenz for discussions.

References

[1] J. Howard. *Mechanics of motor proteins and the cytoskeleton.* Sinauer, Sunderland, Massachusetts, 2001.

[2] E. Karsenti and I. Vernos. The mitotic spindle: a self-made machine. *Science*, 294(5542):543–547, 2001.

[3] D. Vavylonis, J. Wu, S. Hao, B. O'Shaughnessy, and T. Pollard. Assembly mechanism of the contractile ring for cytokinesis by fission yeast. *Science*, 319(5859):97–100, 2008.

[4] S. Moores, J. Sabry, and J. Spudich. Myosin dynamics in live *Dictyostelium* cells. *Proc. Natl. Acad. Sci. USA*, 93(1):443–6, 1996.

[5] S Hird and J White. Cortical and cytoplasmic flow polarity in early embryonic cells of *Caenorhabditis elegans. J. Cell Biol.*, 121(6):1343–55, 1993.

[6] M. Mayer, M. Depken, J. Bois, F. Julicher, and S. Grill. Anisotropies in cortical tension reveal the physical basis of polarizing cortical flows. *Nature*, 467:617–621, 2010.

[7] T. Surrey, F. Nédélec, S. Leibler, and E. Karsenti. Physical properties determining self-organization of motors and microtubules. *Science*, 292(5519):1167–71, 2001.

[8] F. Nedelec, T. Surrey, A. Maggs, and S. Leibler. Self-organization of microtubules and motors. *Nature*, 389(6648):305–308, 1997.

[9] C. Hentrich and T. Surrey. Microtubule organization by the antagonistic mitotic motors kinesin-5 and kinesin-14. *J. Cell Biol.*, 189(3):465–480, 2010.

[10] R. Urrutia, M. McNiven, J. Albanesi, D. Murphy, and B. Kachar. Purified kinesin promotes vesicle motility and induces active sliding between microtubules *in vitro. Proc. Natl. Acad. Sci. USA*, 88(15):6701 –6705, 1991.

[11] E Karsenti, F Nedelec, and T Surrey. Modelling microtubule patterns. *Nat. Cell. Biol.*, 8(11):1204–11, 2006.

[12] D. Humphrey, C. Duggan, D. Saha, D. Smith, and J. Käs. Active fluidization of polymer networks through molecular motors. *Nature*, 416(6879):413–416, 2002.

[13] D. Smith, F. Ziebert, D. Humphrey, C. Duggan, M. Steinbeck, W. Zimmermann, and J. Käs. Molecular motor-induced instabilities and crosslinkers determine biopolymer organization. *Biophys. J.*, 93:4445 – 4452, 2007.

[14] G. Koenderink, Z. Dogic, F. Nakamura, P. Bendix, F. MacKintosh, J. Hartwig, T. Stossel, and D. Weitz. An active biopolymer network controlled by molecular motors. *Proc. Natl. Acad. Sci. U.S.A.*, 106(36):15192–7, 2009.

[15] EW Janson, J Kolega, and DL Taylor. Modulation of contraction by gelation/solation in a reconstituted motile model. *J. Cell Biol.*, 114(5):1005–15, 1991.

[16] D. Mizuno, C. Tardin, C. Schmidt, and F. MacKintosh. Nonequilibrium mechanics of active cytoskeletal networks. *Science*, 315(5810):370–373, 2007.

[17] PM Bendix, GH Koenderink, D Cuvelier, Z Dogic, BN Koeleman, WM Brieher, CM Field, L Mahadevan, and DA Weitz. A quantitative analysis of contractility in active cytoskeletal protein networks. *Biophys. J.*, 94(8):3126–36, 2008.

[18] H Strzelecka-GolasZewska, U. Piwowar, and B. Pliszka. Changes in the ultrastructure of actomyosin gel during hydrolysis of ATP under various ionic conditions. *Eur. J. Cell Biol.*, 24:116–123, 1981.

[19] R DeBiasio, G LaRocca, P Post, and D Taylor. Myosin II transport, organization, and phosphorylation: evidence for cortical flow/solation-contraction coupling during cytokinesis and cell locomotion. *Mol. Biol. Cell*, 7(8):1259–82, 1996.

[20] M. Werner, E. Munro, and M. Glotzer. Astral signals spatially bias cortical myosin recruitment to break symmetry and promote cytokinesis. *Curr. Biol.*, 17(15):1286–1297, 2007.

[21] A. Verkhovsky, T. Svitkina, and G. Borisy. Myosin II filament assemblies in the active lamella of fibroblasts: their morphogenesis and role in the formation of actin filament bundles. *J. Cell Biol.*, 131(4):989–1002, 1995.

[22] A. Verkhovsky and G. Borisy. Non-sarcomeric mode of myosin II organization in the fibroblast lamellum. *J. Cell Biol.*, 123(3):637–652, 1993.

[23] C. Mandato and W. Bement. Contraction and polymerization cooperate to assemble and close actomyosin rings around *Xenopus* oocyte wounds. *J. Cell Biol.*, 154(4):785–797, 2001.

[24] G. Blanchard, S Murugesu, R. Adams, A. Martinez-Arias, and N. Gorfinkiel. Cytoskeletal dynamics and supracellular organisation of cell shape fluctuations during dorsal closure. *Development*, 137(16):2743 –2752, 2010.

[25] J. Franke, R. Montague, and D. Kiehart. Nonmuscle myosin II generates forces that transmit tension and drive contraction in multiple tissues during dorsal closure. *Curr. Biol.*, 15:2208–2221, 2005.

[26] A. Martin, M. Kaschube, and E. Wieschaus. Pulsed contractions of an actin-myosin network drive apical constriction. *Nature*, 457(7228):495–9, 2009.

[27] M. Rauzi, P. Verant, T. Lecuit, and P. Lenne. Nature and anisotropy of cortical forces orienting *Drosophila* tissue morphogenesis. *Nat. Cell Biol.*, 10(12):1401–1410, 2008.

[28] J. Astrom, P. Kumar, and M. Karttunen. Aster formation and rupture transition in semi-flexible fiber networks with mobile cross-linkers. *Soft Matter*, 5(15):2869–2874, 2009.

[29] K. Kruse, J. Joanny, F. Julicher, J. Prost, and K. Sekimoto. Asters, vortices, and rotating spirals in active gels of polar filaments. *Phys. Rev. Lett.*, 92(7):078101, 2004.

[30] F. Ziebert and W. Zimmermann. Nonlinear competition between asters and stripes in filament-motor systems. *Eur. Phys. E Soft Matter*, 18(1):41–54, 2005.

[31] H. Lee and M. Kardar. Macroscopic equations for pattern formation in mixtures of microtubules and molecular motors. *Phys. Rev. E*, 64(5):056113, 2001.

[32] F. Gittes, B. Mickey, J. Nettleton, and J. Howard. Flexural rigidity of microtubules and actin filaments measured from thermal fluctuations in shape. *J. Cell Biol.*, 120(4):923–934, 1993.

[33] M. Vicente-Manzanares, X. Ma, R. Adelstein, and A. Horwitz. Non-muscle myosin II takes centre stage in cell adhesion and migration. *Nat. Rev. Mol. Cell Biol.*, 10(11):778–790, 2009.

[34] F. MacKintosh and A. Levine. Nonequilibrium mechanics and dynamics of motor-activated gels. *Phys. Rev. Lett.*, 100(1):018104, 2008.

[35] K. Kruse and F. Julicher. Self-organization and mechanical properties of active filament bundles. *Phys. Rev. E*, 67(5):051913, 2003.

[36] A. Lau, B. Hoffmann, A. Davies, JC. Crocker, and T. Lubensky. Microrheology, stress fluctuations, and active behavior of living cells. *Phys. Rev. Lett.*, 91(19):198101–4, 2003.

[37] W. Koopmans, A. Brehm, C. Logie, T. Schmidt, and J. van Noort. Single-Pair FRET microscopy reveals mononucleosome dynamics. *J. Fluoresc.*, 17(6):785–795–795, 2007.

[38] H Huxley. Electron microscope studies on the structure of natural and synthetic protein filaments from striated muscle. *J. Mol. Biol.*, 7:281–308, 1963.

[39] F. Pepe and B. Drucker. The myosin filament. VI. myosin content. *J. Mol Biol.*, 130(4):379–393, 1979.

[40] F Backouche, L Haviv, D Groswasser, and A Bernheim-Groswasser. Active gels: dynamics of patterning and self-organization. *Phys Biol.*, 3(4):264–273, 2006.

[41] C. Brangwynne, G. Koenderink, F. Mackintosh, and D. Weitz. Nonequilibrium microtubule fluctuations in a model cytoskeleton. *Phys. Rev. Lett.*, 100(11):118104, 2008.

[42] V. Schaller, C. Weber, C. Semmrich, E. Frey, and A. Bausch. Polar patterns of driven filaments. *Nature*, 467(7311):73–77, 2010.

[43] S. Sankararaman, G. Menon, and P. Kumar. Self-organized pattern formation in motor-microtubule mixtures. *Phys. Rev. E*, 70(3):031905, 2004.

[44] M. Eisenberg and R. Guy. A proof of the hairy ball theorem. *Amer. Math. Mon.*, 86(7):571–574, 1979.

[45] M. Footer, J. Kerssemakers, J. Theriot, and M. Dogterom. Direct measurement of force generation by actin filament polymerization using an optical trap. *Proc. Natl. Acad. Sci. USA*, 104(7):2181 –2186, 2007.

[46] T. Liverpool and M. Marchetti. Instabilities of isotropic solutions of active polar filaments. *Phys. Rev. Lett.*, 90(13):138102, 2003.

[47] A Verkhovsky, T Svitkina, and G Borisy. Polarity sorting of actin filaments in cytochalasin-treated fibroblasts. *J. Cell Sci.*, 110(5):1693–1704, 1997.

[48] J. Tan, S. Ravid, and J. Spudich. Control of nonmuscle myosins by phosphorylation. *Annu. Rev. Biochem.*, 61(1):721–759, 1992.

[49] M. Zhou and Y. Wang. Distinct pathways for the early recruitment of myosin II and actin to the cytokinetic furrow. *Mol. Biol. Cell*, 19(1):318–26, 2008.

[50] J. Finer, R. Simmons, and J. Spudich. Single myosin molecule mechanics: piconewton forces and nanometre steps. *Nature*, 368(10):113–119, 1994.

[51] J. Kuhn and T. Pollard. Real-time measurements of actin filament polymerization by total internal reflection fluorescence microscopy. *Biophys. J.*, 88(2):1387–1402, 2005.

[52] D. Pantaloni, C. Clainche, and M Carlier. Mechanism of actin-based motility. *Science*, 292(5521):1502–1506, 2001.

[53] E. Reichl, Y. Ren, M. Morphew, M. Delannoy, J. Effler, K. Girard, S. Divi, P. Iglesias, S. Kuo, and D. Robinson. Interactions between myosin and actin crosslinkers control cytokinesis contractility dynamics and mechanics. *Curr. Biol.*, 18(7):471–80, 2008.

[54] C. Wilson, M. Tsuchida, G. Allen, E. Barnhart, K. Applegate, P. Yam, L. Ji, K. Keren, G. Danuser, and J. Theriot. Myosin II contributes to cell-scale actin network treadmilling through network disassembly. *Nature*, 465(7296):373–377, 2010.

[55] A. Carvalho, A. Desai, and K. Oegema. Structural memory in the contractile ring makes the duration of cytokinesis independent of cell size. *Cell*, 137(5):926–937, 2009.

[56] S. Köhler, V. Schaller, and A. Bausch. Structure formation in active networks. *Nat. Mater.*, 10(6):462–468, 2011.

[57] J. Bartles. Parallel actin bundles and their multiple actin-bundling proteins. *Curr. Opin. Cell Biol.*, 12(1):72–78, 2000.

[58] D. Courson and R. Rock. Actin crosslink assembly and disassembly mechanics for alpha-actinin and fascin. *J. Biol. Chem.*, 2010.

[59] D. Morse. Viscoelasticity of tightly entangled solutions of semiflexible polymers. *Phys. Rev. E*, 58(2):1237–1240, 1998.

[60] E. Prochniewicz, Q. Zhang, P. Janmey, and D. Thomas. Cooperativity in F-Actin: binding of gelsolin at the barbed end affects structure and dynamics of the whole filament. *J. Mol. Biol.*, 260(5):756–766, 1996.

Chapter 4

Dynamics of active actin-myosin networks probed by video particle tracking

We probe the spatiotemporal characteristics of myosin-dependent dynamics in actin-myosin networks by video tracking of embedded probe particles. We observed clear signatures of the non-equilibrium contractile activity of the motors in the form of bouts of sudden, directed motion of the probes that were usually followed by relaxation. To quantify the frequency of these active events, we developed an automated segmentation algorithm to distinguish periods of active, directed motion from periods of random motion. We found that directed motion occurs mainly during the first 30 minutes after sample preparation, whereas later it becomes infrequent. This age-dependence is reflected in the ensemble averaged dynamics, which show large mean square displacements and non-Gaussian displacement distributions in the first 30 minutes, whereas after 30 minutes the ensemble averaged dynamics resembles that of passive (no myosin) samples. The time-dependence of the active dynamics matches the time-dependence of motor-driven coarsening of the actin network, which we observed with confocal fluorescence microscopy. Detailed analysis of active translocation and relaxation events of probe particles by kymographs indicated that network coarsening is accompanied by large (up to $25\ \mu\mathrm{m}$*) displacements of beads and plastic network deformation. After 30 minutes, there were only sporadic, and small, contractile fluctuations, likely because the motors were mostly concentrated in clusters and depleted from the intervening network. It will be interesting to extend existing theories of active gel dynamics to account for the time-dependent and spatially inhomogeneous structure of actin-myosin gels and to explore implications of this coupling between structure and dynamics for microrheology in cells.*

Based on manuscripts under preparation by Marina Soares e Silva*, Björn Stuhrmann*, Fred C. MacKintosh, Gijsje H. Koenderink. Björn designed and performed the automated analysis protocol. *Shared 1st author.

4.1 Introduction

Living cells are viscoelastic materials that are out of thermodynamic equilibrium as a result of dissipative processes in the cytoplasm fueled by metabolic energy [1]. The cytoskeleton is constantly remodeled by active (de-)polymerization of filamentous actin (F-actin) and microtubules (MTs), and by motor proteins that slide these filaments or that move cargo across them [2]. These processes lead to active transport of cellular components that add up to the ubiquitous thermal fluctuations that all cellular components are subject to.

Several studies have sought to quantify, through microrheological approaches, how these active processes influence dynamics of probe particle inside the cytoplasm or on the exterior cell surface. The cytoplasm can be probed using endogenous particles such as endosomes, melanosomes or lipid granules [3, 4, 5], or by tracking exogenous probes imported by microinjection or phagocytosis [6, 7, 8]. Microspheres attached on the cell surface can be physically coupled to the intracellular actin cytoskeleton via transmembrane integrin receptors [9, 10, 11]. There are two complementary microrheology methods. Active microrheology probes the viscoelastic properties of the cell by directly measuring the displacement of probe particles in response to a force applied with optical or magnetic tweezers [12, 13, 14, 15, 16]. Instead, passive microrheology probes the spontaneous displacements of beads in the absence of an external force [17, 18, 19]. In thermal equilibrium, beads are subject only to thermal fluctuations, so passive microrheology measures the same material response function as active microrheology, as stipulated by the fluctuation-dissipation theorem (FD) of statistical physics [20]. The FD theorem is a generalization of Einstein's description of Brownian motion of probe particles in a viscous liquid [21]. In a liquid, the viscosity can be extracted from the bead fluctuations using Stokes law, while in a viscoelastic fluid, the complex shear modulus can be extracted using a generalized Stokes law [7, 17, 22]. If there is a discrepancy between the response function measured by active microrheology and passive microrheology, this is strong evidence of non-equilibrium activity. Several studies in cells combining passive and active microrheology indeed present evidence that intracellular activity leads to a violation of the FD theorem, in particular at low frequency [5].

While there is clear evidence of non-equilibrium dynamics in cells [5, 10, 12, 13, 14, 16, 23], the exact microscopic origin of this phenomenon is difficult to disentangle. The complex molecular composition and architecture of cells renders it difficult to identify the molecules or processes responsible for out-of-equilibrium fluctuations. To circumvent this complexity, several studies have focused instead on minimal model systems reconstituted from purified cytoskeletal components, in particular actin and myosin II. It was shown that single-headed myosin II subfrag-

ments (known as S1) can increase the effective temperature of an actin network [24]. Myosin II filaments, which are more processive than S1 subfragments, were shown to cause contractile fluctuations in actin networks, which lead to a violation of the FD theorem at low frequencies [25] and to diffusive-like motion of spherical probes and short-length scale bending of embedded microtubules [26]. Another signature of non-equilibrium activity that has been reported is non-Gaussianity in the distribution of displacements (or Van Hove correlation functions) of spherical and rod-shaped particles [26]. Particles inside a network that is in thermal equilibrium and has a homogeneous structure are expected to display Gaussian Van Hove correlation functions [19]. Non-Gaussianity can arise from temporal or spatial heterogeneities [19], or from non thermal activity [26]. In crosslinked networks, motor activity may cause sustained build-up of tension, which can lead to substantial network stiffening [14]. To account for these experimental observations, theoretical models have been proposed that model the motors as force dipoles in a homogeneous, continuum elastic medium [27, 28, 29]. These models predict violations of the FD theorem at frequencies below the characteristic frequency of motor detachment. The physical picture is that the motors gradually build up tension when they attach to F-actin, followed by sudden detachment and passive relaxation of the built-up stress.

Recent studies of motor-driven organization of actin networks *in vitro* have revealed that motors substantially affect the spatial structure of these networks. In entangled solutions of actin, the motors form large clusters which locally condense the actin network into disordered shell-like structures (see *chapter 3*, and references [30, 31]). Crosslinking with biotin-streptavidin accelates coarsening, and leads to larger condensed structures. Bundling of actin with fascin generates different types of collective reorganization, involving clusters of actin bundles [32] and networks of asters or vortices [31, 32, 33]. The consequences of this time-dependent restructuring of actin networks for the dynamics of probe particles in these networks have, to the best of our knowledge, not yet been addressed in experimental or theoretical studies.

In this chapter, we use an *in vitro* model system of weakly crosslinked actin-myosin networks to characterize non-equilibrium network dynamics by microrheology and to relate these dynamics to the time-dependent remodeling of the networks by myosin contractile activity. We examined active networks in two limits of motor density, which differ in the extent of motor-driven remodeling. At high motor density (1:65 myosin:actin ratio), the motors cause massive network coarsening (Fig. 4.1, high density, scheme), whereas at low motor density (1:200 myosin:actin ratio), the networks also coarsen, but slower and at smaller length scales (Fig. 4.1, low density, scheme). We focus the microrheology analysis on the low motor density regime, where the probe particles are homogeneously distributed and can be used for spatiotemporal mapping of network dynamics. We identify signatures of non-

equilibrium activity in the ensemble averaged dynamics of the particles. To investigate the microscopic origin of this activity, we moreover examine the single particle trajectories. We propose a new algorithm to segment trajectories into episodes of active, directed motion and random (undirected) motion, and use this to quantify the spatiotemporal frequency of activity and to identify collective particle motion. Moreover, we perform kymograph analysis of the trajectories to quantify the time scales, displacements, and velocities associated with active, directed particle motion.

4.2 Materials and Methods

4.2.1 Particle surface passivation

For particle tracking experiments we used polystyrene microspheres (lot♯GK0470701B, G.Kisker, Steinfurt, Germany), with a diameter of $2\,\mu\mathrm{m}$. This diameter was optimal for tracking active dynamics in actin networks of $1\,\mathrm{mg/mL}$. Smaller microspheres ($1\,\mu\mathrm{m}$) were clustered by motor-driven network condensation, even at low motor density (myosin:actin ratio of 1:200). In contrast, larger particles ($5\,\mu\mathrm{m}$) were insensitive to active network rearrangements induced by motor activity, not showing perceptible displacements ($<$3 events in a movie with a total duration of 75 minutes, N=30 particles in the field of view). To prevent protein adsorption to the probe particles, the particle surface was passivated by adsorption of PLL-PEG (PLL(20)-g[3.5]-PEG, SuSos, Switzerland), using $1.98 \times 10^{-8}\,\mathrm{mg}$ PLL-PEG per m^2 of particle surface. The positively charged PLL block adsorbs to the negatively charged microsphere surface, while the PEG block forms a brush layer that presents a steric barrier against protein adsorption. Particles from a stock solution ($30\,\mu\mathrm{L}$ of suspension of 2.5% solid fraction) were first sonicated to break up any clusters, pelleted by centrifugation for 5 minutes at $13.2\,\mathrm{krpm}$, and resuspended in $300\,\mu\mathrm{L}$ water containing $0.25\,\mathrm{mg/mL}$ PLL-PEG. The microspheres were incubated for 30 minutes in the tube while constantly rotating on a wheel at $10\,\mathrm{rpm}$ to prevent particle sedimentation. The solution was subsequently centrifuged for 5 minutes at $8.9\,\mathrm{krpm}$ and the supernatant was removed. The particles were finally resuspended in $60\,\mu\mathrm{L}$ of $25\,\mathrm{mM}$ imidazole-HCl (pH 7.4).

4.2.2 Actomyosin network reconstitution

Myosin synthetic filaments were pre-formed by fast dilution of unlabeled or DyLight594-labeled myosin II. To this end, myosin stock solution in $25\,\mathrm{mM}$ imidazole, $4\,\mathrm{mM}$ $MgCl_2$, pH 7.4 containing $300\,\mathrm{mM}$ KCl was mixed on ice with all buffer components, resulting in a final KCl concentration of $70\,\mathrm{mM}$ KCl. Myosin filaments were

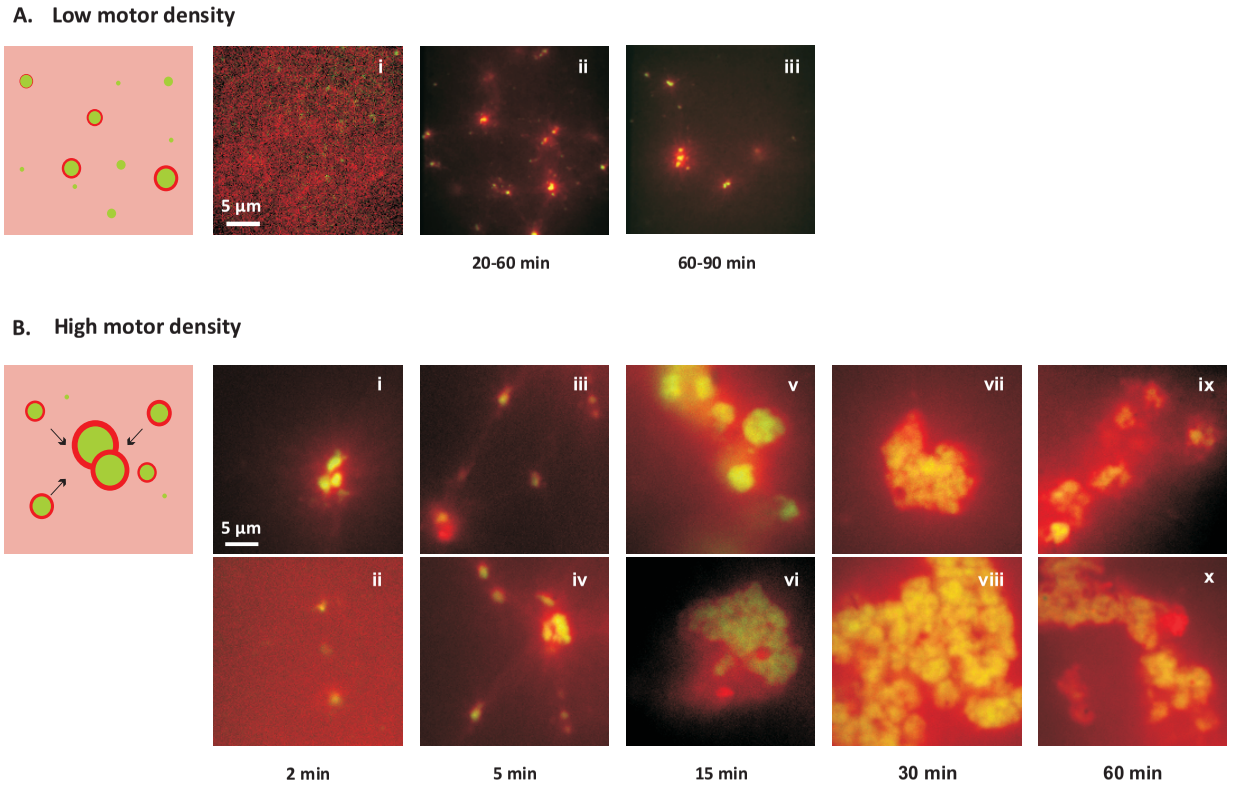

Figure 4.1: Actin-myosin networks coarsen over a time period of 90 minutes in a motor-density dependent manner. **A.** *Scheme* Low motor density: myosin foci surrounded by actin shells distributed homogeneously throughout the network. ***i-iii*** Confocal micrographs of myosin (green) in actin networks (red) organizing over 90 minutes into randomly distributed small myosin foci surrounded by actin shells. **B.** *Scheme* High motor density: myosin foci surrounded by actin shells cluster together into large structures to form a highly heterogeneous network. ***i-x*** Confocal micrographs of myosin (green) in actin networks (red) organizing over a period of 60 minutes into large condensed clusters of myosin foci surrounded by actin. All fields of view are of equal x/y dimensions and scale bars are $5\,\mu\mathrm{m}$.

formed for 5 minutes at room temperature. Actin-myosin networks were prepared in assembly buffer with final concentrations of $25\,\mathrm{mM}$ imidazole-HCl, $0.1\,\mathrm{mM}$ MgATP, $50\,\mathrm{mM}$ KCl, $0.1\,\mathrm{mM}$ MgATP, $2\,\mathrm{mM}$ $MgCl_2$, $1\,\mathrm{mM}$ DTT, and pH 7.4. To prevent photobleaching, we added $2\,\mathrm{mM}$ Trolox [34], and to prevent ATP depletion, we included a regeneration mixture containing $1.25\,\mathrm{mM}$ creatine phosphate and $26\,\mathrm{units/mL}$ creatine kinase (both from Roche Diagnostics, Almere, the Netherlands) [25, 35]. PLL-PEG-passivated polystyrene microspheres were added to actomyosin samples in a volume ratio of 1 to 2.

The actin concentration was $23.8\,\mu\mathrm{M}$ $(1.0\,\mathrm{mg/mL})$ in all experiments. The actin network was fluorescently labeled by mixing Alexa488-labeled G-actin and unlabeled actin in a 1:20 molar ratio. We controlled the number crosslink points per actin filament by co-polymerizing biotinylated G-actin with unlabeled G-actin in a molar ratio of 1:1000. The average number of available crosslink points per actin filament is about 2, based on an average filament length of $6\,\mu\mathrm{m}$ and assuming that crosslink points occur in equally probable random placement along the filaments. Excess streptavidin (streptavidin:actin molar ratio of 1:25) was included to form crosslinks between the biotinylated actin filaments. The molar ratio between myosin and actin was either 1:200 (low motor density regime) or 1:65 (high motor density regime).

Actomyosin network formation was initiated by adding monomeric G-actin and transferring the samples to glass flow cells and warming to room temperature. The flow cells were assembled with a standard microscope slide and 2 glass spacers $(150\,\mu\mathrm{m}$ height), cut from ♯1 coverslips (Menzel, Braunschweig, Germany) and brushed with a thick layer of optical adhesive Norland #81 (Edmund Optics, York, UK), and finally topped with a $24 \times 24\,\mathrm{mm}$ #1 coverslip (Menzel, Braunschweig, Germany). The optical adhesive was cured under a 8-Watt EA-180 UV lamp ($365\,\mathrm{nm}$ wavelength, Distrilab BV, Leusden, the Netherlands) for 20 minutes. The flow cell surface was passivated with $0.1\,\mathrm{mg/mL}$ κ-casein diluted in assembly buffer to avoid non-specific interactions with the networks. The chambers were sealed with silicone grease to prevent solvent evaporation.

4.2.3 Image acquisition

The particles embedded in the actin-myosin networks were imaged in brightfield on a Ti-Eclipse Nikon inverted microscope with a Nikon 40x oil immersion objective lens (numerical aperture 1.0), making sure that optimal Köhler illumination was achieved. For video tracking the following recording protocol was implemented: movies of 27000 frames were recorded at 5 frames per second starting within 2 minutes after initiation of actin polymerization, using a Photometrics Coolsnap HQ2 digital CCD camera (Photometrics, Tucson AZ, USA) controlled by NIS Elements AR 3.0 software

(Nikon Instruments Europe BV, Amsterdam, the Netherlands). The field of view was either 352x520 pixels (half of the camera chip area) or 704x1040 pixels (full size of the camera chip). The 12-bit frames were either not binned in space for smaller fields of view (pixel size $0.16\,\mu\mathrm{m}$) or 2x binned for the larger fields of view so as to reduce the recorded file size (pixel size $0.32\,\mu\mathrm{m}$). Binning did not influence the accuracy of particle tracking, which was subpixel and on the order of order $10\,\mathrm{nm}$, as checked by tracking beads immobilized on a coverslip. The exposure time was always $1\,\mathrm{ms}$. Raw data was stored as .nd2 files (NIS Elements format) and later converted to 16-bit tiff files for image processing. We imaged particles in the middle of the flow cell, to avoid any influence from the walls.

4.2.4 Particle tracking

Video particle tracking was performed using BeadTracker tracking software written in C♯ (Microsoft .Net Framework 4.0, Redmond, U.S.A.) by Marco Seynen of the Software Engineering department at AMOLF. The tracking algorithm was based on existing algorithms written originally in IDL (Interactive Data Language, ITT VIS, U.S.A.) by J. Crocker and D. Grier [36]. The software was able to swiftly analyze large data sets ($>$10000 frames or $> 15\,\mathrm{Gb}$). The new software has two principal advantages over the original IDL version. First, it can handle larger datasets, since it loads and processes 1 frame at a time instead of loading all frames at once. Second, it is faster because it calculates boxcar and Gaussian filters during image processing steps (details below) on a graphics-card using CUDA (NVIDIA Corporation, Santa Clara, USA) and using C-sharp (or C#, a third-generation language, 3GL), which is faster than IDL (a fourth generation language, 4GL).

BeadTracker offers an interactive user interface that uploads each movie frame individually and shows detection results immediately when parameters are changed. Particle tracking can be performed either on the full field of view or on a selected region of interest. Furthermore, BeadTracker has several additional post-tracking functions in addition to the original tracking algorithm. These functions include the option to connect particle coordinates with selected pixel and frame ranges and the option to correct missing particle coordinates. The latter correction can be executed either by filling missing positions with the last detected position of a segment of a trajectory, or by interpolating the position between the last frame of a segment and the first frame of the following one. Other functions are fast data navigation and inspection, including the ability to directly overlay trajectories on the corresponding raw data, and screening raw images frame by frame accompanied by a dynamic position marker along the trajectory. Also featured is zooming in and out on raw data and trajectories, as well as removal of tracks that have defects caused, for instance,

by particles moving out of focus.

The particle tracking algorithm devised by Crocker and Grier [36] comprises several steps. It is optimized for small and relatively well separated spherical particles. The first step consists of a background removal operation using a filter that is a convolution kernel of the original image $A_w(x,y)$, with a boxcar average over a region of $2w+1$ pixels:

$$A_w(x,y) = \frac{1}{(2w+1)^2}\Sigma_{ij}^w = -A_w(x+i,y+j),$$

$$A_\lambda n(x,y) = \frac{1}{B}\Sigma_{ij}^w = -A_w(x+i,y+j)e^{\frac{i^2+j^2}{4\lambda_n^2}},$$

where w is an integer larger than a single sphere's apparent radius (in pixels) and B is a normalization factor [36]. The boxcar average in Eq. (1) removes background contrast gradients, while the Gaussian surface in Eq. (2) reduces random noise due to digitization, which typically has a correlation length $\lambda_n \sim 1\,\mathrm{pixel}$ [36]. In the BeadTracker interface, LP (low pass, Gaussian filter) and HP (high pass, boxcar filter) parameters control the noise removal, and a TH (threshold) parameter controls the thresholding step (Fig. 4.2A red box).

$$\begin{pmatrix} \epsilon_x \\ \epsilon_y \end{pmatrix} = \frac{1}{m_0}\Sigma_{i^2+j^2\leq w^2}\begin{pmatrix} i \\ j \end{pmatrix} A(x+i,y+j)$$

where m_0 is the integrated brightness of the sphere's image, and the refined location is $(x,y) = (x+\epsilon_{x,y}+\epsilon_{xy})$ [36]. The particle detection step (Fig. 4.2A blue box) in BeadTracker uses as parameters Min (minimum particle size, which is 2-5 pixels depending on the binning of the image and resulting apparent particle size) and Max (maximum particle size, which is 5-11 pixels, also depending on the binning), Ratio (representing the percentage of roundness of a particle, where a perfect sphere has a Ratio of 100%, while elongated elliptical particles have a Ratio up to 150%) and COM (center of mass, particles which have a center of mass that is off by more than 30-50% from the real center of mass after position refinement will also not be detected).

The final step in the tracking procedure consists of connecting coordinates into linked trajectories by evaluating criteria of proximity in space and time for each position detected [36]. The BeadTracker parameters to connect particle positions (Fig. 4.2B green box) include Len, which determines the number of frames a particle is allowed to be absent, and Space which is the maximum distance allowed between consecutive particle coordinates. Here, Min (not to be confused with the parameter Min for minimum particle size) is the minimal length of consecutive frames for a trajectory to be accepted for the output file. The final particle trajectories were dedrifted by subtracting the average displacement of all beads between two frames. We retrieved a total of 965 trajectories for movie 1, 273 for movie 2, 593 for movie 3, and 246 for movie 4.

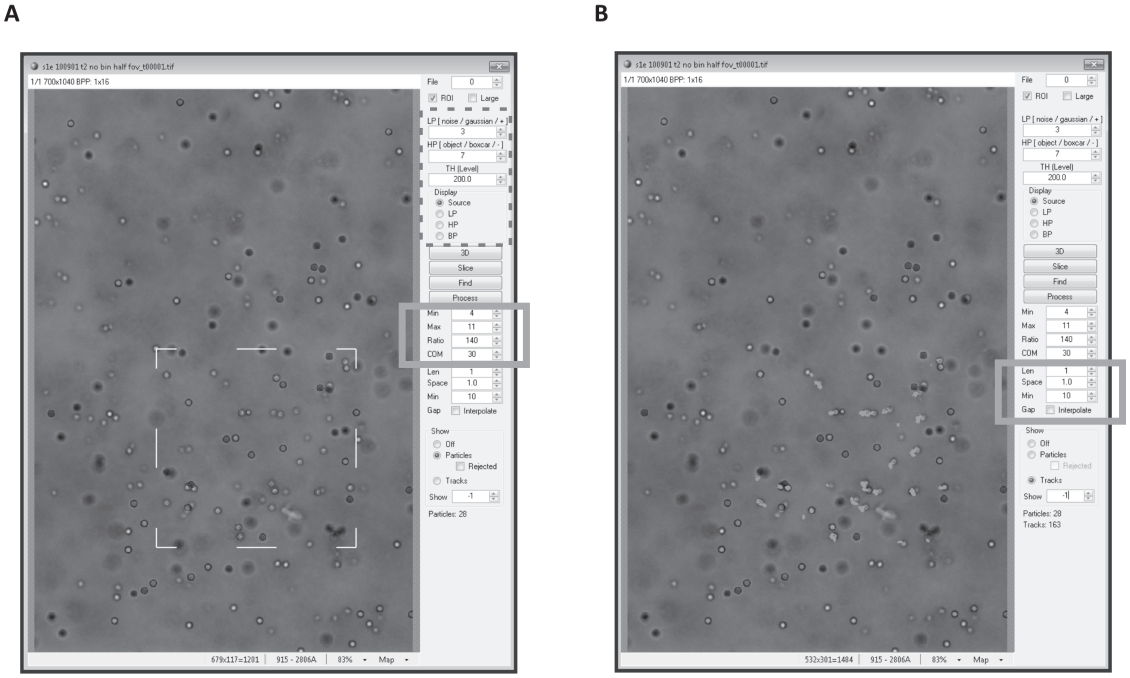

Figure 4.2: Main tracking-related functions of the user interface of C-Sharp based particle tracking software BeadTracker. **A.** Print screen of the BeadTracker interface during the detection (Find) step. White dashed square is the selected region of interest (ROI) for detection. Red circles are superposed on detected particles. *Dashed dark grey box* Noise reduction parameters LP and HP define convolution kernel parameters for noise removal. TH defines threshold of brightness. *Solid grey box* Detection parameters for particle size Max and Min, correction for the center of mass refinement COM and Ratio for the aspect ratio of detected particles. **B.** Print screen of the BeadTracker interface after the tracking step (Process). Green trajectories represent the tracks obtained for the selected ROI. *Solid grey box* Trajectory connection parameters define the maximum length and time scales allowed in order to connect nearest neighbor coordinates.

4.2.5 Automated microrheological analysis of active networks

To identify periods of directed active motion in single particle trajectories (Fig. 4.3A), we computed instantaneous particle velocity components $v_(x,n)$ and $v_(y,n)$ from particle tracking data as a function of time

Velocity components were smoothed with a moving average filter with a window size of $3\,\mathrm{s}$, which spaces data equally on either side of a time point of interest. Smoothed velocity components, $\langle v_{x,n}\rangle_t$ and $\langle v_{y,n}\rangle_t$, were transformed into particle translocation direction changes, $\Delta\theta_n$ (Fig. 4.3B), using the relation

$$\cos\triangle\theta_n = \frac{\langle\overrightarrow{v_n}\rangle_t\,\langle\overrightarrow{v_{n+1}}\rangle_t}{|\langle\overrightarrow{v_n}\rangle_t|\,|\langle\overrightarrow{v_{n+1}}\rangle_t|} \tag{4.1}$$

where $\langle\overrightarrow{v_n}\rangle_t = \begin{pmatrix}\langle v_{x,n}\rangle_t \\ \langle v_{y,n}\rangle_t\end{pmatrix}$ is the direction of the window-averaged velocity vector at frame number *n*. The differential angle, $\Delta\theta_n$, measures the straightness (or directional persistence) of particle motion. It is large if a particle exhibits random fluctuations and it is small if a particle moves in a directed fashion. Time spans with $\Delta\theta_n$ smaller than a threshold angle $\Delta\theta_{thr}$ thus represent events of directed particle translocation, which we term *segments* (Fig. 4.3C). We only considered segments with a duration exceeding $8\,\mathrm{s}$ and which involved particle displacements larger than $0.5\,\mu\mathrm{m}$. These criteria were selected to prevent overly sensitive and hence erroneous detection. We confirmed that zero segments were detected for particles embedded in a passive control network devoid of myosin motors.

4.2.6 Statistics

Averages and standard deviations (error bars) reported in the bottom panels of Fig. 4.7 and 4.10-4.13 were calculated using the raw data shown in the corresponding top panels. Statistical tests were performed in Origin 8 using students T-tests or ANOVA tests.

4.3 Results

In this chapter we present a study of the dynamics of active actin networks with a constant actin concentration ($1\,\mathrm{mg/mL}$) and crosslink density ($0.1\,\mathrm{mole\%}$ biotinylated actin), and a constant ATP concentration of $0.1\,\mathrm{mM}$ which ensures processivity of the motors. We tested two different myosin:actin molar ratios, namely 1:200 and 1:65. Myosin was assembled into synthetic filaments with a mean length of $0.85\,\mu\mathrm{m}$, corresponding to 100 myosin molecules per filament (see *chapter 2*). We probed the

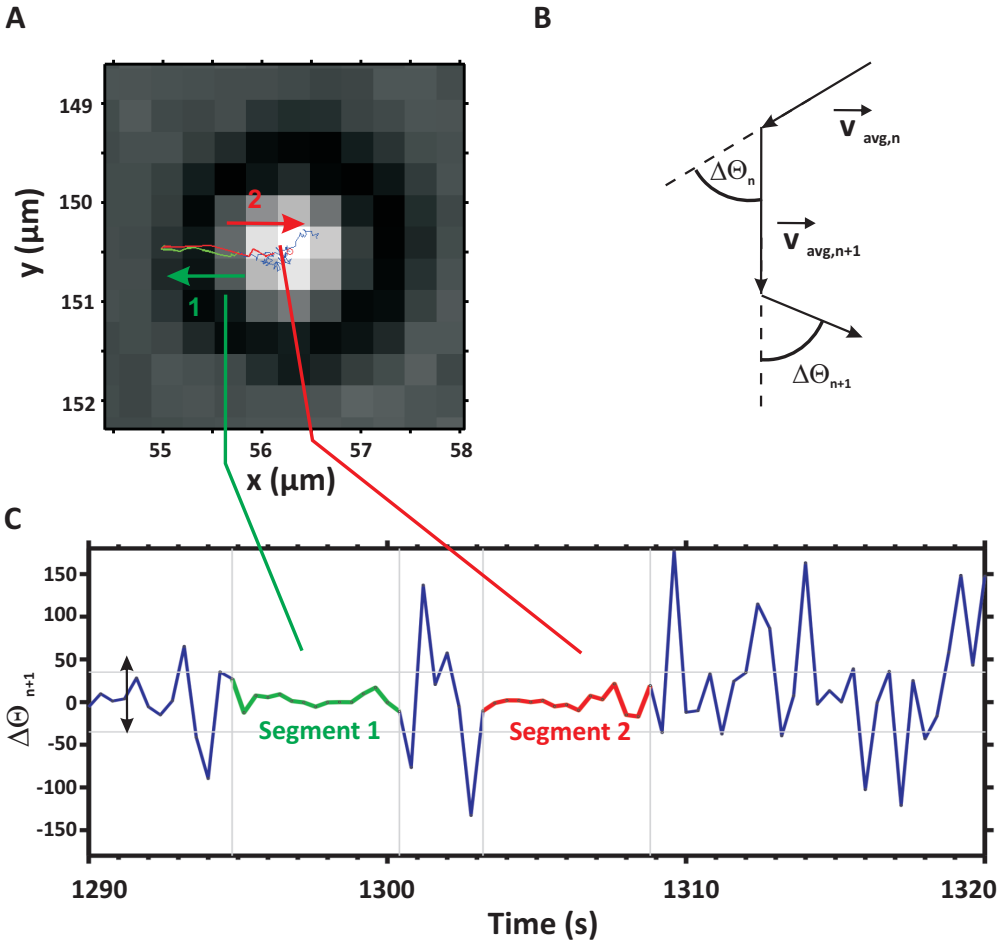

Figure 4.3: Detection of events of active directed tracer motion in single particle trajectories. **A.** Bright field micrograph of a polystyrene bead embedded in an actin-myosin gel, with particle track overlaid in blue (non-directed motion) and green/red (directed motions). **B.** Definition of the differential angle, θn, which is the change in direction of particle motion between two subsequent frames of a movie. **C.** Thresholding of the differential angle to retrieve time spans of directed motion, which are termed segments.

network dynamics by embedding spherical probe particles, whose positions can be automatically tracked with sub-pixel accuracy. The particles had a diameter of $2\,\mu\mathrm{m}$, much larger than the average network mesh size, which is $300\,\mathrm{nm}$ [37].

4.3.1 Microscopic structure of actively coarsening actin-myosin networks

To relate the origin of active fluctuations in the network to the underlying microscopic structure, we performed confocal microscopy on fluorescently labeled actin-myosin networks. We observed that different motor densities yield strikingly different structural regimes. At low motor density (1:200 myosin:actin ratio), the samples started off as homogenous networks of actin filaments (Fig. 4.1A, panel i, in red) with randomly distributed myosin filaments (in green). However, the networks coarsened within 20-60 minutes after assembly, forming dense foci of myosin surrounded by actin shells (Fig. 4.1A, panel ii, myosin in green, actin in red). Within 90 minutes, these foci were condensed into clusters with maximum sizes of 10-$20\,\mu\mathrm{m}$ (Fig. 4.1A, scheme and panel iii).

At high motor density (1:65 myosin:actin ratio), the networks coarsened much faster and on a larger scale. Within 2-5 minutes of sample preparation, there were already myosin foci surrounded by actin (Fig. 4.1B panels i-iv), and already after 15 minutes these foci were clustered together (Fig 4.1B panels v-vi). At later stages (30 minutes), the networks became highly inhomogeneous with dense regions of actomyosin that were at least $30\,\mu\mathrm{m}$ in size (Fig. 4.1B, scheme and panels vii-x). In this stage, contractility was no longer observed. In *chapter 3* we propose a physical mechanism to explain this motor-driven network coarsening, based on buckling of the actin filaments under the forces applied by the myosin foci.

4.3.2 Macroscopic mechanical properties of active actin-myosin networks

To characterize the bulk mechanical properties of the active networks, we performed macroscopic rheology using a CP20-1 cone and plate geometry (see *chapter 2*). Weakly crosslinked passive networks (no myosin, 1:1000 biotin-actin:actin) had a small elastic modulus of only $0.4\,\mathrm{Pa}$ (Fig. 4.4A, black closed stars). The elastic modulus was frequency-independent, and larger than the viscous modulus (black open stars) by about a factor of 5. This indicates that the network behaves as a weak viscoelastic solid. The elastic modulus of the crosslinked network (blue open triangle in Fig. 4.4B i labeled *No motor*) was comparable to that of the corresponding uncrosslinked networks (black open circle in Fig. 4.4B i labeled *No motors*). This indi-

cates that the actin is only weakly crosslinked by biotin-streptavidin, in accordance with the low density of biotinylated actin used.

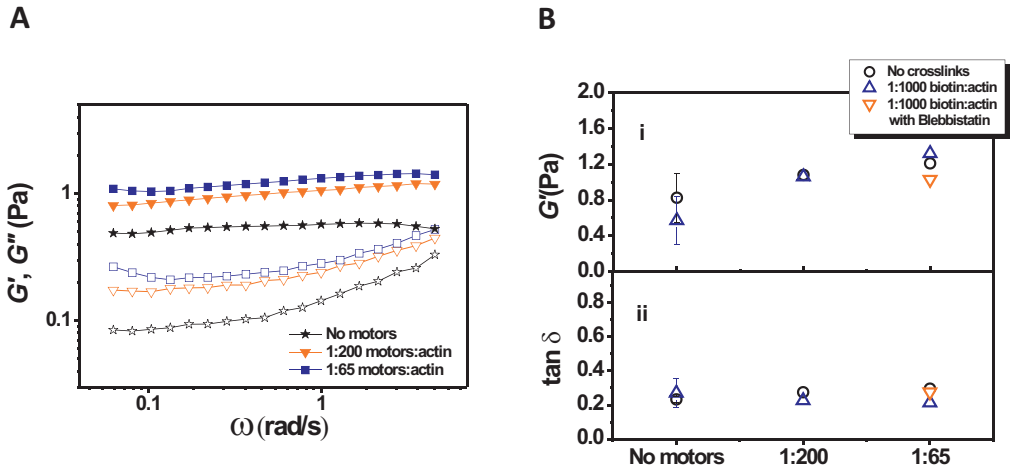

Figure 4.4: Rheology of active actin networks. **A.** Dependence of elastic modulus *G'*, and viscous modulus *G"*, on frequency, ω, at varying motor density, with 1:1000 crosslinks. **B.** ***i*** G' and ***ii*** loss tangent at ω=1 rad/s, as a function of motor density and crosslinking. Orange inverted triangle represents active sample in the presence of 1 mM ($\pm$) blebbistatin (Merck Chemicals, Nottingham, UK).

To test whether myosin itself can act as a crosslinker, we measured the influence of myosin on the stiffness of uncrosslinked actin solutions (black circles in Fig. 4.4Bi). Myosin increased the stiffness by only a factor of 1.5 at a myosin:actin ratio of 1:65. This rather small increase suggests that the motors act as weak, transient crosslinkers (as expected in the presence of $0.1\,\mathrm{mM}$ ATP, where the attachment lifetime per head is $\sim 50\,\mathrm{ms}$ (38)). Moreover, this observation suggests that there is no significant contamination with myosin dead heads. For comparison, double-headed heavy meromyosin subfragments at zero ATP, which enforces rigor conditions, caused a much larger, ten-fold increase in *G'* at a comparable myosin and actin concentration [38].

We next tested the influence of myosin on the rheology of biotin-streptavidin crosslinked actin networks. The motors increased the elastic and viscous modulus two-fold over that of the passive network, as shown in Fig. 4.4A for myosin:actin ratios of 1:65 (blue squares) and 1:200 (orange triangles). Fig. 4.4Bi summarizes the elastic moduli of samples with different motor densities (blue triangles), again showing little effect of the motors. The frequency dependence of the shear moduli was not noticeably affected by the presence of myosin (Fig. 4.4A). The networks all behaved

as weak viscoelastic solids with a loss tangent on the order of ~ 0.2, independent of crosslinking or motor density (Fig 4.4B bottom). The rather modest effect of myosin on network stiffness is somewhat surprising in light of the significant network rearrangement seen by confocal microscopy, especially at high motor density. Recent simulations of active networks suggest that motors may cause substantial stiffening of actin networks by pulling out thermal slack or bends of actin filaments [39]. However, it is conceivable that the network structure is not sufficiently connected to obtain a macroscopically measurable effect on the elasticity. Also, it is possible that depletion of actin from the network to form dense condensates counteracts an increase in the modulus of the network due to increased tension. We note that prior studies of biotin-streptavidin crosslinked actin networks also report minimal stiffening by myosin II at $> \mu$M ATP levels [25, 35].

Finally, to test whether stiffening by myosin was dependent on motor activity, we measured the shear moduli of an actin-myosin network in the presence of the myosin ATPase inhibitor, blebbistatin [40]. Blebbistatin did not significantly change the stiffness (Fig. 4.4B i, inverted orange triangle) nor the loss tangent (Fig. 4.4B ii, inverted orange triangle). This indicates that there is no appreciable stiffening connected to motor activity. We conclude that crosslinking and contractile activity of the motors only minimally affects the bulk viscoelastic properties of the networks.

4.3.3 Particle trajectories in active networks

Probe particles in active networks having a low motor density were homogeneously distributed throughout the network (Fig. 4.5A). This is consistent with the confocal microscopy observations showing that these networks coarsen only on small length scales, below $10-20\,\mu$m. This homogeneous distribution is ideal for multiple particle tracking. By contrast, probe particles in networks having a high motor density were recruited into large particle clusters (Fig. 4.5B), which likely correspond to the large actomyosin aggregates depicted in Fig. 4.1 vii-x. The particles clustered within 5 minutes, comparable to the formation time of large actin-myosin clusters observed by confocal microscopy. This clustering hampers multiple particle tracking. For this reason, we focus in the remainder of this chapter on the low motor density regime, where the probe particles can be used to spatially map dynamics in the network by multiple particle tracking.

To confirm the absence of non-specific interactions between the passivated probes and the actin and myosin filaments, we performed confocal microscopy on fluorescently labeled networks at low motor density. Actin/myosin foci formed (Fig. 4.5B, white arrows), but even at 2 hours after assembly, there was no accumulation of either myosin (green) or actin (red) on the surface of the particles (Fig. 4.5B, particles

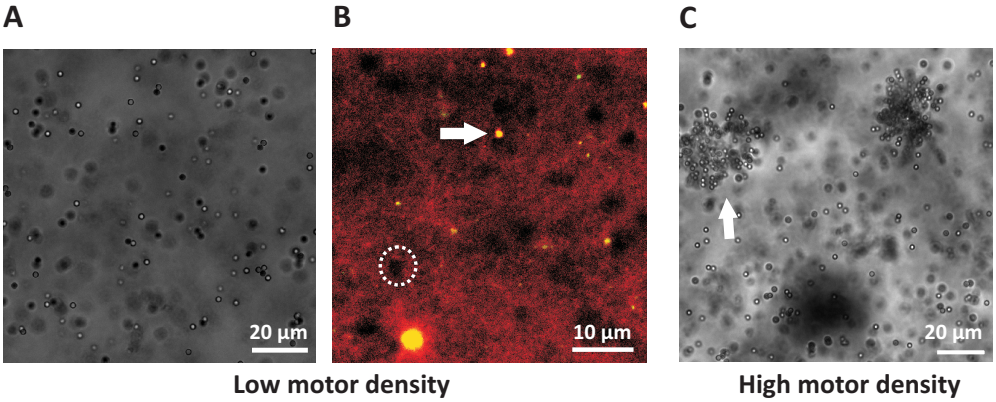

Figure 4.5: Structure of fluorescently labeled actin-myosin networks crosslinked using $0.1\,\mathrm{mole}\%$ biotinylated actin, with embedded passivated polystyrene particles. **A.** Bright field image of the network at low motor density (1:200 motors:actin). Particles are homogeneously distributed. Scale bar is $20\,\mu\mathrm{m}$. **B.** Confocal micrograph of homogenously distributed probes in networks at low motor density (1:200 motors:actin) after 2 hours of sample preparation. White dashed circle indicates the position of an unlabeled probe particle (which shows up as a dark circular hole). Scale bar is $10\,\mu\mathrm{m}$. **C.** Bright field micrograph showing clustering of probe particles in a network at high motor density (1:65 motors:actin). Scale bar is $20\,\mu\mathrm{m}$.

are visible as dark circular holes in the red actin background; example inside white dashed circle). This confirms that the surface of the particles is nonadhesive and that the particles are therefore suitable reporters of the network dynamics.

We recorded videos with a total duration of 90 minutes starting within 2 minutes after sample preparation using sampling rates of 5 frames per second. We tracked particle positions in four independently prepared samples, yielding a total of N=2077 trajectories. Any spurious trajectories, such as the example inset in figure 4.6A, were manually removed from the final set of tracks. Trajectories of probe particles in a passive control network in the absence of myosin motors looked like compact, isotropic clouds, as exemplified in Fig. 4.6A. This trajectory is typical of probe particles trapped in an elastic network which confines thermal particle excursions. In comparison, trajectories of unconfined particles suspended in the solvent were much wider (Fig. 4.6B). There was no evidence of any particle hopping between network pores, as expected given that the particle size exceeds the mesh size [18]. The trajectories of particles in active actin-myosin networks were qualitatively different from the trajectories in passive networks. We observed two classes of trajectories in active samples. The first class looked similar to trajectories in passive networks, confined and rather compact (Fig. 4.6C). However, the second class of trajectories showed small fluctuations interspersed with sudden large and clearly directed walks, departing from a given position and often returning back, sometimes repeatedly, and in different directions (Fig. 4.6D, blue arrows).

4.3.4 Automated segmentation of active particle trajectories

Since the confocal microscopy analysis showed that the actin-myosin networks actively coarsened during the first 30-60 minutes after preparation, we tested whether the dynamics of the probe particles was dependent on sample age. To this end, we performed automated segmentation of trajectories to distinguish active, directed motion from smaller amplitude, random fluctuations. Note that random fluctuations can be thermal in origin, but can also originate from motor-driven active fluctuations [25, 41]. We selected directed trajectory segments by evaluating temporal changes in the angle of the direction of particle movement between consecutive frames (*see section 4.2.5*). The maximum accepted angle change between frames was $\pm 45°$. We furthermore only accepted segments which involved displacements larger than $0.5\,\mu\mathrm{m}$ and had durations of at least $8\,\mathrm{s}$.

Based on these criteria, we used the algorithm to quantify the frequency of events of directed motion as a function of sample age. We divided the entire movie of 90 minutes into 18 bins of 5 minutes each. The number of active segments decreased significantly with sample age, from N=1489 in the first 0-5 minutes after sample

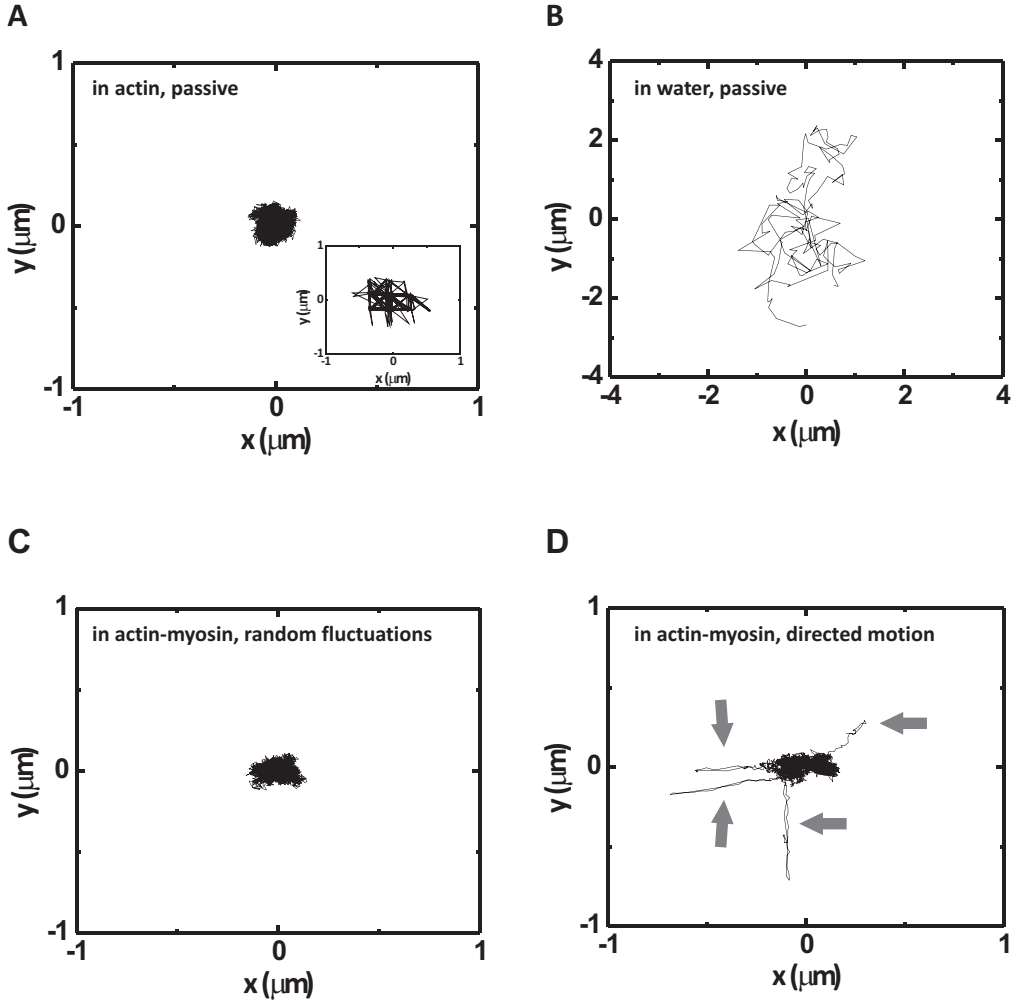

Figure 4.6: Probe particle trajectories reflect the dynamics of the embedding material. **A.** Example trajectory of a microsphere ($2\,\mu$m diameter) embedded in a passive actin network at $1\,\mathrm{mg/mL}$ crosslinked with $0.1\,\mathrm{mole\%}$ biotin-actin and a 1:25 streptavidin to actin ratio. **B.** Example trajectory of a microsphere ($2\,\mu$m diameter) in water. **C** and **D**: Two different examples of trajectories of microspheres ($2\,\mu$m diameter) embedded in a crosslinked active actin network at $1\,\mathrm{mg/mL}$ with a myosin:actin ratio of 1:200. The bead in C shows only random (though not necessarily purely thermal) fluctuations, whereas the bead in D shows 4 bouts of sudden directed motion followed by recoil, indicated by blue arrows.

preparation, to only 8 at 75-80 minutes after sample preparation. To compare different movies, the number of segments was normalized by the total tracked time (for all particle trajectories in the bin). The thus obtained frequency of segments per time and per bead showed a strong dependence on sample age for all four samples. In the first 5 minutes after sample preparation, the frequency was ~ 0.34 (Fig. 4.7, i). However, within 30 minutes, the frequency decreased to reach a constant value of $\sim$0.1. The decay with sample age was exponential (red line in Fig. 4.7i). There was some difference in *activity* between the four movies, but all samples showed the same trend with sample age. Interestingly, the time scale over which the *activity* drops to a low and constant value is consistent with the time scale of network coarsening seen with confocal microscopy. Apparently, the probe particles show the most activity while the myosin motors still organize into clusters and condense the actin, whereas the activity becomes infrequent when this coarsening process is complete.

The segmentation algorithm also returned the duration of active segments. This duration did not show a clear dependence on sample age (Fig. 4.7, ii and iii). In each bin, the duration varied between 5 and 36 s, with an average value of 6 s (Fig. 4.7, iii). This time scale is consistent with time scales on the order of seconds for contractile fluctuations observed with spherical probe particles [25] or microtubules [41] in other studies. This time scale indicates a rather large processivity time, much larger than the attachment time of a single myosin motor, which is around 50 ms [42].

4.3.5 Ensemble microrheological analysis of active gels

We next tested whether the ensemble averaged dynamics of the probe particles displayed any signatures of non-equilibrium activity. For a randomly diffusing particle in a viscous liquid, the average displacement in a time t is zero, while the mean squared displacement (MSD) increases linearly with time [21] as

$$\langle MSD^2 \rangle \sim Dt \tag{4.2}$$

where the brackets denote an ensemble average over all particles and D is the diffusion coefficient. In contrast, a particle in a viscoelastic polymer network with a pore size smaller than the particle diameter will exhibit subdiffusive motion [43]:

$$\langle MSD^2 \rangle \sim Dt^{\alpha}, \tag{4.3}$$

with a diffusive exponent $\alpha < 1$. In active (non-equilibrium) systems, particles can exhibit superdiffusive motion, characterized by an exponent $\alpha > 1$. This type of motion has been reported for cargo particles in cells transported by motors along cytoskeletal filaments [6].

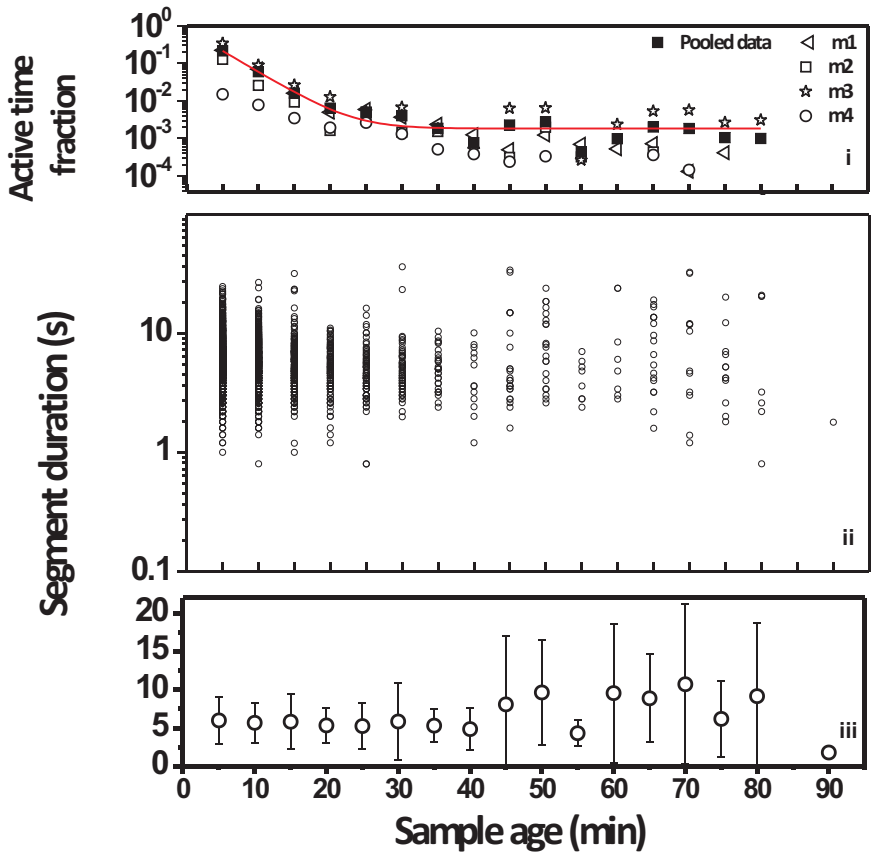

Figure 4.7: Automated analysis of active trajectory segments. ***i*** Fraction of active segments (number of segments normalized per bead and per unit of time) as a function of sample age. Solid line is to guide the eye. ***ii*** Duration of active segments as a function of sample age. ***iii*** Average duration of active segments as a function of sample age.

In passive control networks, the MSD showed subdiffusive behavior, with exponents $\alpha < 1$ (Fig. 4.8A bottom). This scaling is characteristic of particles trapped in a viscoelastic network, and is consistent with prior measurements on passive F-actin [17, 18, 19, 44]. The exponent alpha was 0.3 in the first 10 minutes, and decreased to 0.2 for the remainder of the experiment.

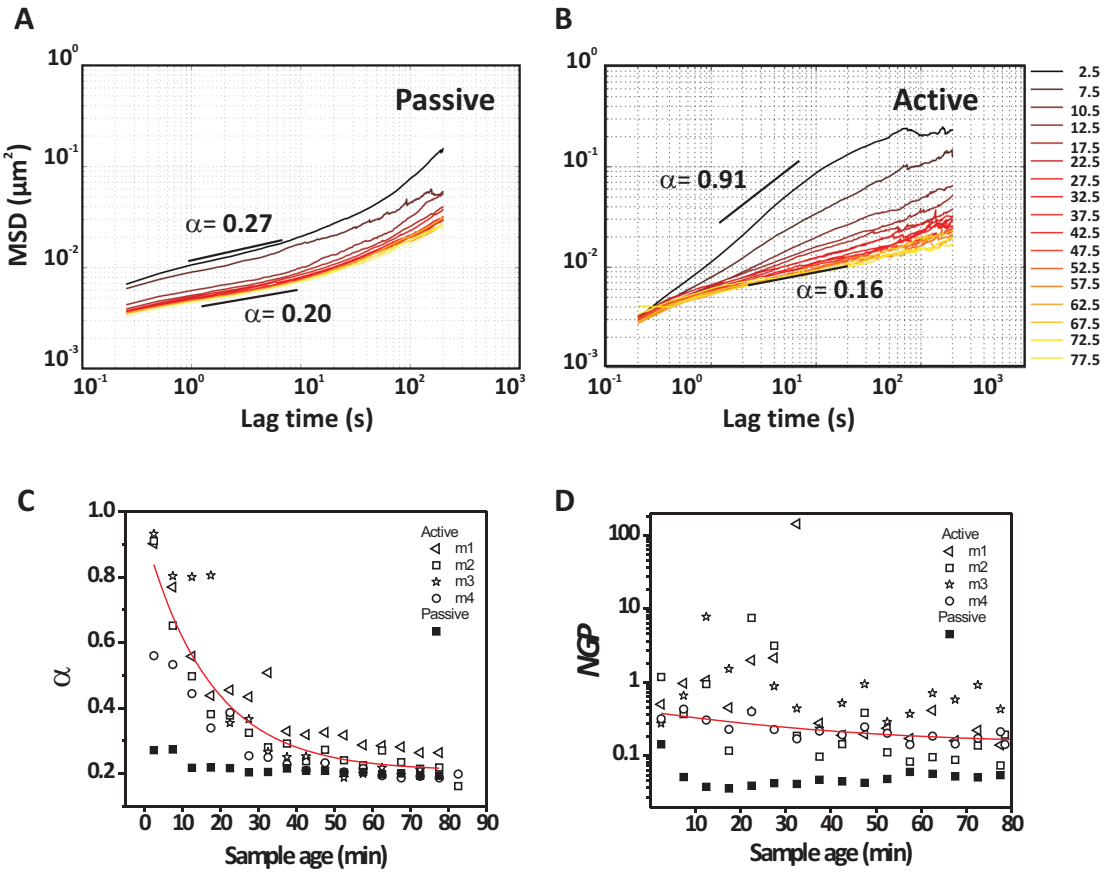

Figure 4.8: Ensemble microrheological analysis of active and passive gels. **A.** Ensemble-averaged mean squared displacement (MSD) of tracer particles in an active sample and **B.** in a passive sample for different sample ages, as indicated in the legend on the right (time in minutes). Dashed lines are power-law fits to the MSD to extract the diffusive exponent, α (values of α at the beginning and end (90 min) of the experiment are shown in the graph.) **C.** Exponent α as a function of sample age for all four samples examined in this study. **D.** Non-Gaussian parameters (NGP) at a lag time of $10\,\mathrm{s}$ as a function of sample age. Solid lines in panels C and D are to guide the eye.

The MSD of particles in active networks was strikingly different compared to passive networks, in particular during the first 25 minutes after sample preparation (Fig.

4.8A top). In the first 10 minutes, the MSD was much larger than in the passive network and it showed a diffusive exponent of 0.9. With increasing sample age, the MSD became smaller and the exponent gradually decreased to reach a constant value of $\sim$ 0.2 at 25 minutes. After 25 minutes the MSD resembled the MSD in passive networks (Fig. 4.8B). For the passive sample, α was slightly larger during the first 10 minutes than in the rest of the movie, perhaps due to small initial sample rearrangements related to actin polymerization. In contrast, active samples started with an exponent α between 0.8 and 0.95 during the first 10 minutes, and α subsequently decreased to 0.2. Similar to the frequency of active motions counted by the segmentation algorithm, the exponent α varies between the four different samples, but the dependence on sample age is invariant. Interestingly, the time scale over which α decreases to reach a value similar to that of the passive network again mirrors the time scale of active network remodeling observed by confocal microscopy (Fig 4.1 i and ii).

The MSD only represents the second moment of the probability distribution of particle displacements. It has been experimentally reported [25, 41] and proposed on the basis of theoretical models [26] that non-equilibrium activity may also appear in higher-order moments of the distribution. To test for this in our data, we considered the Van Hove distribution functions and calculated the fourth moment, or kurtosis. The Van Hove function should be Gaussian for homogeneous samples in thermal equilibrium. Non-Gaussianity can point to spatial or temporal heterogeneities [19], and to non-equilibrium activity [45]. In line with another recent study on actin-myosin networks [45], we define a non-Gaussianity parameter, abbreviated as *NGP*,

$$NGP = \frac{k}{3} - 1 \tag{4.4}$$

where k is the kurtosis, or fourth moment of the distribution of particle displacements, Δx, in a lag time τ :

$$k = \frac{\langle \delta x(\tau)^4 \rangle}{\langle (\tau)^2 \rangle^2}. \tag{4.5}$$

For a Gaussian distribution, $k = 3$ so NGP should be zero [46]. Passive samples were nearly Gaussian, with NGP close to zero (Fig. 4.9). In the first 10 minutes, the NGP was slightly larger than zero, consistent with the observation that the diffusive exponent was slightly different from the exponent in later stages. This slight deviation likely reflects inhomogeneities of the network related to network formation. In strong contrast, active networks showed marked non-Gaussianity: the Van Hove distributions had large tails and the NGP were invariably larger than zero. The Van Hove functions were unfortunately noisy, with tails that were not smooth. We speculate that the large displacements observed in the tails may originate from displacements of large areas of the sample, which we could observe by visual inspection of movies. During periods of seconds to minutes, particles in the field of view were seen to col-

lectively move in the same direction, often out-of-of focus. These large scale, collective motions occurred sporadically and subsequent events occurred in different directions indicating that they were not caused by sample drift. Such collective motion may increase the NGP. Note that the particle trajectories were dedrifted, so the collective motion was probably to some extent smoothed out. We also observed that the NGP sometimes showed an anisotropy between the x and y directions, which may be a consequence of local heterogeneities (data not shown).

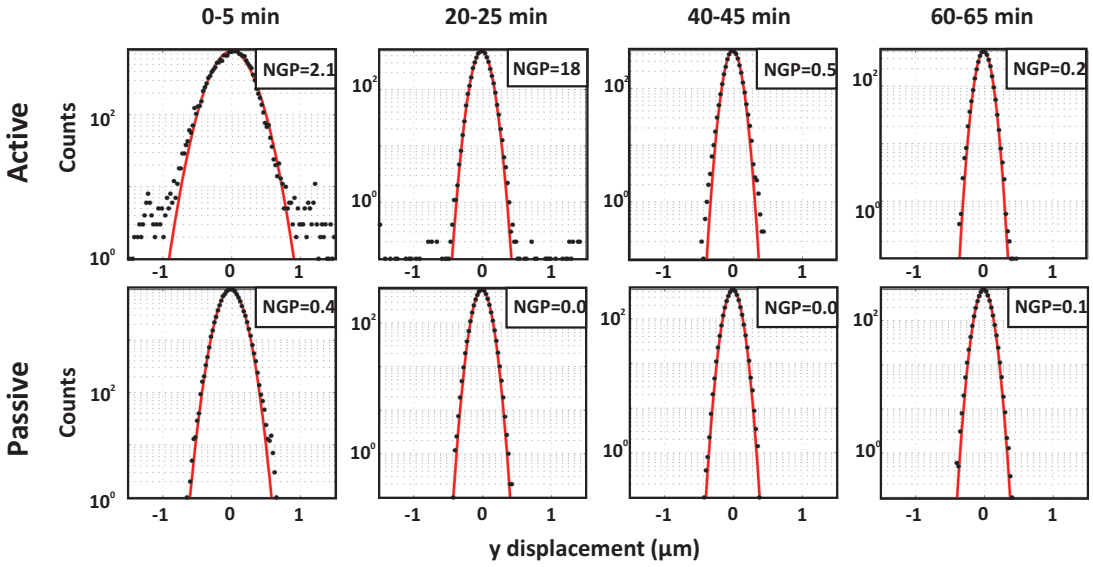

Figure 4.9: Van Hove distribution of particle displacements for an active (top) and a passive (bottom) sample at different sample ages, for a fixed lag time of $10\,\mathrm{s}$. Lines are Gaussian fits. Corresponding non-Gaussian parameters (NGP) are indicated in the upper right of each graph.

Fig. 4.8D summarizes the NGP as a function of sample age for four different samples. The NGP values varied widely, between 0.1 and 35. There was a weak trend of decreasing NGP with increasing sample age. For comparison, prior microrheology studies of actin-myosin networks showed NGP values of up to 15 (lag time of $0.4\,\mathrm{s}$) with microtubule probes [41], and NGP values up to 2.5 (lag time of $10\,\mathrm{s}$) with spherical probe particles [45].

4.3.6 Single particle kymograph analysis

With the help of the automated segmentation procedure, we were able to quantify the frequency of active, directed segments of particle motion in single particle tra-

jectories. However, we did not yet automate the detailed analysis of particle motion within active segments. In particular, we did not yet automate detection of particle pauses or discrimination between translocation and relaxation events.

Instead, we resorted to kymograph analysis for a detailed analysis of the salient features of active trajectories exhibiting long-distance directed motion. From videos of actively moving probes such as shown in Fig. 4.10A, we constructed kymographs along the approximate overall direction of particle motion using ImageJ. The result is a projection of the change in position r over time t (Fig. 4.10B). For reference, Fig. 4.10C shows the trajectory of the same particle in the xy-plane. The kymographs revealed several interesting features of active particle motion. Typically, we observed that particles first moved in a directed manner into a particular direction (which we denote as a translocation, T), occasionally experiencing stationary periods (S) of variable duration, and then abruptly moved back to their original position (Fig. 4.10B). We denote this reversal feature as a relaxation (R). Some probe particles simply halted and did not return back to their original position (Fig. 4.10D and E). Interestingly, a number of particles displayed simultaneous active directed motions that were either positively (Fig. 4.10F) or negatively (Fig. 4.10G) correlated in their direction of translocation. From the kymographs, we manually extracted the durations of directed particle motion events, the distance D covered in these events, and the velocity of directed motion v (see annotations for T, R, and S events in Fig. 4.10B, *zoom in/scheme*).

The duration of translocations (T) varied between 0.5 and 20 seconds (Fig. 4.11A top), with an average value of $3.9 \pm 3.2\,\mathrm{s}$. The duration of relaxation events (R) also varied over a broad range, of 0.4 and $20\,\mathrm{s}$. The average relaxation time of $2.3 \pm 2.5\,\mathrm{s}$ was slightly (but significantly) smaller than the translocation time (Fig. 4.11A bottom). The duration of stationary periods (S) varied from 1 to $15\,\mathrm{s}$, with an average of $3.3 \pm 2.6\,\mathrm{s}$. The total duration of active segments (sum of T, R and S) varied between 2 and 40 seconds (Fig. 4.11A, Total E) with an average of $11.1 \pm 8.0\,\mathrm{s}$. Some particles exhibited repeated contractile fluctuations with pause times (P) between fluctuations of $\sim 20\,\mathrm{s}$ (Fig. 4.11A, P).

Since the ensemble averaged dynamics showed an evolution with sample age, we tested whether the durations of active events were age-dependent. The average translocation time (T) slightly increased with increasing sample age during the first 20 minutes, corresponding to the time period in which the network structure actively coarsened (Fig. 4.11B). This increase was statistically significant ($p = 0.027$, ANOVA test). However, the overall trend with increasing sample age was not clear. The variability in translocation time may reflect active evolution of the sample. The average relaxation time (R) was independent of sample age (Fig. 4.11C). There was no obvious correlation between translation and relaxation times (Fig. 4.11D).

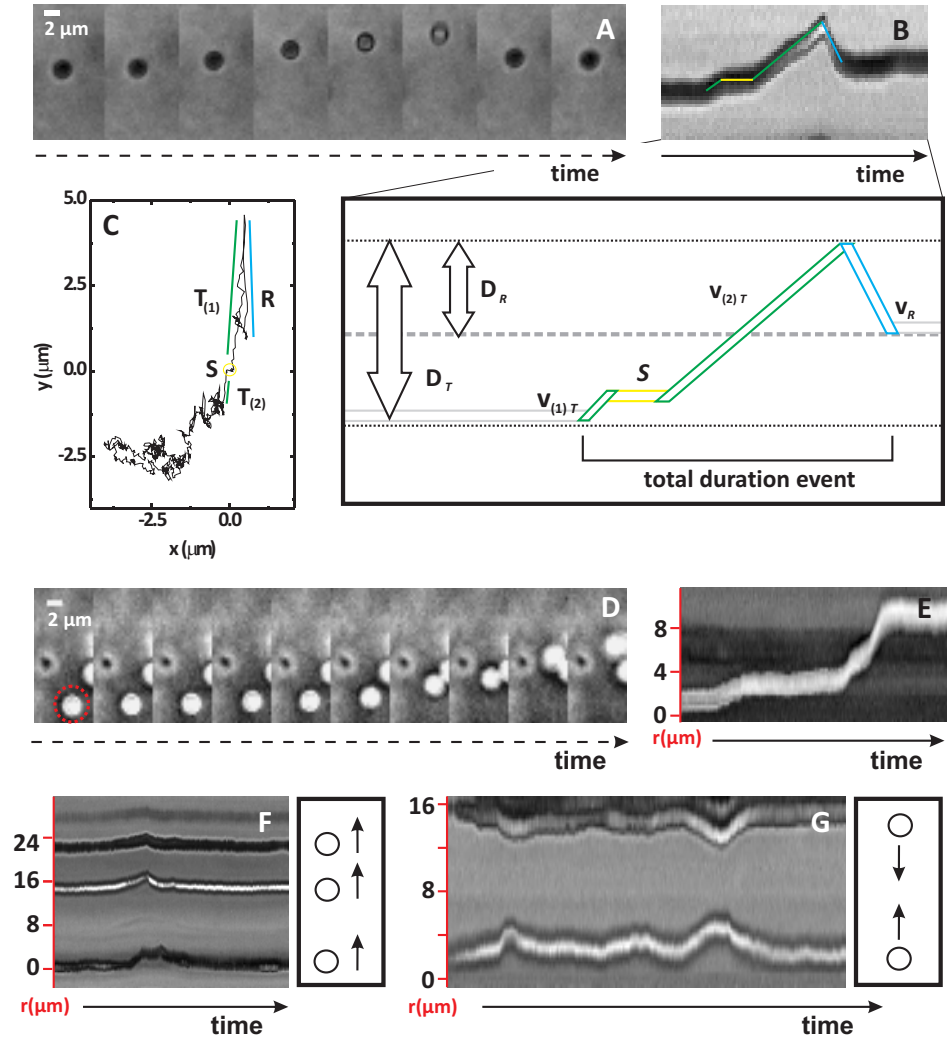

Figure 4.10: Bright field images and kymographs of directed motion of inert polystyrene probes in active actin-myosin networks (1:200 myosin:actin). **A.** Sequence of micrographs of particle probe undergoing a translocation and subsequent relaxation. Scale bar is $2\,\mu\mathrm{m}$. **B.** Kymograph along the overall direction of particle motion corresponding to sequence A. Green lines highlight translocations T, yellow line a stationary moments S, and relaxations R are marked in blue. *Zoom in* Schematic drawing of different features in a kymograph. In green, translocation periods T with a slope v_T; in blue, relaxation periods R with a slope v_R; in yellow, stationary periods S. Large white arrow represents maximum T displacement and small white arrow represents maximum R displacement. **C.** Trajectory in the x,y plane corresponding to panel B. **D.** Sequence of micrographs of particle probe undergoing a translocation without subsequent relaxation. Scale bar is $2\,\mu\mathrm{m}$. **E.** Kymograph corresponding to sequence C. **F.** Kymograph of three probes that move simultaneously in a positively correlated fashion, though with different displacement amplitudes (red arrows). *Inset* Scheme of the direction of motion of the probes in the xy-plane. **G.** Kymograph of two probe particles that show several consecutive contractile fluctuations (red arrows). *Inset* Scheme of the direction of motion of the probes in the xy-plane.

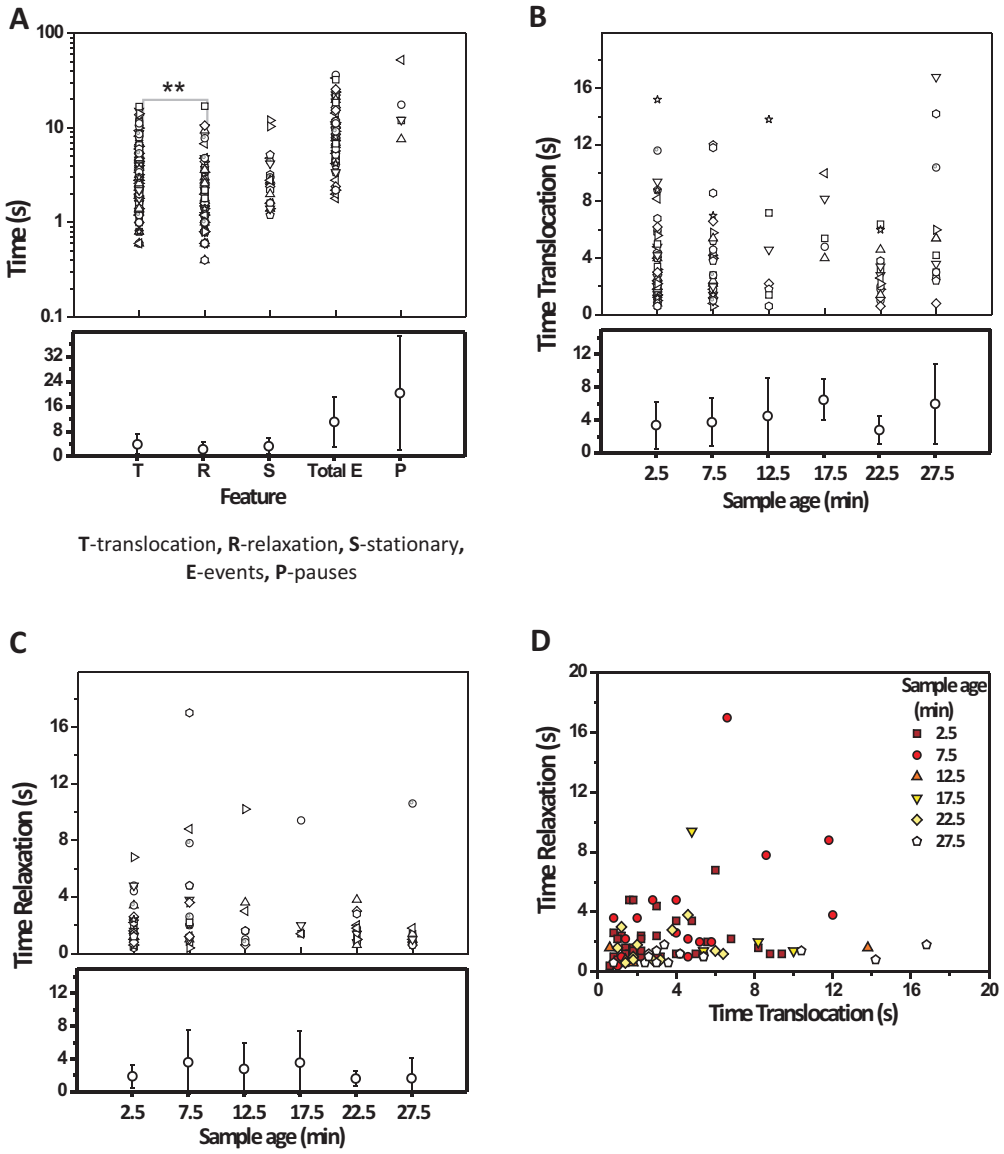

Figure 4.11: Durations of active events detected in particle trajectories in active networks by kymograph analysis. **A.** *Top* Distributions of durations for different kymograph features: translocation (T), relaxation (R), stationary moments within an event (S), total event duration (Total E) and pauses (P). Asterisks denote statistically significant differences ($\star\star = p < 0.001$, student-T test). Durations of T and R are statistically different ($p = 3 \times 10^{-18}$). *Bottom* Average duration per analyzed feature. **B.** *Top* Distributions of translocation times as a function of sample age. *Bottom* Average translocation time as a function of sample age, determined in bins of 5 min. **C.** *Top* Distributions of relaxation times as a function of sample age. *Bottom* Average relaxation time as a function of sample age. **D.** The translocation time is weakly correlated with relaxation time (data of the first 30 minutes pooled) with a correlation coefficient $R = 0.223$ ($p = 0.025$).

The displacements of particles during translocation (T) events ranged from 0.8 to $25\,\mu$m with an average of $4\pm\,4\,\mu$m (N=74) (black bars in Fig. 4.12A). Interestingly, the distribution of translocation distances depended on sample age. There were multiple examples of large (5-$25\,\mu$m) excursions of probes during the first 10 minutes of sample aging, whereas afterwards the displacements were limited to a maximum of $5\,\mu$m (Fig. 4.12B top). The average displacement of particles after 15 minutes was around $2\,\mu$m, independent of sample age (Fig. 4.12 bottom). This age dependence is consistent with the confocal microscopy analysis of the network structure (Figure 4.3A), which showed that large-scale coarsening occurred only in the first 30 minutes.

The displacements of particles during relaxations (R) showed a narrower distribution than the distribution of translocation distances, ranging from 0.6 to $9\,\mu$m (N=61) (red bars in Fig. 4.12A). The average displacement during relaxation was $2.2\pm\,1.4\,\mu$m, which is significantly less than the average translocation displacement ($p = 4\times10^{-9}$, student T-test) (Fig. 4.12A). These data suggest that probe relaxation occurs to varying degrees. To quantify this statement, we calculated the percentage of return of a probe to its initial position after a translocation. As illustrated in Fig. 4.12B, the percentage of return is defined as the ratio between the displacement during relaxation, D_R, and during translocation, D_T:

$$\textit{Return} = 100\frac{D_T - D_R}{D_T}. \tag{4.6}$$

A small percentage (14%) of particles returned to their original position, while about half of the beads made an incomplete recovery and a small percentage (14%) did not recover at all (Fig. 4.12C). On average, particles returned back by 70% of the translocated distance. Note that some microsphere trajectories showed a circular-like motion on returning to the initial position instead of a straight walk back to the original position. Probe relaxation may have two possible origins. On the one hand, it may be a passive relaxation of the network, following detachment of the motors that drive the initial translocation [27]. In this case, incomplete recovery points to some irreversible, plastic deformation of the network [41]. On the other hand, relaxation could also result from other motors pulling the network that the bead is confined in into a different direction. There is some evidence that this occurs. While the majority ($\sim$ 85%, total N=72) of the probes moved back less than the original translocated distance, a significant fraction of 14% of the particles moved back further than their original distance (Fig. 4.12C). These *overshoots* may be caused by *relaxation* by an active, motor-dependent mechanism.

Since we observed evidence of some plasticity, we investigated whether the percent recovery in relaxation (R) was correlated with the distance over which probes moved during the preceding translocation (T). As shown in Fig. 4.12D, the percentage of return of the probes to their initial position showed a significant trend to decrease

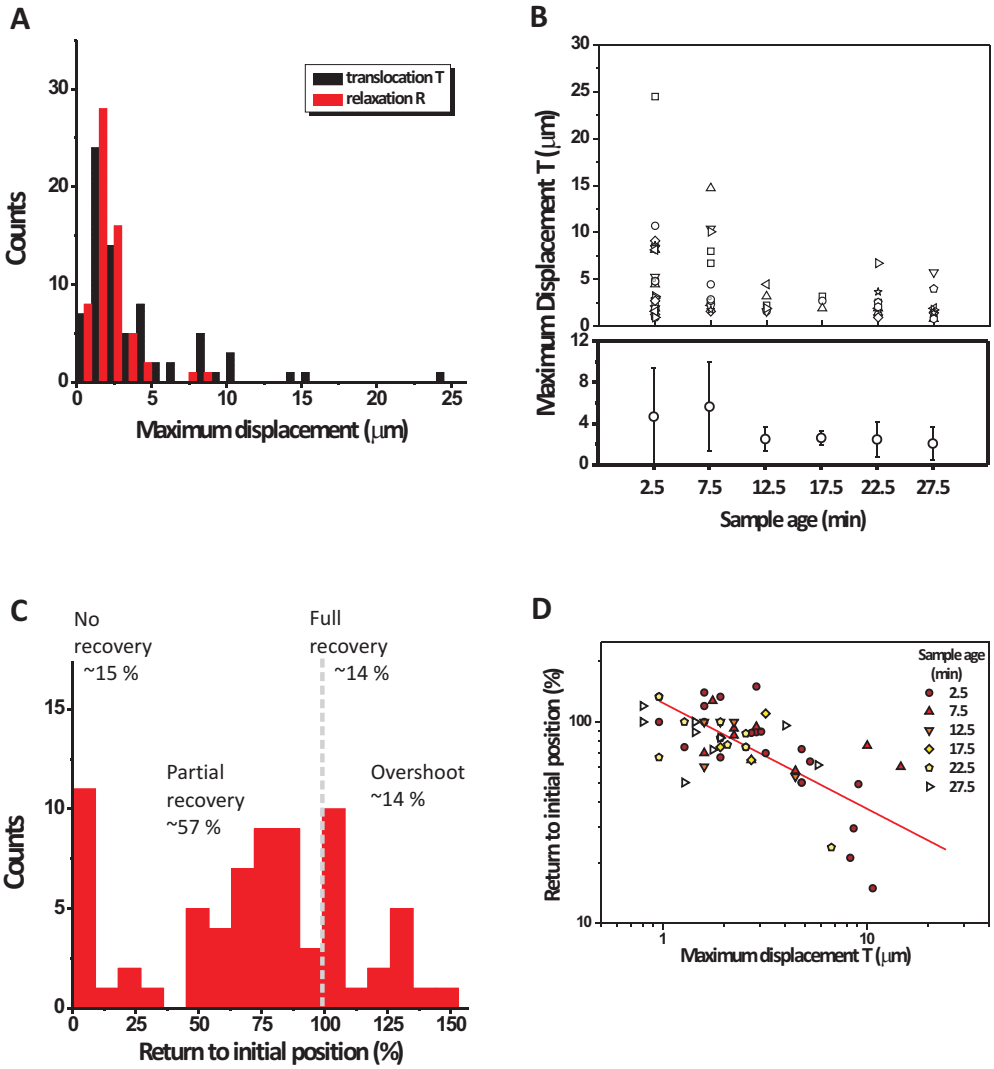

Figure 4.12: Maximum displacements in directed motion events and percentage of return to initial position, obtained by kymograph analysis. **A.** Histogram of maximum displacements during translocation (black) and relaxation (red). **B.** *Top* Distributions of maximum displacement during translocations as a function of sample age. *Bottom* Average maximum displacement during translocation as a function of sample age. **C.** Histogram of the percentage of return to initial position, where 100% (dashed grey line) represents full recovery. **D.** Maximum displacement T is significantly anticorrelated with the percentage of return to initial position during the first 30 minutes after sample preparation, with a correlation coefficient $R = -0.57$ ($p = 4 \times 10^{-7}$).

with increasing translocation distance. The decrease may be fitted by a power law with exponent of -0.5 (indicated by the line). Thus, large displacements of the probes, which occurred during the first 10 minutes after sample preparation, tended to show a certain degree of irreversibility, whereas beads displaced over smaller distances tended to recover their initial position or even move back beyond their original position. These data suggest that during the first 10 minutes after sample preparation, network coarsening is accompanied by large, irreversible rearrangements, whereas afterwards only smaller, reversible bead displacements occur.

Finally, we computed the velocities at which the particles moved during translocation and relaxation. Velocities during translocation and relaxation were comparable. The average velocity during translocation was 0.8$\pm$ 0.6 μm/s (N=78), slightly but significantly ($p = 4 \times 10^{-19}$, student-T test) slower than the velocity during relaxation, which was 1.0$\pm$ 0.6 μm/s (N=65) (Fig. 4.13A). These values are comparable to velocities of actively contracting myosin foci in reconstituted actin-myosin networks, and also in vivo (see Table A.3 in *appendix A*). These velocities are slightly smaller than the unloaded translocation speed of actin filaments on myosin-coated substrates in motility assays [47]. The velocities of translocation (Fig. 4.13B) and of relaxation (Fig. 4.13C) were independent of sample age. This is reasonable in view of the macroscopic viscoelastic properties of the networks, which appeared to be rather insensitive to the presence of myosin (Fig. 4.4). There appears to be a small positive correlation of relaxation velocity with translocation velocity (Fig. 4.13D).

4.3.7 Automated analysis of active collective particle behavior

We occasionally observed correlated motions of multiple beads, as exemplified by the kymographs in Fig. 4.10. Sometimes, multiple beads were synchronously translocated in the same direction and synchronously recoiled (Fig. 4.10F). Also, sometimes two beads moved towards one another and then relaxed back; sometimes a bead pair experienced multiple contractile fluctuations (Fig. 4.10G). The contractile fluctuations are reminiscent of contractile fluctuations seen in actin-myosin networks crosslinked by biotin-streptavidin at low (μM) ATP [25].

To quantify the frequency of these correlated directed motions, we implemented an automated recognition algorithm by looking for temporal overlaps of active segments in the trajectories of probe beads (Fig. 4.14A). We define an overlap as two pieces of segments which occur simultaneously, with the criterion that the time shared by the two segments is at least 0.8 s. Furthermore, we require that the overall direction in which either particle moves during the overlap must not deviate by more than $\pm 20^\circ$ from the line connecting their positions at the beginning of the overlap

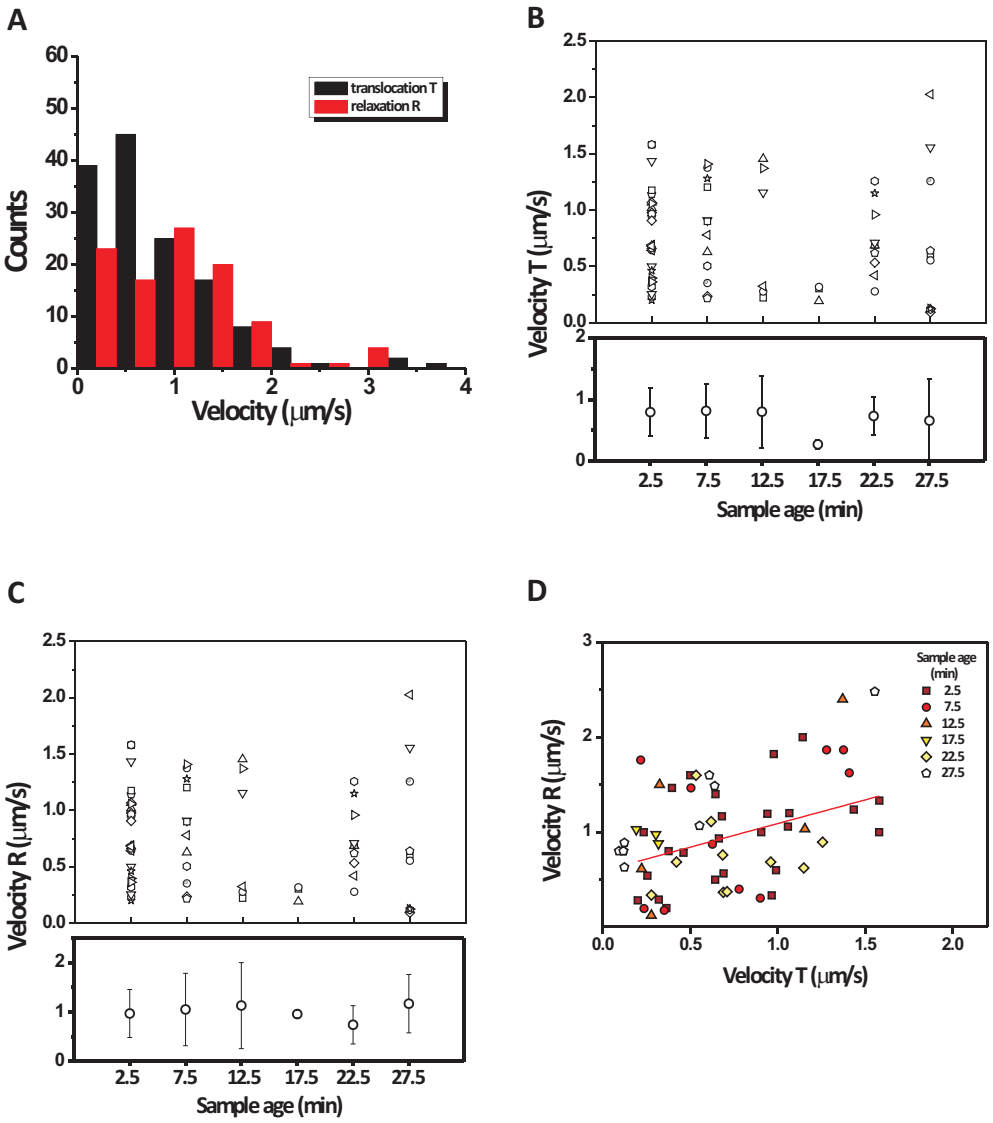

Figure 4.13: Velocity of directed particle motion from kymograph analysis. **A.** Histogram of velocities of translocation (black) and relaxation (red). **B.** *Top* Distribution of velocities of translocation as a function of sample age. *Bottom* Average velocities of translocation during the first 30 minutes after sample preparation. **C.** *Top* Distribution of velocities of relaxation as a function of sample age. *Bottom* Average velocities of relaxation during the first 30 minutes after sample preparation. **D.** The velocity of relaxation is significantly correlated with the velocity of translocation (data shown for first 30 minutes), with a correlation coefficient $R = 0.46$ ($p = 2 \times 10^{-4}$).

(Fig. 4.14A). In analogy to the normalized fraction of segments per time and per bead (*see section 4.3.4*), we defined a normalized fraction of overlaps in a given time span as the summed durations of detected overlaps normalized by the total tracked time of all particles in this time span.

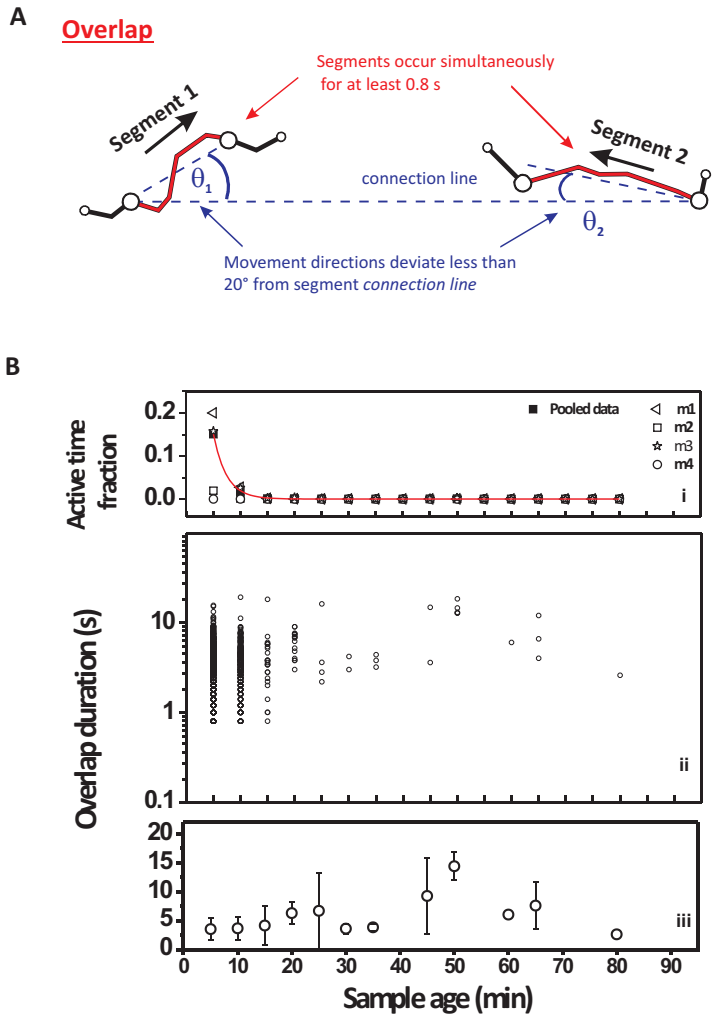

Figure 4.14: Automated analysis of collective directed motion of particles in actin-myosin networks. **A.** An overlap is defined as a pair of segment fragments (red lines) occurring simultaneously for a minimum time of $0.8\,\mathrm{s}$, with the overall directions of movement relative to the connection line, θ_1 and θ_2, both falling below $\pm 20°$. **B.** ***i*** Fraction of overlaps, normalized by time and per bead, as a function of sample age. ***ii*** Distribution of duration of overlaps as a function of sample age (N=4 samples). ***iii*** Average duration of overlaps.

During the first 5 minutes after sample preparation, the fraction of overlaps (normalized per time and per bead) was around 10 overlaps per second per bead (Fig.

4.14B i). With increasing sample age, the fraction of overlaps decreased, reaching a constant, low value of ∼0.1% after 20 minutes. The absolute number of detected overlaps decreased from N=1765 at 0-5 minutes to zero at 35-40 minutes after sample preparation. Thereafter, overlaps were detected only occasionally. There was variation in the frequency of overlaps in the four different samples, but the dependence on sample age was similar for all samples. Interestingly, this decrease of the frequency of overlaps within 20 minutes mirrors exactly the decrease in the frequency of active segments (Fig. 4.7 i), and the decrease in MSD, diffusive exponent and NGP in the ensemble averaged dynamics (Fig. 4.8). Moreover, the decreased frequency is correlated with the confocal observations of the network structure, showing that active coarsening occurred only during the first 30 minutes and then reached steady state (Fig. 4.1, top). This correlation suggests that collective directed motion of particles occurs mainly when the sample is still actively coarsening. The duration of overlaps ranged between about 1 and 10 seconds, as shown in figure 4.14B ii. The average duration was 6 seconds, and did not appear to depend on sample age (Fig. 4.14B iii).

To distinguish positively correlated motion from negatively correlated motion, we projected the velocities of two particles which had an overlap onto the line connecting the starting positions of the particles at the beginning of the overlap (Fig. 4.14A). If the time-averaged product of the projected velocities was positive (negative), the particle motion was considered positively (negatively) correlated. To test whether the negatively correlated motions were associated with a contractile event, we additionally measured whether the separation distance between the particles decreased during the overlap, by calculating the difference between the separation at the start and the end of the overlap. We visualized the spatial distribution of correlated activity by overlaying detected overlaps as lines connecting the particles onto bright field images of the entire field of view.

Figure 4.15 shows the outcome of this analysis for two movies, each having a duration of 90 minutes, of samples that differed greatly in the number of detected overlaps. Red lines represent particle pairs that show negatively correlated motion, while green lines represent particles pairs with positively correlated motion. The more active sample (Fig. 4.15B) shows 1634 overlaps, of which 862 are negatively correlated and 772 positively correlated. About half of the negatively correlated overlaps involve contraction, where the separation distance between the beads decreases during the event. The less active sample (Fig. 4.15A) shows only 19 overlaps, of which 8 are negatively correlated (6 involve a contraction) and 11 positively correlated. The separation distance of particle pairs with correlated motion can be quite large, occasionally spanning nearly the entire field of view. There is no clear spatial localization of overlaps. However, the localization may depend on sample age, which we did not yet test. There is no clear evidence of more than two beads moving together, but this issue

still merits a more detailed analysis. In addition, we plan to analyze the distribution of separation distances of beads exhibiting correlated motion as a function of sample age. We sporadically observed by visual inspection of the movies that large areas of the sample moved collectively. This collective motion was (partly) taken out by dedrifting the particle trajectories. A careful analysis of these large scale collective events and how they influence overlaps is still required.

4.4 Discussion

In this chapter, we studied dynamics in active actin-myosin networks at a 1:200 myosin:actin molar ratio. We focused on actin networks of $1\,\mathrm{mg/mL}$ that were weakly and isotropically crosslinked by biotin-streptavidin. With confocal microscopy, we observed that the motors actively coarsened the networks to form dense actomyosin condensates with sizes of 10-$20\,\mu\mathrm{m}$. On larger scales, the networks remained rather homogeneous. Network coarsening proceeded over a period of 30 minutes after sample preparation. After 30 minutes, the network structure appeared to have reached a steady state (Fig. 4.1, low motor density). Despite the microscopically heterogeneous network structure, the bulk elastic modulus was minimally changed as compared to passive networks having no motors (Fig. 4.4). The stiffness was increased by a factor 1.5, likely due to transient crosslinking by the active motors. This extent of stiffening is consistent with observations in similar systems [25, 35]. To probe the motor-driven active dynamics in the networks, we performed video particle tracking microrheology of embedded spherical probe particles. The particles were homogeneously distributed in the network at low motor density throughout the entire 90 minutes duration of the assay, permitting spatiotemporal mapping of network dynamics. In contrast, at higher motor density (1:65), the particles were rapidly contracted into large clusters (Fig. 4.5B), likely corresponding to the large condensed actin-myosin structures seen by confocal microscopy in Figure 4.1 (high motor density). This clustering obstructed multiple particle tracking analysis. We therefore analyzed only particle motion in samples of low motor density. We obtained data for 4 different samples, which showed similar dependencies on sample age, but differed somewhat in the degree of *activity*, as evident from the ensemble averaged MSD and the frequency of directed motion events in single particle trajectories.

4.4.1 Ensemble averaged particle dynamics

The ensemble averaged motion of the probe particles revealed striking differences between active networks (with myosin) and passive networks (without myosin). Beads in passive networks showed subdiffusive motion characterized by a diffusive

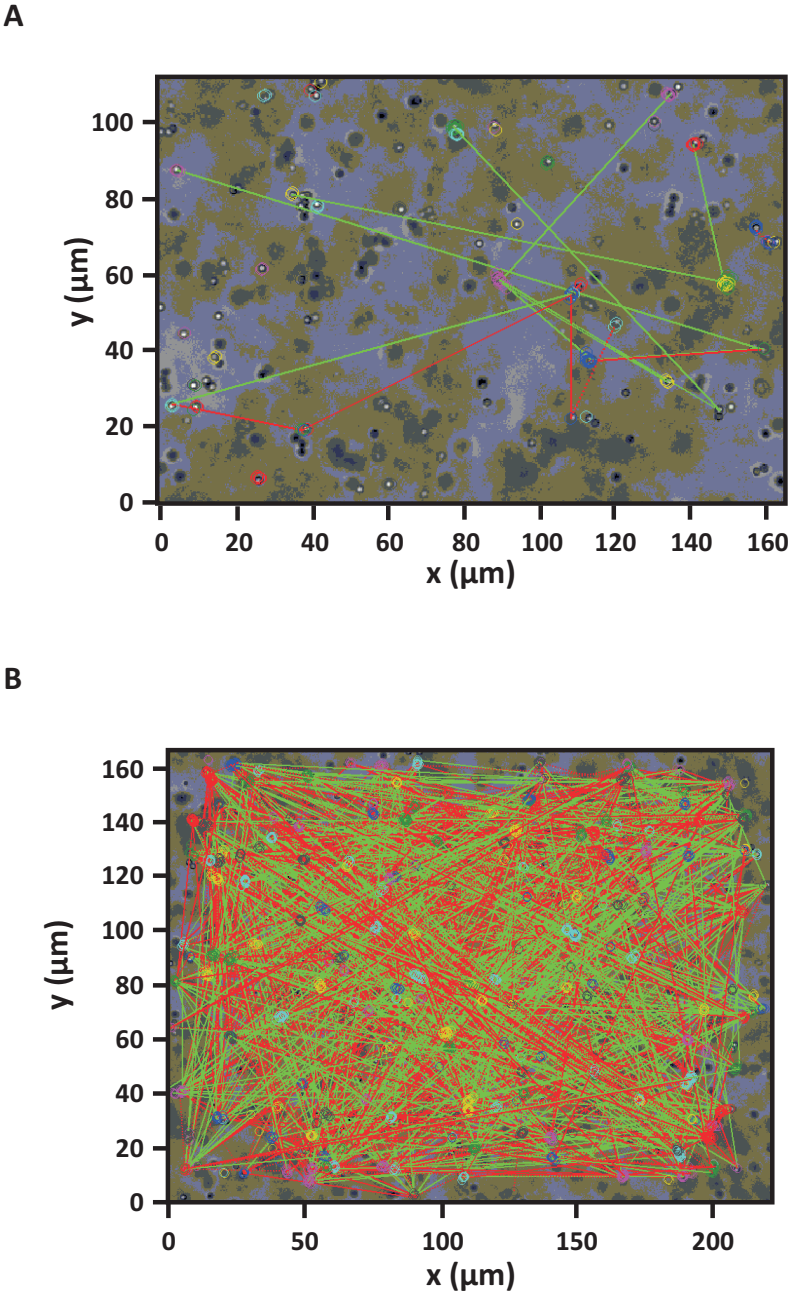

Figure 4.15: Spatial distribution of correlated directed motion of particle pairs during a 90 min observation time. Overlaps are represented as lines (green: positively correlated motion; red: negatively correlated motion) connecting particle locations (circles). **A.** Sample displaying moderate activity, very few overlaps. **B.** Sample displaying high activity, high density of overlaps. Both samples contain 1mg/mL actin and a ratio of 1:200 motors:actin)

exponent of 0.2. Beads in active networks also showed subdiffusive motion, but in the first 30 minutes after sample preparation the MSD was much larger than in passive networks (Fig. 4.8B). The diffusive exponent showed a distinct dependence on sample age, decreasing from 0.9 at early times to 0.2 within about 30 minutes (Fig. 4.8C). Interestingly, this decay time mirrors the time dependence of the active coarsening process observed by confocal microscopy. The diffusive exponent is enhanced compared to passive networks during the first 30 minutes, in which the motors are actively coarsening the network. The exponent becomes comparable to that of passive networks once the network structure has reached a steady state.

It was previously shown that signatures of motor activity in actin networks can also be visible in higher order moments of the distribution of particle displacements. In particular, microrheology with beads and microtubules showed evidence of pronounced non-Gaussianity in the Van Hove correlation functions [41]. To test for non-Gaussianity, we computed Van Hove functions at a lag time of $10\,\mathrm{s}$, and analyzed the dependence on sample age. Again, we observed striking differences between active and passive networks. Van Hove functions were Gaussian for passive networks, whereas they showed pronounced tails for active samples observed within 30 minutes after sample preparation. For active samples older than 30 minutes, the Van Hove functions were more Gaussian. We quantified the non-Gaussianity by a non-Gaussianity parameter NGP) which is zero for a Gaussian distribution. The NGP was less than 0.1 for passive networks, wheras it had large positive values for active networks, in particular in the first 30 minutes after sample preparation (Fig. 4.8D). This age-dependence is consistent with the finding that the MSD significantly deviates from the MSD in passive networks only at early stages.

In combination, microrheology data and confocal imaging suggest that deviations in the ensemble averaged MSD in active networks compared to passive networks are only obvious while the network is coarsening. However, detailed analysis of single particle trajectories showed that there were still particles exhibiting clearly non-Brownian, directed motion after 30 minutes (Fig. 4.7i). Apparently the frequency of these events is too low to show up in the ensemble averaged dynamics. This indicates that an ensemble averaged analysis may miss infrequent, nonthermal events. It is therefore useful to complement ensemble analysis with a single particle trajectory analysis. The decreasing frequency of active directed motion when the samples age is likely a consequence of the accumulation of myosin motors in clusters. At early times, the motors are homogeneously distributed, and can be modeled as force dipoles distributed throughout a homogeneous and isotropic network of actin filaments [27]. After 30 minutes, the motors are concentrated in large clusters that are widely separated. Once these clusters have condensed the surrounding actin into a dense shell, there does not appear to be much remaining contractile activity. The

motor density in the network inbetween the large clusters is strongly reduced compared to the intial density. Therefore, there are only sporadic, contractile events at late times, which are probably caused by remaining myosin filaments not incorporated in clusters.

The diffusive exponent of the MSD in the most active samples at early times is ~ 0.9. This value is close to values of $\sim$1 observed in earlier microrheology work on actin-myosin using rod-like microtubule probes [41]. Moreover, this value is consistent with diffusive exponents observed in some cases in cells, where endogenous [3, 5, 6] or exogenous probe particles [8, 13] were tracked. However, there are also observations of superdiffusive motion, in reconstituted actin-myosin networks bundled by fascin [32], and also in cells [3, 3]. Theoretical models of contractile force dipoles in an elastic background material provide a rationale for apparent diffusive (exponent 1) motion driven by motors [27, 41]. The force dipoles build up tension during a processivity time window, followed by sudden release and active relaxation of the built-up tension.

4.4.2 Elucidating the spatiotemporal activity with single particle analysis

To investigate the origin of the non-equilibrium signatures in the ensemble averaged dynamics of beads in active samples, we inspected single particle trajectories. We implemented an automated segmentation of particle trajectories to distinguish *segments* of directed motion from otherwise nondirected (random) motion. This analysis revealed a striking dependence of directed motion events on sample age: the frequency of events per bead and per unit of time decreased from 30% in the first 5 minutes after sample preparation, to $\sim$0.1% over a time period of 30 minutes. Again, this time scale matches the time scale of active coarsening observed by confocal microscopy.

As explained above, single particle trajectory analysis appears to be more sensitive to active, nonthermal motion than ensemble analysis. Moreover, the single particle analysis permits a detailed analysis of the characteristics of directed motion events. In the first 10 minutes after sample preparation, beads showed large, up to $25\,\mu\mathrm{m}$, translocations. Translocations were usually (90% of the cases) followed by a relaxation back to the original position. However, this recovery was often incomplete, especially when the original translocation distance was large (Fig. 4.12D). After 10 minutes, translocation distances were smaller (with a maximum of $5\,\mu\mathrm{m}$), and more reversible. These observations suggest that active coarsening of the network, which occurs within 30 minutes after sample preparation, is accompanied by large scale, irreversible network displacements. Once the network structure has reached a steady

state, isolated myosin filaments in regions of the network in between actomyosin condensates still occasionally drive active directed motion of beads.

We performed a qualitative analysis of correlated motion of particles by identifying *overlaps* of active segments of directed particle motion in single particle trajectories. We mainly observed correlated motion during early times (<10 minutes) after sample preparation. Roughly 30-50% of these overlaps involved anticorrelated, or contractile motion, where the beads moved towards one another. Negatively correlated motion is a signature of non-equilibrium motor activity, since it is not expected in thermal equilibrium [25]. Correlated motion occurred with large separations between particles. There was relatively little correlated motion for particles that were close together. This qualitative observation is consistent with a prior study where bending fluctuations of microtubules were observed in actin-myosin networks [41]. It was reported there that there was little correlation between myosin-driven bending in closely spaced microtubules. We found similar behavior when we observed fluorescently labeled microtubules in our networks (Fig. 4.16). We observed occasional short wavelength bending of microtubules, apparently caused by a local contraction of the network by a myosin filament. This activity was highly localized.

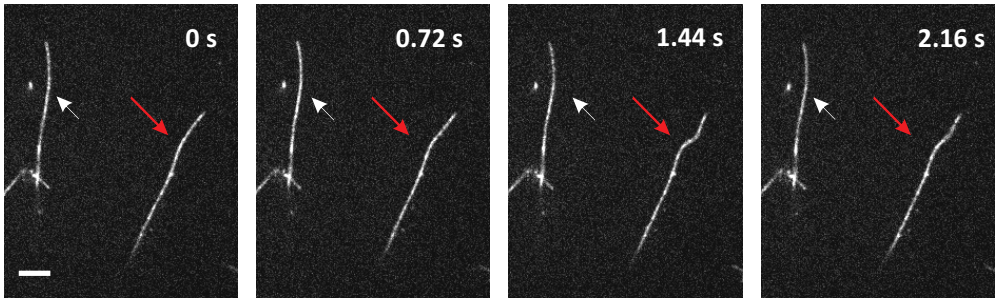

Figure 4.16: Taxol stabilized microtubules probe local force fluctuations in active actin-myosin networks. Sequence of fluorescent micrographs of an Alexa488 labeled microtubule embedded in a dark actin network in the presence of myosin thick filaments. Grey arrow points to local bend in MT probe, white arrow points to straight MT in the vicinity that does not fluctuate. Scale bar is $5\,\mu\mathrm{m}$.

Our microrheology analysis shows that motor-driven active dynamics in actin networks depends on the temporal evolution of the network structure. It will be interesting to extend existing continuum models of active gels that model myosin motors

as non-interacting force dipoles in a purely elastic medium [27, 29] to account for the heterogeneous and time-dependent structure of the networks. A realistic model of actin-myosin gels will need to take into account that the myosin is not present only as individual bipolar filaments, but that the myosin distribution evolves over time, eventually resulting in large foci. These foci interact with many actin filaments of random polarities at the same time, making the interaction very different from the idealized situation of a bipolar filament interacting with two actin filaments of opposite polarity.

It will also be very interesting to relate the non-equilibrium dynamics observed in our minimal actin-myosin system to the non-equilibrium dynamics reported for cells [5, 10, 12, 13, 14, 15, 16, 48]. It is currently difficult to distinguish non-equilibrium activity resulting from active transport of probe particles along the actin and microtubule cytoskeleton by motors (myosins or kinesins) from active particle motion resulting from myosin-II driven contraction of the actin cytoskeleton. We believe that it will be fruitful to combine an analysis of the ensemble averaged dynamics (MSD and non-Gaussianity) with an analysis of single particle trajectories.

4.5 Conclusion

We have systematically quantified the dynamics of active actin-myosin networks at low motor density and related these dynamics to the motor-dependent structural evolution of the network. We showed that the motors actively coarsen the network to form large actomyosin condensates, and that this coarsening is reflected in a time-dependence of the probe particle dynamics. Coarsening is accompanied by large scale, active, directed motion of the probe particles, which is evident in single particle trajectories and shows up as deviations of the ensemble averaged MSD and Van Hove correlation function from thermal equilibrium. It will be interesting to extend theoretical models of actin-myosin networks to account for the time-dependent spatial heterogeneity of these networks. Moreover, this coupling between dynamics and structure may be relevant for interpreting microrheology measurements in living cells.

4.6 Acknowledgments

We would like to thank Marco Seynen for his swift and dedicated work on implementing the BeadTracker software. Björn Stuhrmann was supported by a FP7 IE Marie Curie Fellowship.

4. Dynamics of active actin-myosin networks probed by video particle tracking

References

[1] C. Brangwynne, G. Koenderink, F. MacKintosh, and D. Weitz. Intracellular transport by active diffusion. *Trends Cell Biol.*, 19(9):423–427, 2009.

[2] Jonathon Howard. *Mechanics of Motor Proteins and the Cytoskeleton*. Sinauer, Sunderland, Massachusetts, 2001.

[3] D. Robert, T. Nguyen, F. Gallet, and C. Wilhelm. In vivo determination of fluctuating forces during endosome trafficking using a combination of active and passive microrheology. *PLoS One*, 5(4):e10046, 2009.

[4] A. Snezhko, K. Barlan, I. Aranson, and V. Gelfand. Statistics of active transport in *Xenopus* melanophores cells. *Biophys. J.*, 99(10):3216–3223, 2010.

[5] A. Lau, B. Hoffmann, A. Davies, JC. Crocker, and T. Lubensky. Microrheology, stress fluctuations, and active behavior of living cells. *Phys. Rev. Lett.*, 91(19):198101–4, 2003.

[6] D. Arcizet, B. Meier, E. Sackmann, J. Raedler, and D. Heinrich. Temporal analysis of active and passive transport in living cells. *Phys. Rev. Lett.*, 101(24):248103–4, 2008.

[7] C. Hale, S. Sun, and D. Wirtz. Resolving the role of actoymyosin contractility in cell microrheology. *PLoS One*, 4(9):e7054, 2009.

[8] A. Caspi, R. Granek, and M. Elbaum. Enhanced diffusion in active intracellular transport. *Phys. Rev. Lett.*, 85(26):56555658, 2000.

[9] B. Fabry, G. Maksym, J. Butler, M. Glogauer, D. Navajas, N. Taback, E. Millet, and J. Fredberg. Time scale and other invariants of integrative mechanical behavior in living cells. *Phys. Rev. E*, 68(4):041914, 2003.

[10] B Fabry, G. Maksym, J. Butler, M. Glogauer, D. Navajas, and J. Fredberg. Scaling the microrheology of living cells. *Phys. Rev. Lett.*, 87(14):148102, 2001.

[11] N. Wang, J. Butler, and D. Ingber. Mechanotransduction across the cell surface and through the cytoskeleton. *Science*, 260(5111):1124 –1127, 1993.

[12] B. Hoffman, G. Massiera, K. Van Citters, and J. Crocker. The consensus mechanics of cultured mammalian cells. *Proc. Natl. Acad. Sci. USA*, 103(27):10259–10264, 2006.

[13] K. Van Citters, B. Hoffman, G. Massiera, and J. Crocker. The role of F-Actin and myosin in epithelial cell rheology. *Biophys. J.*, 91(10):3946–3956, 2006.

[14] G. Massiera, K. Van Citters, P. Biancaniello, and J. Crocker. Mechanics of single cells: rheology, time dependence, and fluctuations. *Biophys. J.*, 93(10):3703–3713, 2007.

[15] M. Balland, A. Richert, and F. Gallet. The dissipative contribution of myosin II in the cytoskeleton dynamics of myoblasts. *Eur. Biophys. J.*, 34(3):255–261–261, 2005.

[16] Francois Gallet, Delphine Arcizet, Pierre Bohec, and Alain Richert. Power spectrum of out-of-equilibrium forces in living cells: amplitude and frequency dependence. *Soft Matter*, 5(15):2947–2953, 2009.

[17] M. Gardel, M. Valentine, J. Crocker, A. Bausch, and D. Weitz. Microrheology of entangled F-Actin solutions. *Phys. Rev. Lett.*, 91(15):158302–5, 2003.

[18] I. Wong., M. Gardel, D. Reichman, E. Weeks, M. Valentine, A. Bausch, and D. Weitz. Anomalous diffusion probes microstructure dynamics of entangled f-actin networks. *Phys. Rev. Lett.*, 92(17):178101–4, 2004.

[19] M. Valentine, P. Kaplan, D. Thota, J. Crocker, T. Gisler, R. Prud'homme, M. Beck, and D. Weit. Investigating the microenvironments of inhomogeneous soft materials with multiple particle tracking. *Phys. Rev. E*, 64(6):061506–9, 2001.

[20] L. Landau and E. Lifshitz. *Theory of Elasticity*, volume 7. Butterworth-Heinemann, Burlington MA, USA, 3rd edition, 1986.

[21] A. Einstein. ber die von der molekulartheoretischen theorie der wrme geforderten bewegung von in ruhenden flssigkeiten suspendierten teilchen. *Ann. d. Phys*, 332(17):549–560, 1905.

[22] J. Crocker and B. Hoffman. Multiple particle tracking and two-point microrheology in cells. In *Cell Mechanics*, volume Volume 83, pages 141–178. Academic Press, 2007.

[23] Clifford P. Brangwynne, F. C. MacKintosh, and David A. Weitz. Force fluctuations and polymerization dynamics of intracellular microtubules. *Proc. Natl. Acad. Sci. USA*, 104(41):16128 –16133, 2007.

[24] L. Le Goff, F. Amblard, and E. Furst. Motor-driven dynamics in actin-myosin networks. *Phys. Rev. Lett.*, 88(1):018101, 2002.

[25] D. Mizuno, C. Tardin, C. Schmidt, and F. MacKintosh. Nonequilibrium mechanics of active cytoskeletal networks. *Science*, 315(5810):370–373, 2007.

[26] E. Ben-Isaac, Y. Park, G. Popescu, F. Brown, N. Gov, and Y. Shokef. Effective temperature of Red-Blood-Cell membrane fluctuations. *Phys. Rev. Lett.*, 106(23):238103–4, 2011.

[27] F. MacKintosh and A. Levine. Nonequilibrium mechanics and dynamics of motor-activated gels. *Phys. Rev. Lett.*, 100(1):018104, 2008.

[28] A. Levine and F. MacKintosh. The mechanics and fluctuation spectrum of active gels. *J. Phys. Chem. B*, 113(12):3820–3830, 2009.

[29] D. Head and D. Mizuno. Nonlocal fluctuation correlations in active gels. *Phys. Rev. E*, 81(4):041910–11, 2010.

[30] M. Soares e Silva, M. Depken, B. Stuhrmann, M. Korsten, F. MacKintosh, and G. Koenderink. Active multistage coarsening of actin networks driven by myosin motors. *Proc. Natl. Acad. Sci. USA*, 2011.

[31] D. Smith, F. Ziebert, D. Humphrey, C. Duggan, M. Steinbeck, W. Zimmermann, and J. Käs. Molecular motor-induced instabilities and crosslinkers determine biopolymer organization. *Biophys. J.*, 93:4445 – 4452, 2007.

[32] S. Köhler, V. Schaller, and A. Bausch. Structure formation in active networks. *Nat. Mater.*, 10(6):462–468, 2011.

[33] F Backouche, L Haviv, D Groswasser, and A Bernheim-Groswasser. Active gels: dynamics of patterning and self-organization. *Phys Biol.*, 3(4):264–273, 2006.

[34] W. Koopmans, A. Brehm, C. Logie, T. Schmidt, and J. van Noort. Single-Pair FRET microscopy reveals mononucleosome dynamics. *J. Fluoresc.*, 17(6):785–795–795, 2007.

[35] G. Koenderink, Z. Dogic, F. Nakamura, P. Bendix, F. MacKintosh, J. Hartwig, T. Stossel, and D. Weitz. An active biopolymer network controlled by molecular motors. *Proc. Natl. Acad. Sci. U.S.A.*, 106(36):15192–7, 2009.

[36] J. Crocker and D. Grier. Methods of digital video microscopy for colloidal studies. *J. Colloid Interface Sci.*, 179(1):298–310, 1996.

[37] C. Schmidt, M. Bärmann, Gerhard Isenberg, and E. Sackmann. Chain dynamics, mesh size, and diffusive transport in networks of polymerized actin: a quasielastic light scattering and microfluorescence study. *Macromolecules*, 22(9):3638–3649, 1989.

[38] Y. Luan, O. Lieleg, B. Wagner, and A. Bausch. Micro- and macrorheological properties of isotropically Cross-Linked actin networks. *Biophys. J.*, 94(2):688–693, 2008.

[39] C. Broedersz and F. MacKintosh. Molecular motors stiffen non-affine semiflexible polymer networks. *Soft Matter*, 7(7):3186–3191, 2011.

[40] A. Straight, A. Cheung, J. Limouze, I. Chen, N. Westwood, J. Sellers, and T. Mitchison. Dissecting temporal and spatial control of cytokinesis with a myosin II inhibitor. *Science*, 299(5613):1743 –1747, 2003.

[41] C. Brangwynne, G. Koenderink, F. Mackintosh, and D. Weitz. Nonequilibrium microtubule fluctuations in a model cytoskeleton. *Phys. Rev. Lett.*, 100(11):118104, 2008.

[42] J. Finer, R. Simmons, and J. Spudich. Single myosin molecule mechanics: piconewton forces and nanometre steps. *Nature*, 368(10):113–119, 1994.

[43] R. Metzler and J. Klafter. The random walk's guide to anomalous diffusion: a fractional dynamics approach. *Phys. Rep.*, 339(1):1–77, 2000.

[44] M. Gardel, J. Shin, F. MacKintosh, L. Mahadevan, P. Matsudaira, and D. Weitz. Scaling of f-actin network rheology to probe single filament elasticity and dynamics. *Phys. Rev. Lett.*, 93(18):188102–5, 2004.

[45] T. Toyota, D. Head, C. Schmidt, and D. Mizuno. Non-Gaussian athermal fluctuations in active gels. *Soft Matter*, 7(7):3234–3239, 2011.

[46] A. Rahman. Correlations in the motion of atoms in liquid argon. *Phys. Rev.*, 136(2A):A405–A411, 1964.

[47] S. Kron and J. Spudich. Fluorescent actin filaments move on myosin fixed to a glass surface. *Proc. Natl. Acad. Sci. USA*, 83(17):6272 –6276, 1986.

[48] K. Girard, S. Kuo, and D. Robinson. *Dictyostelium* myosin II mechanochemistry promotes active behavior of the cortex on long time scales. *Proc. Natl. Acad. Sci. USA*, 103(7):2103–2108, 2006.

Chapter 5

Self-organized patterns of actin filaments in cell-sized confinement

Cells use actin filaments to define and maintain their shape and to exert forces on the surrounding tissue. Accessory proteins like crosslinkers and motors organize these filaments into functional structures. However, physical effects also influence filament organization: steric interactions impose packing constraints at high filament density and spatially confine the filaments within the cell boundaries. Here we investigate the combined effects of packing constraints and spatial confinement by growing dense actin networks in cell-sized microchambers with nonadhesive walls. We show that the filaments spontaneously form dense, bundle-like structures above a threshold concentration of $1\,\mathrm{mg/mL}$*, in contrast to unconfined networks, which are homogeneous and undergo a bulk isotropic-to-nematic phase transition above* $5\,\mathrm{mg/mL}$*. Bundling requires quasi-2D confinement in chambers with a depth comparable to the mean filament length* $(6\,\mu\mathrm{m})$*. The bundles curve along the walls and central bundles align along the chamber diagonal or, in elongated chambers, along the long axis. We propose that bundling is a result of the polydisperse length distribution of the filaments: filaments shorter than the chamber depth introduce an entropic depletion attraction between the longest filaments, which are confined in-plane. Bundle alignment reflects a competition between bulk liquid-crystalline ordering and alignment along the boundaries. This physical mechanism may influence intracellular organization of actin in combination with biochemical regulation and actin-membrane adhesion.*

Based on manuscript by Marina Soares e Silva, José Alvarado, Jeanette Nguyen, Nefeli Georgoulia, Bela M. Mulder, Gijsje H. Koenderink, *in print* in Soft Matter. DOI:10.1039/C1SM06060K. José developed the automated image processing and analysis protocol and performed the automated analysis in this chapter.

5.1 Introduction

The shape and internal organization of eukaryotic cells are governed by a complex and dynamic network of filamentous proteins known as the cytoskeleton. The backbone of this cytoskeleton is formed by three types of long and stiff biopolymers: microtubules, actin filaments, and intermediate filaments. The spatial arrangement of these filaments is regulated by a large set of accessory proteins that crosslink the cytoskeletal filaments to each other [1] and to the cell membrane [2]. Moreover, the cytoskeleton is actively remodeled by processes that use metabolic energy, such as filament (de-)polymerization and sliding by motor proteins [3]. This biochemical regulation inevitably operates under constraints set by physical effects.

An important physical constraint is provided by the finite size of cells and their internal compartments. The typical size of eukaryotic cells ranges from $\sim 10\,\mu\mathrm{m}$ for yeast cells to $\sim 50\,\mu\mathrm{m}$ for plant and animal cells [4]. In plants, the cytoplasm is in many parts of the cell confined within a thin layer of only $\sim 1\,\mu\mathrm{m}$ that is sandwiched between the rigid cell wall and the vacuole, which takes up nearly 90% of the cytoplasmic space [5]. In animal cells, the cytoplasm is usually more three-dimensional and is bounded by a lipid bilayer membrane which is soft and deformable. However, many types of animal cells bear a rigid extracellular polymer layer anchored to the cell membrane known as the pericellular coat [6, 7] and in epithelial tissues, membrane fluctuations are constrained by close packing of the cells and active tension imposed by the actin-myosin cytoskeleton [8]. Furthermore, certain regions of the cytoskeleton are often tightly confined in thin cell extensions. Migrating cells advance sheet-like lamellipodia with heights of only $0.1 - 0.2\,\mu\mathrm{m}$, filled with a dense meshwork of actin [9, 10, 11]. Cells also generate long and thin membrane protrusions filled with actin or microtubules, such as filopodia, stereocilia, and neurite processes [12]. Since actin filaments and microtubules are rather rigid on these cellular scales, we expect that geometrical constraints are relevant for their organization *in vivo*. However, the inherent complexity of cells hampers a clear distinction between the effect of confinement and that of regulatory proteins.

Several experimental studies have isolated the influence of confinement on cytoskeletal organization by reconstituting purified actin or tubulin in cell-sized liposomes, emulsion droplets, or microfabricated chambers. Long cytoskeletal filaments confined in small containers with rigid walls have to bend, and the associated energy penalty forces them to align close to the walls [13, 14, 15]. Filaments inside liposomes, however, can avoid bending by generating membrane protrusions, provided that the force resisting protrusion does not exceed the Euler buckling force. Microtubules, which have mm-persistence lengths, have been shown to generate protrusions in the absence of crosslinkers [16, 17, 18, 19], whereas actin filaments, which have a consid-

erably smaller persistence length of $9-15\,\mu\mathrm{m}$ [20, 21], are unable to create membrane protrusions unless they are crosslinked into rigid bundles [22]. In narrow microchannels, the transverse thermal bending undulations of individual actin filaments can be confined, forcing the filaments to stretch [23, 24, 25], similar to stretching of DNA chains in nanoslits [26, 27].

Aside from steric constraints provided by confinement, there are also packing constraints on filament organization coming from the fact that filaments cannot interpenetrate. The excluded volume of a pair of stiff filaments depends on their relative orientation: it is maximal when the filaments are perpendicular and minimal when the filaments are parallel. For filaments with only steric interactions, the lowest free energy state corresponds to a situation where the entropy is maximized. In dilute systems, the free volume will be large and the free energy is minimized by an isotropic distribution of rod orientations that maximizes the orientational entropy. At high densities, however, the reduced free volume will favor a transition to a nematic state with aligned rods. Rod alignment minimizes the excluded volume and thus maximizes the translational entropy, which offsets the loss in orientational entropy. For rigid rods, the isotropic to nematic (I-N) phase transition is governed by the aspect ratio of the rods, which is the ratio between their length, *L*, and diameter, *D*. According to the classic Onsager theory [28], the transition occurs at a rod volume fraction $\phi = 3.340D/L$. Filament flexibility increases the threshold concentration at which the I-N transition occurs [29, 30, 31]. Solutions of actin filaments were shown [32, 33] to undergo an I-N transition at a concentration of $\sim 4\,\mathrm{mg/mL}$ (or ϕ = 0.4%), consistent with the Onsager prediction for filaments with a diameter of $7\,\mathrm{nm}$ and length in the range of $\sim 10-20\,\mu\mathrm{m}$. Moreover, reducing the filament length by capping with gelsolin shifted the I-N threshold to higher concentrations in inverse proportion to length [34, 35, 36]. It is uncertain whether the length and concentration of actin filaments *in vivo* favor a nematic state. The overall actin concentration in cells is typically at least $2\,\mathrm{mg/mL}$and the filament length is around $1-2\,\mu\mathrm{m}$ [37, 38]. However, both the concentration and the length depend on cell type and show spatiotemporal variations due to regulatory processes. In addition, a nematic transition may be counteracted by crosslinking proteins, some of which favor high angles between filaments [39, 40]. Solutions of purified microtubules likewise undergo an I-N phase transition at concentrations consistent with the Onsager theory [41], but *in vivo* microtubule organization is often dominated by nucleation and cross-linking effects.

We anticipate that confinement of cytoskeletal polymers at high density should generate a rich phase space, but so far there have been no experimental or theoretical studies in this regime. There have been studies of (nonbiological) rigid rods in quasi-2D confinement showing that interesting phase behavior emerges due to a

competition between wall-induced rod alignment and bulk liquid crystalline ordering [42, 43]. On a theoretical level, this behavior has only been studied by continuum theories [44] and simulations [45]. For semiflexible rods, such as actin filaments and microtubules, even more complex behavior is expected since the flexibility of the rods introduces enthalpic effects related to filament bending. So far, these enthalpic effects have only been studied for single chains [23, 25] and in dilute systems with polymer volume fractions below the bulk I-N phase transition [13, 14, 15]. Theoretical models addressing geometrical confinement of semiflexible chains have also largely focused on single confined chains [45, 46, 47, 48]. Therefore, the regime of dense confined polymers that is potentially relevant to cytoskeletal organization remains unexplored.

In this chapter, we study the combined effect of confinement and excluded volume interactions on the self-organization of actin filaments over a wide range of actin concentrations $0.1 - 7\,\mathrm{mg/mL}$). To this end, we polymerize purified actin in microchambers produced by photolithography. Unlike intrinsically spherical liposomes or emulsion drops, these allow us to vary the geometrical shape and the degree of confinement in all three dimensions. We demonstrate that spatial confinement induces spontaneous bundling of the filaments above an actin concentration of $1\,\mathrm{mg/mL}$, which is below the bulk I-N transition. We show that confinement-induced bundling requires that at least one confining dimension is comparable to the mean filament length. Finally, we propose a physical mechanism for bundling and discuss the potential physiological relevance of our findings.

5.2 Materials and Methods

5.2.1 Proteins and reagents

Monomeric G-actin was purified from rabbit psoas skeletal muscle without column purification [49]. G-actin was stored at $-80°C$ in G-buffer ($2\,\mathrm{mM}$ Tris-HCl, $2\,\mathrm{mM}$ Na_2ATP, $0.2\,\mathrm{mM}$ $CaCl_2$, $0.2\,\mathrm{mM}$ dithiothreitol (DTT), $0.5\,\mathrm{mM}$ NaN_3, pH 8.0). Actin purification procedures and actin length distribution measurements are described in detail in *Chapter 2*. Recombinant human plasma gelsolin purified from Escherichia coli was a kind gift from Fumihiko Nakamura (Harvard Medical School, Boston). We resuspended gelsolin in G-buffer to a concentration of $60\,\mu\mathrm{M}$. ATP was prepared as a $100\,\mathrm{mM}$ MgATP stock solution using equimolar amounts of Na_2ATP and $MgCl_2$ in a $10\,\mathrm{mM}$ imidazole-HCl buffer (pH 7.4). Rhodamine-phalloidin was from Sigma Aldrich and Alexa 488-phalloidin was from Molecular Probes (Invitrogen, Carlsbad, CA, USA). Other chemicals were purchased from Sigma Aldrich (St. Louis, MO, USA).

5.2.2 Photolithography

Microchambers were fabricated using optical lithography [50]. A layer of SU8 negative photoresist (Microchem, Newton, Massachusetts, USA) was spincoated on a ♯ 1 glass cover slip (Menzel, Germany). To ensure good adhesion of the SU8 film, the glass substrates were cleaned with Base Piranha (water, 30% NH_4OH, and 30% H_2O_2 in a 5:1:1 volume ratio) at $75°C$ for 15 minutes followed by rinsing in MilliQ water and then 2-propanol. Prior to use, the substrates were dried with a stream of nitrogen and subjected to a dehydration bake for 5 minutes at $200°C$ on a hotplate. The thickness of the SU8 layer, which sets the microchamber depth, was varied by using photoresists of different viscosities (type 2005 for $5\,\mu$m; type 2010 for $10\,\mu$m; type 2025 for $20\,\mu$m; type 3025 for $30\,\mu$m) and by using a spinning speed of either 2000 or 3000 rpm on a Delta 80 Spincoater. The coated substrate was baked for 15 minutes at $65°C$ and another 15 minutes at $95°C$ on a hotplate. The coverslip was then exposed to ultraviolet light ($365\,$nm) through a chromium mask on a Karl Süss MJB Mask Aligner. The mask featured custom-designed patterns set in chromium on glass (Delta Mask, Enschede, The Netherlands). The patterns consisted of repeating $15 \times 15\,$mm blocks of circular chambers with diameters ranging from 10 to $40\,\mu$m and triangular, pill-shaped and rectangular chambers with long axes/sides ranging from 15 to $200\,\mu$m. The UV-illumination crosslinked the SU8, which was further enhanced by a post-exposure bake of 15 minutes at $65°C$ and 15 minutes at $95°C$, followed by gradual cooling. Unexposed SU8 was removed by immersing and sonicating the coverslip in a developer (Mr Dev 600, Microchem) for 2 minutes for shallow chambers ($5\,\mu$m deep) and 10 minutes for deeper chambers. A final 30 min baking step at $150°C$ was performed to prevent stress-related cracks in the SU8 film. The final chamber depth was measured with an Alpha-Step 500 Surface Profiler.

5.2.3 PDMS chamber lids

Microchambers were sealed with lids of polydimethylsiloxane (PDMS) rubber deposited on microscope slides. PDMS mixtures were prepared from a Sylgard 184 Silicone Elastomer Kit (Dow Corning, Michigan, U.S.A.) with a 10:1 w/w base:curing agent ratio. Layers of PDMS with a uniform thickness of $\sim 1\,$mm height were spincoated on $76 \times 26\,$mm glass slides and cured in a preheated oven at $80°C$ for 1 hour.

5.2.4 Surface Treatments

The chamber walls were passivated to prevent nonspecific adhesion of actin. PDMS lids were rendered hydrophilic with a corona discharge (BD-20V high frequency generator, Electro-Technic Products, Chicago, IL, USA), which oxidizes the surface and

produces silanol groups [51]. The oxidized PDMS lids were treated with PEG silane (2-[methoxy(polyethyleneoxy) propyl]-trimethoxysilane, ABCR Chemicals, Karlsruhe, Germany) [52, 53] for 2 hours and washed twice in water for 30 minutes prior to use. SU8 chambers were incubated with a $0.1\,\mathrm{mg/mL}$ κ-casein (Sigma Aldrich) solution for 15 minutes at room temperature. Excess κ-casein was removed by washing with polymerization buffer and the chamber slide was dried with a stream of nitrogen.

5.2.5 Confinement assays

We prepared G-actin solutions on ice, in assembly buffer with final concentrations of $25\,\mathrm{mM}$ imidazole-HCl, $50\,\mathrm{mM}$ KCl, $0.1\,\mathrm{mM}$ MgATP, $2\,\mathrm{mM}$ $MgCl_2$, $1\,\mathrm{mM}$ DTT, and pH 7.4. We stabilized the actin filaments with an equimolar amount of fluorescent Alexa488-phalloidin. The buffer contained $2\,\mathrm{mM}$ trolox to minimize photobleaching. The G-actin concentration was varied between 0.1 and $7\,\mathrm{mg/mL}$ ($1\,\mathrm{mg/mL}$ corresponds to a molar concentration of $23.8\,\mu\mathrm{M}$). To determine the filament length distribution, a low density of pre-polymerized filaments was embedded in unlabeled networks of $1\,\mathrm{mg/mL}$ actin. The lengths were measured for 3711 filaments from confocal micrographs using the NeuronJ plugin of ImageJ (http://rsbweb.nih.gov/ij/). To alter the length distribution, gelsolin was included in the mixture at different molar ratios to G-actin. G-actin was always added last, to prevent premature actin polymerization, and $25\,\mu\mathrm{L}$ of the solution was immediately pipetted onto a chip with microchambers and the chambers were sealed with a polydimethylsiloxane (PDMS)-coated glass microscope slide. Actin polymerization was initiated by warming the samples to room temperature. The SU8 and glass surfaces of the chambers were passivated beforehand with $0.1\,\mathrm{mg/mL}$ κ-casein, and the PDSM lid was passivated with PEG-silane (2-[methoxy(polyethyleneoxy)propyl]trimethoxysilane, ABCR).

5.2.6 Bulk assays

To test whether actin filament alignment in chambers was caused by confinement, we prepared control, unconfined actin samples in large chambers consisting of a glass slide and cover slip separated by $25\,\mu\mathrm{m}$ thick spacers of Fluorinated Ethylene Propylene Copolymer (GoodFellow,Huntingdon, England). Surfaces were passivated in the same way as microchambers with $0.1\,\mathrm{mg/mL}$ κ-casein prior to sample inclusion. The spacers were lined with vacuum grease along the inner sides to prevent sample leakage and the chambers were sealed with vacuum grease to prevent solvent evaporation.

5.2.7 Fluorescence microscopy

Samples were observed with a spinning disk confocal scanner (CSU22, Yokogawa Electric Corp., Tokyo, Japan) on a DMIRB Leica inverted microscope. The AlexaFluor488-dye was excited with $488\,\mathrm{nm}$ laser light (Coherent Inc., Utrecht, The Netherlands) and images were recorded with a cooled EM-CCD camera (C9100, Hamamatsu Photonics, Hamamatsu City, Shizuoka, Japan) using an exposure time of $50 - 100\,\mathrm{ms}$. Image stacks were obtained by scanning through the z-direction in steps of $100\,\mathrm{nm}$ with a piezo-driven $100\times$ (1.3 NA) oil immersion objective (PL Fluotar Leica, Wetzlar, Germany).

5.2.8 Image processing and analysis

In order to quantify and compare bundling in actin networks in a systematic and high throughput manner, José Alvarado of the Biological Soft Matter group at AMOLF developed an algorithm based on the ImageJ plugin OrientationJ [54], combined with MATLAB scripts (MathWorks, Natick MA, U.S.A.). Orientation J was originally developed to determine the orientation of elastin filaments in tissue [54]. It quantifies the anisotropy of pixel intensity within a user defined region of interest with a pixel width on the order of the observed feature size. In brief, the maximum and minimum changes in pixel intensity within this region are used to determine the dominant *orientation* of the region and the anisotropy in pixel intensity [54]. This anisotropy is referred to as *coherency* in OrientationJ, and is the basis of the automated protocol to quantify actin bundling due to confinement.

To estimate bundling in fluorescent confocal micrographs, we defined a bundling parameter, B. We categorized structures as *bundles* when they appeared i) brighter than the surrounding background network (based on thresholding) and are at the same time ii) anisotropic (based on coherency). Image thresholding is done with standard OrientationJ thresholding filters, to select pixels that satisfy the brightness criterion. The anisotropy was measured using the coherency of pixels belonging to bundles according to the thresholding criterion. Bright pixels were considered to belong to a bundle when the intensities changed slowly along the bundle axis and fast along the orthogonal direction. Automated computation of B for hundreds of chambers enabled us to quantify the dependence of bundling on geometrical and biochemical conditions. A detailed description of this method will be published elsewhere.

To quantify the degree of bundle accumulation at the periphery of hardwall chambers, José Alvarado developed a new MATLAB script to quantify the pixel intensities for successively larger concentric layers within a chamber. The average pixel intensity per layer (normalized by the total periphery) was plotted as a function of the

layer distance to the center. This allowed us to inspect whether there was any peripheral accumulation of actin. Finally, we also used OrientationJ to determine the angle distribution of orientations of single fluorescent actin filaments embedded in unlabeled networks (Fig. 5.4) and to label the orientation angles of bundles in confocal images of densely labeled actin networks confined in chambers (Fig. 5.8).

5.2.9 Statistics

Data are shown as averages $\pm$ standard deviation. Means were compared using unpaired Student's t-tests.

5.3 Results

To study the effect of spatial confinement on filamentous (F-)actin self-organization, we fabricated cell-sized microchambers using photolithography. We could independently vary the degree of vertical confinement (by varying the chamber depth from 5 to $30\,\mu\mathrm{m}$) and of lateral (in-plane) confinement. Moreover, we systematically varied the in-plane (lateral) shape and anisometry of the confining geometry. We prepared chambers with circular, square, triangular, and pill-shaped cross-sections. We could thus address the influence of wall curvature and chamber symmetry on actin organization. Moreover, the pill-shaped chambers mimic the shape of fission yeast cells [4], while the polygonal shapes resemble shapes of mammalian cells on micropatterned adhesive islands [55, 56, 57] and in embryonic tissues [8]. The photoresist chip contained 1088 duplicate blocks which each featured 19 chambers with different dimensions (Fig. 5.1A). This design enabled us to simultaneously observe networks under different confinement conditions and to test the reproducibility of actin organization. Typically 30% of the chambers were well-sealed, yielding around 300 testable/usable chambers of each size and shape. For all experimental conditions tested, actin networks in duplicate chambers had similar structures. Therefore, we could calculate ensemble-averaged quantities from image analysis. We analyzed images of 3-264 chambers per experimental condition. The chamber surfaces were passivated with κ-casein (bottom and side walls) and PEG-silane (top) to prevent actin adsorption (Fig. 5.1A zoomed-in scheme). Actin was polymerized inside the chambers, in the presence of AlexaFluor488-phalloidin, which binds and stabilizes filamentous actin. Phalloidin raises the persistence length of actin filaments by a factor of 2 [21]. Moreover, the Alexa488 dye permitted visualization of F-actin by confocal laser scanning microscopy. The actin filaments had an exponential length distribution with a mean length of $6\,\mu\mathrm{m}$ (Fig. 5.1B). Networks were equilibrated for 6 hours

after polymerization had been initiated. The networks looked similar when equilibrated for 24 hours.

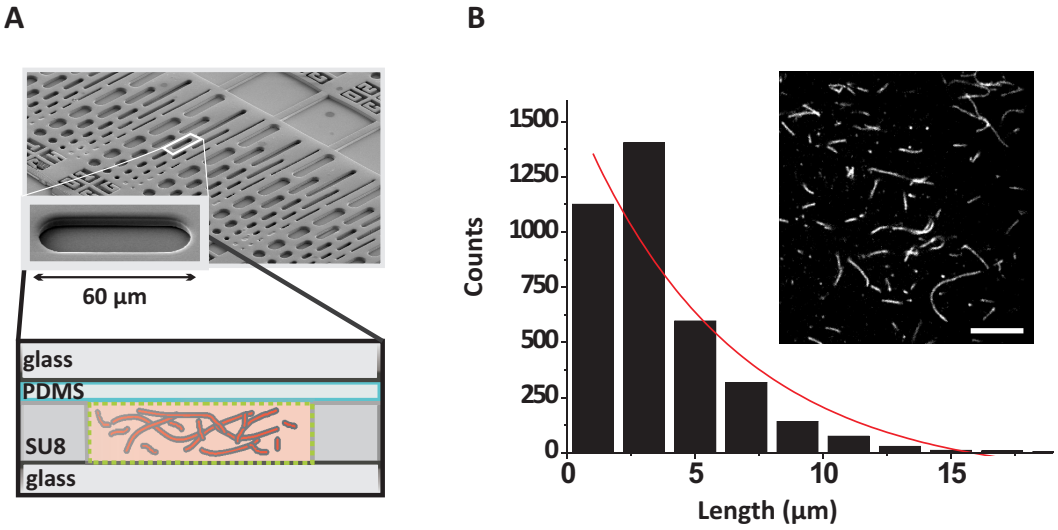

Figure 5.1: Cell-sized confinement of actin networks in microfabricated chambers. **A.** Scanning electron micrograph of a series of pill-shaped microchambers of varying size and aspect ratio. *Inset*: Magnification of a $60\,\mu\mathrm{m}$ long chamber with an aspect ratio of 1:3. *Zoomed-in scheme* Schematic side-view of an actin network confined in an SU8 photoresist chamber sealed with a PDMS-coated glass coverslip. All surfaces are coated with κ-casein (in green) to prevent nonspecific interactions with actin. The PDMS lid is additionally functionalized with PEG-silane. **B.** Filament length distribution measured on 3711 actin filaments by fluorescence microscopy. The distribution is well-fit by an exponential (red line) giving an average filament length of $6\,\mu\mathrm{m}$. Note that short filaments with lengths below $1\,\mu\mathrm{m}$ are underrepresented due to the diffraction-limited resolution of the optical microscope. *Inset* Typical confocal micrograph used for length distribution analysis, showing fluorescently labeled actin filaments embedded in an unlabeled network of 1 mg/mL actin. Around 0.3% of the filaments are labeled. Scale bar is $10\,\mu\mathrm{m}$.

We first observed the organization of actin networks in shallow ($5\,\mu\mathrm{m}$ deep) chambers at different actin concentrations, ranging from 0.1 to 7 mg/mL. We tested three different confining geometries with circular, square and triangular cross-sections, keeping the in-plane (lateral) dimensions constant ($30\,\mu\mathrm{m}$). The two most dilute networks of 0.1 and $0.5\,\mathrm{mg/mL}$ were homogeneous and isotropic in all three types of chambers (Fig. 5.2A left panel). However, at actin concentrations of 1 mg/mL and higher, the networks became inhomogeneous and partially aligned (images above the yellow dotted line). We observed dense, bundle-like structures, which aligned

with the side walls in the chamber periphery and along the diagonal in the chamber center. In the remainder of the chapter we will refer to these structures as *bundles*, but we note that they have a different origin than conventional actin bundles formed in the presence of actin bundling agents [39, 40]. The bundling was most clearly visible at 3 and 5 mg/mL actin. At 7 mg/mL, there was less image contrast between the bundles and the surrounding network.

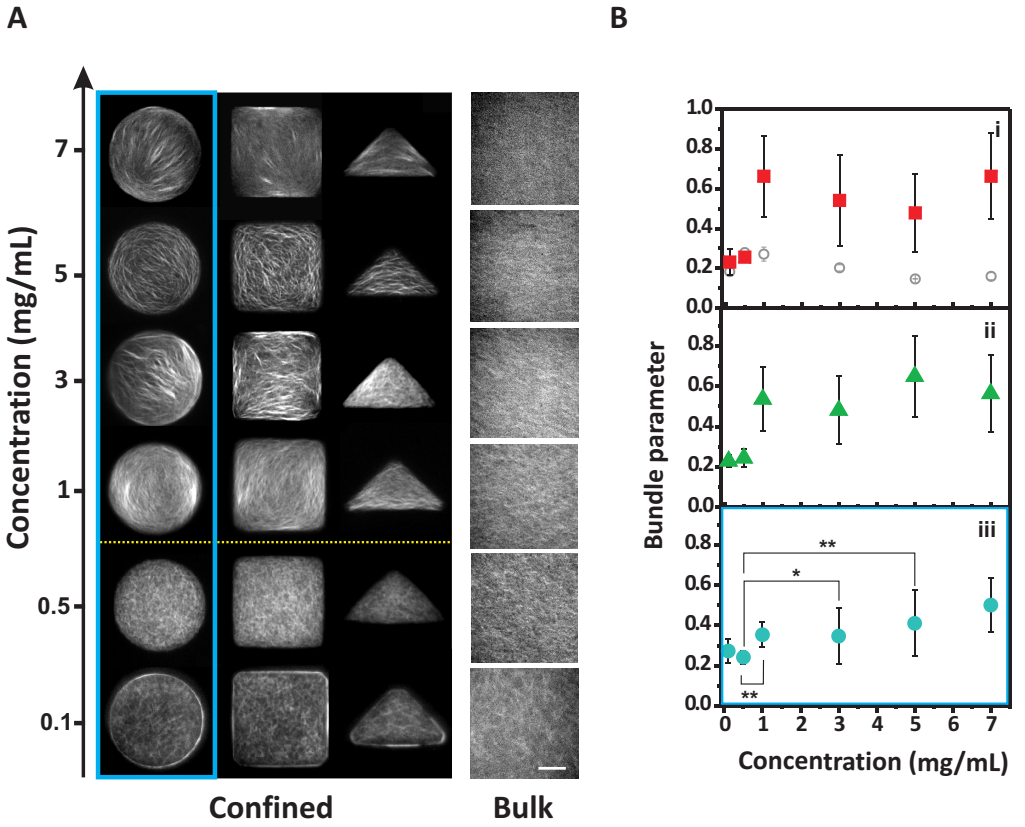

Figure 5.2: Confined actin networks are homogeneous at low concentrations, but show filament alignment and bundling when the actin concentration exceeds 1 mg/mL. **A.** Left panel Confocal micrographs of fluorescently labeled F-actin networks at different concentrations confined in chambers of different shapes but comparable size (circles of $30\,\mu$m diameter, squares and triangles with $30\,\mu$m sides). The chambers have a depth of $5\,\mu$m. Right panel: corresponding unconfined actin networks. **B.** Bundle parameter versus actin concentration for chambers with cross-sections that are ***i*** square, ***ii*** triangular, and ***iii*** circular ($\sim$ 10-100 chambers per condition). Error bars represent standard deviation of the mean. Asterisks denote statistically significant differences (* = P$<$0.05, ** = P$<$ 0.001). Grey open circles (in panel i) represent average bundle parameters of bulk actin networks.

We sought to quantify the bundling transition by image analysis, but this turned

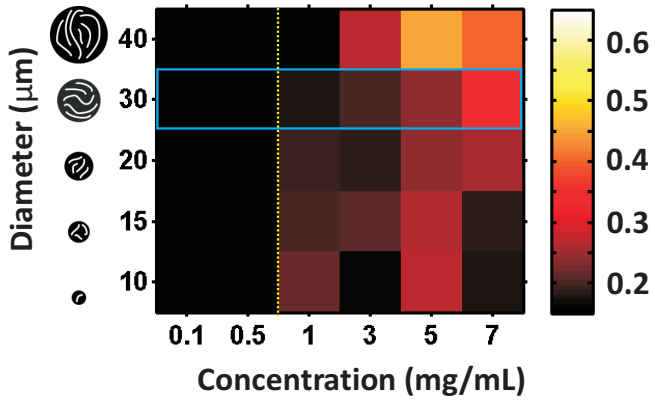

Figure 5.3: Color map representation of the average bundle parameter in circular chambers as a function of chamber diameter and actin concentration (see side bar for color coding). Solid blue line demarcates B-values corresponding to figure 2B iii, and vertical yellow dotted line divides the concentration axis into a homogenous (left) and bundled (right) regime.

out to be challenging. It was impossible to identify and track the contours of individual actin filaments in the confocal images due to the small mesh size of the networks (300 nm at 1 mg/mL) and thermal fluctuations of the actin filaments. Identification of bundles by image thresholding was also impossible due to the low contrast between areas of low and high actin density (the typical ratio between pixel intensities of bundles versus background was only 1.5). For this reason, we decided to quantify the degree of bundling in each image with a bundle parameter based on a weighted average of the coherency of all pixels, where the weight was based on a thresholded image to select areas of high fluorescence intensity. The coherency of a pixel is a dimensionless measure of the anisotropy of a small region around that pixel. The detailed image analysis procedure will be published elsewhere but is summarized in *section 5.2.8*. The bundle parameter can take values between 0, for networks that are homogeneous and isotropic, to 1, for bundles in a completely dark background. We obtained values ranging between 0.2, for homogeneous actin networks (reflecting density inhomogeneities and camera noise), and 0.7, for bundled actin networks (reflecting the non-zero intensity of the background).

All the dilute (0.1 and 0.5 mg/mL) actin networks, which looked homogeneous by visual inspection, had a low bundle parameter of about 0.2 (solid symbols in Figs. 5.2B i, ii, iii). Dense networks (1-7 mg/mL actin) had a significantly larger bundle parameter of 0.5-0.65, in chambers with a square or triangular cross-section (Fig. 5.2B i and ii, respectively). Dense networks in chambers with a circular cross-section also

showed a statistically significant, though smaller, increase of the bundle parameter, to $\sim$ 0.4-0.5 (Fig. 5.2B iii and Fig. 5.4). The lateral chamber size did not change the concentration-dependence of the bundle parameter, as exemplified in Fig. 5.3 for circular chambers ranging in diameter from 10 to 40 μm.

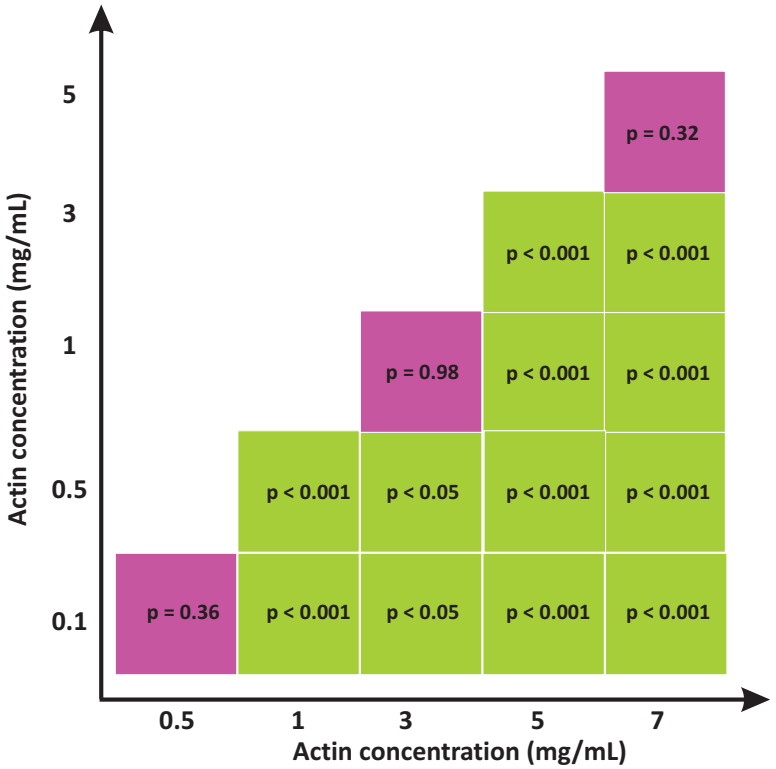

Figure 5.4: Statistical significance of differences between bundle parameters B of actin networks of different concentrations confined in circular chambers. Green boxes refer to pairs which are significantly different ($p<0.001$) and purple boxes refer to pairs which are not significantly different (p-value shown in box). Dilute samples of 0.5 mg/mL actin (which look homogeneous in confocal micrographs and have B-values around 0.2) are significantly different from dense actin samples (1-7 mg/mL) which show bundles and have B-values of 0.5-0.6. Student's t-tests were performed on ensemble averages of 8-81 chambers per experimental condition, averaging over circular chambers of all diameters.

For comparison, we also examined bulk, unconfined samples at the same actin concentrations. In contrast to the confined networks, these samples remained homogenous in density over the entire actin concentration range tested (Fig. 5.2A, right

panel). The bundle parameter of the bulk networks was low ($\sim$0.2) and independent of actin concentration (Fig. 5.2B i, grey open circles). This finding implies that the aligned, bundle-like actin structures observed in microchambers are indeed caused by spatial confinement.

Bulk actin networks are known to undergo an isotropic-to-nematic phase transition at a concentration that depends on filament length [32, 35, 36, 58]. In the fully labeled networks, we could not track individual actin filaments and their orientations. To circumvent this difficulty, we embedded tracer amounts of fluorescent filaments in an otherwise dark actin background, labeling 1 out of every 500 filaments. As shown in Fig. 5.5A, the tracer filaments are randomly oriented in bulk networks of 0.5-3 mg/mL actin, but they are aligned in bulk networks of 5-7 mg/mL. We quantified the degree of filament alignment by plotting histograms of the pixel orientations Fig 5.5B). The orientation angle for each pixel was determined from the local anisotropy of pixel intensities in a 5$\times$5 pixel region centered on that pixel. Below 5 mg/mL, the histograms show a broad distribution of angles, whereas at 5 and 7 mg/mL, the histograms develop a peak indicative of filament alignment. This indicates an isotropic to nematic transition at 5 mg/mL, consistent with prior experimental studies [32, 33, 34, 35, 36, 58] and with the Onsager prediction for hard rods with a length of $6\,\mu$m [28, 29, 31]. Interestingly, the confinement-induced alignment of actin filaments started at an actin concentration of 1 mg/mL which is substantially lower than the bulk phase transition point for liquid crystalline order.

The networks shown in figure 5.2A were confined in shallow chambers with depths of $5\,\mu$m. This depth is comparable to the average filament length, and 20% of the filaments even have a length that is larger than this depth. We therefore hypothesized that confinement-induced bundling in dense networks is caused by quasi-2D confinement, which tends to align the longest filaments in-plane. To test this hypothesis, we produced deeper chambers. Indeed, as soon as the chamber depth was increased from $5\,\mu$m to $10\,\mu$m or more, confinement-induced bundling disappeared, as illustrated by the confocal images in Fig. 5.6A of actin in pill-shaped chambers. The sudden disappearance of bundling was also reflected in significant downward jumps of the bundle parameter, from 0.3 to 0.2 for 1 mg/mL actin, and from 0.5 to 0.2 for 5 mg/mL actin (white and dark gray circles in Fig. 5.6B, respectively). When the chamber depth was further increased, there was a small, though statistically significant, further decrease of the bundle parameter (Fig. 5.7).At 3 mg/mL actin, the bundle parameter started to decrease when the chamber depth was increased from 10 to $20\,\mu$m (light gray circles in Fig. 5.6B). The loss of bundles with increased chamber depth occurred irrespective of the lateral dimensions of the chambers and the in-plane aspect ratio (Fig. 5.8). These findings suggest that confinement requires one of the chamber dimensions to be comparable to the mean filament length. Un-

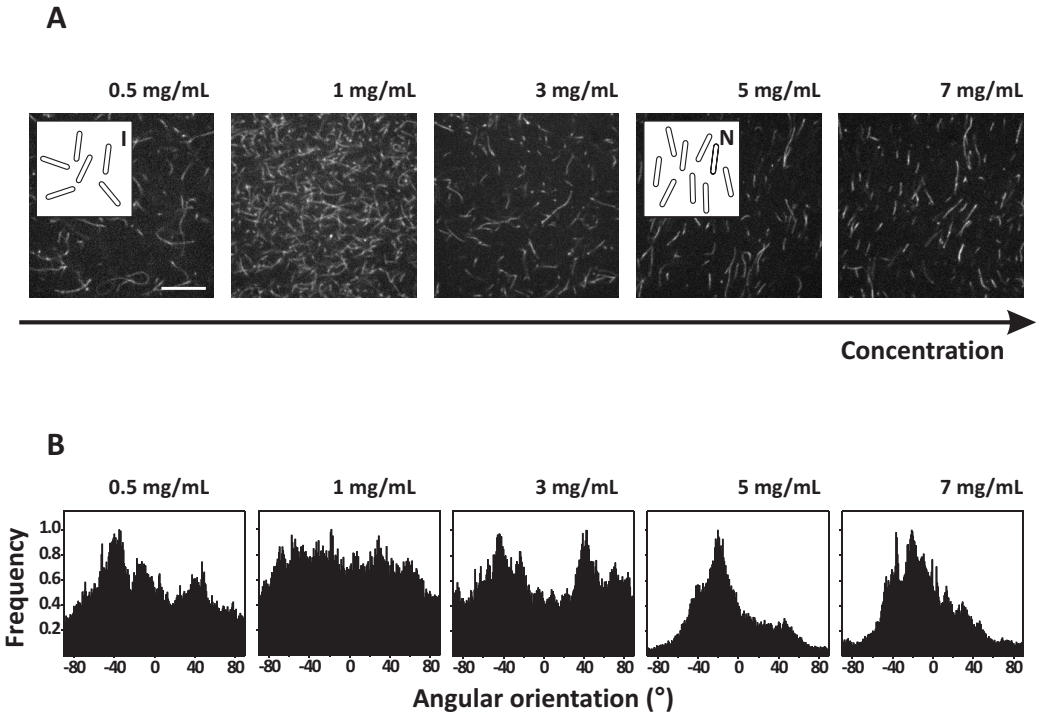

Figure 5.5: Fluorescent actin filaments embedded in a dark F-actin network display orientational alignment above a threshold concentration of 5 mg/mL. **A.** Fluorescent confocal micrographs of tracer actin filaments labeled with 30 mol% Alexa488-G-actin and stabilized with 1:1 phalloidin, embedded in unlabeled networks of 0.5-7 mg/mL F-actin. There is 1 fluorescent filament per 500 nonfluorescent filaments. Scale bar is $10\,\mu\mathrm{m}$. Insets show schematics of an isotropic distribution of rod-like particles (I) and nematically ordered (N) rods. **B.** Histograms of the orientation angles of image pixels corresponding to the images in A.

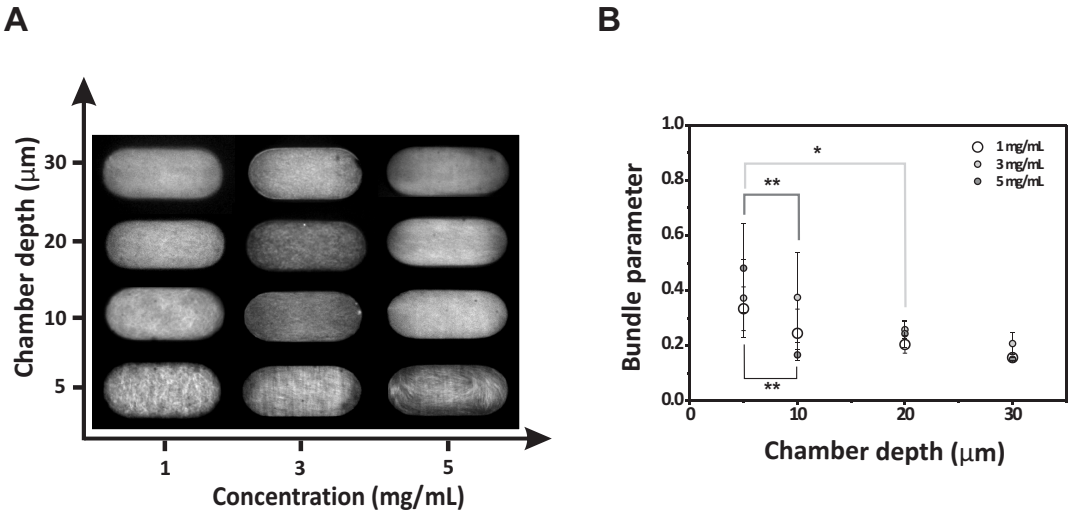

Figure 5.6: Filament alignment and bundling in confined actin networks disappear when the depth of the microfabricated chambers is increased. **A.** Confocal micrographs of fluorescently labeled F-actin networks at different actin concentrations in pill-shaped chambers of varying depth. The lateral dimensions are fixed to a minor diameter of $20\,\mu\mathrm{m}$ and major diameter of $40\,\mu\mathrm{m}$. Filament bundling occurs only in $5\,\mu\mathrm{m}$-deep chambers, a depth similar to the average filament length. **B.** Bundle parameter versus chamber depth for pill-shaped chambers, averaged over chambers with aspect ratios between 1:1 and 1:4 (fixed major diameter of $40\,\mu\mathrm{m}$). Data are shown for actin concentrations of 1 mg/mL (white circles), 3 mg/mL (light gray circles) and 5 mg/mL (dark gray circles). Error bars represent S.D. of the mean. Asterisks denote statistically significant differences (* = $P<0.05$, ** = $P< 0.001$.

der these conditions, a substantial fraction of the filaments is confined to a quasi-2D microenvironment, since they cannot rotate out-of-plane.

As an independent test of the relation between confinement and filament length, we examined whether we could relieve confinement by decreasing the filament length while keeping a constant chamber depth of $5\,\mu\mathrm{m}$. To control filament length we polymerized actin in the presence of the capping protein gelsolin, which caps filaments at the barbed (fast-growing) ends [59]. The mean filament length L decreases with increasing gelsolin:actin molar ratio, R_{GA}, as $L = (1/370R_{GA})$ [59]. Remarkably, addition of 1:740 or 1:370 gelsolin to actin networks of 3 and 5 mg/mL caused the formation of distinct bundles which appeared thicker than in networks made in the absence of gelsolin (Fig. 5.9 A), even though the average filament length was less than the chamber depth (2 and $1\,\mu\mathrm{m}$, respectively). The ratio of pixel intensities between bundles and background was 2-3, which was higher than in networks without gelsolin (where the ratio was $\sim$1.5). When the gelsolin level was further increased to 1:185, corresponding to a mean filament length of $0.5\,\mu\mathrm{m}$ (10-fold less than the chamber depth), the networks did become homogeneous (Fig. 5.9A). In contrast, control bulk networks remained homogenous irrespective of actin concentration and gelsolin:actin ratio (Fig. 5.9B). The bundle parameter confirmed the trends seen by visual inspection, increasing from $\sim$0.4 to $\sim$0.6 upon addition of 1:740 gelsolin, and going back down to $\sim$0.4 with 1:185 gelsolin, both at 3 mg/mL and 5 mg/mL actin (Fig. 5.9C).

The bundle parameter confirmed the trends seen by visual inspection, increasing from $\sim$0.4 to $\sim$0.6 upon addition of 1:740 gelsolin, and going back down to $\sim$0.4 with 1:185 gelsolin, both at 3 mg/mL and 5 mg/mL actin (Fig. 5.10B). The increased bundle parameter of networks with 1:740 or 1:370 gelsolin compared to networks without gelsolin was statistically significant at both 3 and 5 mg/mL actin, but the decreased bundle parameter at 1:185 gelsolin was only significant at 5 mg/mL (Fig. 5.9B). The gelsolin-dependent bundling was independent of the lateral dimensions and in-plane anisometry of pill-shaped chambers, though the gelsolin concentration where the bundle parameter reached a maximum was either 1:370 or 1:740 depending on actin concentration and chamber anisometry (Fig. 5.11).

The orientation of the actin bundles is expected to reflect a competition between alignment effects near the walls and packing constraints in the center. We tested whether we could influence the direction of bundle alignment by elongating the chambers in one direction. We compared actin networks of 3 mg/mL in the presence of 1:740 gelsolin confined in shallow, pill-shaped chambers with length over width ratios going from 1 (circular) to 3:1. Figure 5.12 (left panel) shows histograms of the orientation angles of pixel anisotropies calculated for the images shown on the right. The distribution of orientation angles shifts from being wide and multipeaked

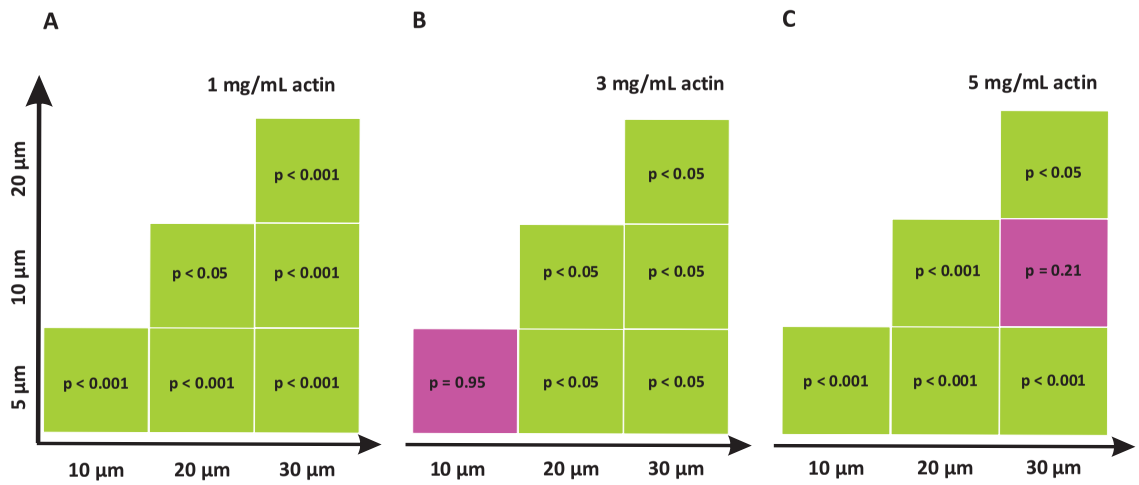

Figure 5.7: Statistical significance of differences between bundle parameters B of actin networks with concentrations of **A.** 1 , **B.** 3 or **C.** 5 mg/mL in shallow chambers ($5\,\mu$m depth) compared to deeper chambers (10-30 μm depth). Green boxes refer to pairs which are significantly different ($p<0.05$ or $p<0.001$) and purple boxes refer to pairs which are not significantly different (p-value shown in box). B in shallow chambers is significantly higher than in deep chambers, except for 3 mg/mL actin in $10\,\mu$m deep chambers. Student's t-tests were performed on ensemble averages of 3-273 chambers per experimental condition, averaging over pill-shaped chambers of varying aspect ratio (1:1 - 4:1) and minor dimension (10-40 μm).

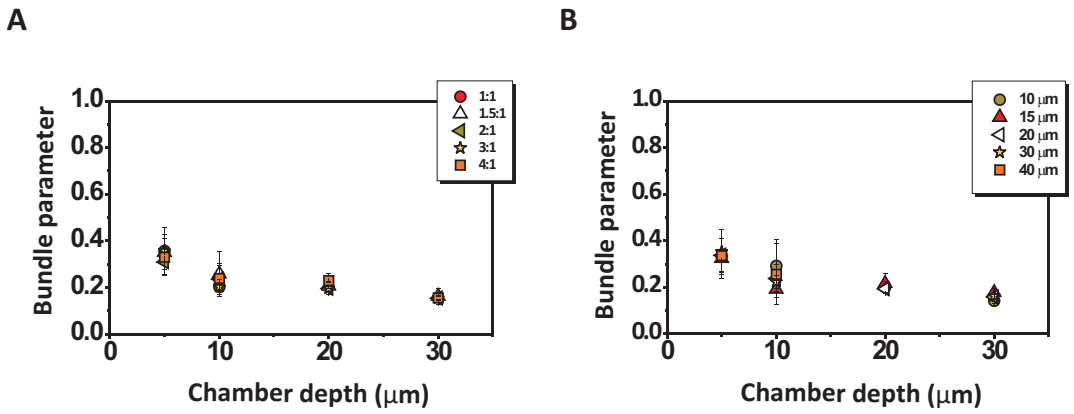

Figure 5.8: Increasing depth of microchambers leads to loss of bundling in confined actin networks (1 mg/mL), irrespective of chamber shape or size. **A.** Bundle parameter for confined actin networks in pill-shaped chambers of increasing depth, for different in-plane aspect ratios as indicated in the legend. **B.** Bundle parameter for confined actin networks in circular chambers of increasing depth, for different chamber diameters as indicated in the legend. Error bars represent standard deviations of the mean.

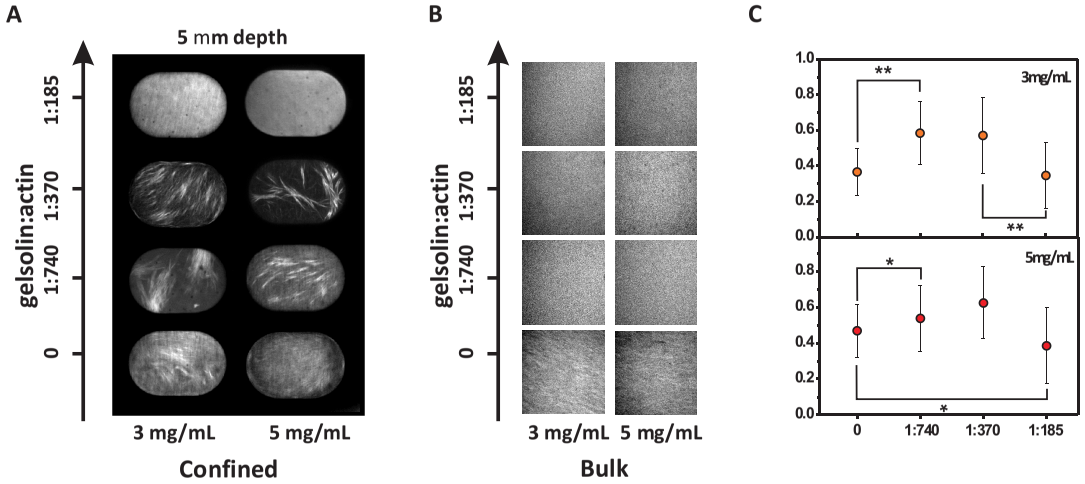

Figure 5.9: Reducing the average filament length with the capping- and severing protein gelsolin enhances filament bundling up to a 1:370 gelsolin:actin ratio, while it homogenizes networks at a 1:185 ratio. **A.** Confocal micrographs of F-actin networks in pill-shaped chambers (minor diameter $30\,\mu\mathrm{m}$ and major diameter $30\,\mu\mathrm{m}$) at four different gelsolin:actin ratios, corresponding to estimated average lengths of 6, 2, 1 and $0.5\,\mu\mathrm{m}$, for two different actin concentrations. **B.** Control networks remain homogenous at all gelsolin:actin ratios. Confocal micrographs of bulk F-actin networks with estimated average filament lengths of 6, 2, 1 and $0.5\,\mu\mathrm{m}$, for two different actin concentrations. Scale bar is $5\,\mu\mathrm{m}$. **C.** Bundle parameter versus gelsolin:actin molar ratio in pill-shaped chambers, averaged over chambers with aspect ratios from 1:1 to 1:4 (fixed major diameter of $40\,\mu\mathrm{m}$). Data are shown for actin concentrations of ***i*** 3 mg/mL and ***ii*** 5 mg/mL. Error bars represent standard deviation of the mean. Asterisks represent statistically significant differences (* = P$<$0.05, ** = P$<$0.001).

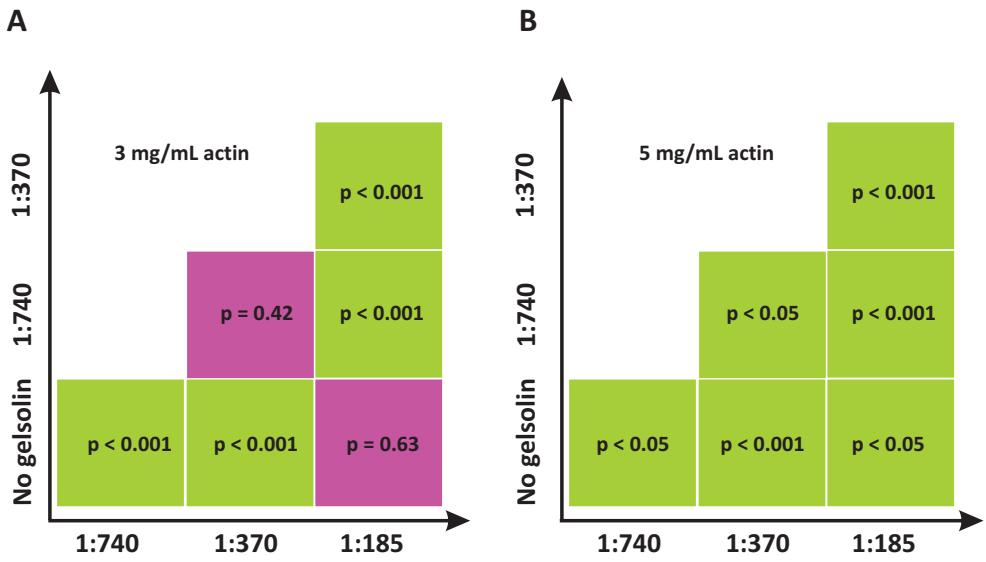

Figure 5.10: Statistical significance of differences between bundle parameters B of actin networks in shallow chambers ($5\,\mu$m depth) in the presence of different concentrations of gelsolin. Data are shown for 3 mg/mL actin (left) and 5 mg/mL actin (right). Nearly all pairs show significant differences (green boxes, $p<0.05$ or $p<0.001$). This implies that adding gelsolin to an actin network causes a statistically significant increase of B up to a 1:370 gelsolin:actin ratio, while causing a decrease of B when added in a 1:185 gelsolin:actin ratio. Student's t-tests were performed on ensemble averages of 38-264 chambers per experimental condition, averaging over pill-shaped chambers of varying aspect ratio (1:1-4:1) and minor dimension (10-40 μm).

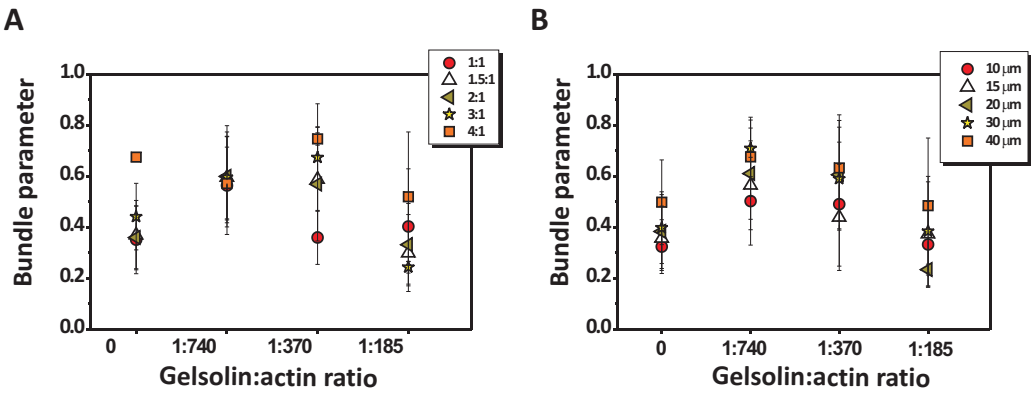

Figure 5.11: Increasing the gelsolin/actin molar ratio from zero to 1:185 for networks of 3 mg/mL actin causes an increase and then a decrease in bundling, irrespective of chamber shape or size. **A.** Bundle parameter for confined actin networks in pill-shaped chambers of different in-plane aspect ratios as indicated in the legend. **B.** Bundle parameter for confined actin networks in circular chambers of different diameters as indicated in the legend. Error bars represent standard deviation of the mean.

at chamber aspect ratios of 1 and 1.5:1 to a more narrow distribution peaking close to an angle of zero degrees with the long axis for aspect ratios of 2 and 3. This indicates progressive alignment of the bundles along the long axis of the chambers, which can also be seen when an orientation color map is overlayed on the original fluorescence micrographs (Fig. 5.12, right panel). This alignment with the long axis is reminiscent of patterns reported for microtubules in rectangular microchambers [18].

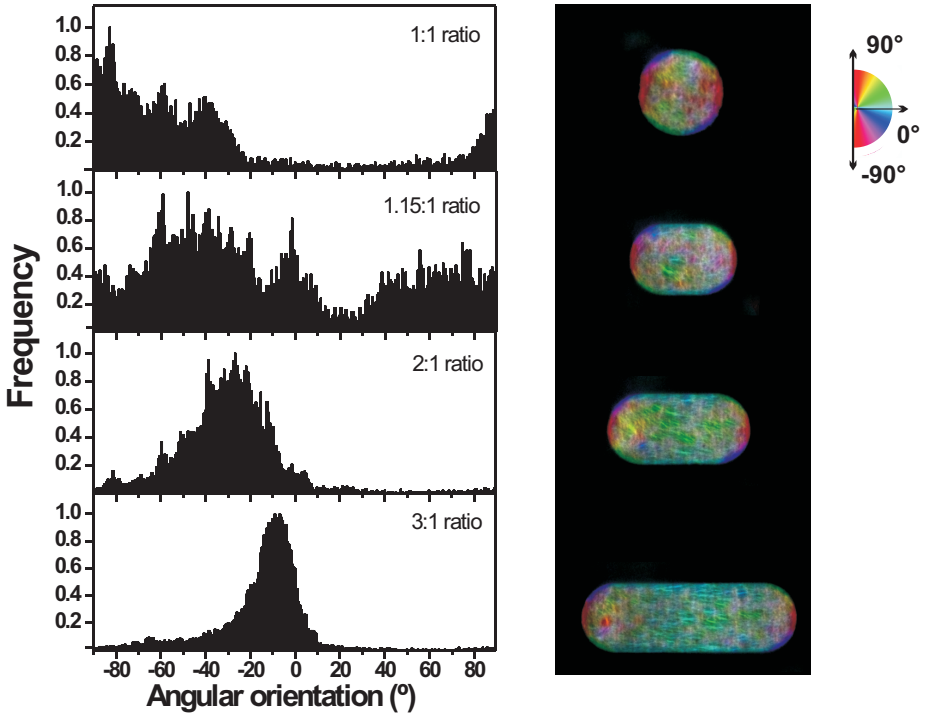

Figure 5.12: Actin bundle-like structures reorient along the long axis of pill-shaped chambers when the chambers become more anisotropic. *Left panel.* Histograms of pixel orientation angles for different chamber aspect ratios for networks of 7 mg/mL actin; the minor axis of all chambers is $20\,\mu\mathrm{m}$. The histograms were calculated for the (single) images shown on the right. *Right panel.* Color map of the orientation angles superposed on raw fluorescence intensity data. The semicircle color scale represents orientation angles in degrees.

For semiflexible polymers, confinement not only influences the configurational entropy, but also the elastic energy associated with polymer bending. Theoretical models predict that long polymers will accumulate at the confining boundary to minimize their curvature and the associated energy cost [60, 61]. This prediction

was confirmed for actin networks in spherical geometries (liposomes and emulsions droplets) [14, 15] and for microtubules in emulsion droplets [19] and rectangular chambers [13]. Confocal images of confined actin networks in microchambers did not indicate preferential accumulation of actin at the periphery (see for example Fig. 5.2A and Fig. 5.9A). To quantify the dependence of actin density on radial distance from the chamber center, we calculated the radially averaged pixel intensity (normalized by perimeter) as a function of radial distance from the chamber edge to the center. We focused on 3 mg/mL actin networks in pill-shaped chambers of various sizes (minor axis 10-$40\,\mu$m) and aspect ratios (1:1 to 1:4). In the absence of gelsolin, the radially averaged pixel intensity normalized by the median intensity remained constant and close to 1 from edge till center (Fig. 5.13A, 264 chambers were analyzed; each trace represents one chamber), corresponding with the visual observation that the confocal images showed no clear radial dependence (darker trace and inset of Fig. 5.13A). The apparent drop in intensity at the edge originates from the abrupt transition from the bright chamber edge to the dark exterior. In the presence of gelsolin, there was similarly no evidence of actin accumulation at the chamber edge (Fig. 5.13B). Out of a total of 126 chambers, we observed only one chamber with edge accumulation (darker trace and inset 5.13B). These results demonstrate that there is no preferential accumulation of actin at the periphery.

5.4 Discussion

By fluorescence imaging of actin networks in microchambers, we discovered that cell-sized confinement can induce spontaneous formation of dense bundle-like structures. This filament bundling required actin concentrations of at least 1 mg/mL, implying a collective phenomenon dependent on filament-filament interactions. The onset concentration for confinement-induced bundling is substantially lower than the I-N phase transition of corresponding unconfined actin solutions, which occurred at 5 mg/mL. The in-plane dimensions (over a range of 10 to $200\,\mu$m) and shape of the chambers had no influence on the extent of filament bundling nor on its dependence on actin concentration. However, the geometry of the confining boundaries did affect the orientation of the actin bundles. Bundles had a tendency to orient mainly along the diagonal in the center of the chambers and along the walls in the periphery. In pill-shaped chambers with a length/width ratio above 2, bundles oriented along the long axis.

While the lateral dimensions had no influence on filament bundling, the vertical depth of the chambers was a crucial factor. Filament bundling required shallow chambers with a depth of $5\,\mu$m, similar to the average filament length. Chambers with depths of $10\,\mu$m or more did not induce filament bundling (at least not for

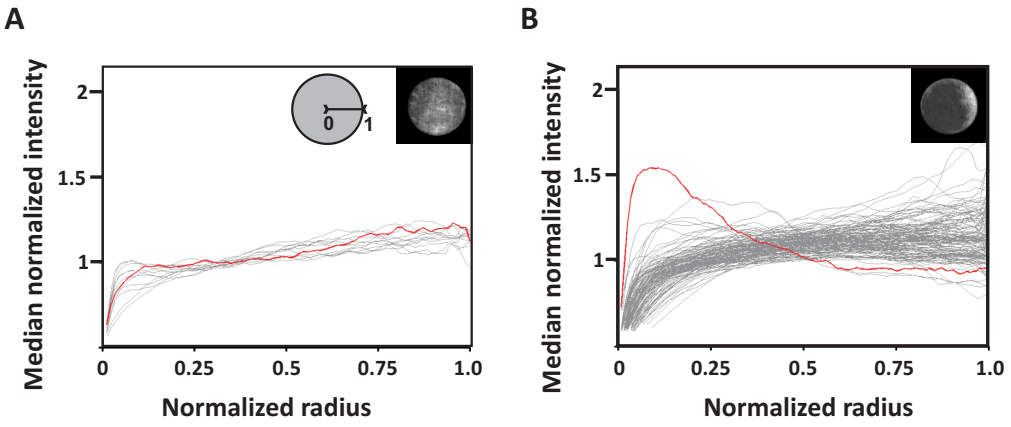

Figure 5.13: There is no peripheral accumulation of actin in circular chambers. The radially averaged fluorescence intensity normalized by the median intensity and by perimeter length is shown as a function of radial distance from the chamber center. The distance is normalized by chamber radius, so a value of 1 corresponds to the edge and 0 corresponds to the center. Each gray trace represents one individual chamber. **A.** For N=264 chambers containing 3 mg/mL actin there is no obvious actin accumulation at the chamber edge. The intensity dip corresponds to the abrupt passage from the inside of a bright chamber to the dark background with zero intensity outside. Dark trace corresponds to example chamber in inset. **B.** For N=126 chambers containing 3 mg/mL actin and gelsolin (1:740 gelsolin:actin) there is also no obvious actin accumulation at the chamber edge, except for one example (red trace and inset).

the actin concentrations explored of up to 5 mg/mL). This observation suggests that physically-induced actin bundling requires quasi-2D confinement. The actin filaments have a highly polydisperse length distribution, ranging from below $1\,\mu\mathrm{m}$ to $18\,\mu\mathrm{m}$. A sizeable fraction (20%) of the filaments is longer than 5 $1\,\mu\mathrm{m}$ and therefore forced to remain in-plane in the shallow chambers. Increasing the chamber depth relieves this in-plane confinement (sketched in Fig. 5.14A).

Theory and simulations predict that confinement of rods between parallel surfaces encourages rod alignment [61, 62], and indeed such alignment was shown for microtubules in thin planar slits [61]. However, for polymers interacting by steric interactions only, we would at first glance not expect any density inhomogeneities or bundling. However, the actin filaments have a highly polydisperse length distribution, and 80% of the filaments are shorter than the chamber depth and can freely rotate out-of-plane. It is conceivable that these short filaments cause an attractive interaction between the long filaments purely due to steric interactions. Such an entropic depletion effect is well-established for bidisperse suspensions of short and long rods [63, 64, 65]. When two long rods aligned in parallel come closer than a distance equal to the width of a short rod, the short rods are excluded from the overlap zone (sketched in Fig. 5.14B). This results in a higher osmotic pressure outside the long rods than in between them, driving them together. The short actin filaments may therefore promote bundling of the longer filaments. Intriguingly, recent experiments on systems of vibrofluidized rigid rods in the presence of spheres, mimicking depletion agents, have shown that this type of bundling can indeed occur, an effect also corroborated by equilibrium Monte Carlo simulations [66]. Although the system studied there is purely 2D, and only bidisperse, with rod aspect ratios far smaller than in the actin system, those findings show that depletion effects can be expected to have a major impact on the spatial organization of rod systems in a quasi 2D geometry.

The presence of a depletion effect may explain the counterintuitive observation that filaments shortened with gelsolin showed more pronounced bundling than unshortened filaments. Shortening should relieve in-plane confinement of the filaments, but the length distribution is still polydisperse so there may still be depletion-induced bundling. Furthermore, there can be a feedback effect since bundles formed in the absence of proteins that regulate bundle length tend to be longer than individual filaments and therefore do experience z-confinement. Bundling may also occur more readily at shorter overall filament length, because kinetic constraints on filament motion originating from chain entanglements are reduced [32]. Reducing the average length to $0.5\,\mu\mathrm{m}$ (1:185 gelsolin) did lead to bundle disappearance, as expected since the average length was tenfold less than the chamber depth.

We could not find any evidence for peripheral accumulation of actin in the mi-

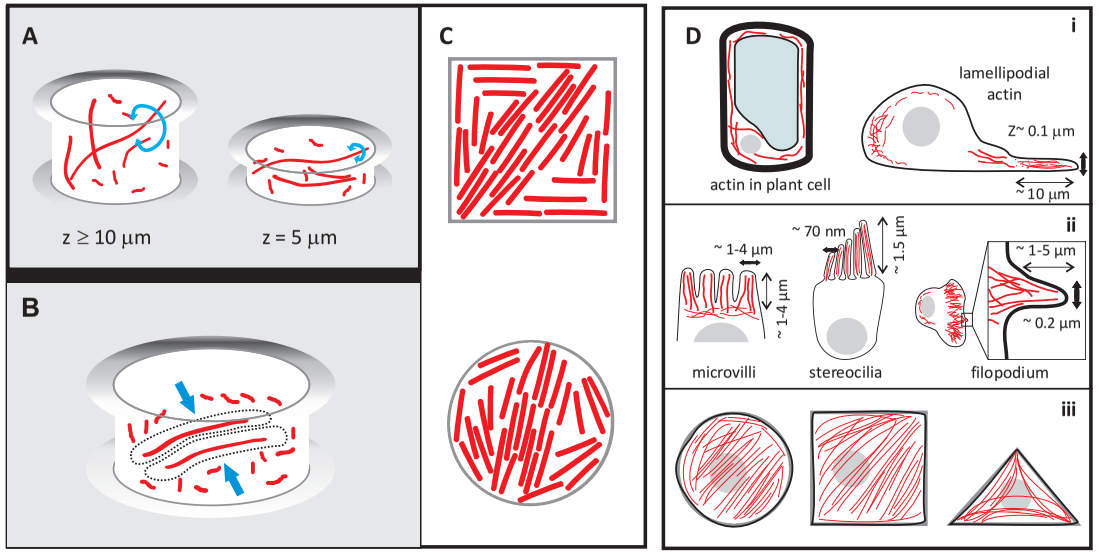

Figure 5.14: Possible mechanisms for spontaneous filament alignment and bundling in confined actin networks, and possible implications for the *in vivo* cytoskeleton. **A.** Chambers with a depth that exceeds the length of the filaments do not impose confinement, because the filaments can freely rotate and explore all three dimensions (aside from chain entanglements). Shallow chambers with a depth less than the average filament length provide quasi-2D confinement, since a large fraction of the filaments cannot freely rotate and is therefore effectively confined in-plane. **B.** A polydisperse length distribution may cause filament bundling due to an entropic depletion effect, where short filaments generate an attractive depletion interaction between the longer ones (blue arrows). **C.** The organization of hard rod liquid crystals in quasi-2D confinement is determined by a competition between rod alignment along the walls and rod nematization in the chamber center. For rods in square or circular wells this competition creates topological defects at opposite poles. **D.** Examples of *in vivo* situations where actin filaments are confined. ***i*** Quasi-2D environment of actin networks in the thin cytoplasmic region between the cell wall and vacuole of plant cells and in the thin lamellipodium of migrating animal cells. ***ii*** Quasi-1D confinement of actin filaments in membrane protrusions. ***iii*** Quasi-2D confinement *in vivo* can be artificially generated by spatially confining cells to micropatterned adhesive islands of defined geometry.

crofabricated chambers, in contrast to prior studies of actin networks in liposomes or emulsion drops which formed thin cortical shells [14, 15]. Similar observations of peripheral accumulation exist for microtubules in emulsion drops and microchambers [13, 19] and for DNA in viral capsids [47]. Semiflexible polymers can remain homogeneously distributed inside a sphere volume when short, but long filaments are forced to bend. The energy cost associated with this bending is minimized when the filaments accumulate at the sphere surface [13]. It is possible that the actin filaments studied here were too short for the bending enthalpy to be relevant. It is also possible that excluded volume interactions between filaments present at the high densities studied here introduce energy terms that compete with the single-polymer effect of bending enthalpy. Bending enthalpy may still play a role in controlling the alignment of actin bundles. Alignment of peripheral bundles along the walls and alignment of central bundles along the long axis in elongated chambers is certainly consistent with a minimization of the bending energy.

The actin patterns in the microfabricated chambers are strikingly similar to patterns recently observed for vibrofluidized granular rods confined in flat chambers with circular or square cross-sections [42, 43]. Similar to the actin filament bundles in microchambers with circular and square cross-sections (Fig. 5.2A), granular rods close to the walls aligned parallel with the wall, while rods in the center aligned with each other, straight across the chamber. Competition between alignment of rods in the bulk and near the boundaries produced patterns with topological defects (sketched in Fig. 5.14C). These patterns were interpreted in terms of a continuum theory for liquid crystals accounting for wall-anchoring and elastic distortions of the bulk nematic phase [67, 68]. The similarity of the granular rod structures to the actin structures and the dominance of excluded volume interactions in both systems suggest that a similar liquid crystal theory may perhaps be formulated for the confined actin system. However, it is presently unclear how to account for microscopic properties such as the finite size of the filaments, the polydisperse length distribution which introduces depletion effects, and the flexibility of the filaments, which introduces bending enthalpy contributions.

We showed that nonadhesive hard-wall boundaries can cause the formation of bundle-like actin structures whose alignment depends on the shape and anisometry of the confinement. Intracellular organization of actin often occurs in highly confined compartments. Animal cells migrating on rigid adhesive surfaces for instance extend a flat lamellipodium which is nearly 2D with a thickness of only $\sim 0.1 - 0.2\,\mu\mathrm{m}$ [9, 10, 11] (sketched in Fig. 5.14D i). Plant cells have a very thin cytoplasmic layer of only $\sim 1\,\mu\mathrm{m}$ containing actin filaments with a definite orientation which facilitates cytoplasmic streaming [69]. Animal cells also extend different types of finger-like membrane protrusions filled with actin such as filopodia and stereocilia, which

have a thickness of less than 100 nm [12, 70] (sketched in Fig. 5.14D ii). However, contrary to filaments in microfabricated chambers, F-actin is not only confined passively. In addition to the effect of cellular boundaries there are the effects of a variety of actin-binding proteins that facilitate the formation of dendritic networks in the lamellipodium and rigid bundles that deform the plasma membrane [71]. Bundles of actin filaments and myosin motors known as stress fibers actively create contractile tension, which promotes spreading of cells on rigid adhesive substrates into flat, quasi-2D shapes. Nevertheless, it is possible that the confined geometries created by actin filaments feeds back on the organization of the actin filaments. For instance, spontaneous alignment and densification of actin filaments induced by confinement in tube-like membrane protrusions may promote F-actin bundling by actin-binding proteins [72]. Indeed, some actin-binding proteins have been shown to form bundles of actin filaments only when these filaments are aligned nearly parallel [73]. However, confinement effects by themselves cannot explain the unipolar direction of actin filaments in many *in vivo* bundles, which likely requires regulated nucleation of actin filament growth and a polarity preference of certain actin-bundling proteins [73, 74].

A natural follow-up to our work would be to functionalize the walls of the microchambers with proteins that couple actin filaments to the cell boundaries or which nucleate actin filament growth [2]. There is already evidence from studies with flat substrates patterned with islands of actin-nucleating proteins of varying geometries, that spatial patterning of actin nucleation has profound effects on actin self-organization [75]. It would also be very interesting to encapsulate contractile actin-myosin cables into microfabricated chambers with adhesive walls, since this could help to mimic the effect of cell shape on the organization of actin stress fibers seen in cells cultured on μm-sized extracellular matrix islands of defined geometry created using microfabrication techniques [55, 56, 57] (sketched in Fig. 5.14D iii).

5.5 Conclusion

In this chapter we studied the effect of spatial confinement on self-organization of actin by polymerizing actin inside cell-sized microchambers made by photolithography. We found that confinement induces spontaneous formation of bundle-like structures. We showed that this spontaneous alignment only occurs above a threshold actin concentration of 1 mg/mL, indicating a collective phenomenon that relies on excluded volume interactions between the filaments. Furthermore, alignment occurred only in shallow chambers, implying that quasi-2D confinement is important. The lateral dimensions of the chambers did not influence the ordering transition. The shape of the chambers influenced the orientation of the bundles. Bundles in circular and square chambers aligned along the wall and along the chamber

diagonal. Bundles in pill-shaped chambers with length/width ratios of 2 or more predominantly oriented along the long axis. We propose that confinement-induced actin bundling is driven by steric repulsions of the filaments with each other and the walls. The quasi-2D confinement aligns the longest actin filaments in-plane, and the shortest actin filaments may push the longer ones into dense bundles by an entropic depletion effect. Minimization of the bending energy of the semiflexible filaments may contribute to the alignment of bundles along the chamber periphery and diagonal/long axis. This physical mechanism may influence intracellular organization of actin in conjunction with biochemical regulation and actin/membrane adhesion.

5.6 Acknowledgements

We thank Chris Rétif and Gijs Vollenbroek for help with microfabrication, and Roland Dries, Ioana Garlea, and Daniel Sage (EPFL) for helpful discussions.

References

[1] C. Revenu, R. Athman, S. Robine, and D. Louvard. The co-workers of actin filaments: from cell structures to signals. *Nat. Rev. Mol. Cell Biol.*, 5(8):635–646, 2004.

[2] M. Sheetz, J. Sable, and H. Döbereiner. Continuous membrane-cytoskeleton adhesion requires continuous accommodation to lipid and cytoskeleton dynamics. *Annu. Rev. of Biophys. Biomol. Struct.*, 35(1):417–434, 2006.

[3] F. Julicher, A. Adjari, and J. Prost. Modeling molecular motors. *Rev. Mod. Phys.*, 69(4):1269–1282, 1997.

[4] B. Alberts, A. Johnson, J. Lewis, M. Raff, K. Roberts, and P. Walter. *Molecular Biology of the Cell.* Garland Science, New York, 5th edition, 2008.

[5] B. Gunning and M. Steer. *Plant Cell Biology, Structure and Function.* Jones & Bartlett Learning, Boston, 1st edition, 1996.

[6] M. Tanaka, F. Rehfeldt, M. Schneider, G. Mathe, A. Albersdörfer, K. Neumaier, O. Purrucker, and E. Sackmann. Wetting and dewetting of extracellular matrix and glycocalix models. *J. Cond. Mat.*, 17(9), 2005.

[7] N. Nijenhuis, D. Mizuno, J. Spaan, and C. Schmidt. Viscoelastic response of a model endothelial glycocalyx. *Phys. Biol.*, 6(2):025014–22, 2009.

[8] R. Fernandez-Gonzalez, S. Simoes, J. Röper, S. Eaton, and J. Zallen. Myosin II dynamics are regulated by tension in intercalating cells. *Dev. Cell*, 17(5):736–743, 2009.

[9] J. Small, M. Herzog, and K. Anderson. Actin filament organization in the fish keratocyte lamellipodium. *J. Cell Biol.*, 129(5):1275 –1286, 1995.

[10] A. Verkhovsky, O. Chaga, S. Schaub, T. Svitkina, J. Meister, and G. Borisy. Orientational order of the lamellipodial actin network as demonstrated in living motile cells. *Molecular Biology of the Cell*, 14(11):4667–4675, 2003.

[11] E. Urban, S. Jacob, M. Nemethova, G. Resch, and J. Small. Electron tomography reveals unbranched networks of actin filaments in lamellipodia. *Nat. Cell Biol.*, 12(5):429–435, 2010.

[12] E. Chhabra and H. Higgs. The many faces of actin: matching assembly factors with cellular structures. *Nat. Cell. Biol.*, 9(10):1110–1121, 2007.

[13] M. Lagomarsino, C. Tanase, J. Vos, A. Emons, B. Mulder, and M. Dogterom. Microtubule organization in three-dimensional confined geometries: evaluating the role of elasticity through a combined *In Vitro* and modeling approach. *Biophys. J.*, 92(3):1046–1057, 2007.

[14] M. Claessens, R. Tharmann, K. Kroy, and A. Bausch. Microstructure and viscoelasticity of confined semiflexible polymer networks. *Nat. Phys.*, 2(3):186–189, 2006.

[15] L. Limozin, M. Bärmann, and E. Sackmann. On the organization of self-assembled actin networks in giant vesicles. *Eur. Phys. J. E*, 10(4):319–330, 2003.

[16] M. Elbaum, D. Fygenson, and A. Libchaber. Buckling microtubules in vesicles. *Phys. Rev. Lett.*, 76:4078–4081, 1996.

[17] V. Emsellem, O Cardoso, and P. Tabeling. Vesicle deformation by microtubules: A phase diagram. *Phys. Rev. E*, 58:4807–4810, 1998.

[18] S. Cortes, N. Glade, I. Chartier, and J. Tabony. Microtubule self-organisation by reaction-diffusion processes in miniature cell-sized containers and phospholipid vesicles. *Biophys. Chem.*, 120(3):168–177, 2006.

[19] M. Pinot, F. Chesnel, J. Kubiak, I. Arnal, F. Nédélec, and Z. Gueroui. Effects of confinement on the self-Organization of microtubules and motors. *Curr. Biol.*, 19(11):954–960, 2009.

[20] F Gittes, B Mickey, J Nettleton, and J Howard. Flexural rigidity of microtubules and actin filaments measured from thermal fluctuations in shape. *J. Cell Biol.*, 120(4):923 –934, 1993.

[21] H. Isambert, P. Venier, A. Maggs, A. Fattoum, R. Kassab, D. Pantaloni, and M. Carlier. Flexibility of actin filaments derived from thermal fluctuations. effect of bound nucleotide, phalloidin, and muscle regulatory proteins. *J. Biol. Chem.*, 270(19):11437 –11444, 1995.

[22] M. Honda, K. Takiguchi, S. Ishikawa, and H. Hotani. Morphogenesis of liposomes encapsulating actin depends on the type of actin-crosslinking. *J. Mol. Biol.*, 287(2):293–300, 1999.

[23] S. Köster, D. Steinhauser, and T. Pfhol. Brownian motion of actin filaments in confining microchannels. *J. Cond. Mat.*, 17(49):S4091, 2005.

[24] M. Choi, C. Santangelo, O. Pelletier, J. Kim, S. Kwon, Z. Wen, Y. Li, C. Pincus, P.and Safinya, and M. Kim. Direct observation of biaxial confinement of a semiflexible filament in a channel. *Macromolecules*, 38(23):9882–9884, 2005.

[25] L. Hirst, Z. Parker, E.and Abu-Samah, Y. Li, R. Pynn, N. MacDonald, and C. Safinya. Microchannel systems in titanium and silicon for structural and mechanical studies of aligned protein self-assemblies. *Langmuir*, 21(9):3910–3914, 2005.

[26] J. Tegenfeldt, C. Prinz, H. Cao, S. Chou, W. Reisner, R. Riehn, Y. Wang, E. Cox, J. Sturm, P. Silberzan, and R. Austin. The dynamics of genomic-length DNA molecules in 100-nm channels. *Proc. Natl. Acad. Sci. PNAS*, 101(30):10979 – 10983, 2004.

[27] D. Bonthuis, C. Meyer, and C. Dekker. Conformation and dynamics of DNA confined in slit-like nanofluidic channels. *Phys. Rev. Lett.*, 101(10):108303–4, 2008.

[28] L. Onsager. The effects of shape on the interaction of colloidal particles. *Ann. N. Y. Acad. Sci.*, 51(4):627–659, 1949.

[29] A. Khokhlov and A. Semenov. Liquid-crystalline ordering in the solution of partially flexible macromolecules. *Physica A: Statistical and Theoretical Physics*, 112(3):605–614, 1982.

[30] Z. Chen. Nematic ordering in semiflexible polymer chains. *Macromolecules*, 26(13):3419–3423, 1993.

[31] Theo Odijk. Theory of lyotropic polymer liquid crystals. *Macromolecules*, 19(9):2313–2329, 1986.

[32] J. Käs, H. Strey, J.X. Tang, D. Finger, R. Ezzell, E. Sackmann, and P.A. Janmey. F-actin, a model polymer for semiflexible chains in dilute, semidilute, and liquid crystalline solutions. *Biophys. J.*, 70(2):609–625, 1996.

[33] E. Helfer, P. Panine, M. Carlier, and P. Davidson. The interplay between viscoelastic and thermodynamic properties determines the birefringence of F-Actin gels. *Biophys. J.*, 89(1):543–553, 2005.

[34] A. Suzuki, T. Maeda, and T. Ito. Formation of liquid crystalline phase of actin filament solutions and its dependence on filament length as studied by optical birefringence. *Biophys. J.*, 59(1):25–30, 1991.

[35] R. Furukawa, R. Kundra, and M. Fechheimer. Formation of liquid crystals from actin filaments. *Biochemistry*, 32(46):12346–12352, 1993.

[36] C. Coppin and P. Leavis. Quantitation of liquid-crystalline ordering in f-actin solutions. *Biophys. J.*, 63(3):794–807, 1992.

[37] J. Podolski and L. Steck. Length distribution of f-actin in *Dictyostelium discoideum*. *J. Biol. Chem.*, 265(3):1312–8, 1990.

[38] TM Svitkina, AB Verkhovsky, KM McQuade, and GG Borisy. Analysis of the actin-myosin II system in fish epidermal keratocytes: mechanism of cell body translocation. *J. Cell Biol.*, 139(2):397–415, 1997.

[39] C. Thomas, S. Tholl, D. Moes, M. Dieterle, J. Papuga, F. Moreau, and A. Steinmetz. Actin bundling in plants. *Cell Motil. Cytoskel.*, 66(11):940–957, 2009.

[40] Y. Puius, N. Mahoney, and S. Almo. The modular structure of actin-regulatory proteins. *Curr. Opin. Cell Biol.*, 10(1):23–34, 1998.

[41] A. Hitt, A. Cross, and R. Williams. Microtubule solutions display nematic liquid crystalline structure. *J. Biol. Chem.*, 265(3):1639 –1647, 1990.

[42] J. Galanis, D. Harries, D. Sackett, W. Losert, and R. Nossal. Spontaneous patterning of confined granular rods. *Phys. Rev. Lett.*, 96(2):028002–5, 2006.

[43] J. Galanis, R. Nossal, W. Losert, and D. Harries. Nematic order in small systems: Measuring the elastic and Wall-Anchoring constants in vibrofluidized granular rods. *Phys. Rev. Lett.*, 105(16):168001–4, 2010.

[44] E. Gartland, P. Palffy-muhoray, and R. Varga. Numerical minimization of the landau-de gennes free energy: defects in cylindrical capillaries. *Molecular Crystals and Liquid Crystals*, 199:429–452, 1991.

[45] Y. Trukhina and T. Schilling. Computer simulation study of a liquid crystal confined to a spherical cavity. *Phys. Rev. E*, 77(1):011701(7), 2008.

[46] F. Wagner, G. Lattanzi, and E. Frey. Conformations of confined biopolymers. *Phys. Rev. E*, 75:050902(4), 2007.

[47] F. Nedelec and D. Foethke. Collective langevin dynamics of flexible cytoskeletal fibers. *New J. Phys.*, 9(427), 2007.

[48] N. Oskolkov, P. Linse, I. Potemkin, and A. Khokhlov. Nematic ordering of polymers in confined geometry applied to DNA packaging in viral capsids. *J. Phys. Chem. B*, 115(3):422–432, 2011.

[49] J. Pardee and J. Spudich. Purification of muscle actin. *Methods Enzymol.*, 85:164–181, 1982.

[50] T. Anhoj, A. Jorgensen, D. Zauner, and J. Hubner. Optimization of SU-8 processing for integrated optics. In *Micromachining Technology for Micro-Optics and Nano-Optics IV*, volume 6110, page 611009. SPIE, 2006.

[51] H. Hillborg and U.W. Gedde. Hydrophobicity recovery of polydimethylsiloxane after exposure to corona discharges. *Polymer*, 39(10):1991–1998, 1998.

[52] V. Sharma, M. Dhayal, S. Govind, Shivaprasad, and S. Jain. Surface characterization of plasma-treated and PEG-grafted PDMS for micro fluidic applications. *Vacuum*, 81(9):1094–1100, 2007.

[53] W. Hellmich, J. Regtmeier, T. Duong, R. Ros, D. Anselmetti, and A. Ros. Poly(oxyethylene) based surface coatings for poly(dimethylsiloxane) microchannels. *Langmuir*, 21(16):7551–7557, 2005.

[54] Edouard Fonck, Georg G. Feigl, Jean Fasel, Daniel Sage, Michael Unser, Daniel A. Rufenacht, and Nikolaos Stergiopulos. Effect of aging on elastin functionality in human cerebral arteries. *Stroke*, 40(7):2552–2556, 2009.

[55] R Singhvi, A Kumar, GP Lopez, GN Stephanopoulos, DI Wang, GM Whitesides, and DE Ingber. Engineering cell shape and function. *Science*, 264(5159):696 –698, 1994.

[56] M. Théry, V. Racine, M. Piel, A. Pépin, A. Dimitrov, Y. Chen, J. Sibarita, and M. Bornens. Anisotropy of cell adhesive microenvironment governs cell internal organization and orientation of polarity. *Proceedings of the National Academy of Sciences*, 103(52):19771 –19776, 2006.

[57] C. Chen, M. Mrksich, S. Huang, G. Whitesides, and D. Ingber. Geometric control of cell life and death. *Science*, 276(5317):1425–1428, May 1997.

[58] J. Viamontes, P. Oakes, and J. Tang. Isotropic to nematic liquid crystalline phase transition of F-Actin varies from continuous to first order. *Phys. Rev. Lett.*, 97(11):118103–4, 2006.

[59] S. Burlacu, P. Janmey, and J. Borejdo. Distribution of actin filament lengths measured by fluorescence microscopy. *Am. J. Physiol. Cell Physiol.*, 262(3):C569–577, 1992.

[60] Y. Liu and B. Chakraborty. Shapes of semiflexible polymers in confined spaces. *Phys. Biol.*, 5(2):026004–12, 2008.

[61] M. Lagomarsino, M. Dogterom, and M. Dijkstra. Isotropic–nematic transition of long, thin, hard spherocylinders confined in a quasi-two-dimensional planar geometry. *J. Chem. Phys.*, 119(6):3535–3540, 2003.

[62] R. van Roij, M. Dijkstra, and R. Evans. Orientational wetting and capillary nematization of hard-rod fluids. *Europhys. Lett.*, 49(3):350, 2000.

[63] H. N. W. Lekkerkerker, Ph. Coulon, R. Van Der Haegen, and R. Deblieck. On the isotropic-liquid crystal phase separation in a solution of rodlike particles of different lengths. *J. Chem. Phys.*, 80(7):3427–3433, 1984.

[64] A. Stroobants. Liquid crystal phase transitions in bidisperse hard-rod systems. *J. Phys.: Condens. Matter*, 6(23A):285, 1994.

[65] R. Sear and G. Jackson. Theory for the phase behavior of a mixture of a rodlike colloid and a rodlike polymer. *J. Chem. Phys.*, 103(19):8684–8693, 1995.

[66] J. Galanis, R. Nossal, and D. Harries. Depletion forces drive polymer-like self-assembly in vibrofluidized granular materials. *Soft Matter*, 6(5):1026–1034, 2010.

[67] P. de Gennes and J. Prost. *The Physics of Liquid Crystals*. Clarendon, Oxford, 1993.

[68] F. Frank. I. liquid crystals. on the theory of liquid crystals. *Discuss. Faraday Soc.*, 25:19–28, 1958.

[69] T. Shimmen and E. Yokota. Cytoplasmic streaming in plants. *Curr. Opin. Cell Biol.*, 16(1):68–72, 2004.

[70] D. DeRosier and L. Tilney. F-Actin bundles are derivatives of microvilli. *J. Cell Biol.*, 148(1):1 –6, January 2000.

[71] J. Bartles. Parallel actin bundles and their multiple actin-bundling proteins. *Curr. Opin. Cell Biol.*, 12(1):72–78, 2000.

[72] A. Liu, D. Richmond, L. Maibaum, S. Pronk, P. Geissler, and D. Fletcher. Membrane-induced bundling of actin filaments. *Nat Phys*, 4(10):789–793, 2008.

[73] D. Courson and R. Rock. Actin crosslink assembly and disassembly mechanics for alpha-actinin and fascin. *J. Biol. Chem.*, 2010.

[74] D. Vignjevic, S. Kojima, Y. Aratyn, O. Danciu, T. Svitkina, and G. Borisy. Role of fascin in filopodial protrusion. *J. Cell Biol.*, 174(6):863 –875, 2006.

[75] A. Reymann, J. Martiel, T. Cambier, L. Blanchoin, R. Boujemaa-Paterski, and M. Théry. Nucleation geometry governs ordered actin networks structures. *Nat. Mater.*, 9(10):827–832, 2010.

Chapter 6

Appendices

Appendices

6.1 Tables

Table A1. Different class II myosins have distinct kinetic behaviors

Skeletal Muscle Myosin II				
Organism	V_{max} (s^{-1})	K_{ATPase} (μM)	Sliding velocity $(\mu m/s)$	Duty ratio (%)
Rabbit	86.1[5]	14 [5]	2.5$^{\pm}$ [6]	$\sim$ 4 [1]
Chicken			4.6$^{\diamond}$ [6]	

Non Muscle Myosin IIA				
Organism	V_{max} (s^{-1})	K_{ATPase} (μM)	Sliding velocity $(\mu m/s)$	Duty ratio (%)
Human	0.17 [3]	72 [3]	0.29 [7]	$\sim$ 5 [3]

Non Muscle Myosin IIB* [8]				
Organism	V_{max} (s^{-1})	K_{ATPase} (μM)	Sliding velocity $(\mu m/s)$	Duty ratio (%)
Human	0.13	59	0.05	23

Non Muscle Myosin IIC* [2]				
Organism	V_{max} (s^{-1})	K_{ATPase} (μM)	Sliding velocity $(\mu m/s)$	Duty ratio (%)
Mouse	0.16	4.6	0.04	—

Smooth Muscle Myosin II				
Organism	V_{max} (s^{-1})	K_{ATPase} (μM)	Sliding velocity $(\mu m/s)$	Duty ratio (%)
Chicken	0.7 [4]	59 [4]	0.58 [1]	$\sim$ 4 [1]

$\pm$ 0.1 mM ATP

$\diamond$ 1 mM ATP

$\star$ non spliced isoforms NMII-B0 and C0

Table 6.1: Summary of literature values for the kinetic parameters of actin-activated MgATPase activity of various types of myosin II. Buffer conditions in which variables were measured are indicated together with the literature reference listed below.

Buffer conditions for references in Table A.1
(see bibliography of *chapter 3*)

Ref.1 ATPase assay: 4 mM Imidazole, 4 mM $MgCl_2$, 10 mM KCl, 1 mM DTT, 1 mM NaN_3, 3 mM NaATP, pH 7.0, $37°C$

Ref.2 In vitro motility: 25 mM Imidazole, 1 mM EGTA, 4 mM $MgCl_2$, 1 mM DTT, 25 mM KCl, 1 mM ATP, pH 7.4, $30°C$

Ref.3- In vitro motility: 25 mM Imidazole, 1 mM EGTA, 4 mM $MgCl_2$, 10 mM DTT, 1 mMATP, pH 7.4 $30°C$

Ref.4 ATPase assay: 10 mM MOPS, 0.15 mM EGTA, 2 mM $MgCl_2$, pH 7.0, $25°C$

Ref.5 In vitro motility: 20 mM MOPS, 0.1 mM EGTA, 5 mM $MgCl_2$, 80 mM KCl, 1 mM ATP, pH 7.4, $30°C$
Ref.6 ATPase assay: 10 mM MOPS, 0.15 mM EGTA, 2 mM $MgCl_2$, 1 mM ATP, pH 7.0, $25°C$

Ref.7 ATPase assay: 20 mM MOPS, 0.1 mM EGTA, 2 mM $MgCl_2$, 0.2 mM CaCl2 1 mM ATP, 50mM DTT pH 7.0, $30°C$

Ref.8 ATPase assay: 5 mM Tris, 1 mM EGTA, 1 mM $MgCl_2$, 10 mM KCl, 0.2 mM $CaCl_2$, 1 mM ATP, pH 7.0, $25°C$

Table A.2 Size of actomyosin condensates

Figure 3B ii					
Motor: actin ratio	$< Size >$ μm	SD μm	N		
1:300	1.75	$\pm$0.72	27		
1:200	2.36	$\pm$1.14	18		
1:50	5.34	$\pm$4.08	39		
ANOVA test	d.f.	SS	MS	F	P
Model	2	239	119	14.4	4.3×10^{-6}
Error	81	669	8.3	—	—
Total	83	808	—	—	—
$P<<0.001$: populations are significantly different					

Figure 3Ci-speed					
Crosslinker: actin ratio	Speed μ/s	SD μm	N		
No crosslinkers	0.10	0.05	3		
1:100	0.63	0.20	4		
1:400	0.51	0.11	2		
1:200	0.03	0.02	4		
Figure 3Cii-size					
Crosslinker: actin ratio	$< Size >$ μm	SD μm	N		
No crosslinkers	2.30	0.91	20		
1:100	1.40	0.89	69		
1:400	0.98	0.28	16		
1:200	1.96	0.92	25		
ANOVA test	d.f.	SS	MS	F	P
Model	3	22	7.4	10.2	4.4×10^{-6}
Error	126	91	0.7	—	—
Total	129	113	—	—	—

d.f. : degrees of freedom; SS: sum of squares; MS: mean square

Table 6.2: Quantification of the size of actomyosin condensates observed in active networks containing varying concentrations of myosin motors (c.f. Fig. 3B) and biotin-streptavidin crosslinkers (c.f. Fig. 3Cii), and quantification of contraction speeds of coalescing condensates (c.f. Fig. 3Ci). Statistical analyses were performed using the ANOVA test in Origin Pro8.

Table A.3 *In vivo* myosin II foci

Contractile ring formation

Organism	Size μm	Reported size	Estimated size	Velocity $\mu m/s$	Reference*
S. pombe	$\leq$0.5 - 1	no	from Fig. 3D	0.03	(3)

Wound healing

Organism	Size μm	Reported size	Estimated size	Velocity $\mu m/s$	Reference*
Xenopus oocyte	1 - 4	no	from Fig. 7C	0.2 - 5.8	(23)

Developing embryos

Organism	Size μm	Reported size	Estimated size	Velocity $\mu m/s$	Reference*
Drosophila	≤ 5	no	from Fig. 3I	none reported	(24)
Drosophila	~ 1	no	from Fig. 1A inset	none reported	(25)
Drosophila	0.5-2	no	from Fig. 1C	0.043$\pm$0.016	(26)

Cortical flows

Organism	Size μm	Reported size	Estimated size	Velocity $\mu m/s$	Reference*
C.elegans	2.21$\pm$1.16	yes: Fig. SI 6C	no	0.24$\pm$0.04	(6)

Numbering following the bibliography list of *chapter 3*

Table 6.3: Summary of reported or estimated sizes of myosin II foci in different organisms and in different cellular or developmental stages. Reference numbers refer to the bibliography of the main text.

References

[1] D. Harris and D. Warshaw. Smooth and skeletal muscle myosin both exhibit low duty cycles at zero load in vitro. *J. Biol. Chem.*, 268(20):14764 –14768, 1993.

[2] S. Jana, K. Kim, J. Mao, S. Kawamoto, J. Sellers, and R. Adelstein. An alternatively spliced isoform of non-muscle myosin II-C is not regulated by myosin light chain phosphorylation. *J. Biol. Chem.*, 284(17):11563 –11571, 2009.

[3] M. Kovacs, F. Wang, A. Hu, Y. Zhang, and J. Sellers. Functional divergence of human cytoplasmic myosin II. *J. Biol. Chem.*, 278(40):38132 –38140, 2003.

[4] S. B. Marston and E. W. Taylor. Comparison of the myosin and actomyosin ATPase mechanisms of the four types of vertebrate muscles. *J. Mol. Biol.*, 139(4):573–600, 1980.

[5] D. Resnicow, J. Deacon, H. Warrick, J. Spudich, and L. Leinwand. Functional diversity among a family of human skeletal muscle myosin motors. *Proceedings of the National Academy of Sciences*, 107(3):1053 –1058, 2010.

[6] Y. Toyoshima, S. Kron, and J. Spudich. The myosin step size: measurement of the unit displacement per ATP hydrolyzed in an *in vitro* assay. *Proc. Nat.l Acad. Sci. of USA*, 87(18):7130 –7134, 1990.

[7] F. Wang, E. Harvey, M. Conti, D. Wei, and J. Sellers. A conserved negatively charged amino acid modulates function in human nonmuscle myosin IIA. *Biochemistry*, 39(18):5555–5560, 2000.

[8] F Wang, M Kovacs, A Hu, J Limouze, EV Harvey, and JR Sellers. Kinetic mechanism of non-muscle myosin IIB: functional adaptations for tension generation and maintenance. *J. Biol. Chem.*, 278(30):27439–27448, 2003.

6.2 Modeling contractility from asymmetric load response

Perhaps surprisingly, microscopically polar, directed motor activity can give rise to net contractility even in macroscopically apolar structures, provided that the load response is asymmetric. Individual actin filaments are highly asymmetric in their response on the micrometer scale, in that they strongly resist extension, yet buckle easily under compressive loads of less than a piconewton. We approximate this load response as that of an inextensible macroscopic rope with zero resistance to compression. For networks of such actin filaments cross-linked on the micrometer scale, the network load response is also expected to be asymmetric. On this scale, such networks are inhomogeneous with loose or floppy regions that we refer to as rope-like structures (RLS). These are analogous to a macroscopic fishnet, which resists extension, but crumples or compresses easily. Such a RLS then supports tensile loads but no compressive loads. This means that only attractive/contractile forces can result from interactions mediated through such a structure.

To illustrate how net contractility can arise from motors interacting with a RLS, we consider the following simple problem. Being random networks, RLS are apolar: at any given point in space, they are likely to have actin filaments of random orientation. Thus, when a motor bind to the RLS, its motion can be regarded as a random walk with a step length that is expected to be small if the motors are non-processive. We first consider two random walkers (RWs) that are rigidly coupled together, e.g. in a large myosin aggregate (see top part of Fig. 6.1A), as we find in stage 2 of myosin driven actin reorganization (see Fig. 3.9B in *chapter 3*). These are allowed to interact with an idealized RLS (see lower part of Fig. 6.1A) that is assumed to be inextensible, but to buckle under the slightest compressive load.

The probability distribution for the contour length s between the RWs kept a fixed distance $x = l$ apart satisfies:

$$\frac{\delta P(s,t)}{\delta t} = D\frac{\delta^2 P(s,t)}{\delta^2}, s > l, P(s,0) = 2\delta(s-l), \frac{\delta P(l,t)}{\delta s} = 0. \tag{6.1}$$

The diffusion constant $D = \Delta s^2/(2\Delta t)$ is set by the step size Δs and stepping time Δt for the RWs. The resulting spreading half Gaussian

$$P(s,t) = \frac{exp{-(s-l)^2/(4Dt)}}{\sqrt{\pi Dt}}, s > l \tag{6.2}$$

gives the average amount of rope pulled in between the RWs as a function of time,

$$\langle s(t)\rangle - l = \sqrt{4Dt/\pi}. \tag{6.3}$$

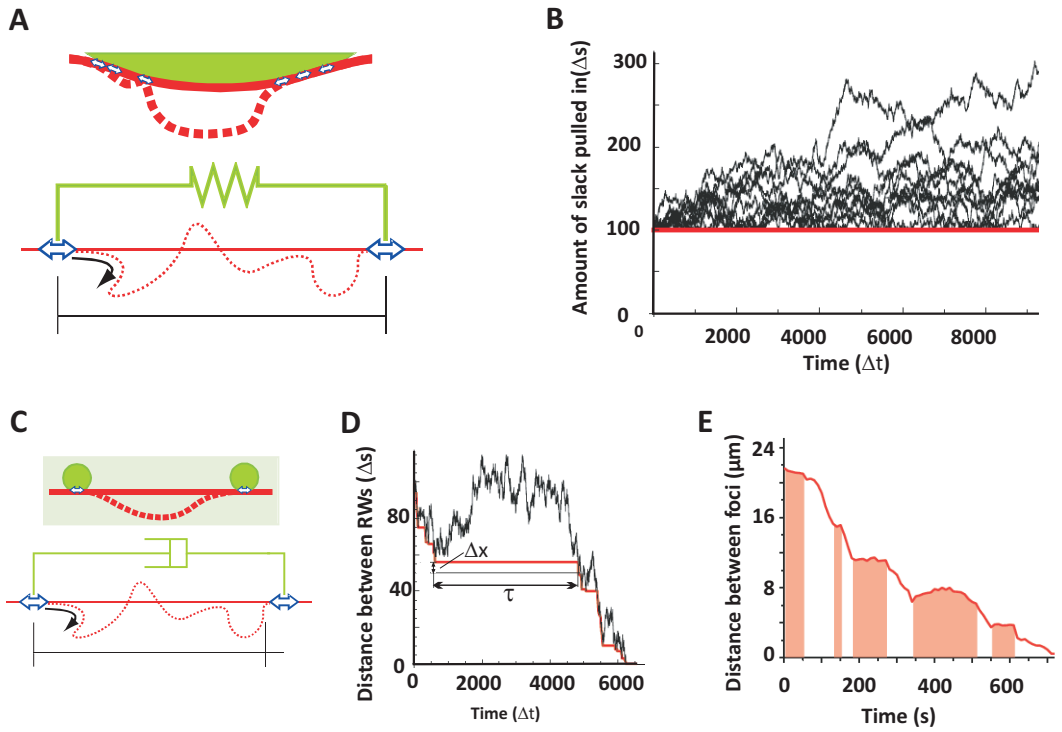

Figure 6.1: **A.** The RLS can either be taut (solid red) or buckled (dotted red) between the random walkers (blue arrows). On top we illustrate a RLS interacting with a larger aggregation of RWs such as present in myosin foci. Below is the idealized model with only two rigidly coupled (green) RWs. Though the walkers are able to push in slack between themselves they are unable to extend a taut RLS. **B.** The amount of RLS contour length between the walkers, s, performs a random walk reflected at $s = l$ (RLS is taut). Here we show time traces for 10 different realizations. **C.** The RLS can either be taut (solid red) or buckled (dotted red) between the random walkers (blue arrows). On top we illustrate two myosin foci immersed in a viscous background and interacting with a buckle prone network structure. Below we show the simplified model describing this situation. The walkers are unaffected by the viscosity coupling them together through the background network (green dash-pot). When the RW both stochastically pull on an already taut RLS, it brings the RWs together. Though the viscous coupling is assumed weak enough not to hinder the motors, it is assumed to be strong enough to induce buckling as soon as the rope is put under compression by the motors. If the RWs randomly compress the RLS, it buckles as material is fed in between the RWs. This excess material has to be pulled out before the RLS can be made taut and move the RWs closer in space. **D.** In black we show a numerical realization of the diffusion of the contour length, and in red the corresponding distance between the RWs. **E.** Experimentally measured distance between the two contracting myosin foci shown in Movie S13. Shaded areas indicate regions where the connecting structure may be under compression, rendering the foci immobile.

The contraction is diffusive, and acts best over short distances. This idealized case where an asymmetric load response leads to contraction over time could be generalized to more realistic situations describing, e.g. myosin filaments in a focus interacting with a disordered actin network structure (see top part of Fig. 6.1A). With a bias, which could be thought of as capturing the network turnover bridging parts of buckled structures, the rate of contraction would remain finite also over large distances. The unbiased model of figure 6.1A is numerically realized 10 times in figure 6.1B, starting with $s = l = 100\Delta s$.

We next consider the case of RWs that are not connected, but interact dissipatively through the background (see Fig. 6.1C)-mimicking, e.g., two myosin foci both interacting with the same buckle prone actin structure and a dissipative background network (corresponding to stage 3 in Fig. 3.9C main text). Simultaneous pulling on a taut structure will bring the walkers together while simultaneous compression will make the RLS buckle and arc-length will be gathered in between the RWs while they remain fixed in space. This asymmetry drives the RWs together over time. According to the above, the contour length between the RWs performs a random walk, while the distance between RWs tracks the minimum distance attained by this random walk up to the present time (see Fig. 6.1D). The probability over the contour distance *s* again satisfies the diffusion equation,

$$\frac{\delta P(s,t)}{\delta t} = D\frac{\delta^2 P(s,t)}{\delta s^2}. \tag{6.4}$$

The transition-time distribution $\Psi(\tau, \Delta x)$ for taking the step in real space $x \to x + \Delta x$, starting with a taut rope $x = s$, can be calculated as:

$$\Psi(\tau, \Delta x) = \frac{\Delta x exp{-\Delta x^2/(4Dt)}}{4\sqrt{\pi D}\tau^{3/2}}. \tag{6.5}$$

The distribution of transition times is broad, with a wide tail falling off as $\frac{1}{\tau^{3/2}}$. The average time to take a step forward diverges in this model, indicating that the dynamics is highly irregular with long pauses to contraction. The average velocity remains positive,

$$\langle v \rangle = \langle \Delta x/\tau \rangle = \int_0^\infty d\tau(\Delta x/\tau \Psi(\tau, \Delta x)) = D/\Delta x \tag{6.6}$$

showing the possibility of rapid contraction over short distances. This simple model can be extended to the situation with multiple RLS connecting the RWs. Here, the distance between RWs would track the minimum contour length attained in any one of the multiple diffusion processes. In figure 6.1E we show an example of an experimentally measured time evolution of the distance between the two contracting myosin foci shown in Movie S13 (see video caption in *appendix 6.3*). The motion is clearly directional, but seems interspersed by pauses of apparent inactivity-as is

the case for the simple model presented here. These simple examples show idealized cases where an asymmetric load response of the material connecting the motors results in an overall net contraction. We could further consider more complex material responses, allowing for reversible and irreversible deformations of the background network and the RLS. The limits we have considered assume the existence of floppy portions of the network with slack that can be ”pulled-out”. While this is expected to be the case for realistic networks, it is not captured by the largely continuum mechanical models that have been used to date to model these networks, usually on larger scales. To the extent that continuum linear elasticity applies, the mechanism we propose would not result in contractility. Continuum mechanics, however, is unlikely to describe well the relatively loose meshwork of filaments expected for our system at the microscopic scale of a few microns.

6.3 Movie captions

Video S1 Reconstruction of a three-dimensional stack of 40 fluorescence images of an actin/myosin condensate formed in stage 2 of the multi-stage coarsening process, obtained using confocal microscopy. Actin (shown in red) accumulates in a dense, disordered shell all around the surface of a globular myosin aggregate (shown in green). The crosslinker:actin ratio is 1:1000 and the myosin:actin ratio is 1:200. Corresponding 2D slices are shown in Fig. 3.5A.

Video S2 Reconstruction of a three-dimensional stack of 50 fluorescence images of a superaggregate of multiple actin (red)/myosin (green) condensates formed in stage 3 of the multi-stage coarsening process, obtained using confocal microscopy. The crosslinker:actin ratio is 1:1000 and the myosin:actin ratio is 1:50. Corresponding 2D slices are shown in Fig. 3.5B.

Video S3 Fluorescently labeled myosin filaments are initially homogeneously distributed throughout the actin network (actin not labeled). In the first 5 minutes after sample preparation (stage 1 of the multi-stage coarsening process), they move in an apparently diffusive fashion either through the mesh or actively in a preferred direction, presumably walking along actin filaments. Myosin filaments that meet sometimes fuse into small aggregates. No crosslinkers were added and the myosin:actin ratio is 1:300. White arrows represent examples of active walks. Movie total duration is 110 s, 10x real frame rate. Scale bar is $10\,\mu\mathrm{m}$.

Video S4 Cropped region of Video S3, where two fluorescently labeled myosin filaments (or small aggregates thereof) fuse upon meeting. Movie total duration is 55 s, 5x real frame rate. Scale bar is $5\,\mu\mathrm{m}$.

Video S5 At the beginning of stage 2 of the multistage coarsening process, two myosin foci in an unlabeled actin network abruptly and permanently coalesce with each other as a result of network contractility. The larger one is virtually immobile while the small one suddenly approaches and merges with it. The crosslinker:actin ratio is 1:1000 and the myosin:actin ratio is 1:200. Movie total duration is 45s, 5x real frame rate. Scale bar is $5\,\mu\mathrm{m}$.

Video S6 During stage 2 of the multistage coarsening process, a ring-like actin pattern incorporates a fragment of the surrounding actin network (indicated by the white arrow; note that myosin is not labeled). The crosslinker:actin ratio is 1:1000 and the myosin:actin ratio is 1:200. Movie total duration is 12 s, 3x real frame rate.

Scale bar is $5\,\mu\mathrm{m}$.

Video S7 An actin condensate incorporates multiple fragments of the surrounding actin network (myosin is not labeled). The crosslinker:actin ratio is 1:1000 and the myosin:actin ratio is 1:200. White arrows represent examples of network fragments being dragged in by the actin ring-like pattern. Movie total duration is 12.3 min, 50x real frame rate. Scale bar is $10\,\mu\mathrm{m}$.

Video S8 Example of a contractile fluctuation event, where two actin ring-like structures move towards each other and suddenly relax (myosin is not labeled). The parallel white arrows indicate the movements towards and away from each other. The crosslinker:actin ratio is 1:1000 and the myosin:actin ratio is 1:200. Movie total duration is 52 s, 10x real frame rate. Scale bar is $10\,\mu\mathrm{m}$.

Video S9 Example of a repeated contractile fluctuation event, where two small actin ring-like structures move towards each other and slowly relax two consecutive times (myosin is not labeled). White circles indicate the beginning of active events. The crosslinker:actin ratio is 1:1000 and the myosin:actin ratio is 1:200. Movie total duration is 117 s, 5x real frame rate. Scale bar is $5\,\mu\mathrm{m}$.

Video S10 Example of a repeated contractile fluctuation event, where two large actin structures move towards each other and slowly relax three consecutive times (myosin is not labeled). White circles indicate the beginning of active events. No crosslinkers were added. The myosin:actin ratio is 1:50. Movie total duration is 104 s, 5x real frame rate. Scale bar is $5\,\mu\mathrm{m}$.

Video S11 Example of a permanent coalescence event, where two actin (red)/myosin (green) condensates coalesce and crumple the actin network between them. The crosslinker:actin ratio is 1:1000 and the myosin:actin ratio is 1:200. The white arrow represents an actin network fragment (in red) that becomes compressed in between the two structures. Movie total duration is 62 s, 10x real frame rate. Scale bar is $10\,\mu\mathrm{m}$.

Video S12 Actin cables form in an actin/myosin network due to contractility. Several actin/myosin condensates appear to be momentarily connected by bundle-like actin structures that collapse when foci approach each other or after foci walk along and drag them. The crosslinker:actin ratio is 1:1000 and the myosin:actin ratio is 1:200. White arrows represent examples of such cables emerging. Movie total duration is 22.7 min, 100x real frame rate. Scale bar is $10\,\mu\mathrm{m}$.

Video S13 Example of a myosin focus coalescing in an intermittent fashion with a cluster of foci. The crosslinker:actin ratio is 1:1000 and the myosin:actin ratio is 1:200. The white circle indicates the focus moving towards the cluster in formation. Movie total duration is 16.5 min, 100x real frame rate. Scale bar is $5\,\mu\mathrm{m}$.

Summary

There are infinite numbers of natural *matrioskas* in our Universe. Inside our cosmos there are planets. Our planet happens to be the home to numerous species of living organisms. And the latter are made of building blocks named cells. Cells are the actual fundamental units that store the genetic information which defines an organism's body plan. A larger amount of genetic information paves way for more complexity and contrary to simple unicellular bodies like bacteria, cells of higher order organisms can cooperate with each other to organize into structures as complex as thousands of years old forests of aspen, a whale or a human brain.

In multicellular organisms, cells act as small autonomous, but not independent, machines. By dividing and moving, especially during an organism's early development, cells organize together to form the adequate body form. This is only possible because, far from being a little "bag of water", a cell contains components that both maintain shape and allow for dynamic changes in shape. The material that is primarily responsible for such plasticity is the actin cytoskeleton. The actin cytoskeleton is a three dimensional "fishnet-like" structure of filamentous proteins which provides the cell with mechanical integrity. Actin filaments assemble by addition of monomeric units at both ends of the polymer. However, as one end grows at a faster rate, it is named the plus end. These filamentous proteins can organize into different higher order structures (review Fig. 5.13). So-called filopodia, fine tubular membrane extensions filled with actin filaments, allow cells to probe the surrounding environment. Lamellipodia are sheet-like protrusions at the front of motile cells which propel cells forward. In addition to these actin assemblies, dividing cells form rings of actin at their middle which serve to constrict the cell and help pinch off two daughter cells. Such rings are contractile due to the presence of myosin II. This molecular motor protein is able to transform chemical energy (ATP) into mechanical force which remodels the organization of actin filaments. Myosin II molecules have a tail domain and two head or motor domains. These domains function as hands and arms

pulling on a rope as they walk toward the plus end of actin filaments. Under physiological conditions, myosin tails attach to each other and form bipolar filament structures. The head domains are at the two ends and attach to actin filaments. As ATP, the energy source, binds to these head domains, they change conformation to pull on the actin filaments. The movement resembles the arms and hands of a person pulling on a rope to dock a boat. Instead of a single pair of hands/arms, myosin bipolar filaments have up to hundreds of myosin head domains pointing in opposite directions which allows them to tug on the surrounding actin network and rearrange its architecture. In fact, many processes regulating cellular shape are driven by myosin II-dependent rearrangements of the actin cortex. These include the formation of stress fibers or the contractile cortex at the rear ends of migrating cells. However, it is unclear how motor-generated forces reorganize networks of actin filaments to generate functional contractile structures.

The aim of my PhD research was to understand how physical mechanisms on the molecular scale lead to structural changes in the actin network and translate into active behavior at the cellular scale. To investigate the structure of active networks, I performed confocal microscopy of minimal *in vitro* networks of purified fluorescently labeled actin and myosin proteins. I characterized the dynamics of these networks using microrheology approaches, and elucidated the effect of membrane confinement on the structure of the actin cortex by polymerizing actin inside cell-sized hardwall microchambers. *Chapter 2* provides a summary of protein characterization techniques and of the *in vitro* approaches used.

In *chapter 3*, to elucidate the mechanisms which govern the formation of contractile actin structures, I set up a simplified model of the actin cortex that is devoid of biochemical regulation. This minimal model is composed of fluorescently labeled skeletal muscle myosin and actin proteins. I was able to show with time-resolved confocal microscopy that contractile activity of the motors resulted in actin network coarsening through a process of condensation-like steps. First, myosin motors form dense foci by moving along the actin network and permanently coalescing. Once myosin clusters are immobilized in the network, they accumulate actin filaments in a shell around them. Eventually, these intermediate actin-myosin clusters coalesce as a consequence of motors pulling on surrounding actin filaments that are not fully straightened and still thermally fluctuate.

We propose that the physical origin of this multistage cluster formation is the highly asymmetric response of actin filaments to force. While actin filaments can support large tensions when they are stretched, they easily buckle under minute compressive forces. In networks where actin filaments are weakly attached to each other, the connected network buckles under the tugging forces of the myosin motor-generated forces which are much larger than the buckling threshold. The same buckling effect of actin leads to the coalescence of isolated actin-myosin clusters into larger superaggregates. The resulting structures bear a striking resemblance to the structure and dynamics of myosin clusters observed in various types of living cells. Such in vivo foci are involved in myosin-dependent morphogenetic processes and in cell division. Our results suggest that this characteristic organization of actomyosin networks is an intrinsic outcome of the forces exerted by myosin motors on actin filaments.

Learning about the mechanism underlying motor-driven actin reorganization made it possible to quantitatively investigate the spatiotemporal characteristics of actomyosin network dynamics. In *chapter 4*, I thus focused on the microrheological properties of active networks by imaging and video tracking of embedded inert microspherical probes. This study provided insight into the out-of-equilibrium network fluctuations caused by myosin contractile activity, which is superposed on the omnipresent thermal jittering common to all natural systems.

I observed non-thermal microsphere trajectories, with periods of non-directed (random) motion interspersed with episodes of active, directed motion. These clear signatures of the contractile activity of the motors in the form of bouts of sudden, directed motion of the probes were usually followed by relaxation. These motions reflect the biochemical cycle of the myosin filaments. In contrast to assumptions of network homogeneity made in existing active gel theories, the motor-driven forces propagate in a highly heterogeneous filamentous network. These physical properties may contribute to the non-continuous, pulsatile cell shape changes that have been observed during morphogenetic events in developing embryos.

We developed new automated analysis to segment microsphere particle trajectories into active and non-active portions of the movement. This analysis allowed us to identify a pronounced age-dependence of activity. During the first 30 minutes after sample preparation, I observed fre-

quent periods of sustained directed motion, whereas at later times such directed motion became very infrequent. This sample age-dependence was consistent with the ensemble averaged dynamics of the particles, which showed a transition from large mean square displacements and non-Gaussian displacement distributions of beads at early times, to dynamics resembling that of passive (no myosin) samples at later times. The time-dependence of the active dynamics also matches the time-dependence of motor-driven coarsening of the actin network that I describe in *Chapter 3*. Detailed analysis of the translocation and relaxation of probe particles indicated that network coarsening is accompanied by large displacements of beads and plastic deformation of the network, as evidenced by incomplete relaxation. This study provides the first quantification of active network dynamics *in vitro* correlated with network structure, revealing the dynamic processes that lead to specific steady state configurations. It will be interesting to extend existing theories of active gel dynamics to account for the time-dependent and spatially inhomogeneous structure of actin-myosin gels and to explore implications of this coupling between structure and dynamics for the microrheology of cells.

In *chapter 5*, I focused on how pure physical constraints influence actin network organization. In addition to the influence of actin binding proteins, actin filaments are also subject to physical effects such as steric interactions imposed by the packing constraints of filaments at high actin density and the spatial confinement of filaments within the cell boundaries. I investigated how these physical constraints influence the spatial organization of dense solutions of actin filaments *in vitro*. Fluorescent actin was polymerized in cell-sized microchambers with nonadhesive walls at varying actin densities. Confocal micrographs revealed that actin filaments spontaneously organize into dense, bundle-like structures above a threshold concentration of 1 mg/ml. This contrasts with the behavior of unconfined networks, which are homogeneous and undergo a bulk isotropic-to-nematic phase transition above 5 mg/ml. In confinement, bundles align with the longest axis of anisometric chambers and with the diagonal in isometric chambers.

We propose a mechanism of bundling based on the concerted effect of quasi-2D confinement of the longest filaments in a mix of filaments with an exponential length distribution, and depletion interactions induced by the shortest filaments. The short filaments cause an attraction between the long filaments by a crowding (depletion) effect, and the long

filaments are confined in-plane. Quasi-2D confinement was sufficient to cause bundling in chambers with a depth comparable to the mean filament length. This mechanism differs from the isotropic-to-nematic transitions previously observed in bulk actin networks. We propose that the steady-state orientation of the bundles results from a competing liquid-crystalline ordering in the chamber center and alignment along the boundaries. This ordering effect of confinement might influence cytoskeletal organization in vivo. Cellular actin concentrations can be as high as 10 mg/mL which could promote local bundling in confining cell compartments such as the plant cell cortex or membrane protrusions.

I expect that building a more realistic actin-cytoskeleton could further help to elucidate the physical basis of cellular shape control. Combining confinement with polymerization of active actin-myosin gels would thus be a logical follow-up assay to understand the effect of boundaries mimicking the cell membrane on the active organization of the actin cytoskeleton. It will be important to modulate also network connectivity by adding crosslinking proteins or factors that regulate the filament length.

Samenvatting

De structuur en dynamica van actieve actine-myosine netwerken een *in vitro* perspectief

Het universum herbergt oneindig veel natuurlijke matroeskjas. In ons heelal bestaan planeten en onze planeet is een thuis voor een enorme diversiteit van levende organismen. De bouwstenen van deze organismen zijn weer cellen. De cel is de fundamentele eenheid van elk organisme, immers hier is de genetische informatie, die de verschijningsvorm van ieder organisme definieert, opgeslagen. Een hoge complexiteit van een organisme gaat vaak gepaard met een grote hoeveelheid genetisch informatie n, in tegenstelling tot simpele eencellige organismen zoals bacteriën, kunnen cellen van hogere orde organismen samenwerken en zich organiseren in meercellige ingewikkelde structuren, zoals een duizendjarige boom, een walvis of de menselijke hersenen.

Elke cel van een meercellig organisme werkt als een autonome, maar niet onafhankelijke machine. De correcte lichaamsvorm van een organisme onstaat doordat cellen zichzelf door celdeling en beweging ordenen, vooral tijdens de vroege ontwikkelingsfase van een organisme. Dit kan alleen omdat cellen componenten hebben die zowel zorgen voor het behoud van de specifieke celvorm als voor het actief wijzigen van diezelfde vorm; cellen zijn dus absoluut niet slechts *gevulde zakjes water*. Voor deze plasticiteit is voornamelijk het actine-cytoskelet verantwoordelijk. Dit is een drie-dimensionale, visnetachtige, structuur van draadvormige eiwitten, dat de cel voorziet van zijn mechanische stevigheid. Deze draadvormige eiwitten, zogenaamde actine filamenten, groeien doordat van beide kanten monomeren aan het actine polymeer plakken. Aangezien één uiteinde van het polymeer harder groeit dan het andere, wordt dit uiteinde het plus-eind genoemd. Deze filamenten kunnen verschillende hogere orde structuren vormen (zie Fig. 5.14), bijvoorbeeld filopodia en lamellipodia. Met behulp van filopodia, kleine, cilindervormige, met actine filamenten gevulde membraan-uitstulpingen, kunnen cellen hun omgeving aftasten. Lamellipodia zijn tapijtachtige

uitstulpingen aan de voorkant van bewegende cellen, die de cel voortbewegen.

Actine vormt ook verschillende structuren die zorgen voor actieve samentrek van de cel. In het midden vormt een delende cel een ring van actine eiwitten, die dient om de cel samen te trekken en zo twee dochtercellen te creëren. De samentrekking van deze actine-ring gebeurt onder invloed van het eiwit myosine II. Dit eiwit is een moleculaire motor en kan, een mechanische kracht uitoefenen op de actine filamenten. Myosine II eiwitten hebben één staart domein en twee hoofd, of motor, domeinen. De trekkracht wordt verkregen doordat ATP, de energiebron van de cel, bindt aan de hoofddomeinen en daardoor een conformatie verandering van deze domeinen veroorzaakt.

In fysiologische condities komen tientallen tot honderden myosine motoren met hun staart aan elkaar tot een bipolair filament. In een bipolair filament bevinden de hoofddomeinen zich aan de uiteinden en binden daar aan actine filamenten. De beide myosine uiteinden trekken aan twee antiparallelle actine filamenten in een tegenovergestelde richting. Dit is enigszins vergelijkbaar met iemand die haar boot naar de kant trekt bij het instappen. Om naar het plus-eind van een actine filament te lopen, grijpen deze hoofddomeinen het filament en trekken dit naar zich toe, zoals iemand die aan een touw trekt. In tegenstelling tot een mens met slechts één paar handen, hebben de myosine II bipolaire filamenten honderden paren hoofddomeinen, die in tegenovergestelde richtingen wijzen. Hierdoor kunnen deze motor-filamenten effectief aan het omringende actine netwerk trekken en zo de structuur van dat netwerk veranderen. Deze actieve reorganisatie is cruciaal voor allerlei verschillende processen aan, die allemaal verantwoordelijk zijn voor de celvorm. Tot deze processen behoren onder andere de vorming van stress-vezels en de samentrekkende cortex aan de achterkant van bewegende cellen. Echter, onduidelijk is hoe myosine-motor gedreven krachten het netwerk van actine filamenten reorganiseren om functionele contractiele structuren te krijgen.

Het doel van mijn promotie-onderzoek was om inzicht te krijgen in de fysische mechanismes op de moleculaire schaal die leiden tot de structurele veranderingen in het actine netwerk op celniveau. Om de structuur van actieve netwerken te onderzoeken, heb ik met confocale microscopie minimale *in vitro* eiwit-netwerken van gezuiverd actine and myosine II, beiden gemarkeerd met een fluorescerende kleurstof, bestudeerd.

Vervolgens heb ik, met behulp van microreologie, de dynamische eigenschappen van deze netwerken gekarakteriseerd. Als laatste heb ik de gevolgen van van de actine cortex opsluiting binnen een kleine ruimte ter grootte van een typische cel verhelderd. Dit heb ik gedaan door actine te polymerizeren in zogenaamde micro-kamers, een ruimte die qua afmeting vergelijkbaar is met een cel, maar die een harde wand heeft.

Om de mechanismen op te helderen die zorgen voor de vorming van samentrekkende actine structuren, heb ik in hoofdstuk 3 een nieuw vereenvoudigd model van de actine cortex ontwikkeld. Dit model bestaat slechts uit twee componenten, myosine II eiwit en actine eiwit. Beide componenten zijn verkregen uit skeletspieren en zijn daarna zichtbaar gemaakt met een fluorescerende kleurstof. Met behulp van tijdopgeloste confocale fluorescentie-microscopie heb ik laten zien dat de samentrekkende eigenschap van de motoren leidt tot een clustering van het netwerk via een serie van condensatie-achtige stappen. In de eerste stap hopen de myosine motoren zich op, doordat ze over het netwerk lopen en aan elkaar vastplakken, waardoor balletjes (ofwel foci) met een hoge dichtheid ontstaan. In de tweede stap, als deze balletjes zo groot zijn dat ze in het actieve netwerk geïmmobiliseerd raken, trekken ze actine filamenten aan en deze filamenten vormen een schil rondom de myosine motoren. In de laatste stap fuseren deze balletjes samen tot grotere clusters, doordat de motoren trekken aan actine filamenten die nog niet volledig zijn uitgestrekt en daarom nog thermisch fluctueren.

We stellen een simpel fysische mechanisme voor ter verklaring van dit fenomeen, gebaseerd op de sterk asymmetrische reactie van actine filamenten op externe krachten. Actine filamenten kunnen grote trekspanningen weerstaan, maar ze buigen zodra ze zachtjes worden ingedrukt. Dit betekent dat in netwerken waarin de actine filamenten zwak aan elkaar zijn gekoppeld, delen van het netwerk eenvoudig buigen door de trekkrachten die door myosine motoren worden uitgeoefend. Ditzelfde buigeffect leidt ook tot de vorming van superclusters van actine-myosine foci. De patronen die het gevolg zijn van de hierboven beschreven processen vertonen opmerkelijke overeenkomsten met de structuren en de dynamica van myosine clusters in verschillende typen levende cellen. Dit soort clusters lijken een rol te spelen in verscheidene morphogenetische processen en ook gedurende celdeling. Onze resultaten suggereren dat deze karakteristieke organisatie van het actine-myosine netwerk een resultaat is van de intrinsieke krachten die myosine motors op de actine filamenten uitoefenen.

Doordat we het mechanisme dat ten grondslag ligt aan motor gedreven actine reorganisatie begrepen, werd het mogelijk om ook kwantitatief zowel de ruimtelijke als tijd afhankelijk eigenschappen van de dynamica van het actine-myosine netwerk te bestuderen. Ik heb me geconcentreerd op de microreologische kenmerken van actieve netwerken, door inerte minuscule bolletjes in de netwerken in te bedden en deze te volgen met een microscoop. De resultaten hiervan staan in hoofdstuk 4 beschreven. Dit onderzoek geeft inzicht in de niet-evenwichts fluctuaties van het netwerk, die worden veroorzaakt door de samentrekkende activiteit van myosine. Deze fluctuaties bestaan naast de alomtegenwoordige thermische fluctuaties.

Met microreologie was het mogelijk om de niet-thermische paden, die de minuscule bollen aflegden, te volgen. Deze paden bestonden uit periodes van ongerichte (willekeurige) beweging, afgewisseld met periode van actieve gerichte beweging. Deze duidelijke tekenen van de samentrekkende activiteit door de motoren werden meestal gevolgd door periodes van passieve ontspanning van het netwerk. Deze bewegingen geven een fraaie weergave van de krachten die de myosine filamenten oorzaken op het actine netwerk. In tegenstelling tot de aannames die worden gedaan in bestaande active gel theorieën, verspreiden de krachten zich in dit experimentele model door een sterk heterogeen draadvormig netwerk. De fysische eigenschappen van deze netwerken en motoren zouden zijn waarschijnlijk de onderliggende oorzaak van de niet-continue, pulserende veranderingen van celvorm, die zijn waargenomen tijdens morphogenetische processen in ontwikkelende embryo's.

We hebben een nieuwe, geautomatiseerde analysemethode ontwikkeld om de paden van de bolletjes te splitsen in de actieve en niet-actieve beweging. Hierdoor was het mogelijk om te meten hoe de mate van actieve beweging afhing van de leeftijd van het monster. Tijdens de eerste dertig minuten na monster preparatie heb ik frequente periodes van gerichte beweging waargenomen, terwijl ik deze beweging na een langere wachttijd zelden zag. Deze leeftijdsafhankelijkheid is consistent met het gemiddelde gedrag van alle bolletjes. Dit gedrag vertoont een overgang van een grote gemiddelde kwadratische verplaatsing en niet-Gaussische verplaatsings distributies van de minuscule bollen vlak na monster preparatie, naar, op latere tijdstippen, dynamische karakteristieken die meer lijken op een passief (zonder myosine) monster. De tijdsafhankelijkheid van de actieve dynamica komt ook overeen met de

tijdsafhankelijkheid van de clustering door myosine, zoals beschreven in hoofdstuk 3. Een gedetailleerde analyse van de verplaatsingen, door samentrekking en ontspanning van het netwerk, laat zien dat de clustering van het netwerk gepaard gaat met grote verplaatsingen van de bollen en plastische deformatie van het netwerk. Dit laatste blijkt uit de incomplete ontspanning van het netwerk. Dit onderzoek laat zien dat actieve dynamica gekoppeld is aan veranderingen in netwerk architectuur. Het is interessant om de huidige theorieën die actieve gelen beschrijven uit te breiden en ook toe te passen op de tijdsafhankelijke en ruimtelijk inhomogene actine-myosine gelen. Daarnaast kunnen de implicaties van de koppeling tussen structuur en dynamica voor de mechanische eigenschappen van cellen worden onderzocht.

In hoofdstuk 5 heb ik me tenslotte gericht op de vraag wat de invloed van fysieke beperkingen op het actine netwerk is. Behalve door de eiwitten die actine binden, worden actine filamenten ook beïnvloed door sterische wisselwerking. Deze interacties zijn een gevolg van de beperkte stapelmogelijkheden bij een hoge actine concentratie en van de tegelijkertijd beperkte ruimte binnen een cel. Ik heb onderzocht hoe zulke fysieke belemmeringen de ruimtelijke organisatie van sterk geconcentreerde actine oplossingen *in vitro* beïnvloeden. Hiervoor heb ik fluorescerend actine in verschillende concentraties in micro-kamers met niet-plakkende wanden gepolymeriseerd. Op confocale afbeeldingen is duidelijk te zien dat de opgesloten actine filamenten spontaan bundelachtige structuren met een hoge dichtheid vormen, boven een minimum concentratie van 1 mg/ml. Dit in tegenstelling tot het gedrag van de filamenten in onbegrensde homogene actine netwerken, waarin bij concentraties boven 5 mg/ml een isotrope-naar-nematische faseovergang plaats vindt. De bundels lijnen, in de beperkte ruimte van de microkamer, op met de langste as in anisometrische kamers en met de diagonaal in isometrische kamers.

Gebaseerd op mijn metingen, stellen wij een bundelmechanisme voor dat is gebaseerd op een combinatie van factoren. In een mix van filamenten met een exponentiële lengte verdeling, ontstaat bundeling van de langste filamenten door een quasi-2D ruimtebeperking, en door het feit dat de korte filamenten delen van de beperkte ruimte bezetten. Doordat een gedeelte van de ruimte wordt bezet door de korte filamenten en de lange filamenten beperkt zijn tot bewegingen in een 2D-vlak ontstaat een aantrekkingskracht tussen de lange filamenten. In microkamers met een hoogte gelijk aan of kleiner dan de gemiddelde filament lengte, is de

quasi-2D ruimtebeperking voldoende om bundeling te veroorzaken. Dit mechanisme verschilt van de isotroop-naar-nematische overgang zoals die eerder is waargenomen in onbegrensde actine netwerken.

Wij stellen voor dat de steady-state oriëntatie van de bundels het gevolg is van concurrende effecten die met elkaar in competitie zijn, namelijk de vloeistof-kristal ordening in het centrum van de microkamer en, dichtbij de kamerwand, de uitlijning van de bundels met deze wand. Het effect van een beperkte ruimte op de netwerk architectuur kan ook invloed hebben op de architectuur van het cytoskelet in de cel. Actine concentraties in een cel kunnen hoger zijn dan 10 mg/ml, wat waarschijnlijk voldoende is om lokaal bundels te vormen op plaatsen met ruimtegebrek, zoals in membraan uitstulpingen en de dunne cortex van een plantencel.

In de toekomst is het interessant om een combinatie te bestuderen van actieve netwerken met myosin in opsluiting in micro-kamers, om te achterhalen hoe motor-activiteit en fysieke beperkingen samen de architectuur van het cytoskelet bepalen